Selective and sensitive electrochemical detection of the Human Epidermal Growth Receptor 2 breast cancer biomarker, using Co (II) phthalocyanine-nanoparticle based platforms.

A thesis submitted in fulfilment of the requirements for the degree

of

Doctor of Philosophy (PhD)

in

Chemistry

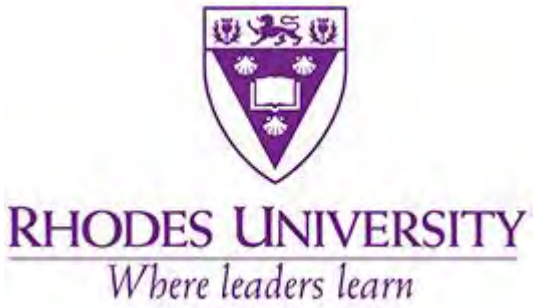

Sixolile Sibongiseni Centane

Supervisor

Distinguished Professor Tebello Nyokong

December 2023

Acknowledgements

Now to Him who is able to do exceedingly abundantly above all that we ask or think, according to the power that works in us, to Him be glory...

-Ephesians 3:20-21

I would like to extend my outmost and heartfelt gratitude to my supervisor Professor Tebello Nyokong, for her commitment and guidance throughout my PhD journey.

I would like to thank Prof Mack, Prof Philani Mashazi, Dr Britton, Mr Francis Chindeka and Miss Gail Cobus, for their support and help during the course of this research.

I am grateful to my good friends Dr Yolande Openda and Dr Aviwe Magadla for their constant support and push throughout my journey in and out of the academic space.

A special thanks to Dr Nobuhle Ndebele and Dr Azole Sindelo for making my PhD journey worthwhile, in ways I could never put in words.

Thank you to Rhodes University Chemistry Department staff members and students.

A special thanks to Dr Van Niekerk and Marvin Randall at the Rhodes University EM unit.

Thank you to my colleagues from the Tebello Nyokong Institute of Nanotechnology Innovation.

I am grateful for financial support from the National Research Foundation (NRF) of South Africa through DST/NRF South African Research Chairs Initiative for Professor of Medicinal Chemistry and Nanotechnology (UID 62620).

Preface

Breast cancer is the world's leading cause of cancer related deaths in women worldwide. The main reason lies in its late detection, mostly in the metastatic stage resulting in poor after-therapy prognosis, despite advances in methods of diagnosis and therapy. The reason for late-stage detection, is because breast cancer like any other cancers is asymptomatic in its early stages. Significant and characterizable features present in the later stages. Furthermore, conventional methods for breast cancer detection are more useful in the identification of the phenotypic features of cancer cells that arise at a later stage of the disease. Another issue with conventional methods where cancer diagnosis is concerned is that they tend to be specialist-dependent, time consuming and costly. Thus, easy, fast and inexpensive detection methods need to be developed urgently. Biomarker-based cancer diagnosis has emerged as one of the most promising strategies for early diagnosis, monitoring disease progression, and subsequent cancer treatment. This thesis focuses on the design and development of novel electrochemical biosensor platforms towards the low cost, efficient, sensitive and simple detection of early-stage breast cancer biomarker, human epidermal growth factor 2 (HER2). The electrochemical method is preferred because of its moderate cost, rapid response, ease of operation, readily quantifiable signal as well as high sensitivity and selectivity with lower detection limits. This thesis reports on two strategies towards signal amplification and sensitive detection of HER2, namely signal based amplification and target-based amplification. The former focuses on electrode or transducer modification techniques for

improved signal to noise ratio. In which case; novel nanocomposites of phthalocyanines, graphene quantum dots, gold nanoparticles and cerium oxide nanoparticles are used for electrode modification for signal amplification and biorecognition element immobilization. The biorecognition elements of choice, are an aptamer and antibody known to be specific to the HER2 antigen for an enhanced sensor sensitivity and specificity. The second strategy focuses on increasing the number of detectable targets on the electrode surface towards enhanced sensitivity, precision and sensor accuracy. In which case; the performance of the aptamer and the antibody as recognition elements was explored. Furthermore, the effect of arrangement of these recognition elements on the electrode surface is investigated and reported upon. The strategies covered in this thesis are expected to result in novel biosensor platforms that can detect the HER2 biomarker with high precision, reproducibility, sensitivity and stability; towards low cost and effective early-stage breast cancer diagnostic tools.

Contents

Table of Contents

Chapter 1

Chapter 2

List of abbreviations

BE = binding energy

BSA = bovine albumin serum

CeO_2NPs = cerium oxide nanoparticles

CoP-BNF = cobalt porphyrin binuclear framework

CoPc = cobalt phthalocyanine

CV = cyclic voltammetry

DBU = 1,8-Diazabicyclo [5.4.0] undec-7-ene

DMF = dimethylformamide

DMSO = dimethylsulphoxide

EIS = electrochemical impedance spectroscopy

EDC = 1-ethyl-3-(3-dimethylaminopropyl) carbodiimide

FTIR = Fourier transform infra-red

GCE = glassy carbon electrodes

GQDs = graphene quantum dots

HER2 = human epidermal growth factor receptor 2

H_2P = free base porphyrin

MPcs = metallophthalocyanines

NP = nanoparticles

NHS = N-hydroxy succinimide

PBS = phosphate buffer saline

PPy = polypyrrole

SEM = scanning electron microscopy

SNGQDs = sulphur nitrogen doped graphene quantum dots

TEM = transmission electron microscopy

UV/vis = ultraviolet/visible

XPS = X-ray photoelectron spectroscopy

XRD = X-ray diffraction

List of Symbols

C = concentration

R_{ct} = charge transfer resistance

D = diffusion coefficient

Cdl= double layer capacitance

A = electrode surface area.

eV = electron volt

F = Faraday's constant

f = frequency

Z" = imaginary impedance

I_D= intensity of Raman D band

I_G= intensity of Raman G band

n = number of electrons

ΔE = Peak potential separation

Z' = real impedance.

R_s= solution resistance

δ = standard deviation

Γ = surface coverage

W = Warburg Impedance

Abstract

This thesis reports on the design and development of novel biosensor platforms towards the electrochemical detection of HER2 on a glassy carbon electrode (GCE). Electrochemical biosensors combine the sensitivity and selectivity of a sensor or biosensor surface. The biorecognition element in the sensor recognizes an analyte and produces an electrical signal which is proportional to the analyte concentration. Herein, the GCE transducer is modified with various nanocomposites based on novel cobalt based phthalocyanines, a cobalt binuclear porphyrin, sulphur nitrogen doped graphene quantum dots, gold nanoparticles and cerium oxide nanoparticles for signal amplification and immobilization of HER2 antigen biorecognition elements for sensitive and selective detection. Various electrode modification strategies including, electropolymerization, binary nanocomposites and adsorption were explored for maximum electron transfer and signal transduction of the designed nanomaterial and related composites. On the modified electrodes, an aptamer and antibody were immobilized accordingly as the biorecognition elements, for enhanced specificity and selectivity of the designed sensors. Electrochemical impedance spectroscopy (EIS) was employed for characterization of the sensors, as well as the determination of limit of detection and sensitivity values of each sensor. The sensors were able to detect HER2 with high sensitivity and LOD values lower than the 15 ng/mL cut off value. The potential in real-life applicability of the designed sensors was proven by detection of HER2 in human serum samples. The designed sensors showed good stability and accuracy towards HER2. Furthermore, the sensor surfaces were successfully regenerated proving to be reusable and applicable toward low cost and simple detection of HER2. Overall, the designed probes have considerable potential as diagnostic tools for early breast cancer.

1. Introduction

This chapter provides background information and an overview of electrochemical biosensors, including their construction and characteristics towards the electrochemical detection of the human epidermal growth factor receptor 2 (HER2). Metallophthalocyanines, metalloporphyrins, graphene quantum dots, gold nanoparticles and cerium oxide nanoparticles are introduced as electrode modifiers for signal amplification and biorecognition element immobilization platforms towards sensitive detection of HER2, an early-stage breast cancer biomarker. For the first time, the said nanomaterials in combination with an aptamer and/or an antibody are used, on a glassy carbon electrode for the design and development of breast cancer early diagnostic tools. This chapter further describes the objectives and summary aims of this thesis.

1.1. Background: Breast Cancer

Breast cancer is a kind of malignant tumour that mainly appears in the inner lining of milk ducts, epithelial tissues, or lobules with different degrees of spread, invasiveness, and heredity [1,2]. Breast cancer is also the leading cause of cancer-related mortality in females, worldwide [3,4]. For effective treatment, reliable and efficient diagnosis is necessary. The earlier cancer can be detected, the better the chance of a cure. Currently, many cancers are diagnosed only after they have metastasized throughout the body [5,6]. At present, the main diagnostic techniques available for the detection of breast cancer are mammography [7], breast ultrasound [7,8], and magnetic resonance imaging (MRI) examination [7,9]. However, these methods require professional practitioners and are expensive. Furthermore, the said clinical methods tend to be invasive and taxing on the patients [10]. As a result, it remains a critical challenge and an unmet need to establish minimally invasive, simple, rapid, and economical techniques for the early diagnosis of breast cancer. In this context, cancer biomarkers, which can be readily obtained from the patient's body fluids, offer the possibility of a "liquid biopsy" for cancer diagnosis, health monitoring, and personalized treatment [11,12].

1.1.1. Biomarkers for Breast Cancer Diagnosis and Management

The National Cancer Institute (NCI) defines a biomarker as "a biological molecule found in blood, other body fluids, or tissues that is a sign of a normal or abnormal process or of a condition or disease. A biomarker may be used to see how well the body responds to a treatment for a disease or condition" [13]. Cancer biomarkers are potentially one of the most valuable tools for early cancer detection [14]. Biomarkers provide information about how cancer develops and progresses in the body. Blood, urine, saliva, and other body fluids all

contain biomarkers [15], and can be used as analytes in sensor development. Various scientific studies have listed some promising single biomarkers. At present, there are only four Food and Drug Administration (FDA) approved established breast cancer biomarkers for assessing breast cancer in bodily fluids [16,17]: cancer antigens (CA); CA 15-3, CA 27-29, Human Epidermal Growth Factor 2 (HER2), and circulating tumour cell (CTC).

1.1.2. Human Epidermal Growth Factor Receptor 2 (HER2): Role in Breast Cancer

HER2 is a cell membrane protein receptor mediated by the transmission of signals controlling normal cell growth and differentiation [18]. In general, the number of existing HER-2 cell membrane receptors in normal cells is small (**Fig. 1.1a**). When the number of HER-2 receptors is high, the cell signalling is stronger (**Fig. 1.1b**), leading to amplified responsiveness to epidermal growth factors and carcinogenesis (**Fig. 1.1c**) [19].

HER2 is highly expressed in around 20-30% of breast cancer tumours [20], and the outcome of that is a more aggressive ailment, augmented mortality, and higher recurrence rate [21,22]. HER2 amplification is seen in nearly half of all in situ ductal carcinomas without any evidence of invasive disease and HER2 status is maintained during progression to invasive disease, nodal metastasis, and distant metastasis [23]. This then qualifies HER2 as an early-stage breast cancer biomarker, that is measurable and can be utilized to determine the appropriate treatment and therefore improve overall outcome of breast cancer patients.

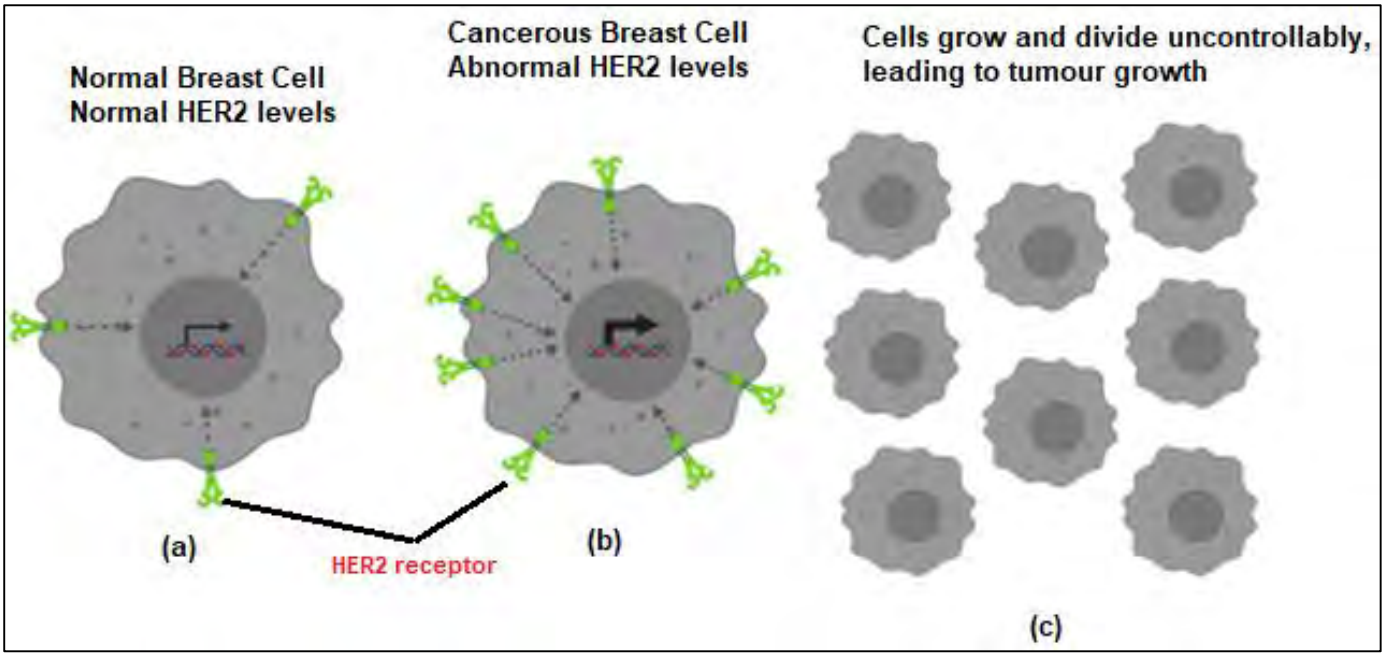

Figure 1.1. HER2 receptors send signals to cells in charge of cell growth (a), thus in breast cancer it causes cells to grow and divide uncontrollably (b), leading to tumour growth (c) [19].

HER2 testing is a standard procedure for all new breast cancer diagnoses, as well as in case of tumour progression and/or residual tumour after neoadjuvant treatment [24]. There are currently two tests commonly used to determine HER2 status of a patient: immunohistochemistry (IHC) - detects overexpression of HER2 protein and fluorescence in situ hybridization (FISH) - detects amplification of the HER2 gene [25,26]. IHC is easier to perform than FISH and is substantially less expensive. IHC can be performed in most surgical pathology laboratories. FISH, on the other hand, is performed only at select sites because specialized equipment and training are required. Despite these arguments in favour of IHC testing, there are concerns that it is less accurate, is not standardized and has poor reliability [27,28]. FISH has generally been shown to have better validity and reliability and is widely considered to be the technique of choice [28].

Developing a high-sensitive and rapid early-stage breast cancer diagnostic method is therefore urgent. As such, great attention and various research efforts have been focused on the development of non-invasive and more convenient diagnostic tools that allow for early detection of breast cancer: as outlined is in thesis using electrochemistry and biosensors.

1.1.3. Electrochemical Biosensors for HER2 Detection

A biosensor is an analytical device that combines a biological component (biorecognition element), a physicochemical detector, and a transducer for the detection of an analyte of biological importance [29,30], **Figure 1.2**. Biological or chemical reactions based on the biorecognition element-analyte interactions on the transducer surface are measured; the generated signal is proportional to the concentration of an analyte in the reaction [31]. These sensors offer advantages such as high selectivity to the target analyte mainly due to the specific interaction of the bioreceptor present in their structure with the target analyte. The target analyte is detected by converting the recognition signal from the specific analyte-bioreceptor interactions, into a detectable output signal [32,33].

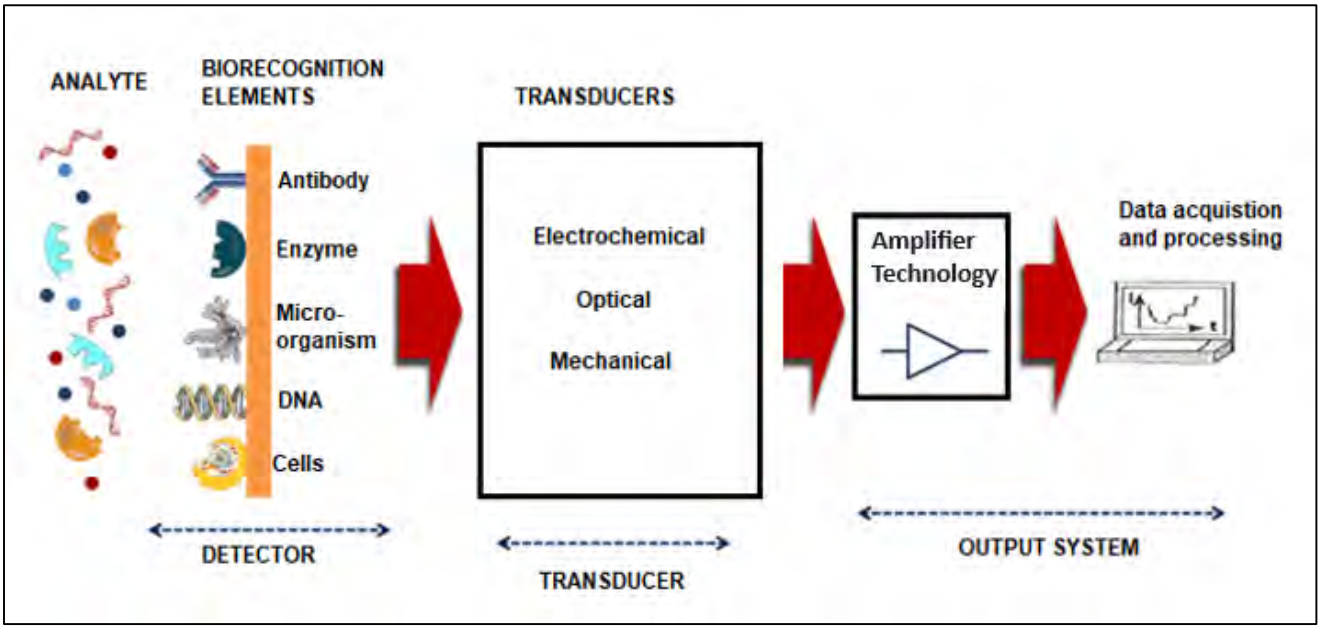

Figure 1.2 Components and characteristics of a biosensor [33].

A wide range of biosensor technologies have been developed for the detection of HER2; including optical [34,35], and electrochemical [36,37] among which electrochemical biosensors have been proven to be superior owing to their high sensitivity and specificity in the presence of biorecognition elements [37]. HER2 concentrations under normal circumstance are in the 2-15 ng/mL range, with the occurrence and progression of aggressive types of breast cancer HER2 concentration is increased to 15-70 ng/mL [38,39].

A suitable bioreceptor/biorecognition element is a biomolecule that can selectively bind to the analyte of interest with high affinity and specificity. There can be various possible receptors for a particular analyte. Having knowledge of the advantages and disadvantages of various biological receptors is key. In the case of HER2 antigen, various biological targets that can specifically bind to the antigen with high specificity exist. These include DNA/RNA aptamers, affibodies, antibodies and peptides [40,41]. This thesis explores the use of both an amino functionalized HB5 DNA aptamer and an antibody (Trasmatuzab) as biorecognition

elements for HER2 detection in the presence of metallophthalocyanines, a porphyrin nanostructure and various nanoparticles.

Antibodies are a class of proteins, immunoglobulins that are generated by the immune system as a response to foreign species such as bacteria, viruses, or parasites [42]. These proteins are characterized by their ability to bind to a target with high affinity and specificity [43]. Structurally, antibodies are "Y" shaped and consist of two heavy and light chains, **Figure 1.3**. The light and heavy chain moieties of the antibody are bound together by disulfide bonds; this region is called the hinge region. A single antibody each has two identical antigen binding sites at the ends of their "Y" arms or top of the light chain [44,45]. The antibody immobilization onto the transducer surface is crucial for maintaining its proper conformation and correct orientation to allow optimal interaction with the target analyte [46,47]. Antibodies suffer from some drawbacks which limit their applicability in point of care diagnostics, namely they are expensive to produce, they require low-temperature storage, they can undergo denaturation if not stored properly and lose their binding ability [46,48]. These limit their utility in making assays for real life applications, as such various alternatives have been considered, such as aptamers.

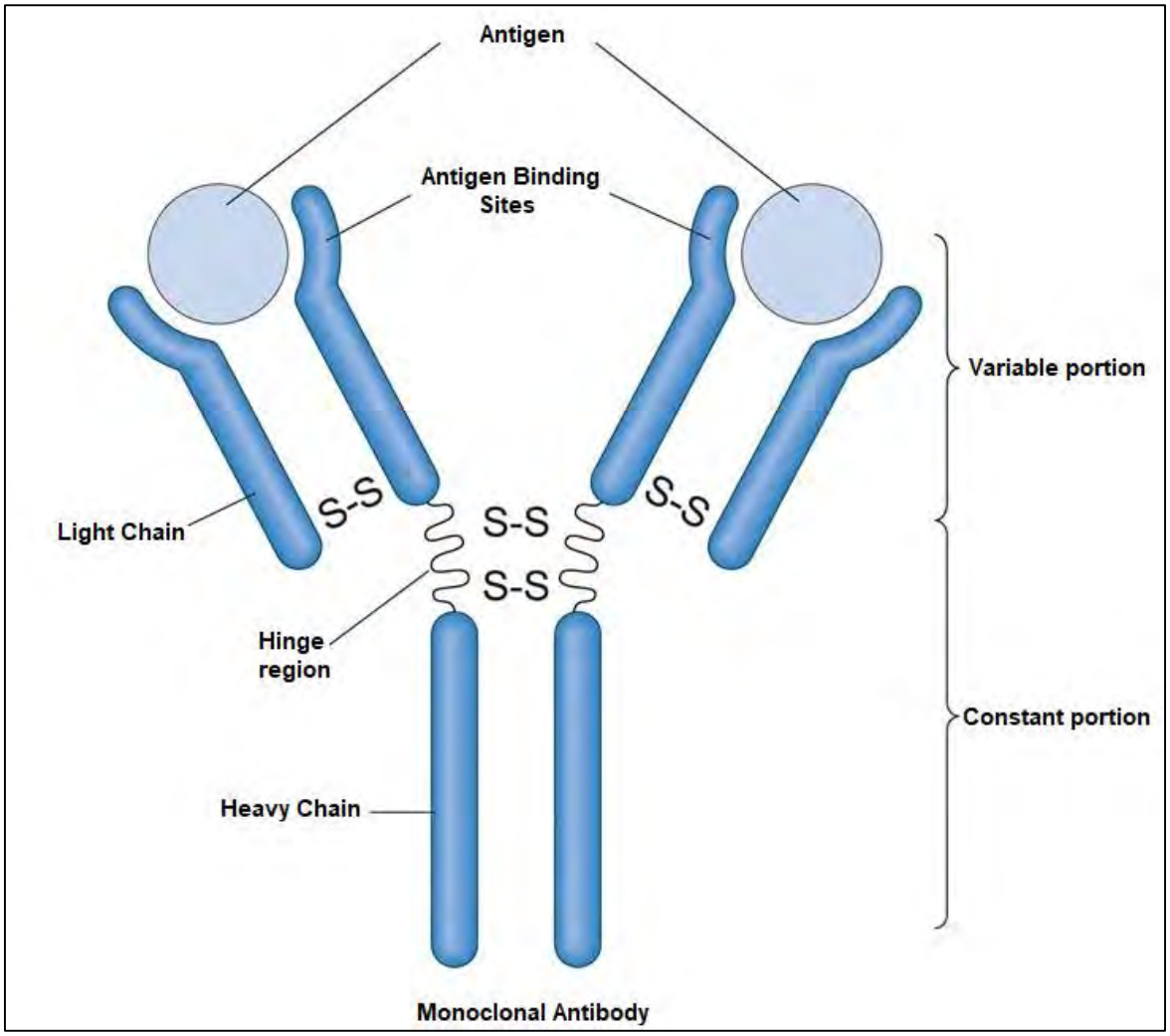

Figure 1.3 General structure of a monoclonal antibody. (Image Credit: periyanayagam/Shutterstock.com)

Aptamers are short single-stranded nucleic acids, that can fold into a 3D structure allowing for interaction with their target analyte [42,48]. Aptamers, similar to antibodies bind to their target via non-covalent interactions [42,49], **Figure 1.4**. Aptamer immobilization on the electrode surface for biosensor design is achieved following same considerations as in antibodies: optimum strategy being that which allows for aptamer-antigen interaction while the aptamer is firmly immobilized onto an electrode surface. These immobilization

chemistries are achieved through modifications of the 3′ and/or 5′ ends of the aptamer with an appropriate functional group [50]. In general, the 3′ end seems to be more suitable, since it is the primary target for exonucleases, and, thus, its coupling to the solid support would simultaneously confer resistance to nucleases. Nevertheless, the nature of solid-phase oligonucleotide synthesis is such that addition of a modifier at the 5′ end of a sequence is the terminal step, generally improving yield and simplifying purification [50,51].

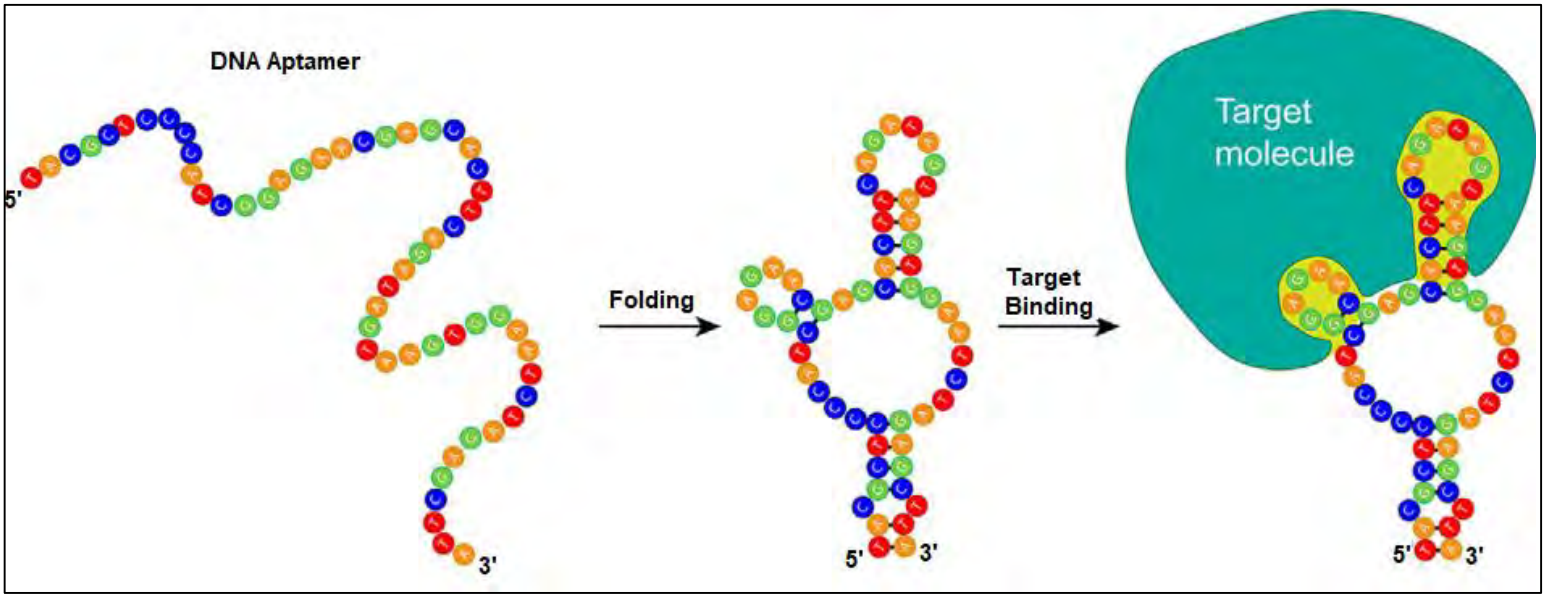

Figure 1.4. Illustration of the 3D folding of aptamers and their binding to their target analyte [42].

Compared to antibodies, aptamers have some significant advantages. Aptamers are produced in an animal- free synthetic approach, following a simpler, inexpensive, robust and scalable method [52]. Aptamers are structurally flexible, their sequence can be tuned in a specific manner, to improve affinity to the target molecule [53]. Even further, aptamers are smaller in size aiding in their ease of immobilization on surfaces, providing more target-binding sites with minimal steric hindrances effects [54]. Consequently, higher biosensing signals are

obtained for an aptamer bound target, compared to an antibody bound target because the aptamer is smaller in size and therefore closest to the transducing surface. Aptamers can undergo significant conformational changes and are stable over a wide pH range, which allows them to bind to a wide array of targets with higher sensitivity than antibodies [50,55]. Aptamer stability is not limited only to physiological conditions, compared to antibodies aptamers exhibit superior chemical stability and can undergo reversible folding and unfolding. This thesis report on the use of both an aptamer and an antibody as recognition elements in biosensor design. Specifically, a DNA HB5 aptamer and the Trastuzumab monoclonal antibody were used in the presence of phthalocyanines, a porphyrin nanostructure and various nanoparticles towards the electrochemical detection of HER2.

1.2. Phthalocyanines and Porphyrins

1.2.1. Background

Phthalocyanines (Pcs) and porphyrins are highly conjugated and planar aromatic macrocycles, both containing 18 delocalized π-electrons [56–58]. Pc molecules are well known for their excellent redox properties, thermal and chemical stability [59]. Both Pcs and porphyrins exist as free base and in the form of metal complexes, hosting a metal via the central cavity [57,60]. The Pc can be substituted accordingly at the α (non-peripheral) and as β (peripheral) positions (**Figure 1.5A**), allowing for the design of Pcs with desired electronic and/or solubilizing properties, depending on the application [56]. Similarly, the core-skeleton of the porphyrin macrocycle as shown in **Figure 1.5B**, can be directly functionalized at the *meso*- and/or β-positions, altering the physicochemical properties to suit desired application [61,62].

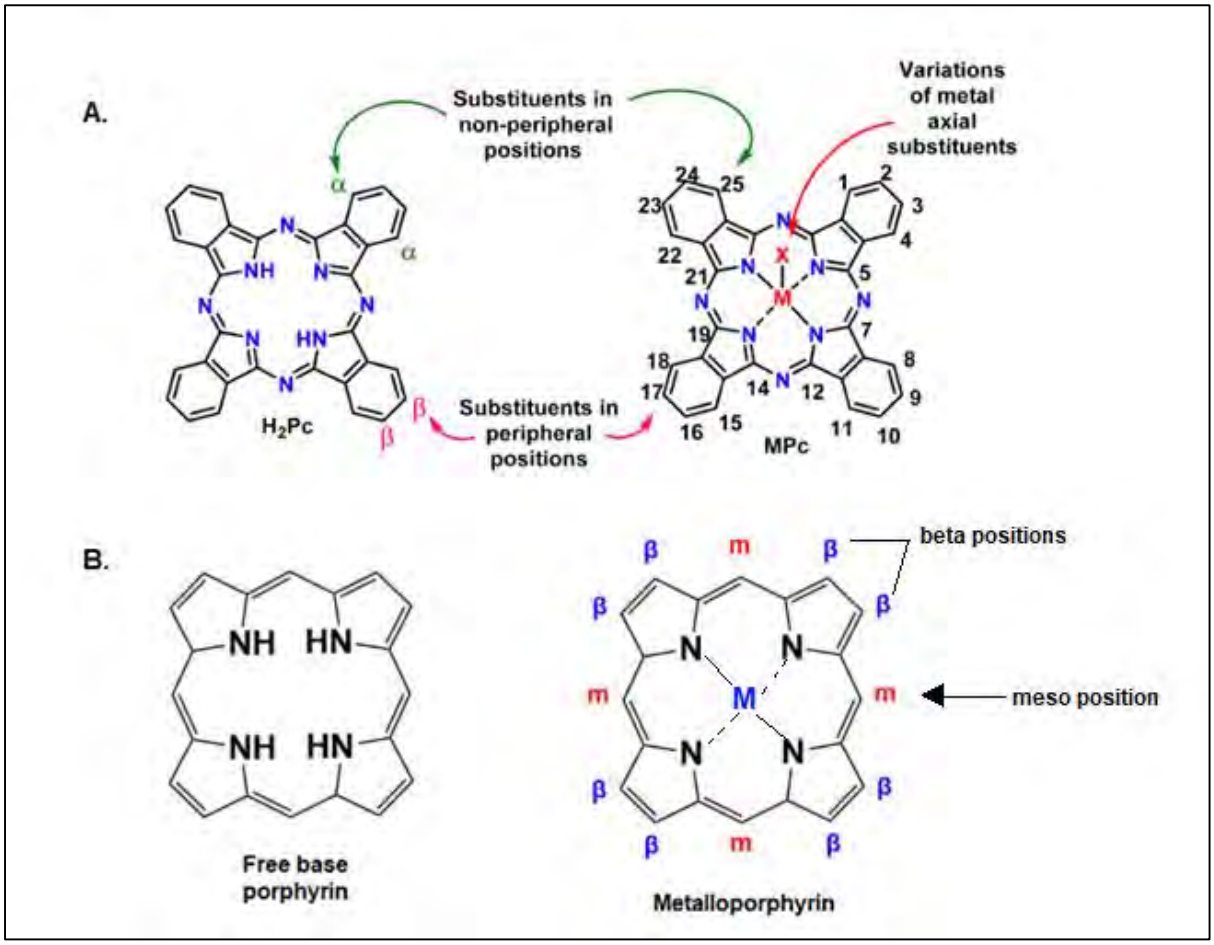

Figure 1.5. Typical structures of (A) phthalocyanines and (B) porphyrins, both free base and metalated are demonstrated. Possible structural substitution sites and ring numbering is also shown [56,62].

In electrochemical biosensing, metallophthalocyanines and metalloporphyrins are used for electrode modification both for signal amplification via electron mediation and immobilization of biomolecules for sensitive analyte detection. Pcs and porphyrins can improve the kinetic parameters of electrochemical reactions by increasing the peak intensity and also reducing the peak potential [63,64]. Furthermore, both molecules allow for low cost and rapid analysis of analytes, which is essential in biosensor design. These molecules are structurally flexible, and allow for structural modification for enhanced properties, varied

applications and interaction with other compounds and/or biological molecules. However, porphyrins as electrocatalysts have proven to be unstable, are easy to deactivate, and difficult to recycle, which limits its application in electrochemical sensor development [63]. To overcome these drawbacks, porphyrins have been integrated as organic ligands into controllable, highly designed and structurally stable frameworks, consisting of more than a single porphyrin, **Figure 1.6** [65–67]. Porphyrin based frameworks provide a very attractive platform and make porphyrin molecular catalysts promising for electrocatalytic applications. These porphyrin-based frameworks have found application in biomedical applications [67], energy conversion [68], photocatalysis [69] and oxygen evolution [70]. The resulting frameworks have shown great stability, electron transfer properties and recyclability [71,72]. On that account, this thesis reports on a cobalt porphyrin binuclear framework (CoP-BNF) towards the detection of HER2 for the first time.

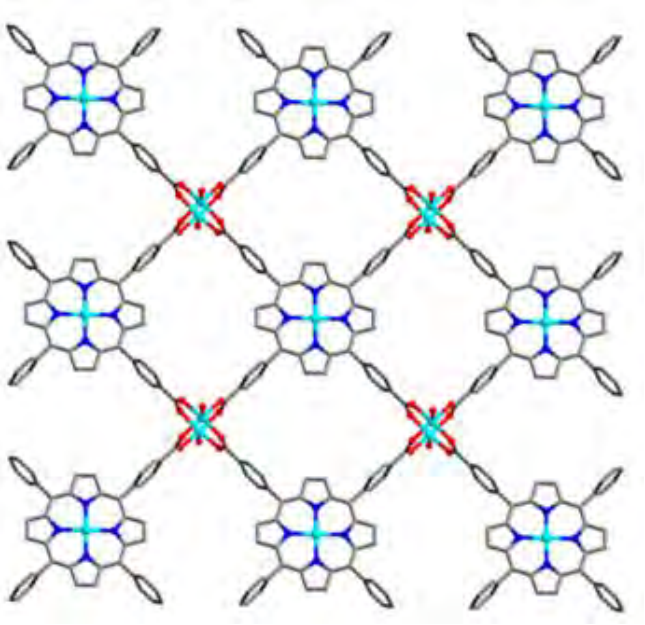

Figure 1.6. An example of a porphyrin-based framework based on a porphyrin monomer [65].

1.2.2. Synthesis

1.2.2.1. Phthalocyanines

Asymmetric MPcs are synthesized by using phthalonitrile derivatives with different substituents in rationed amounts, **Scheme 1.1**. The most common approach, which was used in this work, involves the cross condensation between two phthalonitrile components or diiminoisondolines in a ratio that favours the product, in the presence of a metal salt and a catalyst. The ratio 3: 1 favours the A_3B formation, with a few other isomers. Chromatography is used to obtain the desired mono substituted MPcs, usually obtained in small yields. Symmetric tetra substituted MPcs are obtained through cyclotetramerization of phthalic acid derivatives. The commonly used substituted phthalic acid derivatives are either 3 or 4 phthalonitrile. The cyclotetramerization occurs at high temperatures, in the presence of a solvent, a catalyst, metal of choice as well as the substituted phthalic acid derivative. The yields of each isomer are determined by the nature of the substituent.

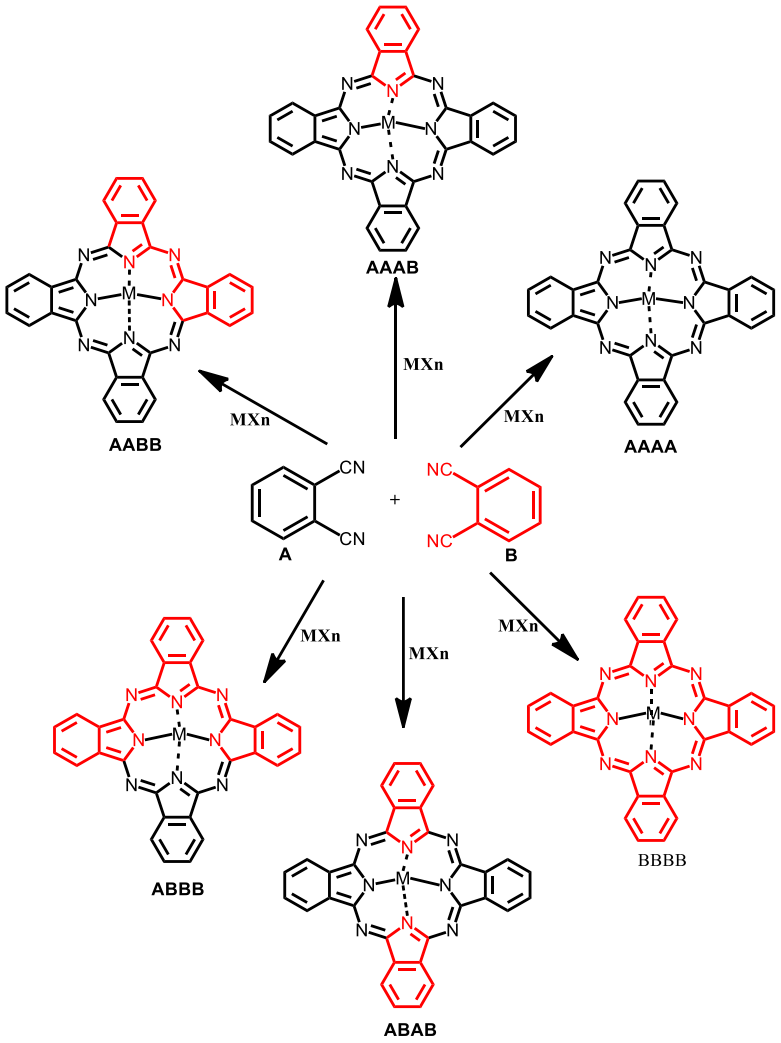

Scheme 1.1. Synthetic route towards asymmetric and symmetric MPcs.

1.2.2.2. Porphyrins and related structures

The route for the synthesis of porphyrins, which was followed in this thesis, involves the mixing of pyrrole with a benzaldehyde under acidic conditions, followed by oxidation of the intermediary product to form a porphyrin, **Scheme 1.2A** [73,74]. Porphyrin based frameworks; are nanostructures whose synthesis uses a porphyrin as a backbone to design a stable framework. There are several strategies reported for synthesizing porphyrin-based frameworks. Among which, the most common and utilized in this thesis is the hydrothermal

method, which involves reacting a porphyrin moiety in a solvent, with a chosen metal salt sealed in a reactor under hydrothermal conditions, **Scheme 1.2B**. The coordination patterns in these solids fall into three different categories according nuclearity (polynuclear, tetranuclear and binuclear) of the interporphyrin metal.

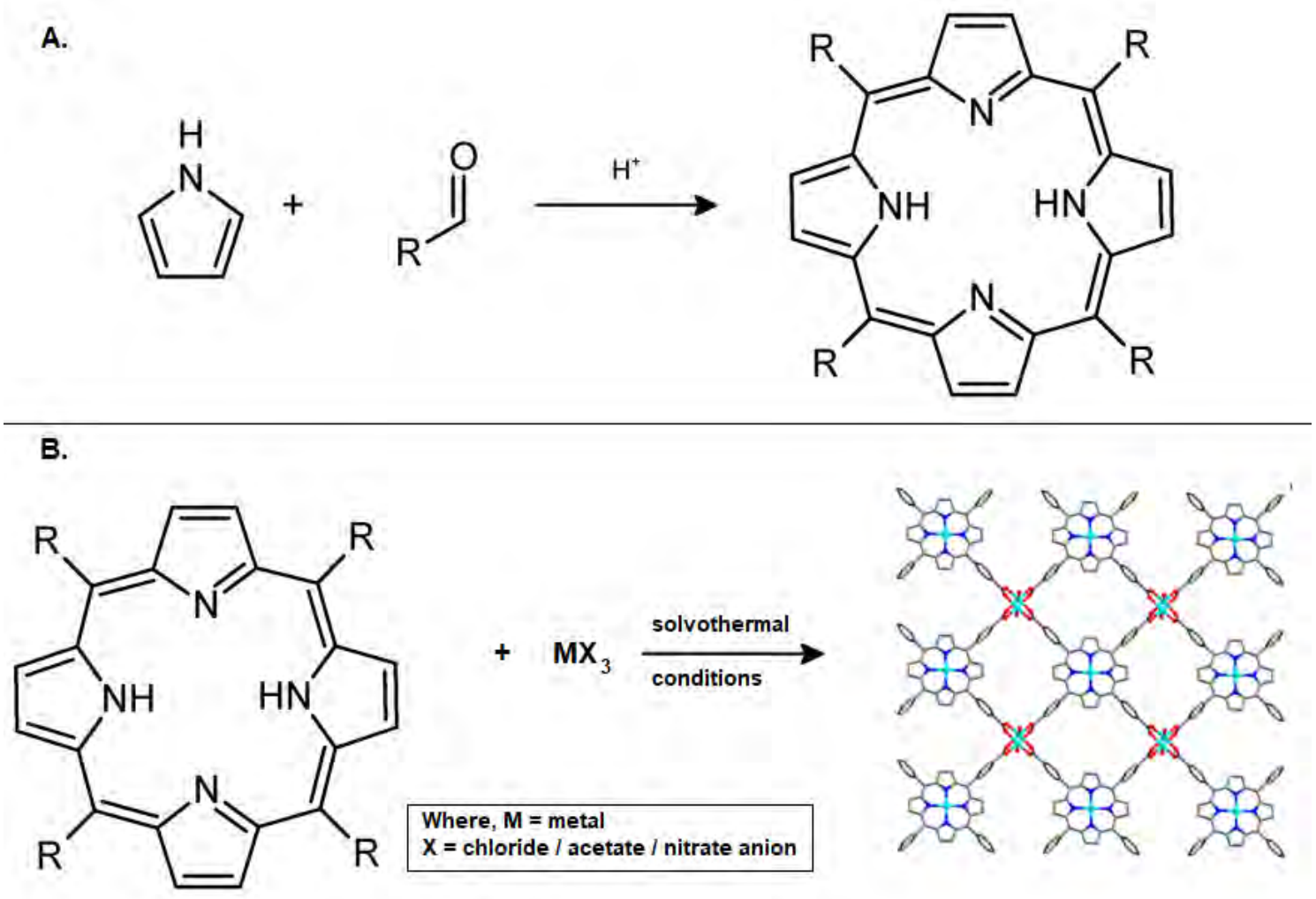

Scheme 1.2. (A) Alder-Longo procedure for the synthesis of meso substituted porphyrins and (B) Procedure towards the solvothermal synthesis of a porphyrin-based framework [65,74].

1.2.3. Phthalocyanines and Porphyrins used in this work

1.2.3.1. Metallophthalocyanines, Table 1.1

This thesis reports for the first time on the use of cobalt-based Pc complexes (**1** – **6**) towards the electrochemical detection of HER2. The cobalt based phthalocyanines [Co tetra carboxy phenoxy phthalocyanine {CoTCPPc} (**1**) [75], Co tetra phenoxy propionic acid {CoTPPc} (**2**), Co tetra phenoxy acetic acid {CoTPAPc} (**3**), Co tetra acetylphenoxy phthalocyanine {CoTAcPhPc} (**4**) [76], Co tris-(acetylphenoxy)-mono-phneoxyacrylic acid phthalocyanine {CoMPhAaPc} (**5**) and Co tris-3,5- dimethyl – phenoxy pyridine (5) -oxy- (2)- carboxylic acid phthalocyanine {CoMPhPyPc} (**6**), were used for electrode modification towards the electrochemical detection of HER2, **Table 1.1**. The cobalt as the choice metal is accredited to its transition metal status, excellent redox and catalytic properties. Complex **1** was used alone and in the presence of the conductive polymer, polypyrrole towards HER2 detection. Complexes **2** and **3** (both novel), were used to investigate the effect of functional groups on the electron transfer properties of phthalocyanines in biosensor design. These two MPcs were coupled with cerium oxide nanoparticles for improved sensitivity and signal generation towards HER2 detection. Complex **3** was additionally studied with gold nanoparticles and graphene quantum dots, to explore the effect of nanoparticles on its activity towards the detection of HER2. Complexes **4** and **5** (the latter novel), were coupled with graphene quantum dots via π-π stacking and applied for HER2 detection. Complexes **1-5**, were all used in label free detection of HER2 using an HB5 aptamer as biorecognition element, **Table 1.1**. Complex **6** (novel), in combination with graphene quantum dots and a novel HB5-bioconjugate was used to design a single and sandwich aptamer assay for the electrochemical detection of HER2. The use of complexes **5** and **6** was influenced by their bulky substituents, which have been reported to reduce aggregation. Furthermore, reports have shown that asymmetric MPcs

have higher electron transfer properties compared to their symmetric counterparts [77]. Complexes **1**, **2**, **3**, **5** and **6**, all contain carboxylic acid functional groups, to which the amino functionalized HB5-aptmer was linked via amide bond formation, and applied towards HER2 detection. Complexes **4** and **5** have acetophenone ligand, to which the HB5 aptamer was linked via acid catalysed imine bond formation, and applied towards HER2 detection.

The following trends using Pc complexes **1** – **6** were explored**:**

(i) Effect of addition of polypyrrole polymer to complex **1** sequentially and premixed during polymerisation

(ii) Effect of substituents of complex **2** and **3** alone, and when combined with cerium oxide nanoparticles

(iii) Effect of nanoparticles; graphene quantum dots, cerium oxide nanoparticles and gold nanoparticles on the activity of complex **3**

(iv) Effect of symmetry for complex **4** and **5** coupled with graphene quantum dots

(v) Effect of bulky substituents on the complex **6** compared to all complexes **1** – **5**

1.2.3.2. Porphyrin related structures

This thesis reports on the use of a cobalt porphyrin binuclear framework (CoP-BNF) towards the electrochemical detection of HER2 for the first time. The CoP-BNF is endowed with carboxylic groups to which the biorecognition elements are linked via amide bond formation. The activity of CoP-BNF alone, and in the presence of graphene quantum dots doped with gold nanoparticles towards the electrochemical detection of HER2 is studied. Two bioreceptors are used and compared: HB5 aptamer and Trasmatuzab antibody for sensing towards HER2 detection. The comparative performance of the HB5 aptamer and Trastuzumab antibody towards HER2 detection is reported in this thesis for the first time. The synergistic effects of the CoP-BNF and graphene quantum dots doped with gold nanoparticles towards HER2 detection is also reported herein, for the first time.

Table 1.1. List of MPcs used in this thesis, with the respective NPs that each complex was coupled, as well as the bioreceptor used, for HER2 detection.

MPc/Porphyrins Used	NPs used	Aptamer/ Antibody (a)*
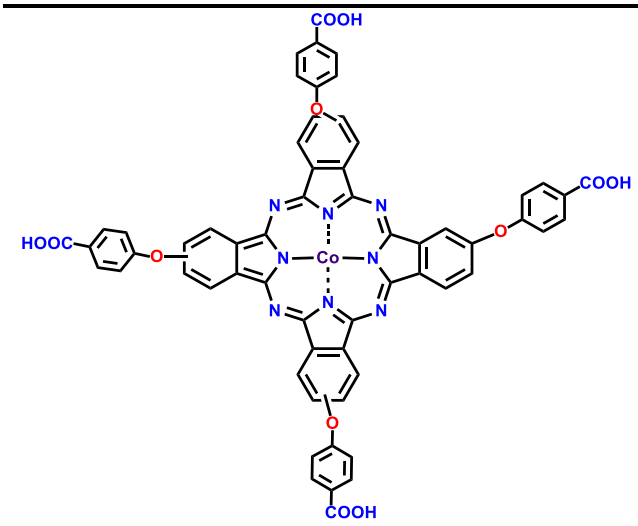 [75] [Co tetra carboxy phenoxy phthalocyanine {CoTCPPc} (**1**)	Polypyrrole SNGQDs	**HB5-aptamer (amide)**
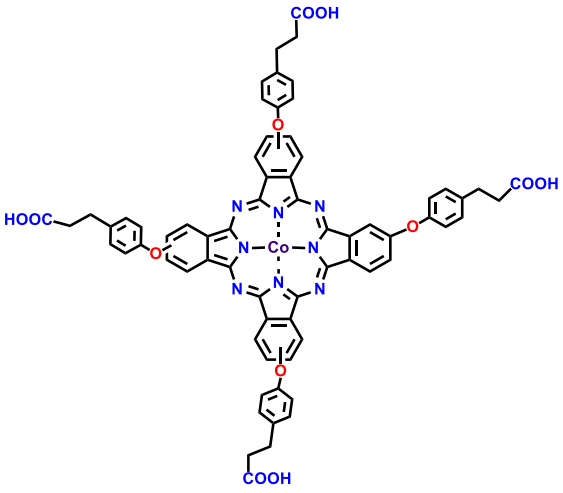 [**New**] Co tetra phenoxy propionic acid {CoTPPc} (**2**)	CeO_2NPs_{COOH}	**HB5-aptamer (amide)**

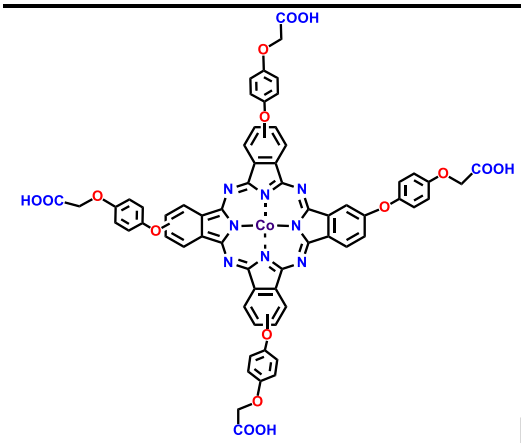 [**New**] Co tetra phenoxy acetic acid {CoTPAPc} (**3**)	CeO_2NPs_{COOH} SNGQDs AuNPs	**HB5-aptamer (amide)**
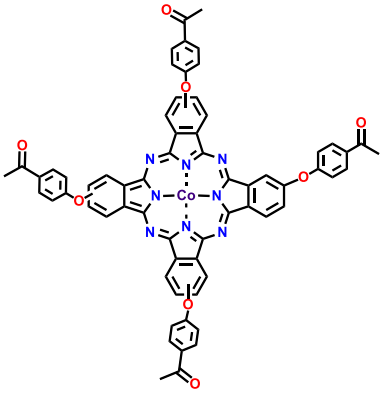 [**76**] Co tetra acetylphenoxy phthalocyanine {CoTAcPhPc} (**4**)	SNGQDs	**HB5-aptamer (imine)**
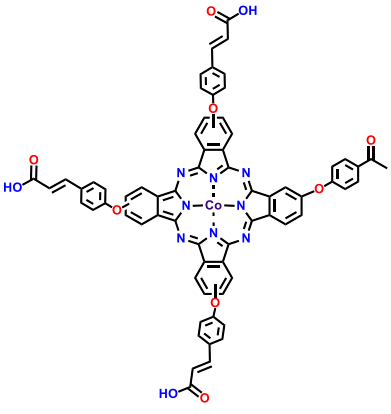 [**New**] Co tris-(acetylphenoxy)-mono-phneoxyacrylic acid phthalocyanine {CoMPhAaPc} (**5**)	SNGQDs	**HB5-aptamer (amide)** **HB5-aptamer (imine)**

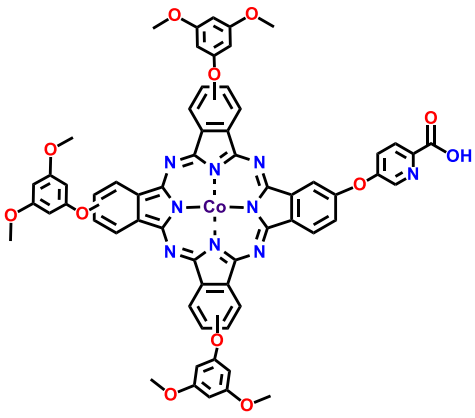 [**New**] Co tris-3,5- dimethyl – phenoxy pyridine (5) -oxy- (2)-carboxylic acid phthalocyanine CoMPhPyPc} (**6**)	SNGQDs@CeO_2NPs	**HB5-aptamer (amide)** **Single aptamer vs. sandwich assay**
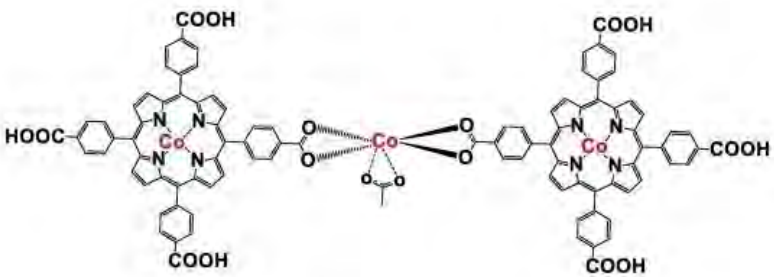 [**New**] Cobalt porphyrin binuclear framework (CoP-BNF)	SNGQDs@AuNPs	**HB5-aptamer (amide)** **Trastuzumab (amide)**

* (a) = specifies the type of bond formed between Pc complex with the relevant biorecognition element.

1.2.4. Phthalocyanines and Porphyrins used for biomarker detection

MPcs have been employed in sensing of various cancer biomarkers such as the prostate specific antigen (PSA) [78–80], and the epidermal growth factor receptor (EGFR) [81–83], **Table 1.2**. The complexes reported in this thesis (complexes **1 - 6**) as shown in **Table 1.1** are structurally different from any phthalocyanines reported for biomarker detection, **Table 1.2**. One report exists where a ZnPc was linked to an H2-ul aptamer towards HER2 targeting and photodynamic therapy (PDT) [84]. This thesis reports for the first time on the use of cobalt-based Pc complexes (**1** – **6**) towards the electrochemical detection of HER2, using the HB5 aptamer. The superior qualities of the HB5 compared to other aptamers for the detection of HER2 has been demonstrated [85]. The use of porphyrins and porphyrin related structures in biomedical applications is well documented: Most commonly porphyrins are used for theranostics related studies [86,87], **Table 1.2**. Not much work has been done on their application towards electrochemical detection of cancer biomarkers [87,88].

Table 1.2. Reported MPc towards the detection of various cancer biomarkers

MPc/Porphyrin in Literature	Analyte	References
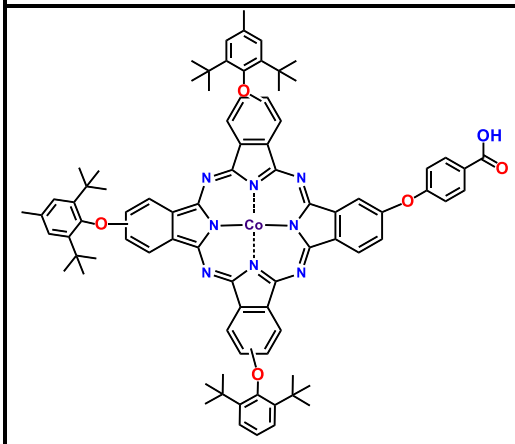	PSA	[78,79]
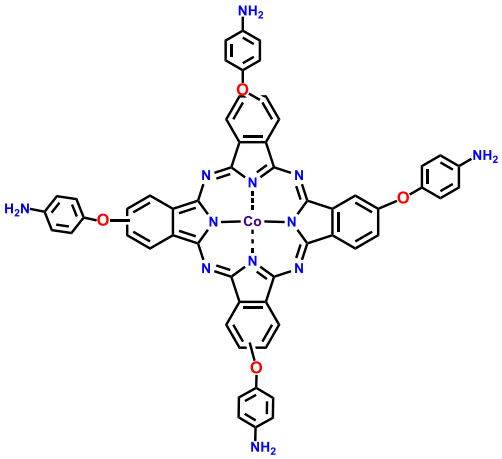	PSA	[80]
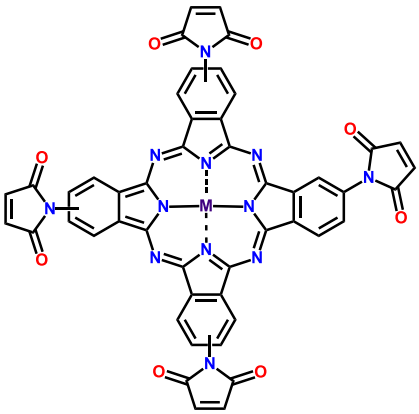	EGFR	[81]

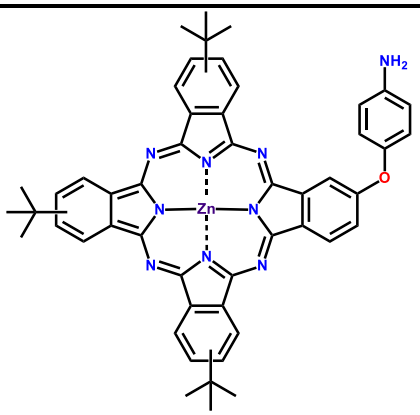	EGFR	[82]
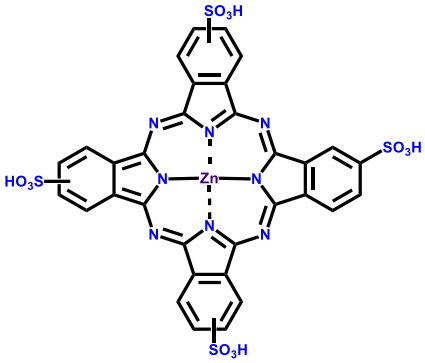	EGFR	[83]
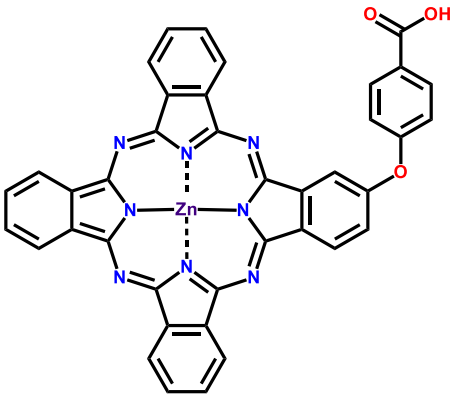	HER2, **applied in PDT.** **H2-uL aptamer**	[84]
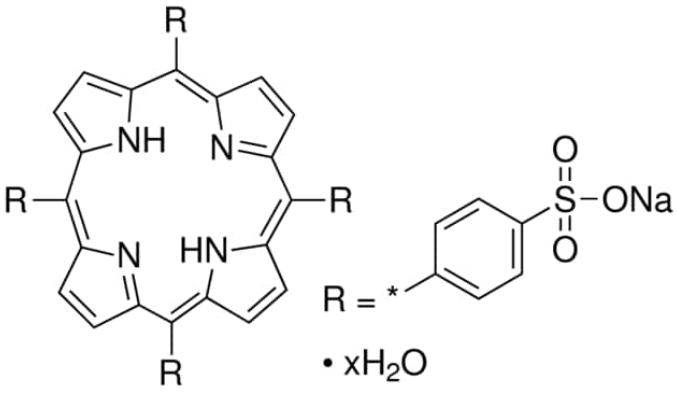	HER1, CEA	[86]

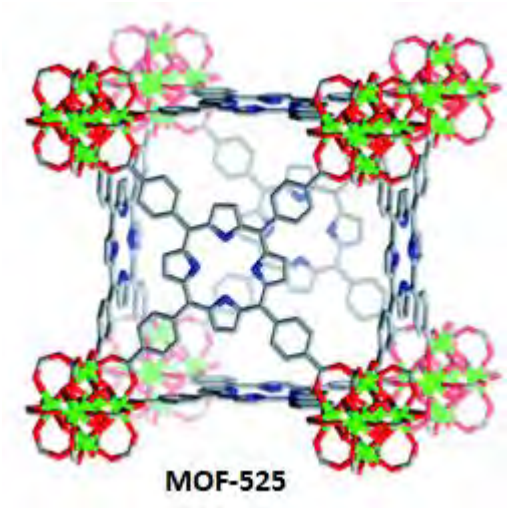	PSA, dopamine	[87,88]

Where, PSA = prostate specific antigen, EGFR = epidermal growth factor, HER = human epidermal growth receptor, CEA = carcinoembryonic antigen, MOF = metal organic framework and PDT = photo dynamic therapy.

1.3. Nanoparticles (NPs) used in this work

1.3.1. Graphene Quantum Dots (GQDs)

GQDs are zero-dimensional nanocrystals of sp^2-bonded carbon atoms that are arranged in a honeycomb crystal lattice of carbon atoms in rings of six atoms [89]. Each atom is covalently bonded to three other carbon atoms, which gives the sp^2 hybridized characteristic and results in π-orbitals perpendicular to the plane of the sheet, **Figure 1.7** [90,91]. The applicability of GQDs in electrochemical biosensing lies in the following properties: quantum confinement, excellent transduction, high electron transfer rate, unique electrocatalytic properties and

specific surface area, chemical inertness [90,92]. Furthermore, the existence of carboxyl and hydroxyl functional groups on their edges results in their ease of functionalization, variable bandgap energy, water solubility and high biocompatibility [93–95].

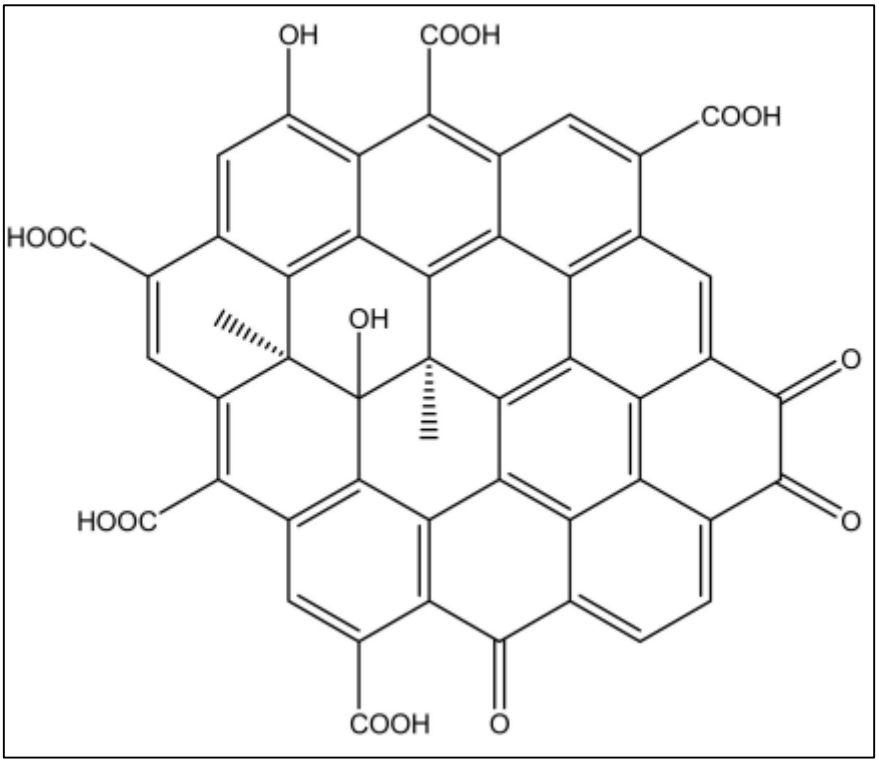

Figure 1.7. Typical structure of GQDs with the possible edges.

The presence of functional groups on GQDs allow for better immobilization of biomolecules for biorecognition in biosensor design [96]. GQDs can be linked to other nanomaterials via covalent or non-covalent interactions for improved catalytic or sensing abilities [97]. Even further, sp^2 framework can be doped or infused with various atoms for enhanced properties: most commonly, heteroatoms such as N and/or S have been used due to comparable atomic sizes and sufficient valence electrons for bonding with the carbon atoms of the GQDs without

disturbing the sp^2 carbon framework [98–100]. The structure, edges and surface defects of the GQDs is dependent on the synthetic route [101]. There are two common routes through which GQDs can be obtained namely, top down and bottom-up route [102–104]. The top-down approach for GQDs involves the cleaving or cutting down of carbon-based materials with a graphitic structure under mild conditions. The main disadvantage of this approach is that there is limited control of the GQDs morphology and size, and gives rise to GQDs with surface defects. Moreover, some routes usually require the use of laborious and multistep procedures, such as strong acids and high temperatures [105,106]. The bottom-up approach, uses small aromatic carbon-based compounds such as L-cysteine, in a controlled process to produce high quality graphene quantum dots. Pyrolysis of these small compounds is the most commonly used approach [107,108]. Compared to the top-down approach, there is better control of the size, morphology, shape, and surface state achieved with bottom-up approaches [109].

This thesis explores the bottom up synthesis of sulfur and nitrogen doped graphene quantum dots (SNGQDs) as surface modifiers towards the detection of HER2. The SNGQDs were also used as platforms for the growth of gold nanoparticles and cerium oxide nanoparticles to form the composites: SNGQDs@AuNPs and SNGQDs@CeO_2NPs respectively. The effect of the SNGQDs and its composite on the electrocatalytic activity of selected CoPc derivatives is investigated and reported. Owing to the fact that both SNGQDs and the CoPc derivatives are catalytic, it is expected that the synergistic effect between the two materials, will result in enhanced sensitivity and signal amplification. There are reports on the electrochemical detection of HER2 using graphene quantum dots: GQDs-magnetic nanoparticles [110], GQDs/Rhodium nanoparticles [111], reduced graphene oxide/chitosan [112], the rest are listed in **Table 1.3** [113,114]. A report on the combination of graphene oxide and gold

nanoparticles added sequentially on the electrode towards the detection of HER2 exists [115]. This thesis reports for the first time, on the growth of gold nanoparticles and cerium oxide nanoparticles on SNGQDs surface to form SNGQDs@AuNPs and SNGQDs@CeO_2NPs composites, respectively, and their application towards the detection of HER2. Even further, this work explores for the first time, on the combination of SNGQDs and related composites with CoPcs towards the electrochemical detection of HER2. **Table 1.3** shows a list of graphene based electrochemical sensors towards HER2 detection. As shown, none of them used doped GQDs alone, or in combination with AuNPs, CeO_2NPs nor cobalt phthalocyanines. This renders the GQDs nanomaterials combination reported in here new, thereby emphasizing the novelty of the reported work.

1.3.2. Cerium Oxide Nanoparticles (CeO_2NPs)

Cerium oxide nanoparticles, are based on the lanthanide group metal cerium [116]. Cerium exhibits exceptional character of cycling between the two ionic states, which is Ce^{3+} and Ce^{4+}, and this is possible due to the presence of ground-state electron in the 4f (Xe $4f^1 5d^1 6s^2$) orbital which enables it to exhibit redox properties [116,117]. Among other NPs, CeO_2NPs have been exploited owing to their unique surface chemistry, high stability and biocompatibility [118,119]. Synthetic methods are important because they determine the solubility, size, surface condition, charge, structural arrangement and morphology of nanoparticles, thus affecting their properties, including catalytic activities. Various synthetic methods for CeO_2NPs include physicochemical methods such as solution precipitation, hydrothermal and solvothermal methods, which tend to be done under harsh conditions, where toxic organic solvents are required accompanied by high temperatures [119,120]. Another method, and mostly preferred is the green synthesis approach; which is environmentally friendly, simpler,

cheaper and can produce nanoparticles of smaller sizes and increased biocompatibility [121,122]. This thesis explores a non-toxic synthesis of CeO_2NPs nanoparticles in aqueous media, at room temperature with no additional surfactant.

CeO_2NPs have been applied in electrochemical sensing owing to their fast electron transfer kinetics, their ability to accelerate electron transfer, low-cost production, high surface area and can improve sensor sensitivity [123,124]. This thesis presents for the first time, the combination of CeO_2NPs with CoPc derivatives towards the electrochemical detection of HER2. This work demonstrates the enhanced sensitivity and signal amplification abilities towards HER2 of selected CoPc derivatives in the presence of CeO_2NPs. The CeO_2NPs were explored as immobilization platforms for biomolecules for enhanced sensitivity and enhanced signal towards HER2 detection. A report on the use of CeO_2NPs to form CeO_2NPs-antibody bioconjugate towards the electrochemical detection of HER2 exists [125], **Table 1.3**. For the first time, this thesis reports on the use of a CeO_2NPs-aptamer bioconjugate towards the electrochemical detection of HER2.

1.3.3. Gold Nanoparticles (AuNPs)

Gold nanoparticles are the most commonly used nanoparticles owing to their good biocompatibility, excellent conductivity, effective catalysis, high density, and high surface-to-volume ratio [126]. Relevant to this work, is their applicability in bioassay related studies and design. AuNPs play an important role in biosensors, not only electrocatalytically but also structurally; these nanoparticles are stable and can easily be modified with biomolecules via S-Au and Au-N bonds while preserving biomolecule integrity [127,128]. AuNPs have been widely reported for their ability to enhance analytical performance of various biosensors towards certain analytes [129,130]. AuNPs have been shown to be structurally flexible and

compatible with a wide range of nanomaterials, and therefore allow for Au-nanomaterial composite formation [131]. AuNPs have shown good sensitivity towards HER2 detection [132–135]. **Table 1.3** lists the electrochemical sensors towards HER2 based on gold nanoparticles. This thesis reports on the seed growth method of AuNPs on sulphur and nitrogen doped graphene quantum dots to form SNGQDs@AuNPs, towards the electrochemical detection of HER2. The use of AuNPs is presumed to prevent restacking of the graphene sheets, to impede aggregation. This thesis further reports for the first time, coupling of AuNPs with the previously mentioned cobalt based framework (CoP-BNF) and a CoPc derivative (complex **3**) respectively, towards the electrochemical detection of HER2.

Table 1.3. Table summary of graphene materials, CeO2NPs, AuNPs materials towards HER2 detection.

GQDs composite	References
GQDs/MNPs-antibody	[110]
GQDs/RhNPs-aptamer	[111]
GQDs/Chitosan-antibody	[112]
Graphene/AgNPs/PANI-aptamer	[113]
GNM-aptamer	[114]
GO/DNA/AuNPs	[115]
CeO_2NPs-antibody	[125]
AuNPs/MW-ILE-antibody	[132]
AuNPs-aptamer	[133]
AuNPs-CN-aptamer	[134]
AuNPs-CuMOF-antibody	[135]

MNPs= magnetic nanoparticles, RhNPs= Rhodium nanoparticles, PANI=polyaniline, GNM=graphene nanomesh, MW=multiwall, ILE= ionic liquid electrode, CN= carbon nanotubes, Cu-MOF=copper metal organic framework.

1.4. Polypyrrole (PPy)

Polypyrrole (PPy) is an organic polymer obtained by oxidative polymerization of pyrrole [136]. PPy is electrically conductive and electroactive in nature with unique chemical and electrochemical properties [136,137]. PPy is by far the most extensively studied among the numerous conducting polymers because of its easy synthesis, stability in oxidized form, high electrical conductivity, and good redox properties [138,139]. The intrinsic properties of PPy are highly dependent on electropolymerization conditions [140]. PPy is commonly synthesized through electrochemical oxidation of pyrrole monomer using an oxidizing agent. The electrochemical oxidation method, allows for an inexpensive and controlled synthesis of PPy [141–143]. As such, the electrochemical method was adopted in this work for PPy synthesis. Despite these excellent properties, PPy also suffers from certain drawbacks, namely, poor solubility and low mechanical stability [144]. These drawbacks can affect the response characteristics and sensitivity of the electrochemical sensor. PPy has been applied in biosensor design for the detection of various analytes, where the compatibility of polypyrrole with different nanomaterials was demonstrated accompanied by enhanced biosensor signals and sensitivities [145–149]. This thesis reports for the first time on electrochemical polymerization of PPy in the presence of SNGQDs and CoPc derivatives respectively. The advantage of the synergetic combination of the properties of phthalocyanines, polypyrrole and SNGQDs as electrode modifiers for the electrochemical biosensing of HER2 is reported.

1.5. Electrode Modification

All electrochemical reactions occur at the electrode/solution interface. Hence, the surface structure of the electrode at the interface plays a distinct role in the electrode reaction and it promotes the pathway for the transfer of electrons at the interface which in turn gives the better electrode kinetics [**150**]. In biosensor design, it is on a nanomaterial modified surface that the biorecognition element can be immobilized to allow for analyte detection [**151**]. Furthermore, signal transduction and sensor stability are highly dependent on the successful modification of an electrode using a selected technique [**152**]. Various electrode modification routes include electropolymerization, self-assembled mono layers, adsorption (dip-dry and drop-dry), click chemistry and electrografting [**152**,**153**]. These methods are easily amenable in low-cost biosensor fabrication because they do not require complicated instruments. This thesis reports on adsorption/drop casting as the major method of modification **Figure 1.8**, for the coating of the glassy carbon electrode (GCE) with various nanomaterials. The GCE is used as a working electrode owing to its broad potential window, low background current, low cost, chemical inertness and suitability for various sensing applications [**154**].

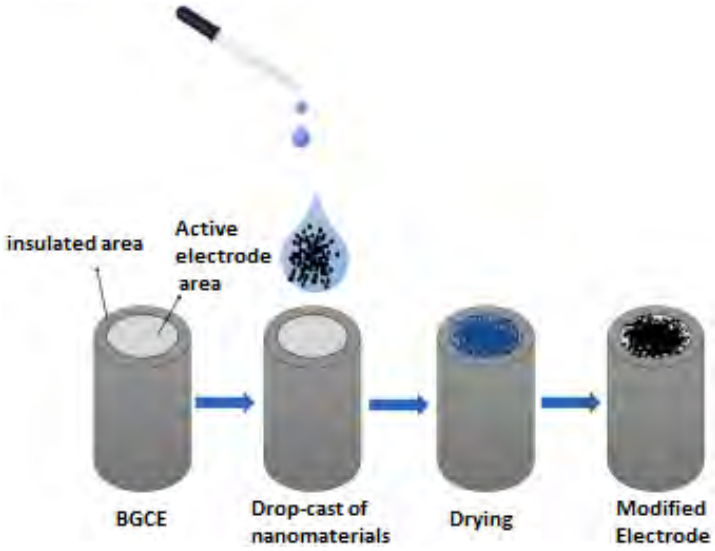

Figure 1.8. A schematic showing the drop-dry method for electrode modification [155]. BGCE = bare glassy carbon electrode

The drop casting method involves, a drop of a solution containing the modifier of interest being drop casted on to the electrode for modification; ideally confined on the conductive electrode area, **Figure 1.8**. The electrode is then subjected to drying, which involves the evaporation of particular solvent used. Drying can be under vacuum or oven, it all depends on the type and polarity of the used solvent [152,155].

1.6. Thesis Summary and Aims

The aim of this work is to develop surface engineering strategies in biosensor design: Towards the design and development of novel biosensor surfaces, with enhanced signal and sensitivity for the electrochemical detection of HER2 biomarker. The strategies employed in this work are divided into two classes and are listed below:

1.6.1. Signal Based Amplification

Signal-based amplification methods are methods applied in biosensor design, that lower the limit of detection (LOD) by modifying the transducer system to improve the signal-to-noise ratio

I. Impedimetric Aptasensor For HER2 Biomarker Using Graphene Quantum Dots, Polypyrrole and Cobalt Phthalocyanine Modified Electrodes

For the first time, the electropolymerization of pyrrole in the presence of SNGQDs and complex **1** is investigated towards the electrochemical detection of HER2 on a glassy carbon electrode. The synergetic combination of the properties of phthalocyanines, polypyrrole and SNGQDs as electrode modifiers for the electrochemical biosensing of HER2 is investigated.

II. Effect of linking a MPcs to CeO_2NPs

Two novel phthalocyanines: complex **2** and complex **3** are coupled with cerium oxide nanoparticles as electrode modifiers for immobilization support and signal amplification towards the electrochemical detection of HER2. The two phthalocyanines, differentiated only by the oxygen atom on the hydrocarbon chain part were investigated towards the electrochemical detection of HER2 as surface modifiers, first alone and when coupled with the CeO_2NPs.

III. Effect of nanomaterial on MPc

A cobalt phthalocyanine, complex **3** is employed for the first time in the presence of three different types of nanoparticles: carbon based (SNGQDs), metallic (AuNPs) and metal oxide (CeO_2 NPs). This is also the first time that an MPc is studied for HER2 detection in the presence of AuNPs. Both SNGQDs and complex **3** contain π electrons and can interact with each other through π-π stacking forming SNGQDs(π)**3**. The nanoparticles and complex **3** contain carboxylic groups to allow for the covalent immobilization of the amino functionalized HB5 aptamer on the electrode surface. The effect of the nature of the nanoparticle on the sensing ability of complex **3**, bearing in mind that size and defects of the nanoparticle affect the conducting abilities was investigated.

IV. Symmetry and Substituent Effect on MPcs

The effect of symmetry and substituent on the electrocatalytic properties of two phthalocyanines; complex **4** and complex **5** (new) is reported. The effect of replacing one acetylphenoxy ligand in the tetra substituted complex **4**, with a phenoxyacrylic acid ligand to form the complex **5** is investigated. The two complexes are compared as surface modifiers and signal amplifiers in the design of novel human epidermal growth factor receptor 2 (HER2) electrochemical biosensors. The performance of both complexes is further investigated in the presence of SNGQDs via π-π interactions, for enhanced electron transfer and signal amplification.

1.6.2. Target Based Amplification Strategies

Target based amplification strategies can be defined as methods that increase the number of detectable targets on the electrode surface. These methods are aimed at improving antigen-receptor interactions for enhanced sensitivity, precision and accuracy of the sensor.

V. Aptamer versus antibody as probes for the impedimetric biosensor for human epidermal growth factor receptor

This thesis reports on a comparative of aptamer and antibody as biorecognition elements towards the detection of HER2. On a glassy carbon electrode modified with a cobalt porphyrin binuclear framework (Co-BNF) and sulfur/nitrogen doped graphene quantum dots functionalized with gold nanoparticles (SNGQDs@AuNPs) both the HB5 aptamer and Trastuzumab were covalently immobilized under equivalent conditions and investigated as biorecognition elements towards HER2 detection.

VI. Single vs Sandwich Aptamers: Towards the Sensitive Detection of HER2 Using Composites of Phthalocyanine, Graphene Quantum Dots and CeO2 Nanoparticles

This thesis explores the effect of arrangement of biorecognition elements on the electrode surface in biosensor design. For the first time, the comparative performance of a single vs. a sandwich aptamer-based assay towards the electrochemical detection of HER2 on an electrode modified with complex **6** and SNGQDs@CeO_2NPs nanocomposite. The sandwich assay was completed by a novel bioconjugate; HB5-SNGQDs@CeO_2NPs for signal amplification strategy.

2. Materials, Equipment and Experimental

This chapter outlines the materials and equipment used in the work reported. It also outlines the synthesis, conjugation and electrode modification protocols followed.

2.1. Materials

2.1.1. General materials and solvents

The following chemicals were purchased from Sigma Aldrich: dimethyl sulfoxide, tetrahydrofuran, ethanol, dimethyl formamide, Aluminium oxide powder, Hexane, sodium phosphate dibasic, monobasic potassium phosphate, Potassium hexacyanoferrate (II) and potassium hexacyanoferrate (III). Millipore water, Type II was obtained from an Elga PURELAB Chorus 2 (RO/DI) system. Phosphate buffer saline (PBS, pH 7.4) was prepared using weighed amounts of Na_2HPO_4, NaH_2PO_4 and NaCl dissolved in Type II water.

2.1.2. MPc/Porphyrin synthesis and conjugates

N-hydroxy succinimide (NHS), 1-ethyl-3-(3-dimethylaminopropyl) carbodiimide (EDC), pyrrole, N, N'-dicyclohexylcarbodiimide (DCC), 1-pentanol, 1, 8-diazabicyclo (5.4.0) undec-7-ene (DBU), cobalt chloride, cobalt $(acetate)_3$, potassium hydroxide, and pyridine were purchased from Sigma Aldrich. The free base porphyrin (H_2P) was synthesized according to literature [**73**].

2.1.3. Nanoparticle Synthesis

The following chemicals were purchased form Sigma Aldrich: ethanol, hydrogen tetrachloroaurate (III) tetrahydrate, diethylamine, trisodium citrate, cerium sulphate (IV) and oleylamine was purchased from Sigma Aldrich. The nitric acid, sulphuric acid, and 25 % ammonia were purchased from B and M Scientific.

2.1.4. Biological Samples

The human serum (AB male plasma, H6914), the protein (HER2), and the monoclonal antibody HER2 (Trastuzumab) were purchased from Sigma Aldrich. The HB5 DNA aptamer (5'−/5 AmMC6/AAC CGC CCA AAT CCC TAA GAG TCT GCA CTT GTC ATT TTG TAT ATG TAT TTG GTT TTT GGC TCT CAC AGA CAC ACT ACA CAC GCA CA-3') was purchased from Integrated DNA Technologies, South Africa. The HB5 DNA aptamer solution was prepared according to the manufacturer's instructions for 100 µM in 10 mM PBS of pH 7.4. HER2 protein (specific target) was sold as a solution, with concentration of 4.4 mg/mL: necessary dilutions were made using PBS (pH 7.4). Similarly, the Trastuzumab antibody was diluted with PBS (pH 7.4) where necessary to obtain desired concentrations. The 1% bovine serum albumin (BSA) for non-specific binding was made using PBS solution (pH 7.4). All stock solutions were made using Millipore water and were kept at 4 °C during the course of the study.

2.2. Instrumentation

- Ground state electronic absorption spectra were recorded on a Shimadzu UV-2550 spectrophotometer.
- The elemental analysis was conducted using a Vario-Elementar Microcube ELIII.
- Infrared spectra were recorded on a Bruker® Alpha IR (100 FT-IR) spectrophotometer.
- X-ray powder diffraction (XRD) patterns were recorded on a Bruker D8 Discover equipped with a Lynx-Eye Detector, using CuKa radiation (= 1.5405 Å, nickel filter).
- The morphologies of nanoparticles were determined by transmission electron microscopy (TEM) using a Zeiss Libra 120 TEM operating at 80 kV.
- The surface of the modified electrodes was assessed using scanning electron microscopy (SEM), the TESCAN Vega TS 5136LM model. Glassy carbon plates (GCP, Goodfellow, UK) of 1 × 1 cm and 2 mm thick were used as a substrate for SEM.
- Mass spectral data were obtained on a Bruker Auto FLEX III Smart-beam TOF/TOF mass spectrometer, using a-cyano-4-hydrocinnamic acid as the matrix in the positive ion mode.
- A Bruker Vertex 70-Ram II Raman spectrometer (equipped with a 1064 nm Nd: YAG laser and liquid nitrogen cooled germanium detector) was used to collect Raman spectral data.
- X-ray photoelectron spectroscopy (XPS) spectra were collected using a Kratos Axis Ultra delay-line detector, using an Al (monochromatic) anode, equipped with charge neutralizer and the operating pressure kept below 5.0×10^{-9} Torr. For wide/survey

XPS scans, the following parameters were used: emission current was kept at 5 mA and the anode voltage at 15 kV. The resolution used to acquire wide/survey scans was at 160 eV pass energy using a hybrid lens in the slot mode. For high resolution scans, the resolution was changed to 40 eV pass energy in the slot mode. Curve fitting was performed using Gaussian-Lorentzian peak shape after performing a linear background correction. Glassy carbon plate was used for XPS.

- Electrochemical impedance spectroscopy (EIS) and cyclic voltammetry (CV) studies were performed using an Autolab Potentiostat PGSTAT30 equipped with Nova software version 2.1. The EIS experiments were performed between 0.1 and 100000 Hz, using 0.01 VRMS sinusoidal modulation. A non-linear least squares (NLLS) method based on the EQUIVCRT programme was used for automatic fitting of the obtained EIS data.

2.3. Synthesis

2.3.1. Nanoparticles

2.3.1.1. Gold nanoparticles (AuNPs) on SNGQDs surface to form composite - (SNGQDs@AuNPs), Scheme 3.1

The synthesis of sulphur-nitrogen doped graphene quantum dots (SNGQDs) and oleylamine capped AuNPs has been reported in literature [156, 157]. Novel composites based on SNGQDs and AuNPs were designed and are reported in this work. The surface functionalization of the SNGQDs with gold nanoparticles was achieved following a seed growth method previously reported [158] as follows: SNGQDs (10 mL, 1 mg/mL in H_2O) solution was sonicated for 10 min to ensure dissolution, followed by heating at 80 °C. To the heated SNGQDs solution, an aqueous solution of trisodium citrate (10 mL, 2.2 mM) was injected. Following that, a $HAuCl_4$ (1 mL, 25 mM) aqueous solution was quickly added to the mixture of SNGQDs and sodium citrate. The temperature of the reaction was increased to 90 °C, and the solution was left to boil for a further 20 min before being cooled down to room temperature. Prior to rotatory evaporation, ethanol was added to the particles to dissolve any unreacted material. The particles (SNGQDs@AuNPs) were dried in an oven overnight.

2.3.1.2. Cerium oxide nanoparticles (CeO_2NPs)

The cerium oxide nanoparticles were synthesized using the coprecipitation method reported in literature [159] as follows: cerium (IV) sulfate (6.5 g, 19.56 mmol) was dissolved in 10 mL of water. The mixture was stirred during dissolution of the salt, to prevent hydrolysis of the cerium salt which can occur when water is in excess. The solution was left to stir for a further 30 min at room temperature. Then, 25 % aqueous ammonia (1.4 M) solution was added dropwise until precipitation occurred. The solution was left under stirring conditions for a

further 2 h. The resultant nanoparticles were washed with Millipore water, followed by centrifugation to remove the ammonium sulfate as the only coproduct of the reaction.

Carboxylation of the CeO_2 nanoparticles: CeO_2NPs_{COOH}

The modification of the bare CeO_2NPs with the carboxylic groups was essential, to allow for the covalent immobilization of the amino functionalized HB5 aptamer on the glassy carbon electrode (GCE) during biosensor design. The carboxylation of the nanoparticles was achieved using the acidic oxidation method, following literature methods [159].

2.3.1.3. CeO_2NPs growth on SNGQDs to form nanocomposite SNGQDs@CeO_2NPs, Scheme 3.1

A novel nanocomposite was synthesized in this work, where the CeO_2NPs are grown onto the sp^2 framework of the SNGQDs as follows: SNGQDs (15 mg) were dissolved in Millipore water (10 mL) followed by sonication to ensure dissolution, **Scheme 3.1**. In an empty flask (1 g, 0.003 mmol) of cerium (IV) sulphate was added, followed by the addition of the SNGQDs solution, the mixture was then immediately subjected to stirring. The brownish yellow mixture, was left to stir for another 30 min at room temperature. To form the nanoparticles, 25 % aqueous ammonia (1.4 M) was added dropwise until precipitation occurred. The resultant mixture was left under continuous stirring for another 2 h. The resulting SNGQDs@CeO_2NPs were washed with water and centrifuged to ensure purification. To speed up the drying process, the nanocomposite was further washed with ethanol. The SNGQDs@CeO_2NPs were dried under vacuum.

2.3.2. Synthesis of CoPc derivatives

The following CoPc derivatives: [Co tetra carboxy phenoxy phthalocyanine {CoTCPPc} (**1**), Co tetra phenoxy propionic acid {CoTPPc} (**2**), Co tetra phenoxy acetic acid {CoTPAPc} (**3**), Co tetra acetylphenoxy phthalocyanine {CoTAcPhPc} (**4**), Co tris-(acetylphenoxy)-mono-phneoxyacrylic acid phthalocyanine {CoMPhAaPc} (**5**) and Co tris-3,5- dimethyl – phenoxy pyridine (5) -oxy- (2)- carboxylic acid {CoMPhPyPc} (**6**) were synthesized. All molecules are new except for molecules **1** and **4**, whose synthetic method shall be omitted [75,76].

2.3.2.1. Co tetra phenoxy propionic acid {CoTPPc} (2), Scheme 3.2

The starting material 3-(4-(3,4-dicyanophenoxy) phenyl) propionic acid was synthesized as reported in literature [160]. Complex **2** was synthesized as follows: a mixture of 1-pentanol (5 mL), 3-(4-(3,4-dicyanophenoxy) phenyl) propionic acid (860 mg, 2.94 mmol), cobalt chloride (44 mg, 0.25 mmol), and DBU (0.2 mL) was heated at 160 °C for 9 h under nitrogen atmosphere. The resulting product complex **2**, was precipitated out using hot ethanol (100 %). The product was further purified using chromatographic methods on a Si_{60} column with THF. Yield: 55 g (43.8%) UV/Vis (DMSO): λ_{max}, nm, (log ε), 671 (4.85), 617 (4.41) and 376 (5.19). IR (Platinum ATR): ν_{max}, cm^{-1}, 3071 (*OH*), 1750 (*C = O*) and 2885 (*C-H*). Calculated for $C_{68}H_{48}CoN_8O_{12}\cdot 3H_2O$: C; 63.65, H; 4.25, N; 8.74 Found: C; 62.80, H; 4.60, N; 7.88. MALDI–TOF MS *m/z*: Calcd.: 1228, Found: ($[M]^+$) 1228.78.

2.3.2.2. Co tetra phenoxy acetic acid {CoTPAPc} (3), Scheme 3.2

The synthesis of the 2-(4-(3,4-dicyanophenoxy) phenoxy) acetic acid phthalonitrile has been reported [161]. Complex **3** was synthesized as described for complex **2** except 2-(4-(3,4-dicyanophenoxy) phenoxy) acetic acid (860 mg, 2.92 mmol) was used instead. The amounts of all the other reagents as well as purification procedure were the same. Yield: 55 g (43.8%)

UV/Vis (DMSO): λ_{max}, nm, (log ε), 697 (5.20), 629 (4.81) and 331 (5.72). IR (Platinum ATR): ν_{max}, cm^{-1}, 3313 (OH), 1589 (C=O), 2928 (C-H) and 1231 (C-O-C). Calculated for $C_{64}H_{40}CoN_8O_{16}$: C; 62.14, H; 3.24, N; 9.06, Found: C; 61.34, H; 3.76, N; 8.14. MALDI–TOF MS *m/z*: Calcd.: ($[M + H]^+$) 1236 Found: ($[M]^+$) 1236.67.

2.3.2.3. Co tris-(acetylphenoxy)-mono-phenoxyacrylic acid phthalocyanine {CoMPhAaPc} (5), Scheme 3.3

The compounds (E)-3-(3-(3,4-dicyanophenoxy) phenyl) acrylic acid [**162**], 4-(3-acetylphenoxy) phthalonitrile [**163**], were synthesized as reported in literature. In a reaction flask containing cobalt acetate (44 mg, 0.25 mmol), a stoichiometric mixture (1:3) of (E) -3-(3-(3,4-dicyanophenoxy) phenyl) acrylic acid (0.25 g, 0.861 mmol) and 4-(3-acetylphenoxy) phthalonitrile (0.67 g, 2.583 mmol) was added. The contents were then dissolved in 1-pentanol (5 mL), accompanied by dropwise addition of DBU (0.2 mL). The mixture was subjected to heating at 160 °C for 9 h under nitrogen atmosphere. The resulting product complex **5**, was precipitated out using methanol (100 %). The product was further purified using chromatographic methods on a Si_{60} column with methanol/THF (1: 5 ratio). Yield: 0.48 g (48.9 %). UV/Vis (DMSO): λ_{max}, nm, (log ε), 666 (5.32), 600 (4.96) and 376 (5.55). IR (Platinum ATR): vmax, cm^{-1}, 3005 (OH), 1750 (C=O) and 2925 (C-H). MALDI–TOF MS m/z: Calcd.: 1135.99 Found: ($[M + 3H]^+$ 1139.20. Elemental Anal. Calc. for $C_{65}H_{40}CoN_8O_9$ C:68.72, N:9.86 Found C: 67.21 N: 9.52.

2.3.2.4. Co tris-3,5- dimethyl – phenoxy pyridine (5) -oxy- (2)- carboxylic acid {CoMPhPyPc} (6), Scheme 3.3

The compounds 4 - (3, 5- dimethoxy-phenoxy) phthalonitrile [**164**] and pyridine (5) oxy (2)- carboxylic acid phthalonitrile [**165**] were synthesized as reported in literature. Complex **6**, similar to complex **5** is an asymmetric CoPc complex and as such the synthesis is similar. A stochiometric mixture (1:3) of 4 - (3, 5- dimethoxy-phenoxy) phthalonitrile and (0.25 g, 0.94 mmol) and pyridine (5) oxy (2)- carboxylic acid phthalonitrile (0.67 g, 2.83 mmol) was added to a flask containing cobalt acetate (44 mg, 0.25 mmol). The contents were then dissolved in 1-pentanol (5 mL), accompanied by dropwise addition of DBU (0.2 mL). The solution was subject to heating at 160 °C for 9 h under nitrogen atmosphere. The desired product (complex **6**) was precipitated out using methanol (100 %). The product was further purified using chromatographic methods on a Si_{60} column with methanol/THF (1: 5 ratio). Yield: 0.42 g (38.2 %). UV/Vis (DMSO): λ_{max}, nm, (log ε), 675 (5.30), 610 (4.97) and 311 (5.55). IR (Platinum ATR): ν_{max}, cm^{-1}, 3067 (carboxylic OH), 1762 (carboxylic C=O), 1594, 1432 (C=C, pyridine C=N). Elemental Analysis for $C_{62}O_{12}N_9H_{43}Co.2H_2O$: Calc. C: 62.17, N:10.49 Found. C: 61.26, N: 8.25. MALDI–TOF MS m/z: Calcd.: 1164.24 Found: ([M]) 1164.83.

2.3.3. Non-covalent π-π stacking of SNGQDs to complexes 3, 4 and 5 to form conjugates, Scheme 3.5

The SNGQDs are sp^2 hybridized and are a highly π - conjugated type of nanomaterial which can undergo π-π interactions with any similarly conjugated nanomaterial. MPcs are π-electron rich molecules and therefore qualify for π-π stacking with the SNGQDs. Various reports have demonstrated that, the combination of MPcs with various nanomaterials results in improved physicochemical properties [**64**]. Non-covalent π-interactions in particular, are a

selected method due to the fact that the involved molecules can interact to form a supramolecule, while the structural integrity of the involved individual molecules is preserved.

The π-π stacking of the SNGQDs with the complexes **3**, **4** and **5** was done as follows: SNGQDs (5 mL, 1 mg/mL in H_2O) were independently added to: complex **3** (5 mL, 8.086×10^{-4} mmol in DMSO)**,** complex **4** (5 mL, 4.55×10^{-3} mmol in DMF) and complex **5** (5 mL, 4.424×10^{-3} mmol in DMF) solutions, respectively as shown in **Scheme 3.4** (showing **3**(π)SNGQDs as an example). Three mixtures were formed, each containing the said Pc complex and SNGQDs for interaction. The resulting mixtures were subject to stirring to ensure complete mixing of the SNQGDs and the respective Pc complex solutions. The π-π interactions were induced by sonication for 4 h, at room temperature of the three mixtures to form **3**(π)SNGQDs, **4**(π)SNGQDs and **5**(π)SNGQDs, respectively.

2.3.4. Synthesis of the cobalt binuclear framework – CoP-BNF, Scheme 3.5

The cobalt porphyrin binuclear framework was synthesized as reported in [**166**]: A free base porphyrin, H_2P (9.2 mg, 0.012 mmol) was dissolved in 2 mL of DMF, followed by addition of aqueous KOH (1 mL, 0.2 M) to assist in the deprotonation of some of the COOH groups in H_2P. To this solution, $Co(acetate)_3$ (8.6 mg/mL aq.) was added followed by pyridine (0.1 mL) to increase solubility. The contents were placed in a 400 mL Teflon lined autoclave and the reaction temperature was set at 150 °C for a period of 50 h, followed by cooling to room temperature. The resultant sample was centrifuged at 24000 rpm at 5 min intervals using ethanol to wash off any unreacted material. The binuclear framework was dried under vacuum overnight. Yield: 7.6 mg (82.6%), IR (Platinum ATR): ν_{max}, cm^{-1} (-OH) 3434 cm^{-1}, ν(c=o) 1797 cm^{-1} and ν(c=c) 1674 cm^{-1}. UV–Vis (in H_2O): λ_{max} (log ε) nm Soret band: 419 (4.87), Q-

band$_1$: 544 (4.01), Q-band$_2$: 580 (3.70). Elemental analysis for $C_{98}H_{57}Co_3N_8O_{18}$ calc.: C, 64.98; H, 3.14; N, 6.18. Found: C, 63.02; H, 3.41; N, 5.98. MS (MALDI-TOF) (m/z): Calculated: 1811.34 Found: 1814.32 [M + 3H+].

2.4. Electrode Modification

A three-electrode electrochemical cell consisting of Ag|AgCl (3 M KCl) as reference electrode, a glassy carbon electrode (GCE) (geometric area of 0.071 cm^2) as the working electrode and a platinum wire as the counter electrode was used. All the solutions were freshly prepared in Milli-Q water and stored at the temperature of 4 °C until use. The GCE was first polished with Al_2O_3 powder (Aldrich, 0.1, 0.05 mm) using Metrohm polishing kit, and rinsed with deionized water, followed by sonication in ethanol and deionized water. Finally, the electrode was allowed to dry at room temperature. All the GCEs were modified by the drop dry method.

2.4.1. Drop and Dry Modification

The synthesized materials (**Section 2.3**) were all used for electrode modification, using the drop and dry method. Each nanomaterial was dissolved in an appropriate solvent to form a solution. For each modifier, 10 µL of solution was placed on the GCE surface, followed by drying in the oven at 60 °C. The GCE electrode was modified with a single nanomaterial, two/more nanomaterials by sequential adsorption and Pc/nanomaterial conjugates as a unit. Sequential adsorption refers to an organized layering of various nanomaterials on the electrode surfaces following a sequence, (electrodes labelled seq.). In most cases the particular nanoparticle is added first, followed by the MPc or CoP-BNF. **Table 2.1** lists the modifiers used, solvent and amounts of each modifier on the GCE surface.

Table 2.1. Summary of amounts of modifiers dispersed in different solvents in preparation for electrode surface modification.

Modifier	Solvent	Concentration
1	DMSO	4.6×10^{-4} mmol
2	DMSO	0.81 mmol
3	DMSO	0.81 mmol
4	DMF	9.09×10^{-4} mmol
5	DMF	8.85×10^{-4} mmol
6	DMF	8.57×10^{-4} mmol
CoP-BNF	H_2O	1.75×10^{-3} mmol
SNGQDs	H_2O	1 mg
CeO_2NPs_{COOH}	H_2O	1 mg
AuNPs	Hexane	1 mg
SNGQDs@AuNPs	H_2O	1 mg
SNGQDs@CeO_2NPs	H_2O	1 mg
CeO_2NPs_{COOH}/**2**(seq.)	H_2O/DMSO	1 mg/0.81 mmol
CeO_2NPs_{COOH}/**3**(seq.)	H_2O/DMSO	1 mg/0.81 mmol
SNGQDs/**3**(seq.)	H_2O/DMSO	1 mg/0.81 mmol

AuNPs/**3**(seq.)	Hexane/DMSO	1 mg/0.81 mmol
3(π)SNGQDs	DMF	1 mg
4(π)SNGQDs	DMF	1 mg
5(π)SNGQDs	DMF	1 mg
SNGQDs@CeO_2NPs/**6**(seq.)	H_2O/DMF	1 mg/8.57×10^{-4} mmol
SNGQDs@AuNPs/CoP-BNF (seq.)	H_2O	1 mg/1.75×10^{-3} mmol

2.4.2. Electrochemical polymerization

This process involves the deposition of a polymer onto the surface of an electrode. This occurs through a generally accepted mechanism that involves the formation of cationic radical by the oxidation of the monomer on the solid electrode material. A known potential is usually applied on the electrode to induce polymerisation. First, the glassy carbon electrode was modified with polypyrrole film by electrochemical deposition of a non-functionalized pyrrole monomer, GCE/PPy. The solution of pyrrole monomer (0.15 mM) was scanned from −0.6 V to 0.8 V vs Ag/AgCl, at a scan rate of 100 mV/s in 10 mM PBS (pH 7.4).

2.4.2.1. Electrodes modified by polymerization of pyrrole in the presence of SNGQDs or CoPc, followed by adsorption

(i) GCE/PPy@SNGQDs: To the electrochemical cell, a pyrrole monomer solution (0.15 mM, 1 mL) was added together with 100 µL SNGQDs (1 mg/mL), followed by mechanical stirring and purged with argon.

(ii) GCE/PPy@**1**: To the electrochemical cell, 100 µL of complex **1** (1 mg/mL, DMSO) was added to pyrrole monomer (0.15 mM, 1 mL) solution, followed by stirring.

(iii) GCE/PPy@SNGQDs/**1**: To the surface GCE/PPy@SNGQDs, 10 µL of the complex **1** solution was added and electrode allowed to dry.

(iv) GCE/PPy@**1**/SNGQDs: To GCE/PPy@**1** surface, 10 µL of SNGQDs (1 mg/mL) were added. The electrode was then left to dry.

2.4.2.2. Sequential electrode modification

The following electrodes were modified via sequential adsorption on GCE/PPy, they are represented with (seq.) at the end:

(v) GCE/PPy/SNGQDs(seq.): To a freshly prepared GCE/PPy electrode, 10 µL of SNGQDs (1 mg/mL) was added. The electrode was left to dry in the oven for 30 min, 60 ◦C to give GCE/PPy/SNGQDs (seq.)

(vi) GCE/PPy/**1**(seq.): To a freshly prepared GCE/PPy electrode, 10 µL of complex **1** (1 mg/mL in DMSO) was added. The electrode was left to dry in the oven for 30 min, 60 ◦C to give GCE/PPy/**1**(seq.)

(vii) GCE/PPy/SNGQDs/**1** (seq.): To the surface GCE/PPy/SNGQDs(seq.), 10 µL of complex **1** (1 mg/mL), was added. The electrode was left to dry in the oven for 30 min, 60 ◦C to achieve GCE/PPy/SNGQDs/**1**(seq.)

(viii) GCE/PPy/**1**/SNGQDs(seq.): To the surface GCE/PPy/**1** (seq.) an aliquot of the SNGQDs (1 mg/mL in PBS) was added. The electrode was left to dry in the oven for 30 min, 60 ◦C to achieve to achieve GCE/PPy/**1**/SNGQD (seq.)

Table 2.2. Summary of GCE surfaces modified by electropolymerization of pyrrole to form (PPy)

Modified GCE surfaces
GCE/PPy
GCE/PPy@SNGQDs
GCE/PPy@**1**
GCE/PPy@SNGQDs/**1**
GCE/PPy@**1**/SNGQDs
GCE/PPy/SNGQDs(seq.)
GCE/PPy/**1**(seq.)
GCE/PPy/SNGQDs/**1**(seq.)
GCE/PPy/**1**/SNGQDs/(seq.)

2.5. Sensor Fabrication

2.5.1. Aptamer Immobilization

The HB5 aptamer used in this work was strategically designed, and endowed with an NH_2 terminal. The different nanomaterials listed were used as immobilization platforms of the HB5 aptamer onto the GCE surface. The chemistry of immobilization was governed by the functional groups present in each nanomaterial. The amounts, concentration and incubation time of the HB5 on each surface was decided by various optimization experiments. **Table 2.3** lists all the nanomaterials, key functional groups and immobilization chemistry to the HB5 aptamer on the GCE surface. The most common chemistry used is amide bond formation via EDC/NHS and DDC/NHS coupling; the former for water soluble nanomaterials (e.g. SNGQDs) and the latter used otherwise (e.g. MPcs). Ligand exchange and acid catalysed imine bond formation techniques was applied for selected nanomaterials.

Table 2.3. List of nanomaterials used for GCE modification, key functional groups and immobilization chemistry to the HB5 aptamer on the GCE surface.

Modifier	**Key Functional Groups**	**Nanomaterial-HB5 aptamer bond**
1	-COOH	amide
2	-COOH	amide
3	-COOH	Amide
4	Ketone	Imine
5	Ketone and -COOH	imine and amide
6	-COOH	Amide
CoP-BNF	-COOH	Amide
SNGQDs	-COOH	Amide
CeO_2NPs_{COOH}	-COOH	Amide
AuNPs	Ligand	ligand Exchange
SNGQDs@AuNPs	-COOH	Amide
SNGQDs@CeO_2NPs_{COOH}	-COOH	Amide
CeO_2NPs_{COOH}/**2**(seq.)	-COOH	Amide
CeO_2NPs_{COOH}/**3**(seq.)	-COOH	Amide
SNGQDs/**3**(seq.)	-COOH	Amide

AuNPs/**3**(seq.)	-COOH	Amide
3(π)SNGQDs	-COOH	Amide
4(π)SNGQDs	-COOH	Imine
5(π)SNGQDs	-COOH	amide and imine
SNGQDs@CeO_2NPs/**6**(seq.)	-COOH	Amide
SNGQDs@AuNPs/CoP-BNF (seq.)	-COOH	Amide
GCE/PPy@SNGQDs	-COOH	Amide
GCE/PPy@**1**	-COOH	Amide
GCE/PPy@SNGQDs/**1**	-COOH	Amide
GCE/PPy@**1**/SNGQDs	-COOH	Amide
GCE/PPy/SNGQDs(seq.)	-COOH	Amide
GCE/PPy/**1**(seq.)	-COOH	Amide
GCE/PPy/SNGQDs/**1**(seq.)	-COOH	Amide
GCE/PPy/**1**/SNGQDs/(seq.)	-COOH	Amide

2.5.1.1. HB5-aptamer immobilization on compound 1, PPy and related surfaces, Scheme 4.1

First, different aptamer concentrations (0.1–1.25 μM) were immobilized on the modified electrodes, at room temperature for 30 min for optimization purposes. The optimization was performed on the GCE/PPy@SNGQDs surface, and the optimum concentration of 1 μM was (to be discussed in **Ch 4**, **Fig. 4.15**) obtained. The aptamer was immobilized onto the 10 individual electrodes surface through a covalent amide linkage via EDC/NHS coupling, owing to the carboxylic group rich SNGQDs and complex **1** interacting with the amine modified HB5 aptamer.

The following freshly modified electrodes: GCE/SNGQDs, GCE/**1**, GCE/PPy@SNGQDs, GCE/PPy@**1**, GCE/PPy@SNGQDs/**1**, GCE/PPy@**1**/SNGQDs, GCE/PPy/SNGQDs (seq.), GCE/PPy/**1**(seq.), GCE/PPy/SNGQDs/**1** (seq.) and GCE/PPy/**1**/SNGQDs (seq.) were all immersed in a solution of EDC (0.0116 mmol, 0.0018 g) and NHS (0.0304 mmol, 0.0034 g) respectively, for 30 min. Following this, the EDC/NHS activated electrodes were immersed in a HB5 aptamer solution (at the optimum concentration of 1 μM) and left for 30 min at room temperature. In order to remove the unbound aptamer molecules on the electrode surface, the electrodes were washed with PBS (pH 7.4). The electrodes were allowed to air dry.

The following surfaces were formed: GCE/SNGQDs/HB5, GCE/**1**/HB5, GCE/PPy@SNGQDs/HB5, GCE/PPy@**1**/HB5, GCE/PPy@SNGQDs/**1**/HB5, GCE/PPy@**1**/SNGQDs/HB5, GCE/PPy/SNGQDs (seq.)/HB5, GCE/PPy/**1**(seq.)/HB5, GCE/PPy/SNGQDs/**1** (seq.) /HB5 and GCE/PPy/**1**/SNGQDs (seq.)/HB5.

2.5.1.2. Amide Linkage

2.5.1.2.1. DCC/NHS coupling for amide bond formation: Complex 2, 3, 5 and 6. Scheme 4.2

Using the MPc based electrode GCE/**3** for optimization: five different concentrations 0.25 µM, 0.5 µM, 0.75 µM, 1.0 µM and 1.25 µM were prepared in PBS at pH = 7.4. The GCE/**3** surface was prepared as outlined in **Section 2.4**. On the electrode DCC (6.0 mg, 0.029 mmol) and NHS (4.0 mg, 0.035 mmol) were added. The electrodes were left at room temperature for 1 h. Following which, 10 µL of each of the HB5 prepared concentrations was dropped on the modified electrode respectively. The HB5 amount (0.75 µM, to be discussed in **Ch 4**, **Fig. 4.16**) was observed as the optimum concentration, and was used for Pc and their related conjugates. The materials used contain COOH groups and are not water soluble, **Table 2.3**.

The following freshly prepared surfaces: GCE/**2**, GCE/**3**, GCE/**5**, GCE/**6**, GCE/**3**(π)SNGQDs, GCE/**5**(π)SNGQDs, GCE/CeO_2NPs_{COOH}/**2** (seq.), GCE/SNGQDs/**3** (seq.) and GCE/AuNPs/**3** (seq.), GCE/CeO_2NPs_{COOH}/**3** (seq.) and SNGQDs@CeO_2NPs/**6** (seq.): were activated using DCC (6.0 mg, 0.029 mmol) and NHS (4.0 mg, 0.035 mmol), for an hour at room temperature. Following which, 10 µL the HB5 optimum amount (0.75 µM) was dropped on the respective modified electrodes. The following surfaces were formed: GCE/**2**/HB5, GCE/**3**/HB5, GCE/**5**/HB5 (amide), GCE/**6**/HB5, GCE/**3**(π)SNGQDs/HB5, GCE/**5**(π)SNGQDs/HB5(amide), GCE/CeO_2NPs_{COOH}/**2**(seq.)/HB5, GCE/SNGQDs/**3**(seq.)/HB5, GCE/AuNPs/**3**(seq.)/HB5, GCE/CeO_2NPs_{COOH}/**3**(seq.)/HB5 and SNGQDs@CeO_2NPs/**6**(seq.)/HB5.

2.5.1.2.2. EDC/NHS coupling: SNGQDs, CeO_2NPs_{COOH}, SNGQDs@AuNPs, CoP-BNF and SNGQDs@CeO_2NPs modified electrodes

All said nanoparticles are water soluble and have carboxylic acid functional groups, with which the HB5 aptamer was covalently linked via amide bond formation using EDC/NHS coupling. The following modified surfaces: GCE/SNGQDs, GCE/CeO_2NPs_{COOH}, GCE/SNGQDs@AuNPs and GCE/SNGQDs@CeO_2NPs were treated with EDC/NHS: EDC (0.0116 mmol, 0.0018 g) and NHS (0.0304 mmol, 0.0034 g) for carboxylic group activation. After this 10 µL of HB5 aptamer (1.0 µM) was added onto the activated surface to form: GCE/SNGQDs/HB5, GCE/CeO_2NPs_{COOH}/HB5, GCE/SNGQDs@AuNPs/HB5 and GCE/SNGQDs@CeO_2NPs/HB5, **Table 2.3**.

The surface GCE/CoP-BNF/HB5 was formed by immersing the probe GCE/CoP-BNF in a solution of NHS (0.3 mL, 100 mM) and EDC (0.1 mL, 50 mM) and were stored for 8 h at 4 °C. In the next step the HB5 aptamer (10 µL) was drop cast onto the activated electrode and left at 4 °C for 8 h.

2.5.1.2.3. Conjugation of the SNGQDs@CeO_2NPs with the HB5 aptamer to form HB5-SNGQDs@CeO_2NPs bioconjugate (Free or not on GCE), Scheme 4.6

The SNGQDs@CeO_2NPs contain graphene quantum dots and as a result has carboxylic acid functionalized edges. The HB5-SNGQDs@CeO_2NPs (free/not on GCE) bioconjugate was formed by amide bond formation between the NH_2-HB5 aptamer and carboxylated SNGQDs@CeO_2NPs. The conjugate was formed as follows: 1 mg of SNGQDs@CeO_2NPs was dispersed in PBS (300 µL, pH 7.4). Then, EDC and NHS (1.0 $mmol \cdot L^{-1}$) were added to activate the –COOH groups followed by shaking (using a shaker) for 4 h. Following this, 100 µL of the

HB5 aptamer (0.75 µM) was added onto the SNGQDs@CeO_2NPs to induce nucleophilic attack onto the activated carbonyl carbons of the SNGQDs@CeO_2NPs. The resulting mixture was kept for 2 h under moderately shaking in the dark to allow successful amide bond formation. To remove the nonconjugated SNGQDs@CeO_2NPs, the mixture was centrifuged (5000 rpm for 20 min) and subsequently washed with phosphate buffer (pH 7.4). The precipitate was suspended in PBS (100 µL, pH 7.4) and stored at 4 °C. The synthesized HB5-SNGQDs@CeO_2NPs bioconjugate is ready for modification of electrode.

2.5.1.3. Imine Bond: complex 4 and 5 based, Scheme 4.3

Complex **4**, contains only ketone groups; the immobilization of the HB5 aptamer on the GCE/**4** was achieved following the acid catalysed imine formation reaction. Imine bonds typically form upon reaction of a ketone (e.g., complex **4**) and a primary amine (e.g., HB5 aptamer) in the presence of a mild acid, **Scheme 4.3**. Considering that the complex **5** has one carboxylic and three ketone functional groups: immobilization of the HB5 aptamer on the GCE/**5** via its ketone ligands was also explored. The same methodology was applied for complex **4** and **5** related conjugates.

The following modified surfaces: GCE/**4**, GCE/**5**, GCE/**4**(π)SNGQDs and GCE/**5**(π)SNGQDs were treated with 10 µL of HB5 aptamer, followed by addition of 10 µL of (dilute H_2SO_4, pH = 4.5), and then the electrodes were left to dry in the oven. The resulting aptasensors are labelled GCE/**4**/HB5, GCE/**5**/HB5 (imine), GCE/**4**(π)SNGQDs/HB5 and GCE/**5**(π)SNGQDs/HB5 (imine). The complex **5** based electrodes are denoted with amine/imine to differentiate on the mechanism of HB5 immobilization.

2.5.1.4. HB5-aptamer immobilization on AuNPs modified electrode via ligand exchange

The procedure for the formation GCE/AuNPs/HB5 was done following a ligand approach method reported in [**167** - **169**]: the HB5 aptamer (10 µL, 1.0 µM) was placed on the GCE/AuNPs to allow the N-Au bond to form. The GCE/AuNPs was first immersed in 500 µL of diethylamine (DEA) solution for 1 h, to displace and replace the oleylamine ligand on the AuNPs surface. The DEA was then removed by rinsing the electrode surface with dilute acetic acid. DEA is a small amine molecule, which can be conveniently removed from the metal surface by protonation with an acid [**168**]. Following that, 10 µL of the HB5 solution was added onto the GCE/AuNPs to form the GCE/AuNPs/HB5 surface.

2.5.2. Antibody Immobilization -Trasmatuzab, Scheme 4.4 & 4.5

Another biorecognition element used in this work is the Trastuzumab monoclonal antibody, which is HER2 specific. Like any other antibody, the Trastuzumab consist of a heavy chain and a light chain both bound together by disulfide bonds. Most significantly, Trastuzumab is endowed with an $-NH_2$ moiety at the heavy chains arising from lysine residues, **Figure 2.1**.

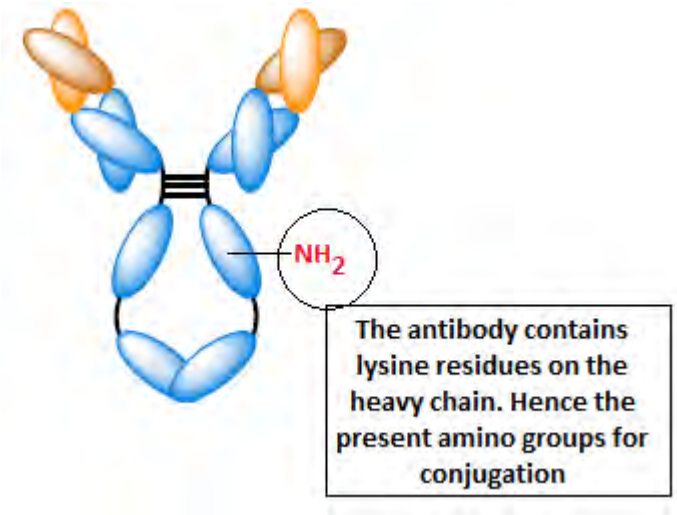

Figure 2.1. Structure of the Trastuzumab antibody [170]

The amino group allows for protein modification and conjugation to various nanomaterials. This work reports on the immobilization of the said antibody on a GCE electrode modified with CoP-BNF and/or SNGQDs@AuNPs. The immobilization was via an amide bond formation using EDC/NHS coupling. Both the CoP-BNF and the SNGQDs@AuNPs have carboxylic groups which were activated using the EDC/NHS coupling reaction as follows: The GCE/SNGQDs@AuNPs/CoP-BNF (seq.), GCE/SNGQDs@AuNPs and GCE/CoP-BNF were separately immersed in an aqueous solution of NHS (0.3 mL, 100 mM) and EDC (0.1 mL, 50 mM) and were stored for 2 h at 4 °C. The activation made it possible for covalent attachment of the Trastuzumab antibody (which has amino groups) onto the electrode surface via an amide bond as follows: Trastuzumab (10 µL) was added separately to GCE/CoP-BNF, GCE/SNGQDs@AuNPs and GCE/SNGQDs@AuNPs/CoP-BNF (seq.) and the electrodes were left for 8 h at 4 °C. The resulting immunosensors: GCE/CoP-BNF/Trastuzumab, GCE/SNGQDs@AuNPs/Trasmatuzab and GCE/SNGQDs@AuNPs/CoP-BNF (seq.)/Trastuzumab were formed.

2.5.3. Non- Specific Binding

In order to limit non-specific binding on the free surface sites on the electrode, 1 % Bovine serum albumin (BSA) was added to the modified electrodes in **Sections 2.5.1** and **2.5.2.** Finally, aptasensors and immunosensors with the BSA blocking layer were ready for capturing the HER2 analyte.

2.5.4. HER2 detection

2.5.4.1. HER2 detection in PBS buffer

The electrochemical response of the electrodes in the presence of varying concentrations of the HER2 antigen was measured using the electrochemical impedance spectroscopy (EIS). Two HER2 concentration ranges of 0 -10 ng/mL and 0 - 21 pg/mL for complexes **1**-**5**; CoP-BNF and complex **6** based probes, respectively were used. The EIS measurements were conducted under the stable open circuit potential with the frequency from 0.1 to 100000 Hz, using 0.01 V_{RMS} sinusoidal modulation.

2.5.4.2. HER2 detection in Human Serum

Preliminary experiments for the determination of HER2 protein in human serum samples were also performed. The designed aptasensors were tested in 1/500 diluted (in 0.1 M PBS buffer, pH 7.4) serum samples spiked by standard addition of HER2 protein. For complex **1**-**5** and CoP-BNF based probes {[HER2] = 1 ng/mL, 3 ng/mL, 5 ng/mL and 7 ng/mL} and for complex **6** based probes {[HER2] = (1 pg/mL, 3 pg/mL, 5 pg/mL and 7 pg/mL)}. The response of the aptasensors and immunosensors was then determined by EIS measurements, under the same conditions used for HER2 calibration curve.

2.5.4.3. Repeatability and stability

The repeatability of the designed probes was investigated by running successive measurements at each HER2 concentrations in triplicate and the standard deviation was calculated. The relative standard deviation (RSD) for all electrodes was determined at each concentration. The stability of the designed sensors was investigated using the shelf-life estimation method. Where, the sensors were stored at 4 ° C over 96 h. The response of each probe was analysed daily over the 96-hour period.

2.5.4.4. Surface Regeneration and Reusability

The surface regeneration and reusability of the designed sensors was investigated following the chemical regeneration approach. In particular, the regeneration of the biosensor surfaces was focused on the different biorecognition elements used, as well as their arrangement on the electrode surface. The successful regeneration of the electrode surfaces was investigated based on three conditions: (i) the stability of the surface chemistry of the biosensor before and after dissociation, (ii) the ability of the antibody-HER2 or aptamer-HER2 interaction to dissociate fully under the set conditions, and (iii) the stability of the capture probes (aptamer/antibody) and their ability to retain activity and detect the analyte after regeneration.

List of Publications

This work comprises of published or submitted material in the following peer reviewed journals. These publications have not been referenced in text.

1. **S. Centane**, S Mgidlana, Y Openda and T Nyokong, Single vs Sandwich Aptamers: Towards the Sensitive Detection of HER2 Using Composites of Phthalocyanine, Graphene Quantum Dots and CeO_2 Nanoparticles, Bioelectrochemistry, 153 (2023) 108496.

2. **S. Centane**, S. Mgidlana, Y. Openda, N. Ndebele and T. Nyokong, Effect of symmetry and substituents of cobalt based phthalocyanines in aptasensor design for the electrochemical impedimetric detection of the human epidermal growth factor receptor 2, Bioelectrochemistry, 941 (2023) 117524.

3. **S. Centane** and T. Nyokong, Co phthalocyanine mediated electrochemical detection of the HER2 in the presence of Au and CeO_2 nanoparticles and graphene quantum dots, Bioelectrochemistry, 149 (2023) 108301.

4. **S. Centane**, S. Mgidlana, Y. Openda and T. Nyokong, Electrochemical detection of human epidermal growth factor receptor 2 using an aptamer on cobalt phthalocyanines – Cerium oxide nanoparticle conjugate, Bioelectrochemistry, 146 (2022) 108146.

5. **S. Centane** and T. Nyokong, Aptamer versus antibody as probes for the impedimetric biosensor for human epidermal growth factor receptor, J. Inorg. Biochem., 230 (2022) 111764.

6. **S. Centane** and T. Nyokong, Impedimetric aptasensor for HER2 biomarker using graphene quantum dots, polypyrrole and cobalt phthalocyanine modified electrodes, Sensing and Bio-Sensing Research, 34 (2021) 100467.

7. **S. Centane** and T. Nyokong, The antibody assisted detection of HER2 on a cobalt porphyrin binuclear framework and gold functionalized graphene quantum dots modified electrode, J. Electroanal. Chem., 880 (2021) 114908.

3. Characterization

This chapter covers the characterization of Pcs, the nanomaterials and their conjugates. The success of the proposed synthetic routes in Chapter 2 is assessed and confirmed herein. Using various analytical techniques, the physicochemical properties of the synthesized materials alone, and in conjugation are discussed.

3.1. Characterization of SNGQDs, CeO_2NPs and AuNPs and related conjugates

Scheme 3.1. shows the synthesis of SNGQDs@AuNPs and CeO_2NPs@SNGQDs conjugates. The well-known affinity of gold to S and N was exploited for the in-situ synthesis of the AuNPs onto SNGQDs, a process which merely involves their self-assembly onto the SNGQDs surface owing to the presence of sulfur and nitrogen groups in the as-synthesized GQDs, **Scheme 3.1(i).** Similarly, SNGQDs were used as a platform for the growth of CeO_2NPs, to form a stable SNGQDs@CeO_2NPs conjugate, **Scheme 3.1(ii).**

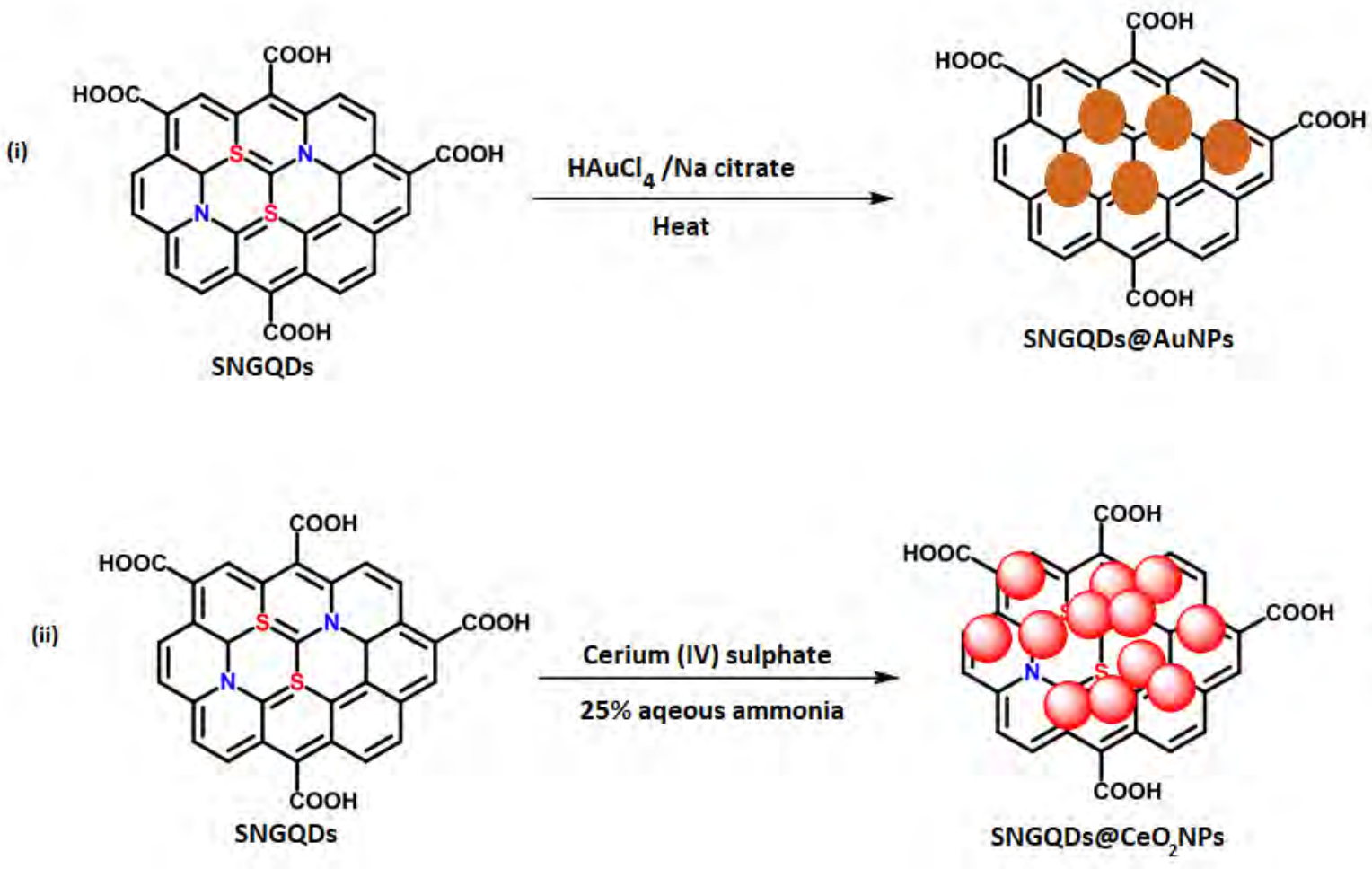

Scheme 3.1. Synthetic strategy towards the synthesis of (i) SNGQDs@AuNPs and SNGQDs@CeO_2NPs (ii) nanoconjugates.

3.1.1. UV-Vis Spectroscopy

The UV-Vis spectra of the three nanoparticles: SNGQDs, AuNPs and CeO_2NPs alone are shown in **Figure 3.1A.** The AuNPs had an absorption peak at 599 nm (**Table 3.1**), corresponding to the surface plasmon resonance (SPR) band of gold nanoparticles, [171] **Fig. 3.1(i)**. The SNGQDs, showed an n-π transition absorption peak at 358 nm, which is typical of graphene quantum dots [172], **Fig. 3.1 (ii)**. Absorbance peaks at 305 nm and 349 nm were observed for the prepared CeO_2NPs and CeO_2NPs_{COOH}, respectively, **Table 3.1**. The spectral shift might be an indication of possible structural change, and therefore successful carboxylation, **Fig. 3.1 (iii) & (iv)**. The absorption spectra of the SNGQDs@AuNPs, SNGQDs@CeO_2NPs and SNGQDs (for reference) are shown in **Figure 3.1B**. The SNGQDs@AuNPs spectrum showed a typical GQDs absorption peak at 350 nm [171], accompanied by a new peak at 539, at the SPR region for gold nanoparticles [172] further suggesting the successful synthesis of AuNPs on the SNGQDs surface to form the conjugate SNGQDs@AuNPs. The SNGQDs@CeO_2NPs composite, showed an absorption peak at 349 nm, which is around the region where both the SNGQDs and CeO_2NPs absorb, suggesting the presence of both materials within the sample, **Table 3.1**.

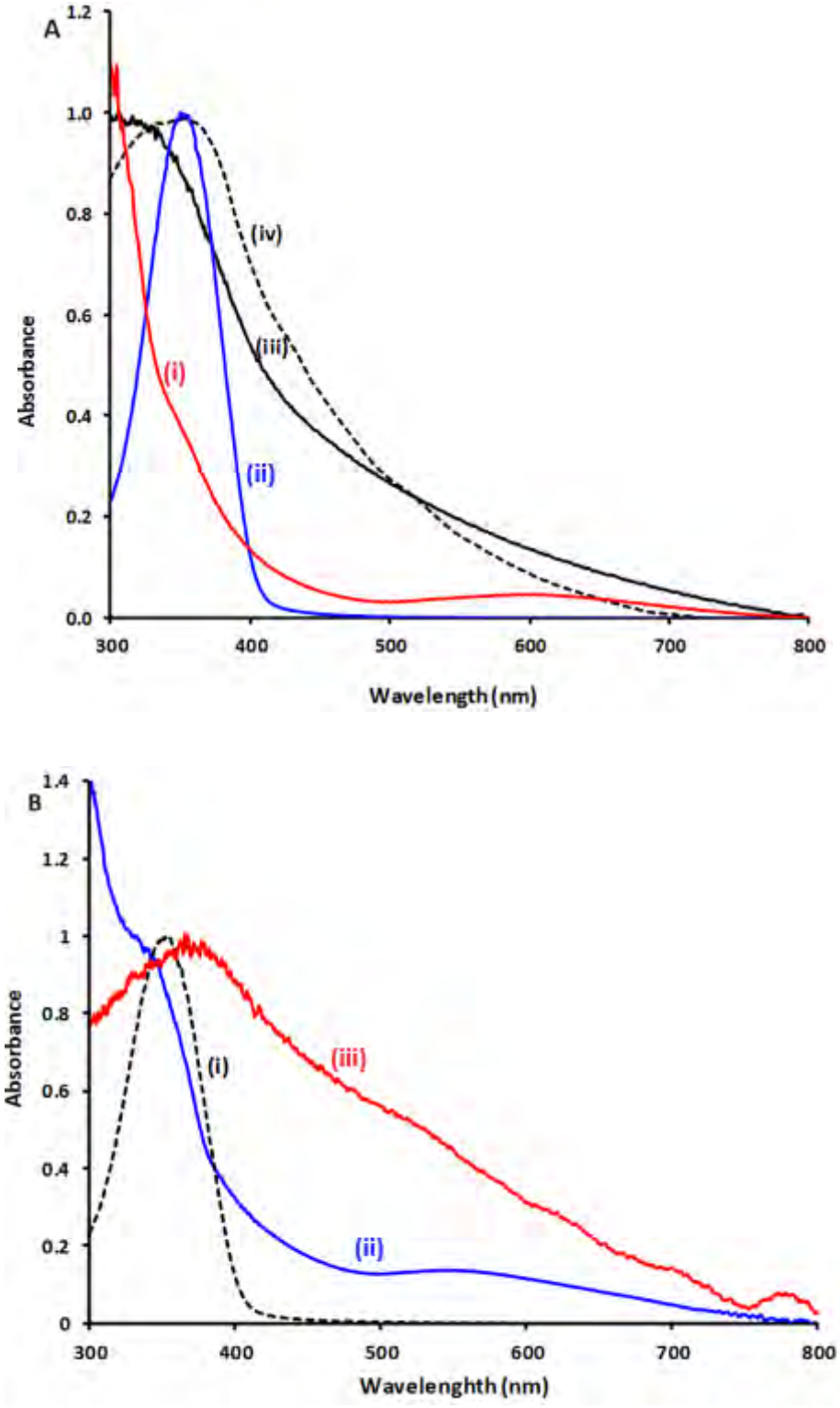

Figure 3.1. UV-Vis spectra of **A**: AuNPs (i), SNGQDs (ii), CeO_2NPs (iii) and CeO_2NPs_{COOH} (iv) and **B:** SNGQDs (i) and SNGQDs@AuNPs (ii) and SNGQDs@CeO_2NPs. The AuNPs were recorded in toluene, all others in water. All run at room temperature.

Table 3.1. Summary of absorbance in nm for all nanoparticles, CoPc's, CoP-BNF and relevant conjugates.

Nanomaterials	Solvent	Absorbance (nm)
AuNPs	Toluene	599
SNGQDs	Water	358
CeO_2NPs bare	Water	305
CeO_2NPs_{COOH}	Water	349
SNGQDs@AuNPs	Water	350, 539
SNGQDs@CeO_2NPs	Water	349
Complex **1**	DMSO	658, 321
Complex **2**	DMSO	671, 329
Complex **3**	DMSO	697, 330
3(π)SNGQDs	DMSO	697, 368
Complex **4**	DMSO	677, 331
4(π)SNGQDs	DMSO	677, 332
Complex **5**	DMSO	664, 327
5(π)SNGQDs	DMSO	664, 329
Complex **6**	DMSO	675, 311
CoP-BNF	Water	580, 544, 419

3.1.2. X-ray Diffractometry (XRD)

XRD was used to study the crystalline phase and components of the various nanoparticle samples, **Fig. 3.2A**. For the SNGQDs sample, a typical XRD pattern for carbon-based nanomaterials was observed, with the 002 peak at around 2θ ~ 21◦,[**173**] **Fig. 3.2(i)**. Five diffraction peaks were observed for AuNPs which indexed to the (111), (200), (220), (311) and (222) reflections of face cantered cubic structure of metallic gold [**174**]**, Fig. 3.2(ii)**. The diffractogram of the bare CeO_2NPs showed peaks with indices (111), (200), (220), (311), (222) and (420), **Fig. 3.2(iii)**. The diffractogram of the CeO_2NPs_{COOH} showed similar peaks, which were more defined with increased in intensity, **Fig. 3.2(iv)**. Moreover, two additional peaks were observed with indices (400) and (331). More importantly, the characteristic peaks did not change; other than the intensity and a minor variation in width after the surface modification process, implying a preserved structural integrity. The effect of combining SNGQDs with AuNPs or with CeO_2NPs_{COOH} was investigated and is demonstrated in XRD data for the respective SNGQDs@AuNPs and SNGQDs@CeO_2NPs_{COOH} conjugates, **Figure 3.2B**. The conjugate SNGQDs@AuNPs had the amorphous carbon peak at ~ 2θ = 18° symbolic of its graphitic nature, accompanied by crystalline peaks: {(111), (200), (220), (311) and (222)} attributed to the presence of gold nanoparticles in the sample, **Fig. 3.2B(i)**. Similarly, the XRD pattern for the SNGQDs@CeO_2NPs conjugate, showed an amorphous broad peak at 2θ = 22 °. Additional peaks were observed and identified and corresponded to those obtained for the CeO_2NP_{COOH}, **Fig. 3.2A (ii)**. The obtained results further confirm the successful synthesis of both conjugates, and that in each conjugate, the resulting structure is a combination of the individual materials combined.

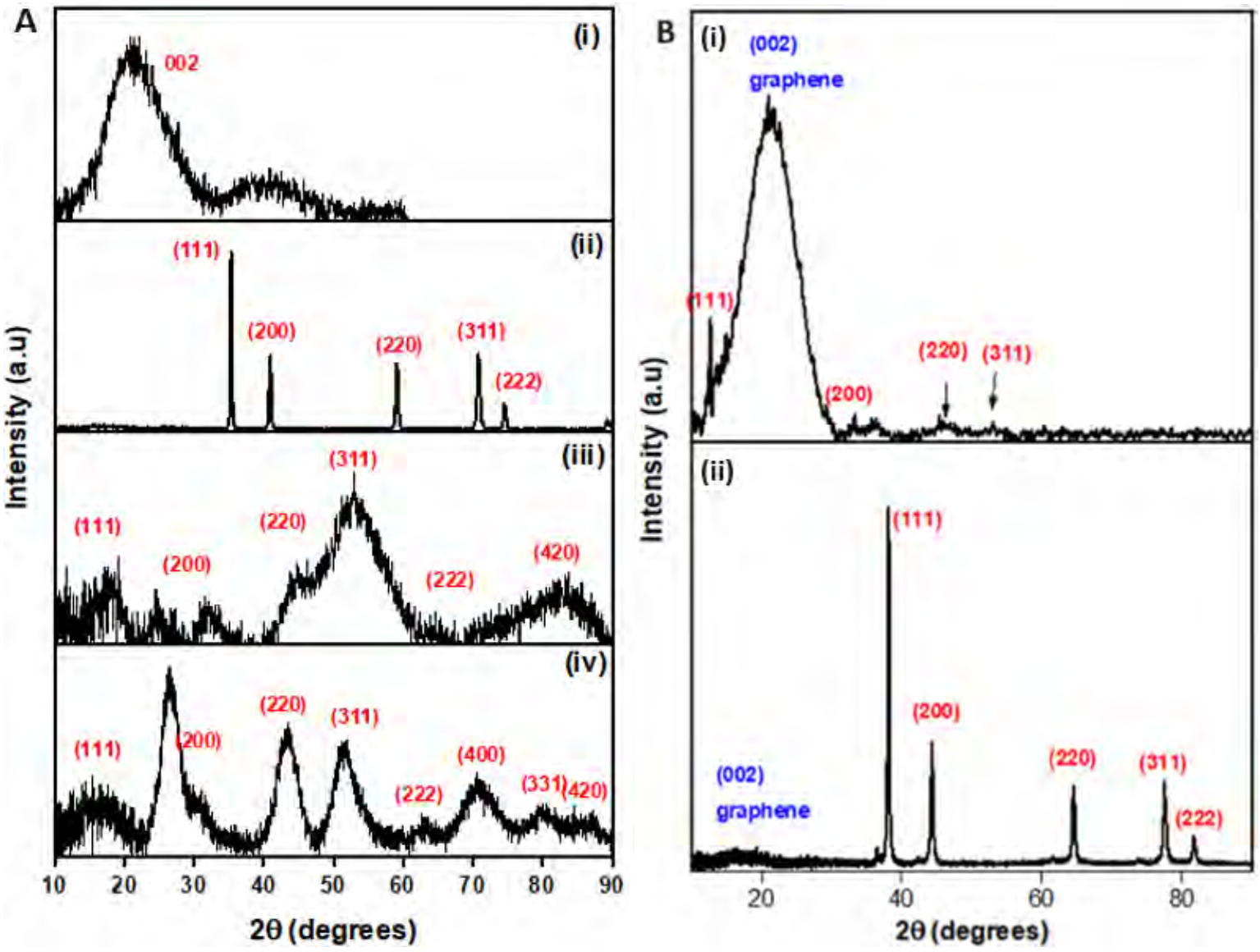

Figure 3.2. XRD data **A**: (i) SNGQDs (ii) AuNPs, (iii) bare CeO_2NPs and (iv) CeO_2NPs_{COOH} and **B:** (i) SNGQDs@CeO_2NPs and (ii) SNGQDs@AuNPs.

3.1.3. Raman Spectroscopy

The various nanomaterial samples were also analysed using Raman Spectroscopy, **Figure 3.3A**. Graphene quantum dots are known to exhibit two characteristic Raman peaks termed the D (disorder/breathing mode, sp^3) band and G (sp^2, tangential mode) band [175]. The synthesized SNGQDs had D-band and G-band occurring at 1297 cm^{-1} and 1573 cm^{-1} respectively, **Fig. 3.3A** (as labelled). The Raman data obtained for the CeO_2NPs_{COOH} alone is shown in **Fig. 3.3A** (as labelled): a first order Raman peak (F_{2g}) at 449 cm^{-1} and five second order Raman peaks prominent at 595 $cm^{-1,}$ 823 $cm^{-1,}$ 895 $cm^{-1,}$ 989 cm^{-1} and 1051 cm^{-1} were observed [176, 177]. The feature at 595 cm^{-1} originates from O^{2-} replacement of cerium (IV) atoms by cerium (III) atoms or impurity atoms in the bulk [177, 178]. The features at 823 cm^{-1} and 895 cm^{-1} are attributed O–O stretching vibration of peroxides. The bands at 989 cm^{-1} and 1051 cm^{-1} are as a result of second order scattering, with the former emanating from the combination of the $A1_g$, E_g, and F_{2g} modes [179]. A typical Raman spectroscopy for AuNPs was obtained and is shown in **Fig. 3.3A** (as labelled), with peaks at 382 cm^{-1}, 521 cm^{-1}, 627 cm^{-1}, 792 cm^{-1}, 1008 cm^{-1}, 1207 cm^{-1}, 1215 cm^{-1}, 1383 cm^{-1} and 1608 cm^{-1}. The peaks observed are in good agreement with what has been reported in previous literature reports for gold nanoparticles [180, 181]. The Raman spectroscopy data obtained for the conjugates SNGQDs@AuNPs and SNGQDs@CeO_2NPs conjugates is shown in **Figure 3.3B**. The surface functionalization of GQDs introduces defects onto the graphene framework. The defects are quantified by the ratio of the intensities of the D and G bands (I_D/I_G). The I_D/I_G ratio for SNGQDs and SNGQDs@AuNPs was found to be 1.38 and 0.85 respectively. The varied ratio might be due to the synthetic method for SNGQDs@AuNPs, which involved heating leading to the alteration of the GQD framework during decoration with AuNPs. Furthermore, the Raman

spectrum of SNGQDs@AuNPs showed broadened D-band and some additional unidentifiable peaks. Appearance of many peaks in the Raman spectra of GQDs has been observed and was attributed to nanosized GQDs with large edge defects [**182**]. The Raman data obtained for the SNGQDs@CeO_2NPs exhibited characteristic Raman modes of both the SNGQDs and CeO_2NPs, **Fig.3.3B** (as labelled). The first three peaks are of CeO_2NPs character, whilst the last two are of the SNGQDs character within the SNGQDs@CeO_2NPs composite. These results further confirm the successful synthesis of CeO_2NPs on the SNGQDs surface, to form SNGQDs@CeO_2NPs.

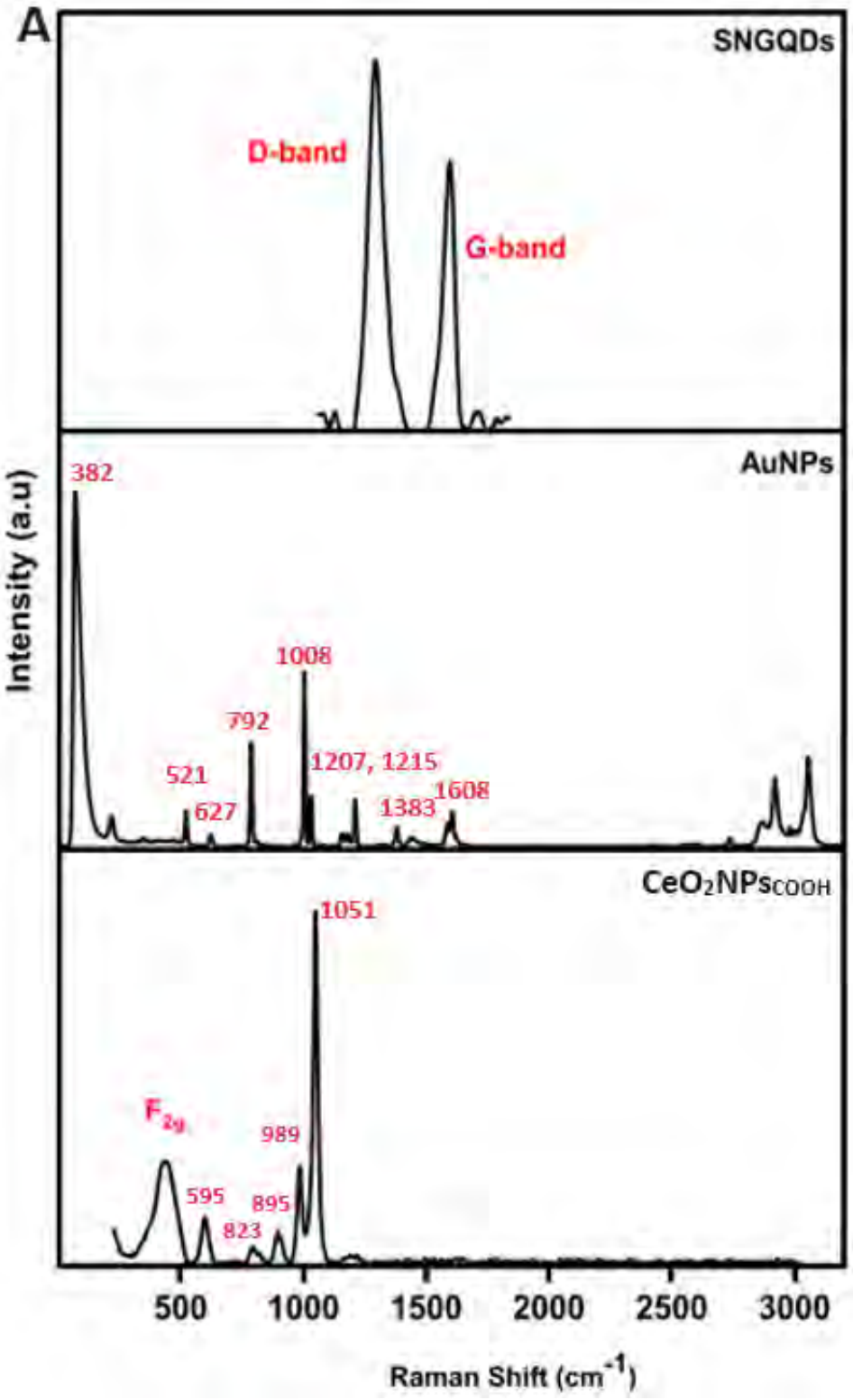
A
SNGQDs
D-band
G-band
AuNPs
382
1008
792
1207, 1215
521
627
1383
1608
CeO2NPsCOOH
1051
F2g
989
595
895
823
Intensity (a.u)
500
1000
1500
2000
2500
3000
Raman Shift (cm-1)

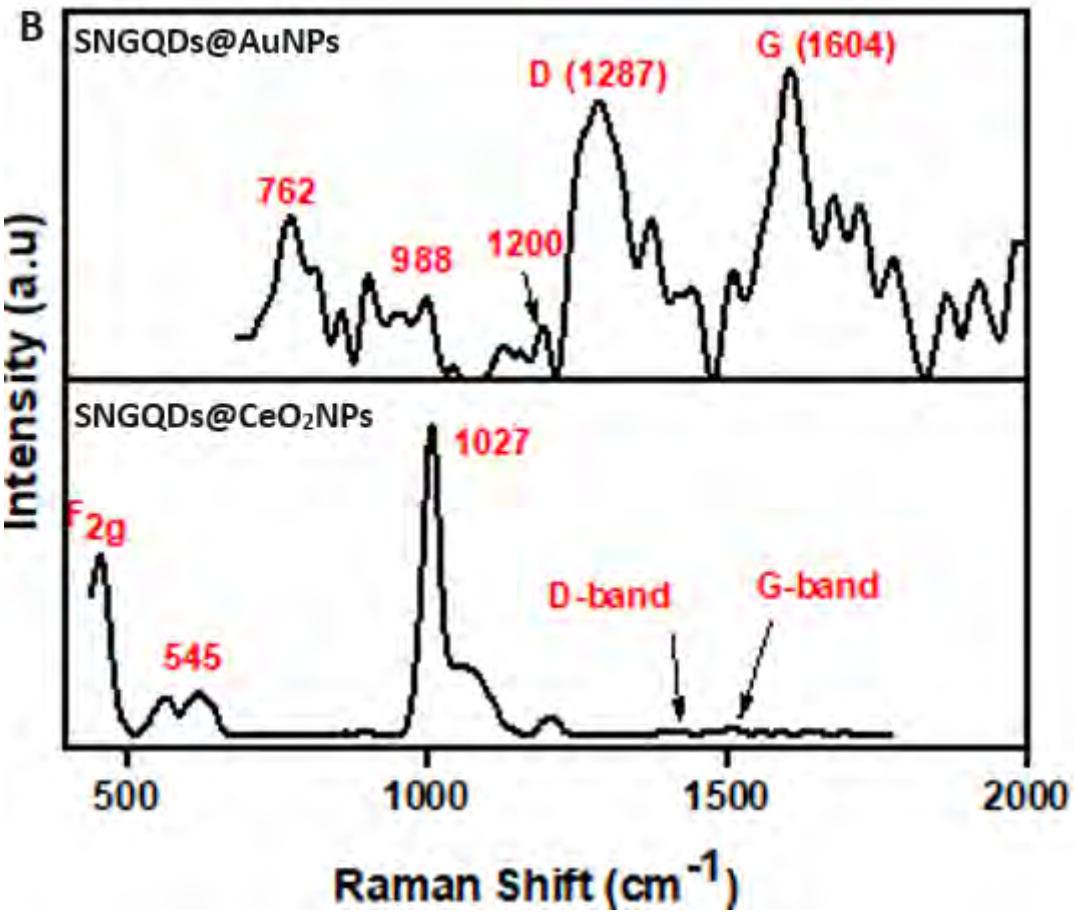

Figure 3.3. Raman Spectra **A**: SNGQDs, AuNPs, CeO_2NPs_{COOH}, **B**: SNGQDs@AuNPs and SNGQDs@CeO_2NPs, all labelled accordingly.

3.1.4. Transmission Electron Microscopy (TEM)

The shape, size and spatial distribution of the different NPs is shown in **Figure 3.4**. Both the SNGQDs and AuNPs showed, spatially dispersed nanoparticles with a spherical shape, **Fig. 3.4(i) & (ii)**. The successful conjugation of SNGQDs with AuNPs to form the composite SNGQDs@AuNPs (not shown) was demonstrated by an observed particle size increase: moving from SNGQDs (2.8 nm) and SNGQDs@AuNPs (5.4 nm), suggestive of successful modification of SNGQDs surface. The unmodified CeO_2NPs **(iii)**, showed more aggregation compared to the surface functionalized CeO_2NPsC_{OOH} **(iv)**. Furthermore, the bare CeO_2NPs had a spherical shape while the CeO_2NPs_{COOH} had a rod like shape, **Fig. 3.4**. It has been reported that the shape of cerium oxide nanocrystals can be changed by controlling the reaction time [**183**] with the change in morphology between nanorod and nanospheres occurring within a short time.

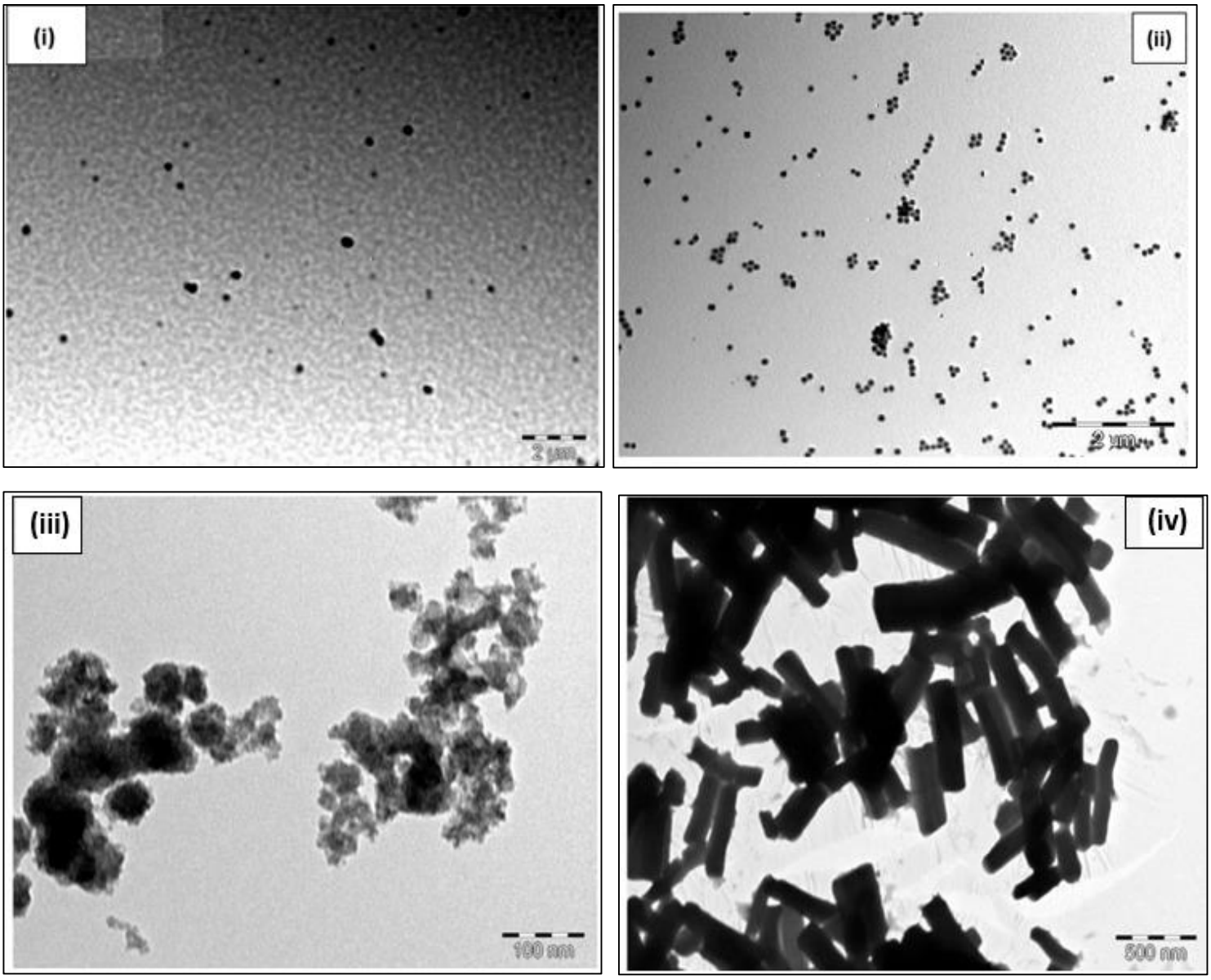

Figure 3.4. TEM images for (i) SNGQDS, (ii) AuNPs, (iii) CeO_2NPs and CeO_2NPs_{COOH} (iv).

3.1.5. FT-IR Spectroscopy

The structural composition of the resulting SNGQDs@AuNPs was investigated using FT-IR spectroscopy, **Figure 3.5**. Graphene quantum dots are known to contain polar groups on their edges including -OH, -COOH, epoxy. This was the case for the SNGQDs and SNGQDs@AuNPs nanoparticles: a broad peak in the 3200–3500 cm^{-1} region was observed for both SNGQDs and SNGQDs@AuNPs. The synthesized SNGQDs and SNGQDs@AuNPs both had bands in the 1400 cm^{-1} - 1800 cm^{-1} region which were associated with vibrational stretch of the carbonyl (C=O) in COOH and O=C-NH (from cysteine as a starting material during synthesis of SNGQDs). Two additional peaks at 1260 cm^{-1} and 1384 cm^{-1} which are due to CS and CN bonds in the SNGQDs were observed, **Fig. 3.5(i)**. The peaks shift to 1249 cm^{-1} and 1395 cm^{-1} and decrease drastically in intensity for SNGQDs@AuNPs, **Figure 3.5(ii)**. The -OH stretch of the SNGQDs@AuNPs is intensified compared to that of the SNGQDs alone. A significant shift in the functional groups related bands mentioned, on the SNGQDs@AuNPs compared to the SNGQDs might be suggestive of structural changes and successful decoration on the SNGQDs. Similarly, for SNGQDs@CeO_2NPs; a peak at 3368 cm^{-1} was attributed to the –OH groups present at the SNGQDs edges within the composite, slightly shifted compared to SNGQDs alone at 3400 cm^{-1}. The peaks at 1749 cm^{-1} and 1624 cm^{-1} for SNGQDs@CeO_2NPs can be attributed to the C=O/C=C carbons from the carboxylic edges as well as the sp^2 hybridized graphene carbon framework, respectively. The shift to higher wavenumbers might suggest the weakening of aromatic ring stacking due to the cerium nanoparticles being intercalated into the SNGQDs sheets [184]. The peaks at 1419 cm^{-1}, 1065 cm^{-1} and 997 cm^{-1} were attributed to –OH bending, C-O stretch and C–H bending all from the SNGQDs in SNGQDs@CeO_2NPs composite, **Figure 3.5 (iii)**. The successful synthesis of the CeO_2NPs on the SNGQDs surface, can be confirmed by the 488 cm^{-1} and 546 cm^{-1} peaks which can be

attributed to the O-Ce-O stretching mode of vibration. The IR data suggests the successful synthesis of the CeO_2NPs on the SNGQDs surface, while preserving the structural integrity of the SNGQDs framework.

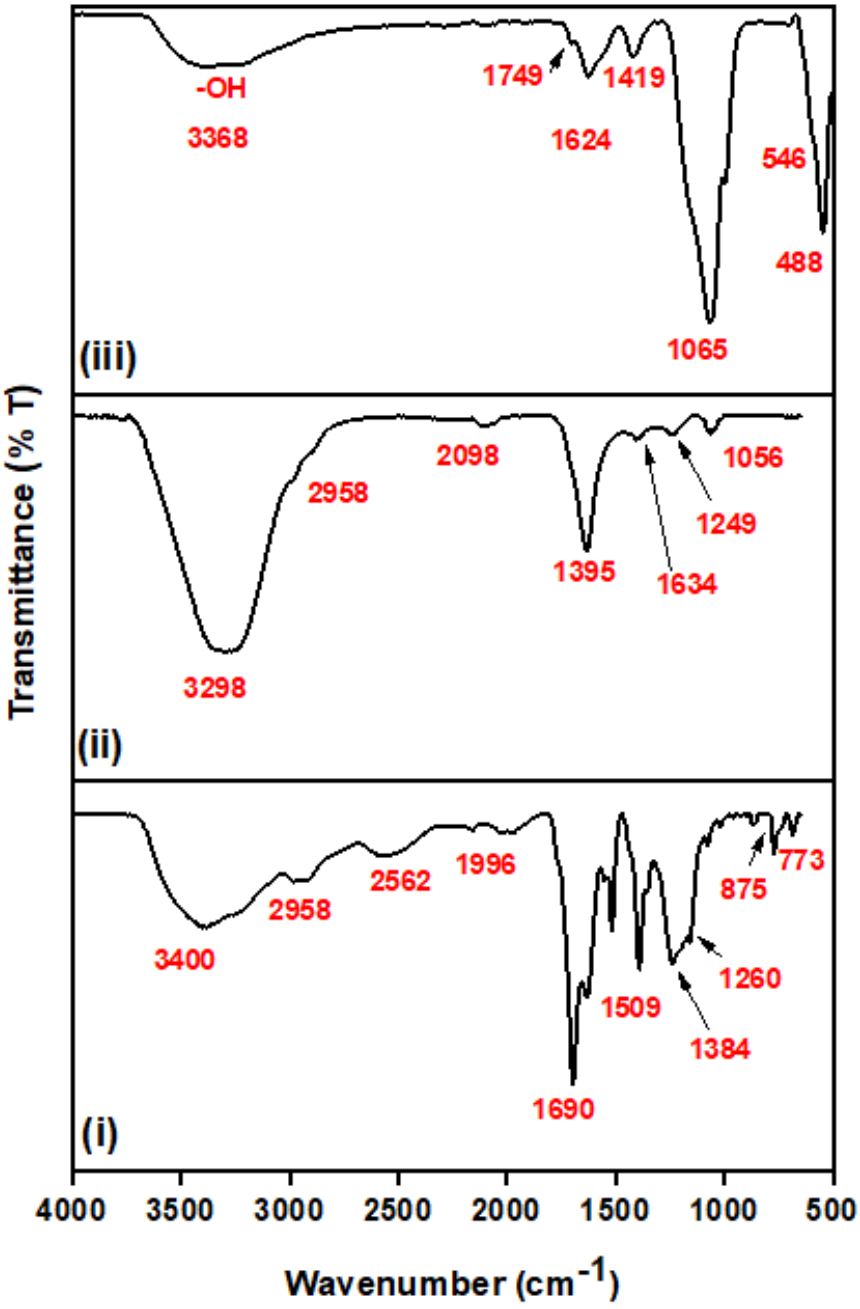

Figure 3.5. FT-IR spectra of SNGQDs (i), SNGQDs@AuNPs (ii) and SNGQDs@CeO_2NPs (iii). All run in powder form, at room temperature

3.2. Synthesis and Characterization of MPcs and relevant conjugates

3.2.1. Synthesis

The MPc complexes **1** and **4** are known, while complexes **2**, **3**, **5** and **6** are new hence discussed here.

3.2.1.1. Symmetrically substituted complexes 2 and 3 (Scheme 3.2)

The phthalocyanine ring systems for both complexes **2** and **3** are known for Zn as a central metal [**160**,**161**], and Co is employed as a central metal for the first time in these ring systems. The two complexes are structurally differentiated by the oxygen atom on the hydrocarbon chain part and additional aliphatic bonds. Complexes **2** and **3** were synthesized following the method shown in **Scheme 3.2**. and are soluble in DMSO. Mass spectrometry and elemental data were obtained for the products and the results were as expected for both complexes **2** and **3**. NMR spectra were not recorded due to the paramagnetic nature of the central metal (Co). The elemental analysis data for complex **2** has hydrates as can happen to many Pcs [**185**]

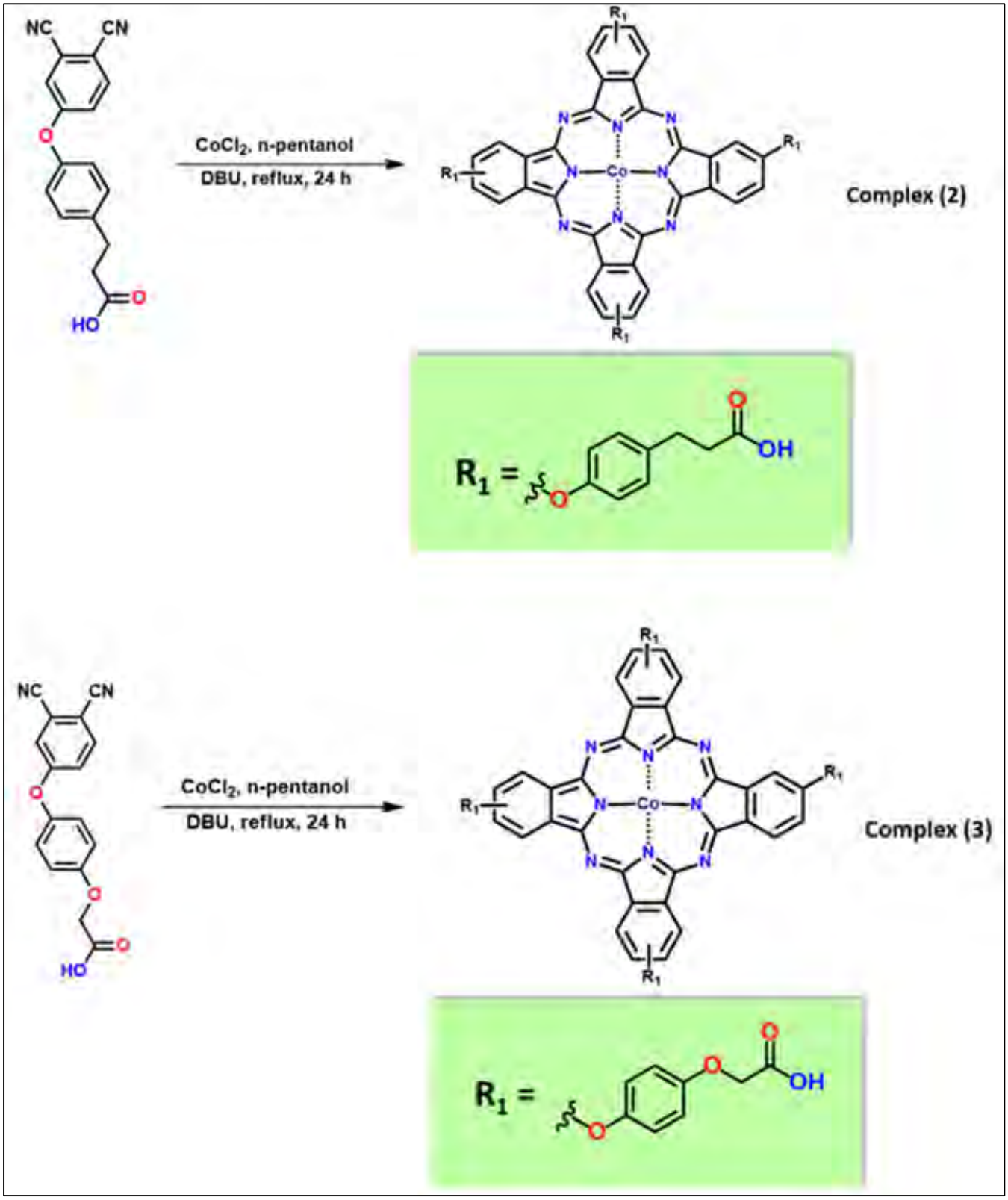

Scheme 3.2. Schematic representation of the synthetic method towards the synthesis of complex **2** and **3**

3.2.1.2. Asymmetrically substituted complexes 5 and 6 (Scheme 3.3)

Complex **5** and **6** were synthesized following the method shown in **Scheme 3.3** and are both soluble in DMSO. Mass spectrometry and elemental data were obtained for the products and the results were as expected for both complexes **5** and **6**. The elemental analysis data for complex **6** has hydrates as can happen to many Pcs [**185**]

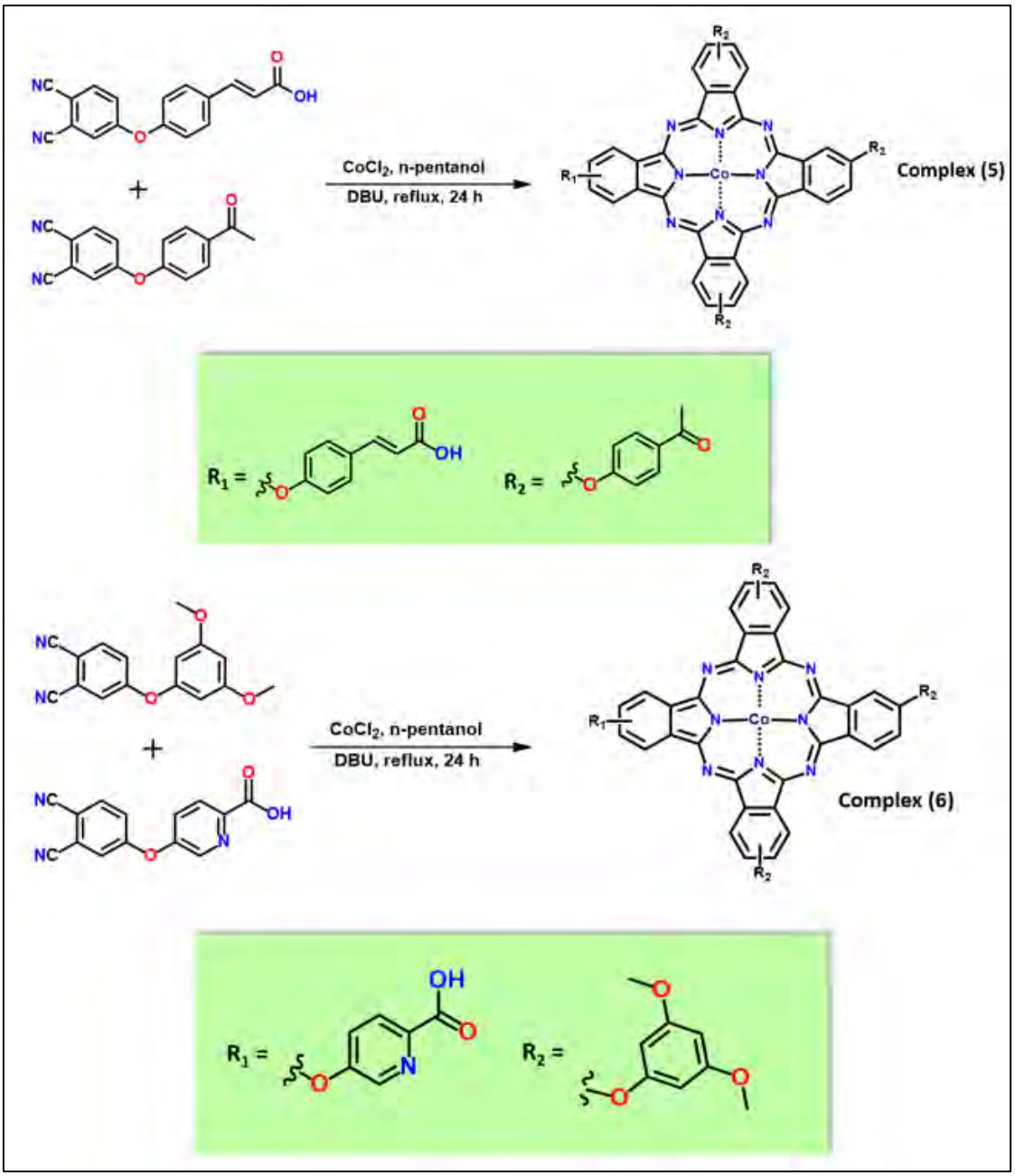

Scheme 3.3. Steps towards the synthesis of the complex **5** and **6**.

3.2.1.3. Synthesis of Pc/SNGQDs π-π conjugates, Scheme 3.4

Non-covalent π–π stacking interactions, are non-destructive and occur between two or more molecules that contain π-electrons. This type of conjugation is especially preferred, because it does not alter the structural or functional properties of the individual materials involved. The said 18 π-electron containing Pc complexes **3 -5** were therefore combined with the sp^2 hybridized SNGQDs, to form stable nanocomposites with improved physicochemical properties. **Scheme 3.4** depicts the conditions towards the formation of the conjugates**,** showing **3**(π)SNGQDs as an example. The **3**(π)SNGQDs conjugate was soluble in DMSO, while **4**(π)SNGQDs and **5**(π)SNGQDs were soluble in DMF.

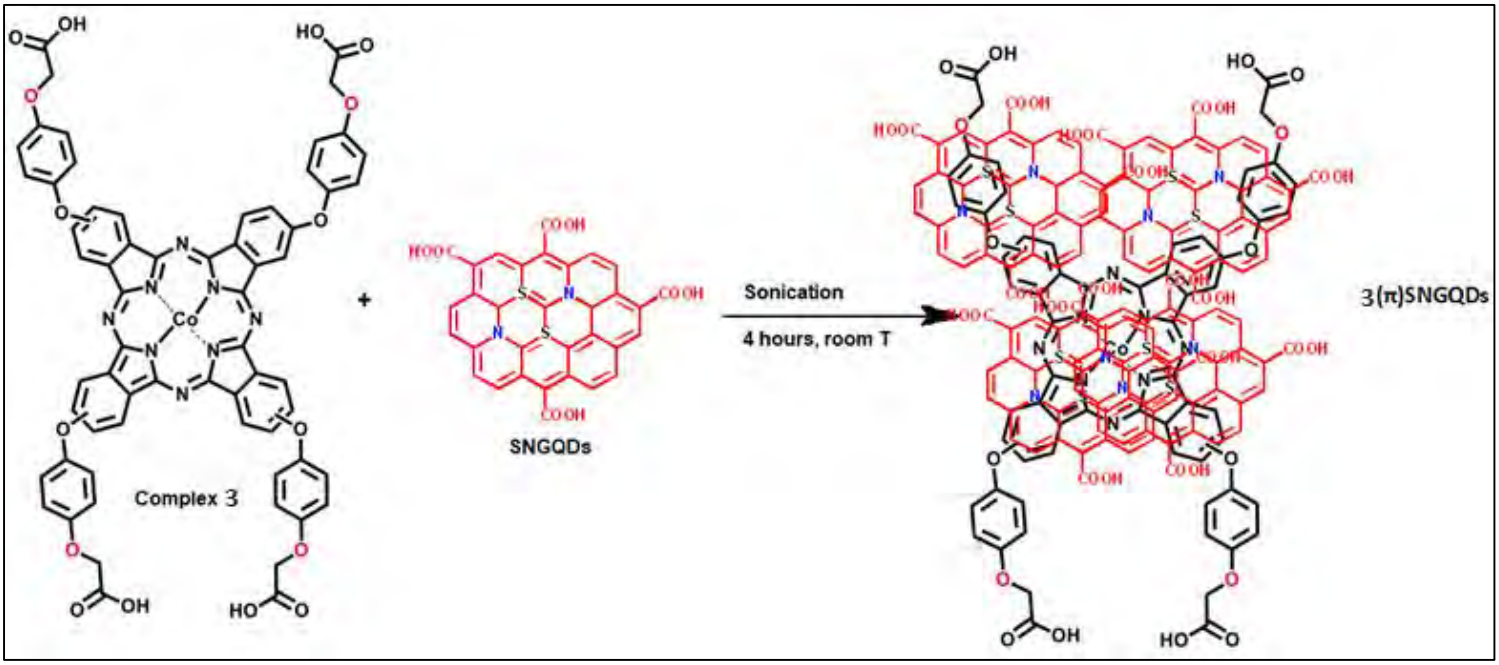

Scheme 3.4. Steps towards the formation of the conjugates, **3**(π)SNGQDs, **4**(π)SNGQDs and **5**(π)SNGQDs, showing **3**(π)SNGQDs as an example.

3.2.2. Characterization

3.2.2.1. UV-Vis Spectroscopy

The UV-Vis spectroscopy of selected Pc complexes is shown in **Figure 3.6**. Complex **1** had a Q-band at 658 and a Soret band at 321 nm, **Table 3.1**. Complexes **2** and **3** showed a characteristic Q band at 671 nm and 697 nm, respectively in DMSO. The spectra showed a monomeric behaviour evidenced by a single and narrow Q band, typical of metallated phthalocyanine complexes [**186**]. The Q band of complex **3** was red shifted compared to that of complex **2** and **1**. The Soret band is observed at 329 nm for complex **2**, while is observed at 330 nm for complex **3**, **Fig 3.6A**. The electronic absorption spectra of phthalocyanines are highly dependent on solvent, with broad peaks being observed in some cases [**187**]. Complexes **4** and **5** showed Q- bands at 677 nm and 664 nm, and Soret bands at 331 nm and 327 nm, respectively, **Table 3.1**. The Q bands are broad, typical of CoPc derivatives [**188**]. The Q band of complex **4** was red shifted due to the presence of four acetyl phenoxy groups which are electron donating, instead of only three of these groups in present in complex **5.** Complex **6**, showed a Q-band and Soret band at wavelengths 675 nm and 311 nm, respectively. The Q band is broad suggesting aggregation in DMSO, **Fig 3.6B**.

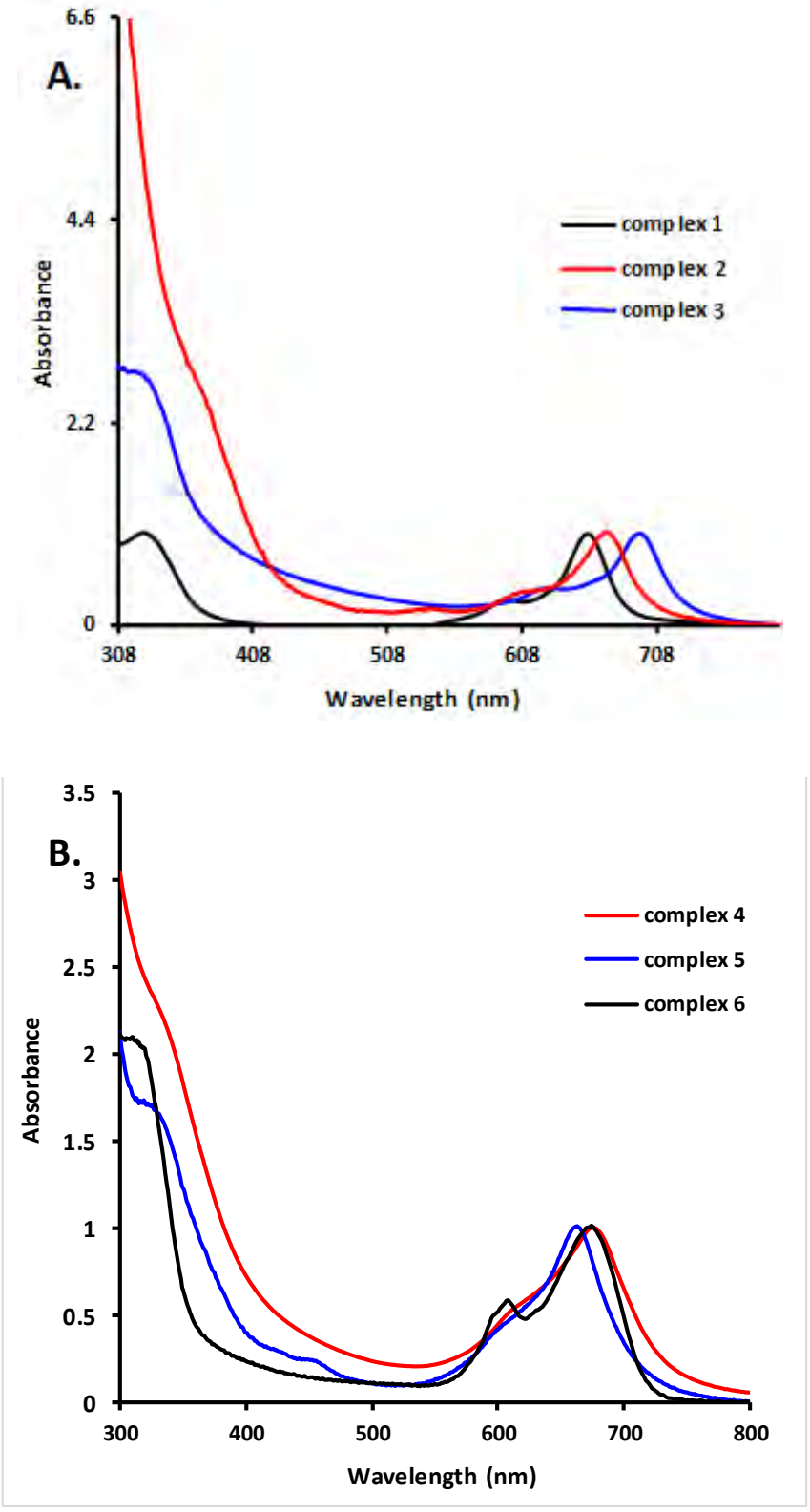

Figure 3.6. UV-Vis spectroscopy of the Pc complexes (**A**) complex **1-3** and (**B**) complexes **4-6**.

Solvent = DMSO

Figure 3.7 shows the UV-Vis spectra of the conjugates **3**(π)SNGQDs (**3.7A**), **4**(π)SNGQDs and **5**(π)SNGQDs (**3.7B**) together with the corresponding Pc complex, **Table 3.1**. The same absorption spectra were obtained for the conjugates as the respective complexes. The Q-bands remained the same; there were no significant spectral shifts except for broadening. This confirms that π-π stacking conjugation did not compromise the structural integrity of the Pcs. In all cases the Soret band intensified and broadened with absorption maxima at 368 nm, 332 nm and 329 nm for conjugates **3**(π)SNGQDs, **4**(π)SNGQDs and **5**(π)SNGQDs, respectively. The changes in the Soret-band can be attributed to the presence of the SNGQDs in each conjugate sample.

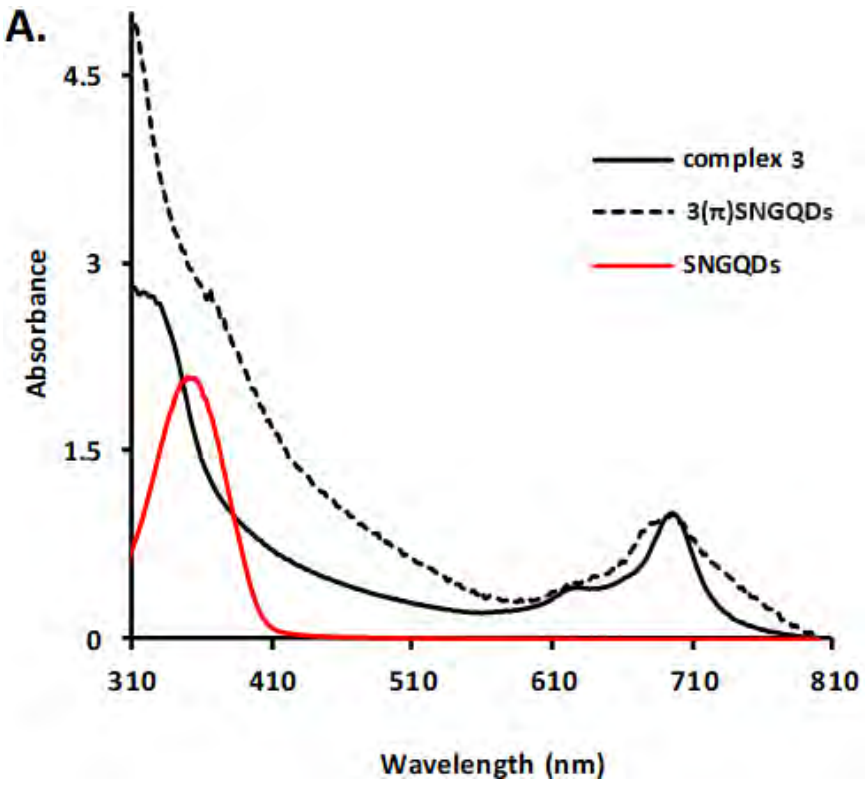

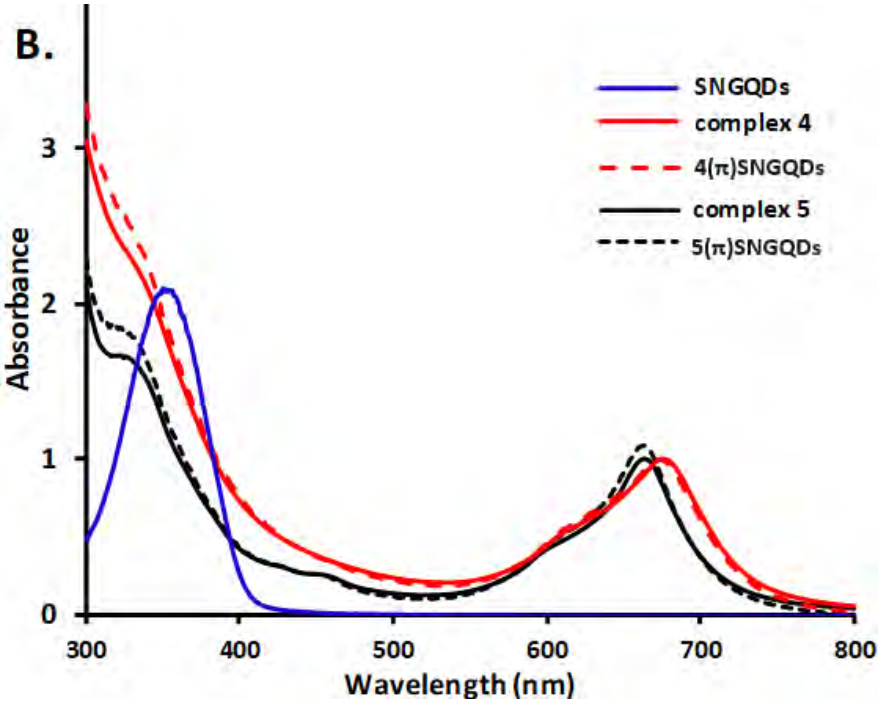

Figure 3.7. UV-Vis spectra of the conjugates **3**(π)SNGQDs (in DMSO), **4**(π)SNGQDs and **5**(π)SNGQDs (in DMF).

3.2.2.2. Raman Spectroscopy

The structural integrity of the SNGQDs before and after conjugation to complexes **3**, **4** and **5** was assessed, focusing on the two GQDs Raman modes, the D-band and the G-band, **Figure 3.8.** As stated above, the G-band is the primary mode in graphene and represents the planar configuration sp^2 bonded carbon, while the D-band is the defect or disorder band originating in structural defects, edge effects and dangling sp^2 carbon bonds that break the symmetry [189, 190]. The D and G bands for the SNGQDs was positioned at 1297 cm^{-1} and 1573 cm^{-1} respectively. For the conjugates the D and G bands were obtained at (1299 cm^{-1}; 1600 cm^{-1}), (1308 cm^{-1}; 1507 cm^{-1}) and (1262 cm^{-1}; 1432 cm^{-1}) for **3**(π)SNGQDs, **4**(π)SNGQDs and **5**(π)SNGQDs, respectively. Raman peaks for graphene quantum dots occurring at ~1260 cm^{-1} and 1430 cm^{-1} have been reported and associated with edge functional groups, COOH or C=O groups [191]. Thus, the presence of the extra COOH groups in **5**(π)SNGQDs arising from

complex **5** compared to the acetophenone groups in complex **4** might have resulted in the obtained spectral shifts. The I_D/I_G ratio was calculated for SNGQDs, **3**(π)SNGQDs, **4**(π)SNGQDs and **5**(π)SNGQDs to be 1.39, 1.44, 0.23 and 0.56, respectively. The higher I_D/I_G ratio of the **3**(π)SNGQDs implies that the sample had more out of plane vibrations attributed to the presence of structural defects, compared to **4**(π)SNGQDs and **5**(π)SNGQDs. It is evident from the data, that the conjugates had the graphitic nature which implies that the π-π stacking preserved the structural integrity involved nanostructures.

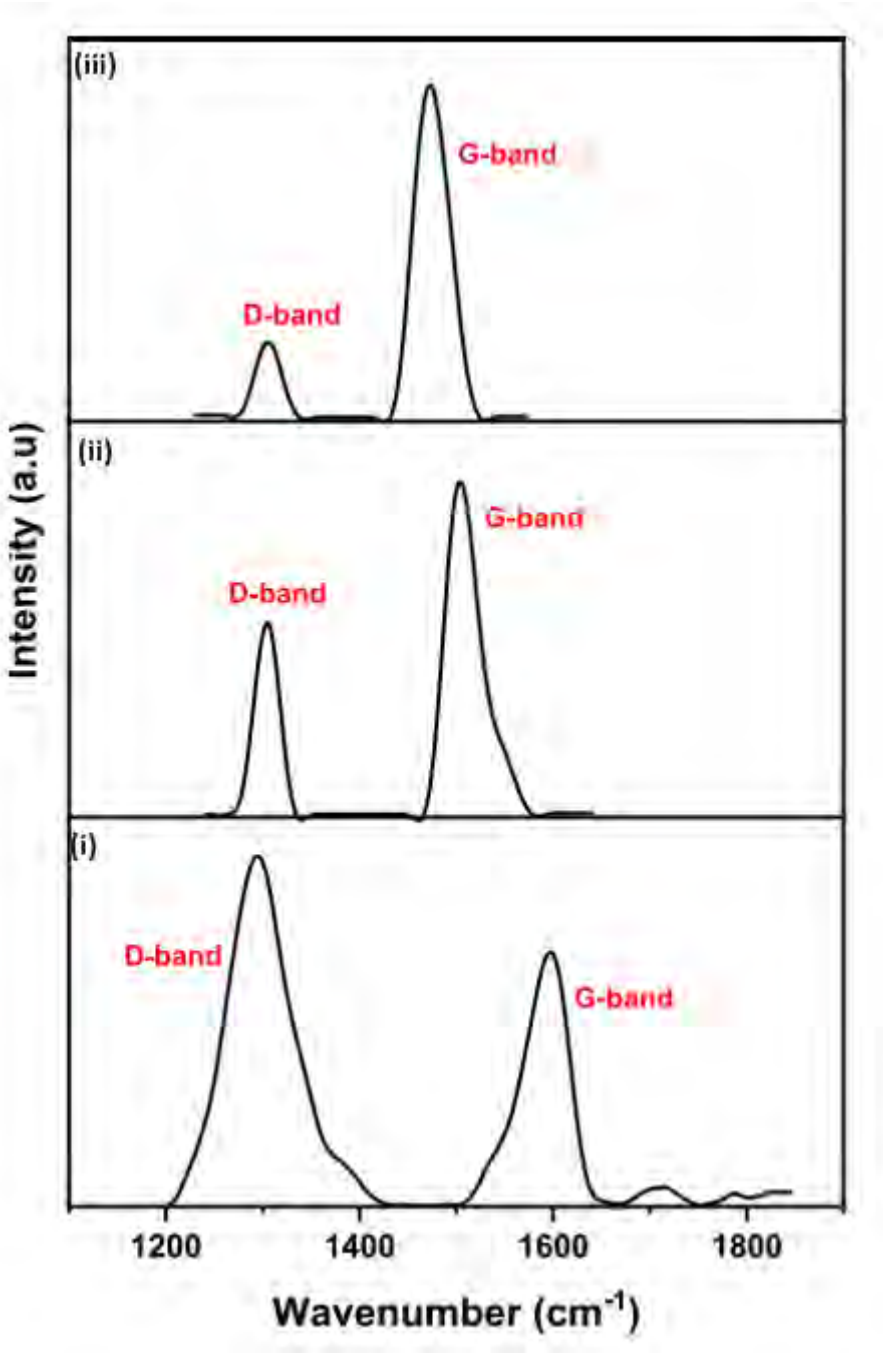

Figure 3.8. Raman spectra of: **3**(π)SNGQDs (i), **4**(π)SNGQDs (ii) and **5**(π)SNGQDs (iii). All samples run in water, at room temperature.

3.3. Synthesis and Characterization of the CoP-BNF, (Scheme 3.5).

3.3.1. Synthesis

The CoP-BNF was prepared by the hydrothermal technique, which involves the metal free tetracarboxy phenoxy porphyrin, dilute KOH for deprotonation of the H_2P carboxylic groups in the presence of Co(acetate)$_3$. The resulting CoP-BNF, is shown in **Scheme 3.5**, with the cobalt ion connecting to two different carboxylate groups (with 6 O atoms including two from the acetate ligand) of two porphyrins. Mass spectra confirmed the formation of a binuclear structure with expected mass of 1811.34 a.u. and found 1814.32 a.u.

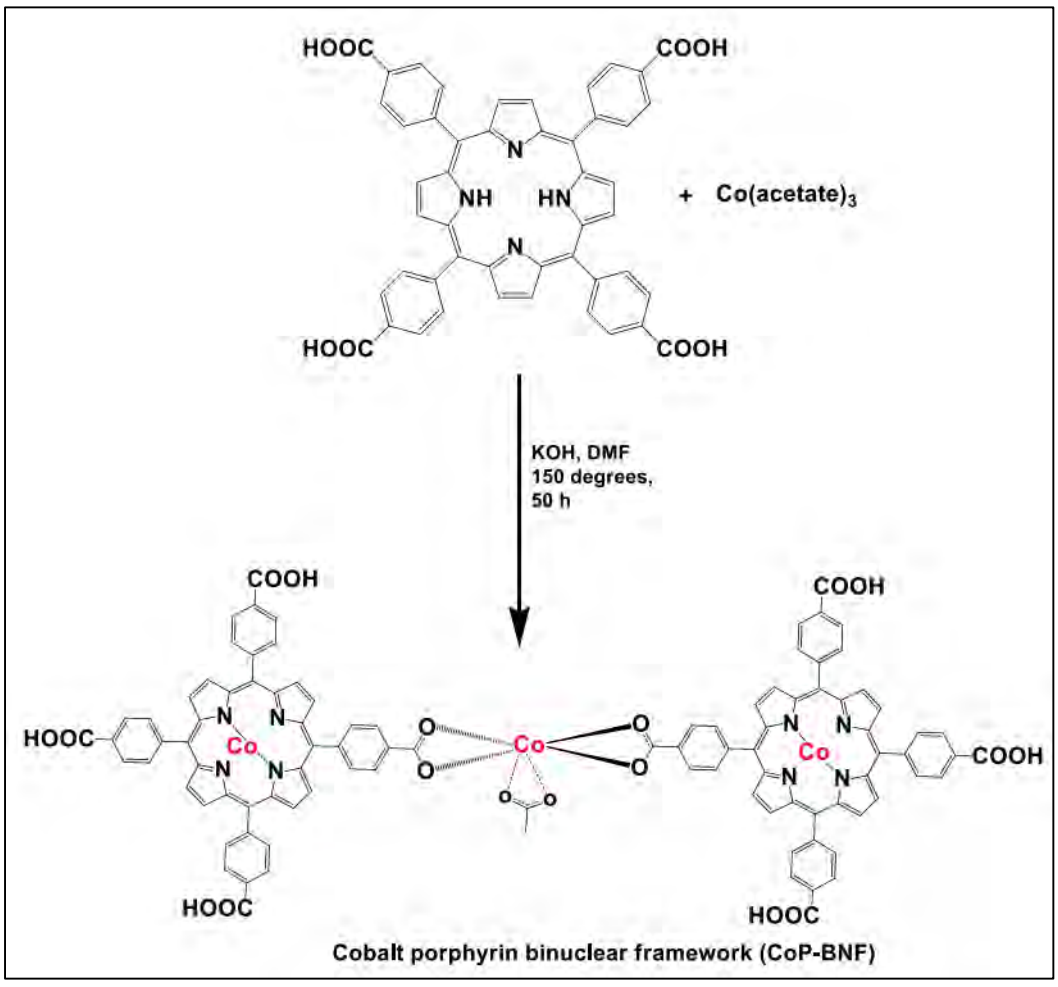

Scheme 3.5. Synthetic route towards the synthesis of the cobalt porphyrin based organic framework (CoP-BNF).

3.3.2. Characterization of CoP-BNF

3.3.2.1. UV-Vis Spectroscopy

The UV–Vis spectroscopic spectra of cobalt tetracarboxyphenyl porphyrin (CoP) and cobalt porphyrin binuclear framework (CoP-BNF) are shown in **Figure 3.9**. The CoP-BNF showed a single Soret band at 419 nm with two Q bands at 544 nm and 580 nm (the latter weak) typical of metalated porphyrin molecules, **Table 3.1**.

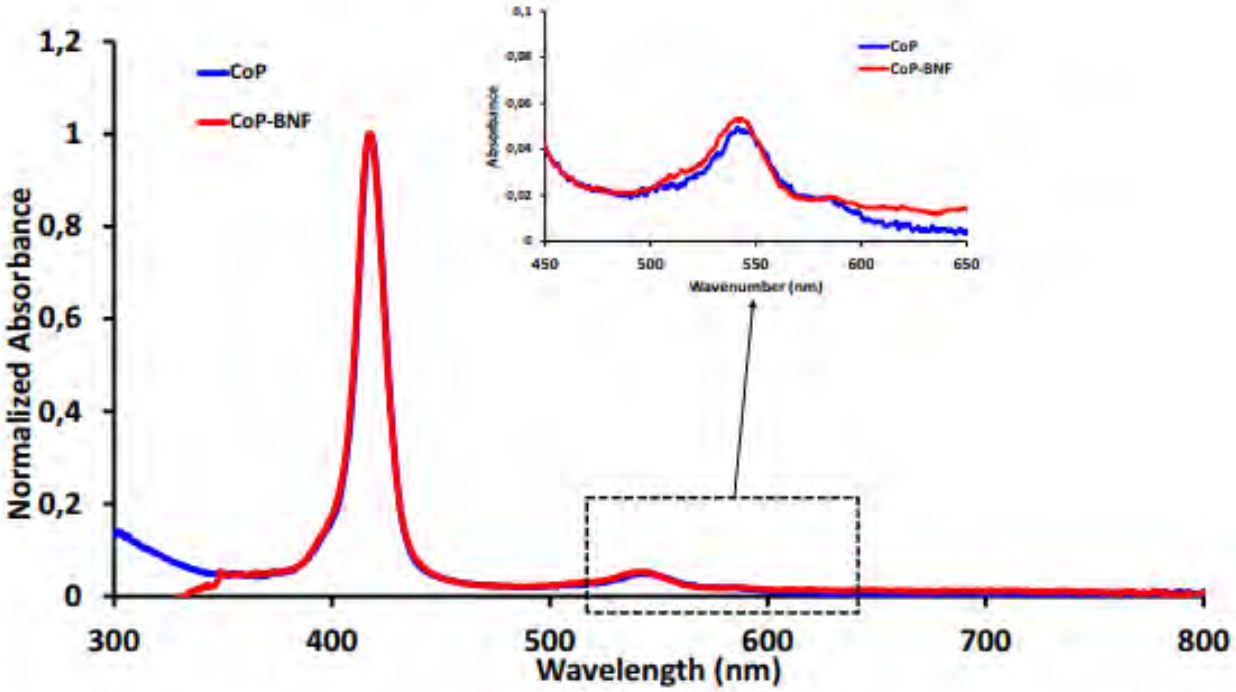

Figure 3.9. UV–Vis spectra of CoP-BNF and the equivalent tetracarboxyphenyl porphyrin (CoP). All in water at room temperature.

3.3.2.2. XRD

The structure of the synthesized CoP-BNF was further explored using XRD, the results are shown in **Figure 3.10**. The CoP-BNF alone showed an XRD pattern similar to that of cobalt tetraphenyl porphyrin (CoP) with a broad peak at 2θ = 21°, confirming the amorphous in nature of the porphyrins. Additional weaker peaks were observed at 2θ = 42° (for CoP) and 2θ = 60° for CoP-BNF [192], for the latter. The XRD patterns of CoP and CoP-BNF are basically similar showing that the π-conjugated structure is retained after the formation of CoP-BNF as observed before [192].

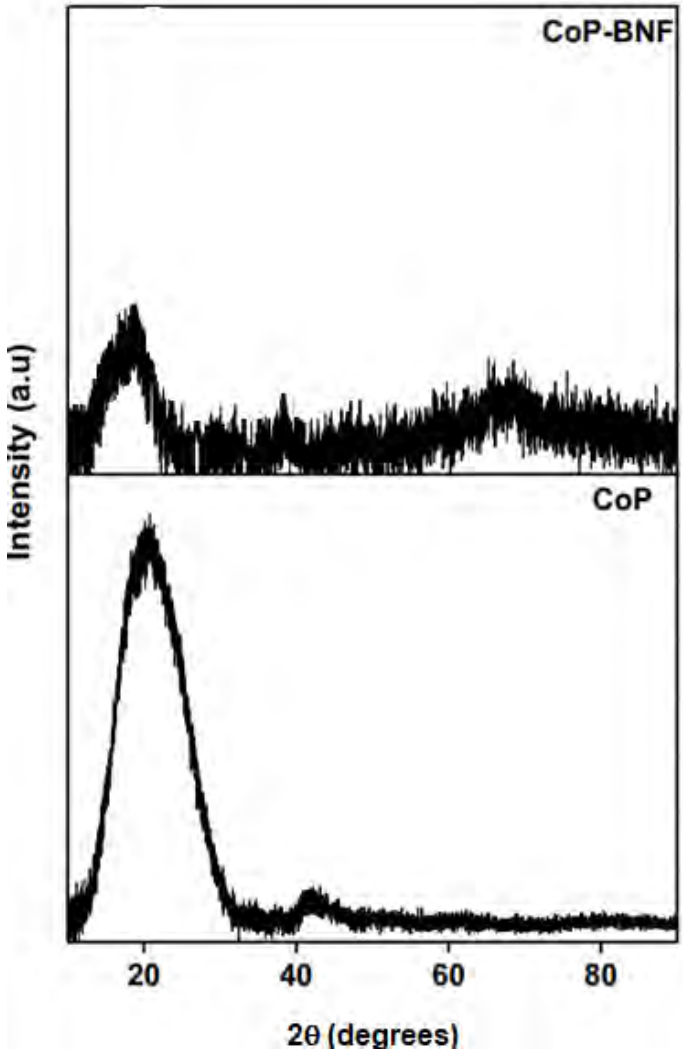

Figure 3.10. XRD data for the mononuclear metalated CoP and the CoP-BNF, as labelled.

3.3.2.3. FT-IR spectroscopy

The FT-IR spectrum of the CoP-BNF is compared to that of an unmetalated tetracarboxyphenyl porphyrin (H_2P), **Figure 3.11**. An unmetalated porphyrin has the inner ring –NH groups, which were confirmed by the peak at 3319 cm^{-1}, **Figure 3.11(i)**. In addition, an expected broad peak at 3349 cm^{-1} was observed, which is due to the –OH of the carboxylic groups in the porphyrin. Peaks at 1685 cm^{-1} and 1606 cm^{-1} associated with the -C=O stretch and -C=C stretch, respectively, were observed. Similar vibrational stretches were observed for the CoP-BNF. There is a shift of the broad carboxylic peak at 3349 cm^{-1} for H_2P to 3434 cm^{-1} for CoP-BNF and the disappearance of the –NH stretch symbolizing successful metalation, **Figure 3.11(ii)**. The presence of the carboxylic acid groups (3434 cm^{-1}) confirms that not all of them were used for the coordination of Co.

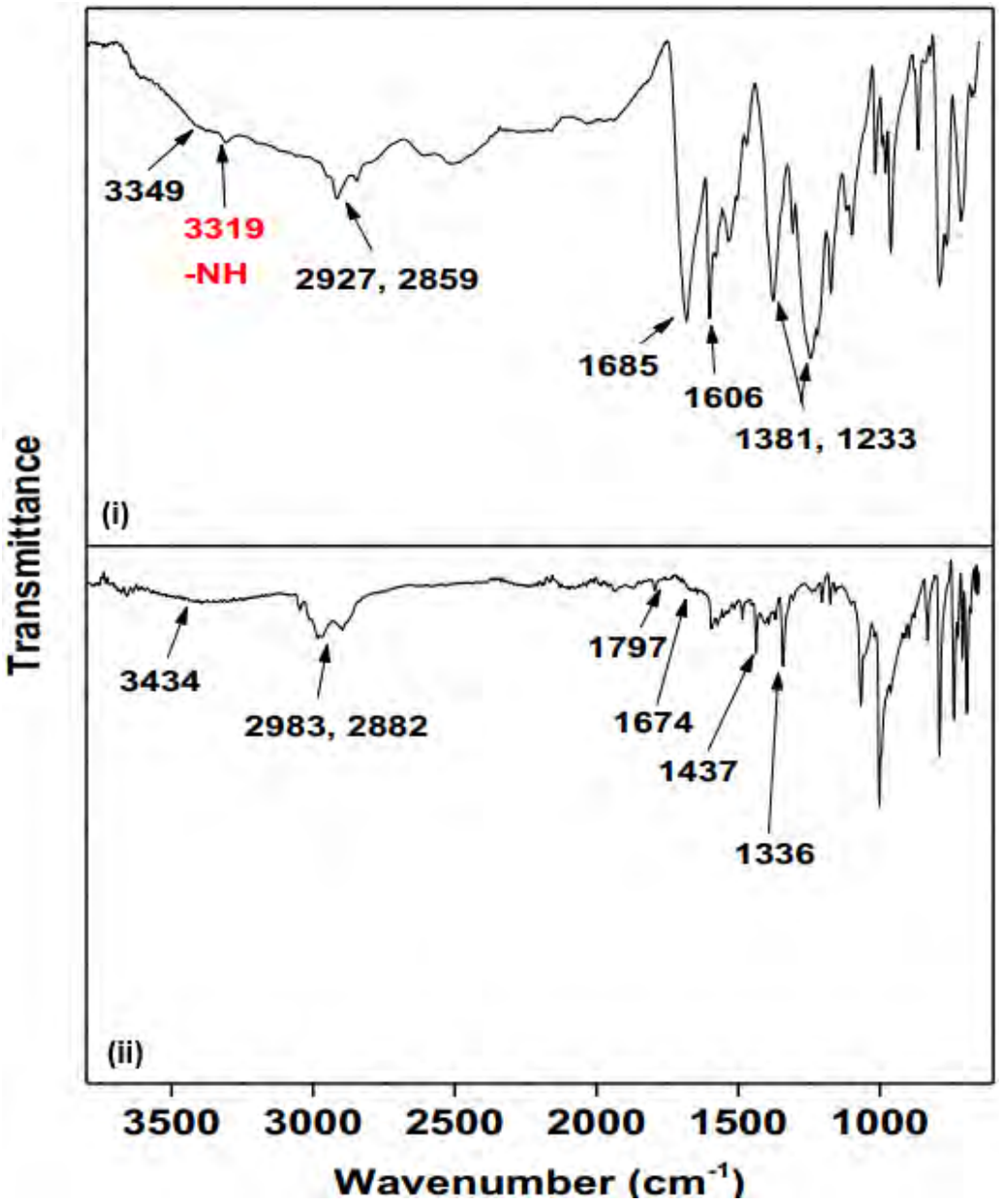

Figure 3.11. FT-IR spectroscopy of (i) unmetalated tetracarboxyphenyl porphyrin (H_2P) (a) and CoP-BNF (ii).

3.4. Conclusion

The desired MPc complexes **1-6** were successfully synthesized, purified and characterized using various techniques. The different optical properties of the Pc complexes as shown by the UV-Vis data, further confirms the different molecular structures of the Pc complexes. The FT-IR, XRD and Raman Spectroscopy data confirmed the successful synthesis of the desired SNGQDs, CeO_2NPs_{COOH} and AuNPs. Successful surface modification of these nanoparticles was confirmed by TEM, as shown by the different size, shape and dispersibility shown. The non-covalent conjugation of MPc complexes to SNGQDs was confirmed using Raman spectroscopy and UV-Vis absorption spectroscopy. Similarly, the successful synthesis of the CoP-BNF was confirmed.

4. Electrode Modification and Characterization

This chapter deals with electrode modification and immobilization of biorecognition elements towards biosensor design. First the electrodes were modified with porphyrin/Pc complexes and/or Pc/NPs conjugates. Electropolymerization and the drop dry method were used as core electrode modification techniques. Immobilization of either the HB5 aptamer and/or Trasmatuzab antibody (biorecognition elements) using DCC/NHS coupling, EDC/NHS coupling and/or acid catalysed imine bond formation coupling methods where appropriate was explored. Characterization of the modified surfaces include surface characterization techniques and electrochemical methods. The modified electrodes are given numbers for ease of reference; the numbers are in blue. Table 4.1 lists all electrode numbers

Table 4.1. List of Modified Electrodes accompanied by their designated electrode numbers used throughout the thesis.

Modified Electrodes	Electrode Number
GCE/PPy	(**1**)
GCE/**1**	(**2**)
GCE/SNGQDs	(**3**)
GCE/PPy@SNGQDs	(**4**)
GCE/PPy@**1**	(**5**)
GCE/PPy@SNGQDs/**1**	(**6**)
GCE/PPy@**1**/SNGQDs	(**7**)
GCE/PPy/SNGQDs(seq.)	(**8**)
GCE/PPy/**1**(seq.)	(**9**)
GCE/PPy/SNGQDs/**1**(seq.)	(**10**)
GCE/PPy/**1**/SNGQDs(seq.)	(**11**)
GCE/**2**	(**12**)
GCE/**3**	(**13**)
GCE/CeO_2NPs_{COOH}	(**14**)
GCE/CeO_2NPs_{COOH}/**2** (seq.)	(**15**)
GCE/CeO_2NPs_{COOH}/**3** (seq.)	(**16**)
GCE/SNGQDs/**3** (seq.)	(**17**)
GCE/ **3**(π)SNGQDs	(**18**)
GCE/AuNPs	(**19**)
GCE/AuNPs/**3** (seq.)	(**20**)
GCE/**4**	(**21**)
GCE/**4**(π)SNGQDs	(**22**)
GCE/**5**	(**23**)
GCE/**5**(π)SNGQDs	(**24**)

Table 4.1 continued…

GCE/SNGQDs@CeO_2NPs	(**25**)
GCE/**6**	(**26**)
GCE/SNGQDs@CeO_2NPs/**6** (seq.)	(**27**)
GCE/SNGQDs@AuNPs	(**28**)
GCE/CoP-BNF	(**29**)
GCE/SNGQDs@AuNPs/CoP-BNF (seq.)	(**30**)

4.1. Effect of polymerization of pyrrole to form polypyrrole (PPy) in the presence of SNGQDs and Complex 1

The electropolymerization of pyrrole in the presence of complex **1** and SNGQDs, respectively on a glassy carbon electrode is investigated. **Scheme 4.1(i)** shows the representation of the steps involved towards electrode modification. Onto the then modified electrodes, the HB5 aptamer was then immobilized as a biorecognition element, **Scheme 4.1(ii)**.

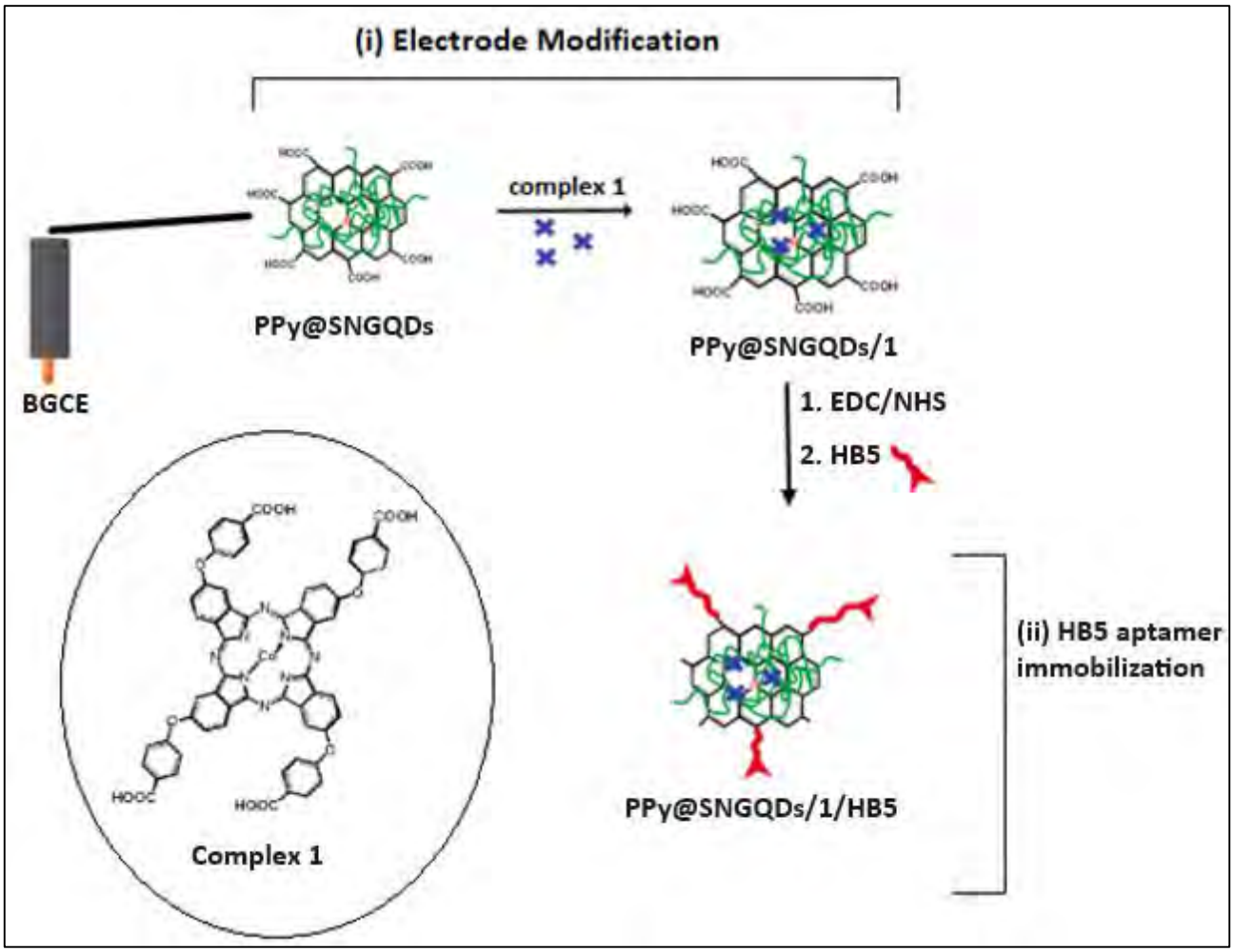

Scheme 4.1. Graphic representation of the GCE modification by PPy/nanomaterial copolymerization for the fabrication of the GCE/PPy@SNGQDs, GCE/PPy@SNGQDs/**1** (i) and GCE/PPy@SNGQDs/**1**/HB5 probes (ii). Where BGCE= bare glassy carbon electrode

4.1.1. Optimization and Electropolymerization

The optimization of pyrrole was performed using CV and EIS, **Figure 4.1**. An increase in current with increasing pyrrole concentration was observed; the plots were stopped at 0.15 mM, since there was measurable current. Four different concentrations of the SNGQDs were explored to investigate the optimum concentration (used for electropolymerization), for the PPy@SNGQDs composite. It was observed that the current decreased with increase in SNGQDs concentration. The highest current was obtained for the lowest concentration of 1 mg/mL, this maybe because GQDs are prone to aggregation at higher concentration. In this study the chosen lowest concentration was 1 mg/mL for SNGQDs and was used throughout. A low concentration of the complex **1** (4.6×10^{-4} mmol) was used.

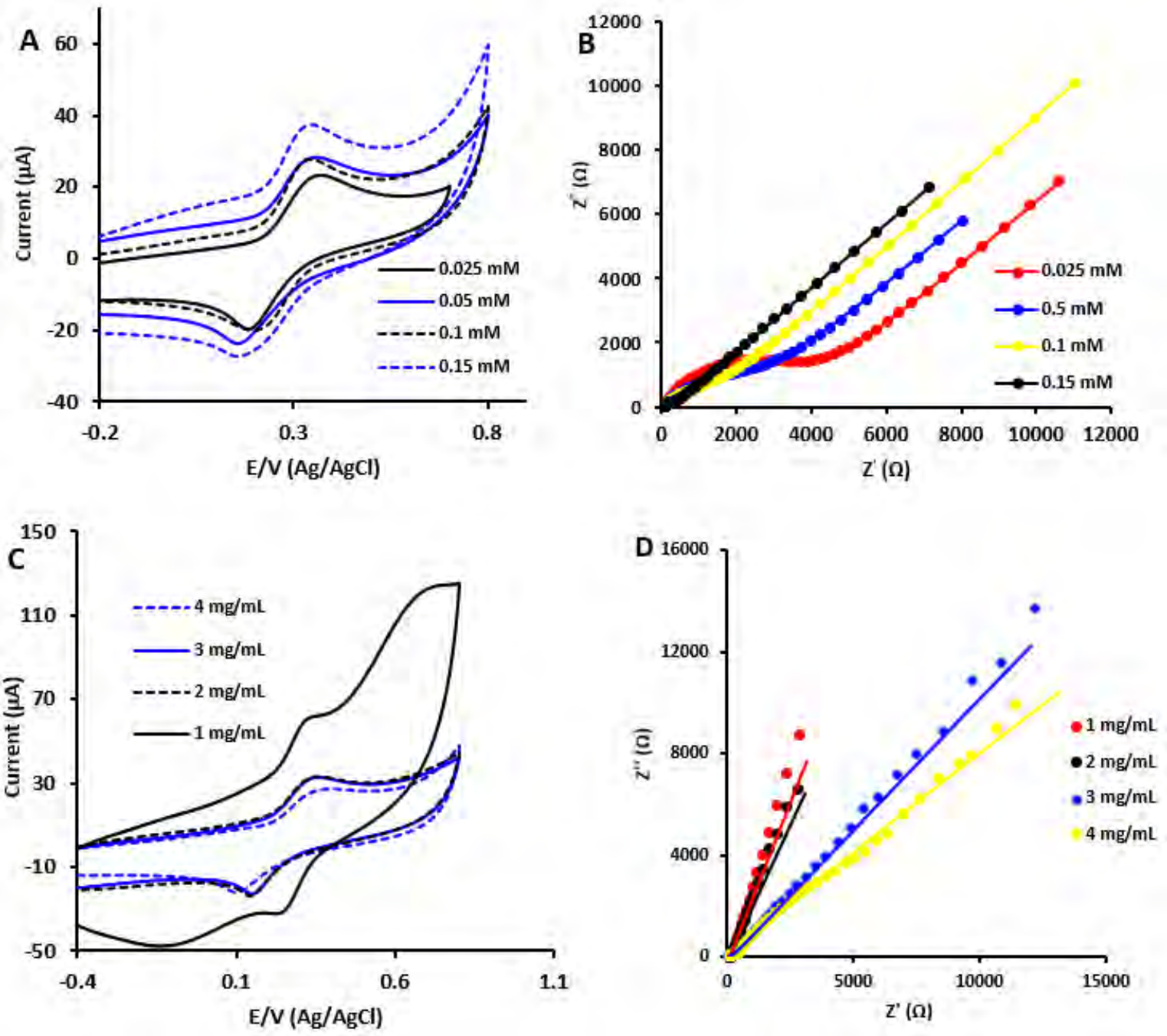

Figure 4.1. CV (**A**) and EIS (**B**) data obtained for polymerization of pyrrole using different monomer concentrations. CV (**C**) and Nyquist plots (**D**) obtained for pyrrole polymerization in the presence of SNGQDs (pyrrole monomer concentration = 0.15 mM) in the presence of SNGQDs (varied concentrations). All studies were conducted in PBS pH 7,4. All in $K_3[Fe(CN)_6]^{3-/4-}$ (1 mM in 0.1 mol·L^{-1} KCl in 10 mM PBS (pH 7.4).

First, the glassy carbon electrode was modified with polypyrrole film by electrochemical deposition of a non-functionalized pyrrole monomer, GCE/PPy (**1**). The solution of pyrrole monomer (0.15 mM) was scanned from − 0.6 V to 0.8 V vs Ag/AgCl, at a scan rate of 100 mV/s in 10 mM PBS (pH 7.4) using cyclic voltammetry. Pyrrole polymerization is evidenced by the increase in current with scan number as reported in literature [**193**]. The observations in **Figure 4.2A** are consistent with deposition of additional layers of polypyrrole on the layer formed by the first scan, resulting in steadily increasing currents [**193**]. Secondly, the electrodes GCE/PPy@SNGQDs (**4**) and GCE/PPy@**1** (**5**) were constructed. This was performed by electropolymerization of pyrrole onto the GCEs in a mixed solution of 0.15 mM pyrrole with SNGQDs (1 mg/mL) in 0.1 PBS (pH, 7.4) or complex **1** (4.6×10^{-4} mmol in DMSO), and scanning from − 0.6 V to 0.8 V, 10 cycles at 100 mV/s. **Figure 4.2B,** shows the cyclic voltammetry changes, when pyrrole was polymerized in the presence of **1**. Cyclic voltammograms similar to those observed during the polymerization of pyrrole alone were observed accompanied by an increased current, hence confirming the formation of PPy in the presence of **1**. The same was observed for polymerization in the presence of the SNGQDs, **Figure 4.2C**. Following this, complex **1** was added on top of GCE/PPy@SNGQDs surface form GCE/PPy@SNGQDs/**1** (**6**). Similarly, SNGQDs were added on top of GCE/PPy@**1** to form PPy@**1**/SNGQDs (**7**). Electrodes were also modified with just polymerization of pyrrole alone, followed by sequential addition of either SNGQDs or complex **1** and are represented as follows: GCE/PPy/SNGQDs (seq.) (**8**), GCE/PPy/**1** (seq.) (**9**), GCE/PPy/SNGQDs/**1** (seq.) (**10**) and GCE/PPy/**1**/SNGQDs (seq.) (**11**). Where seq. is abbreviation for sequential adsorption.

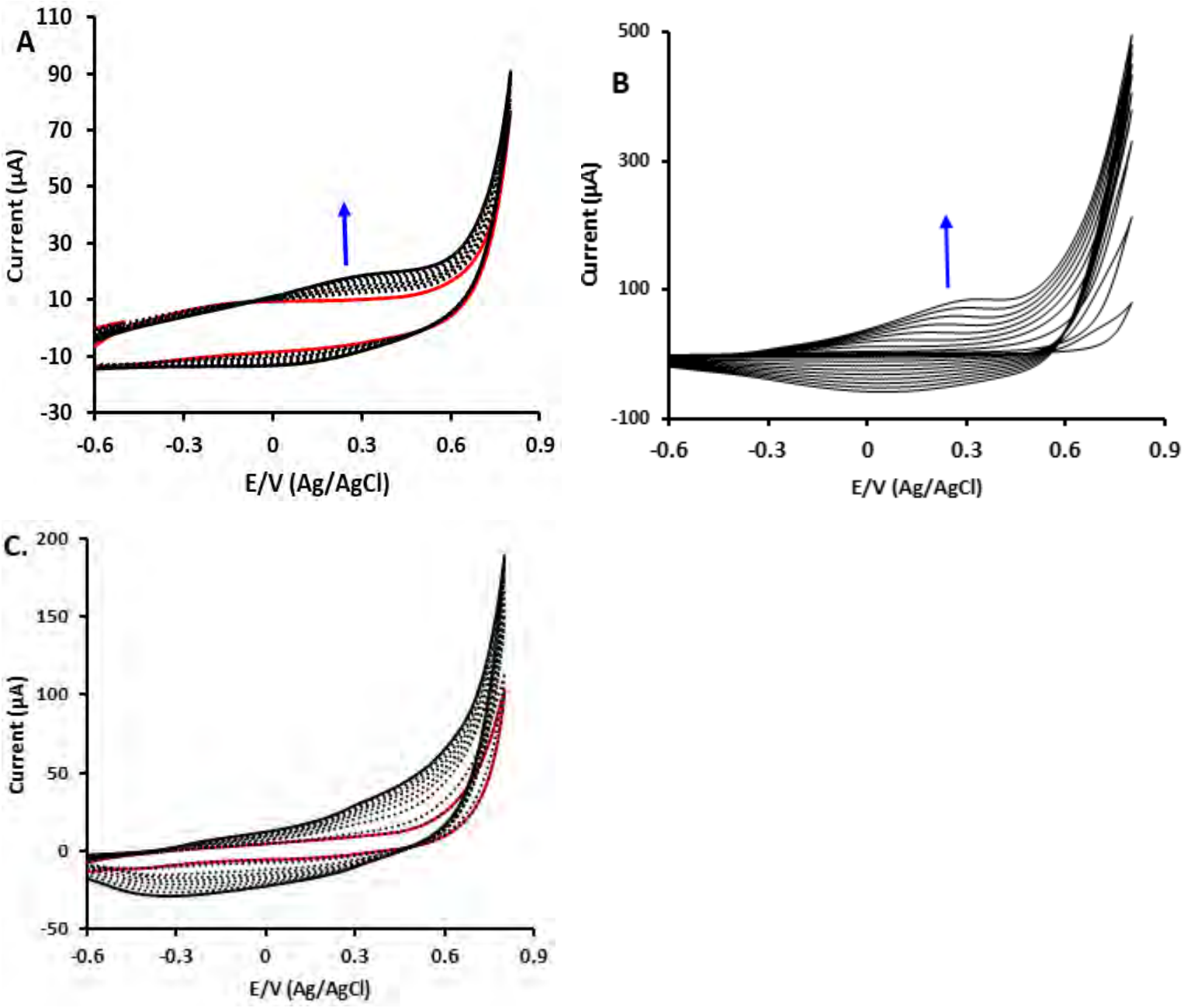

Figure 4.2. CV diagrams for the generation of (A) GCE/PPy in 0.15 M pyrrole, (B) GCE/PPy@**1** {in 0.15 M pyrrole and 4.6×10^{-4} mmol complex **1** (in DMSO)} and (C) GCE/PPy@SNGQDs (in 0.15 M pyrrole and 1 µg/mL SNGQDs). All studies were done in PBS pH 7.4, 10 cycles at 100 mV/s.

4.1.2. Cyclic Voltammetry in $K_3[Fe(CN)_6]^{3-/4-}$, Table 4.2

A total of 11 modified electrodes: GCE/PPY (**1**), GCE/**1** (**2**), GCE/SNGQDs (**3**), GCE/ PPy@SNGQDs (**4**), GCE/PPy@**1** (**5**), GCE/PPy@SNGQDs/**1** (**6**), GCE/PPy@**1**/SNGQDs (**7**), GCE/PPy/SNGQDs (seq.) (**8**), GCE/PPy/**1** (seq.) (**9**), GCE/PPy/SNGQDs/**1** (seq.) (**10**) and GCE/PPy/**1**/SNGQDs (seq.) (**11**) were studied.

Figure 4.3A shows CV diagrams obtained for a selected modified electrode: (i) GCE/PPy (**1**), (ii) GCE/PPy@SNGQDs (**4**) and (iii) GCE/PPy@SNGQDs/**1** (**6**). Furthermore, the electrode **4** is also used to demonstrate the change in ΔE_p upon addition of the HB5 aptamer: GCE/PPy@SNGQDs (**4**)/HB5, on the surface in preparation for analyte detection. The CV diagrams for the rest of the probes is shown in **Figure 4.3B**. Cyclic voltammetry was used to characterize the electron transfer properties of each surface, **Table 4.2**. The electron transfer properties of the different modified surfaces was compared in terms of ΔE_p for which the values increased in the following trend: bare GCE (68 mV) < GCE/SNGQDs (**3**) (73 mV) < GCE/PPy@SNGQDs (**4**) (80 mV) < GCE/PPy (**1**) (154 mV) < GCE/PPy@SNGQDs/**1** (**6**) (166 mV) < ~GCE/**1** (**2**) (165 mV) < GCE/PPy/**1**/SNGQDs(seq.) (**11**) (246 mV) < GCE/PPy/SNGQDs(seq.) (**8**) (288 mV) < GCE/PPy@**1** (**5**) (361 mV) < GCE/PPy@**1**/SNGQDs (**7**) (428 mV) < GCE/PPy/**1** (seq.) (**9**) (467 mV) < GCE/PPy/SNGQDs/ **1** (seq.) (**10**) (515 mV). A ΔEp value close to or lower than ~ 70 mV is synonymous with desirable electron-transporting abilities.

The GCE/PPy@SNGQDs (**4**) (80 mV) showed better electron transfer properties compared to the GCE/PPy (**1**) (154 mV) surface. This might be attributed to SNGQDs containing functional groups (sp^2 carbon, S and N atoms, carboxylic, hydroxyl groups) which promote electron transfer between electrolyte and electrode. Also, the structure of the SNGQDs encourage electron transfer via π-π interaction with the pyrrole structure, hence the improved

conductivity. The polymerization of PPy in the presence of complex **1** and SNGQDs (GCE/PPy@**1** (**5**) and GCE/PPy@SNGQDs (**4**), respectively) gave better electron transfer properties compared to the sequentially modified GCE/PPy/**1**(seq.) (**9**) and GCE/PPy/SNGQDs(seq.) (**8**) counterparts. This may be due to the arrangement and interaction of the nanomaterials on the electrode surface upon modification. During the fabrication of the GCE/ PPy@**1** (**5**) and GCE/PPy@SNGQDs (**4**) surfaces, the nanomaterials are mixed in solution and a potential is applied on the electrode. The interaction of the components is governed by each of their structural properties, which then determines how the nanomaterials are arranged on the electrode surface. The applied potential aids for π-π interaction between the pyrrole, SNGQDs and complex **1**, and all this takes place on the electrode [**194**]. Whereas, for the GCE/PPy/**1**(seq.) (**9**) and GCE/PPy/SNGQDs(seq.) (**8**), the nanomaterials are layered on top of each other. Their interaction and arrangement on the electrode surface are uncontrolled (no applied or external energy) and may sometimes result in passivation of the electrode surface, hence the decreased electron transfer properties. The same trend was observed for the GCE/PPy@SNGQDs/**1** (**6**) (166 mV) and GCE/PPy/SNGQDs/**1**(seq.) (**10**) (515 mV) surfaces, where the sequential adsorption modified surface had poor electron transfer properties compared to polymerization. For the GCE/PPy@**1**/SNGQDs (**7**) (428 mV) and GCE/PPy/**1**/SNGQDs(seq.) (**11**) (246 mV), the surface by sequential adsorption had better electron transfer properties. Shifts observed for oxidation peaks towards the negative values for some electrodes could be attributed to sluggish charge transfer reaction rates, potential shift due to solution resistance, as well as instrumental delay. The electrodes **2-11**, all modified as outlined above were then treated with DCC/NHS to activate the carboxylic groups on the surfaces to allow for immobilization of the HB5 aptamer, which is the biorecognition element, **Scheme 4.1**.

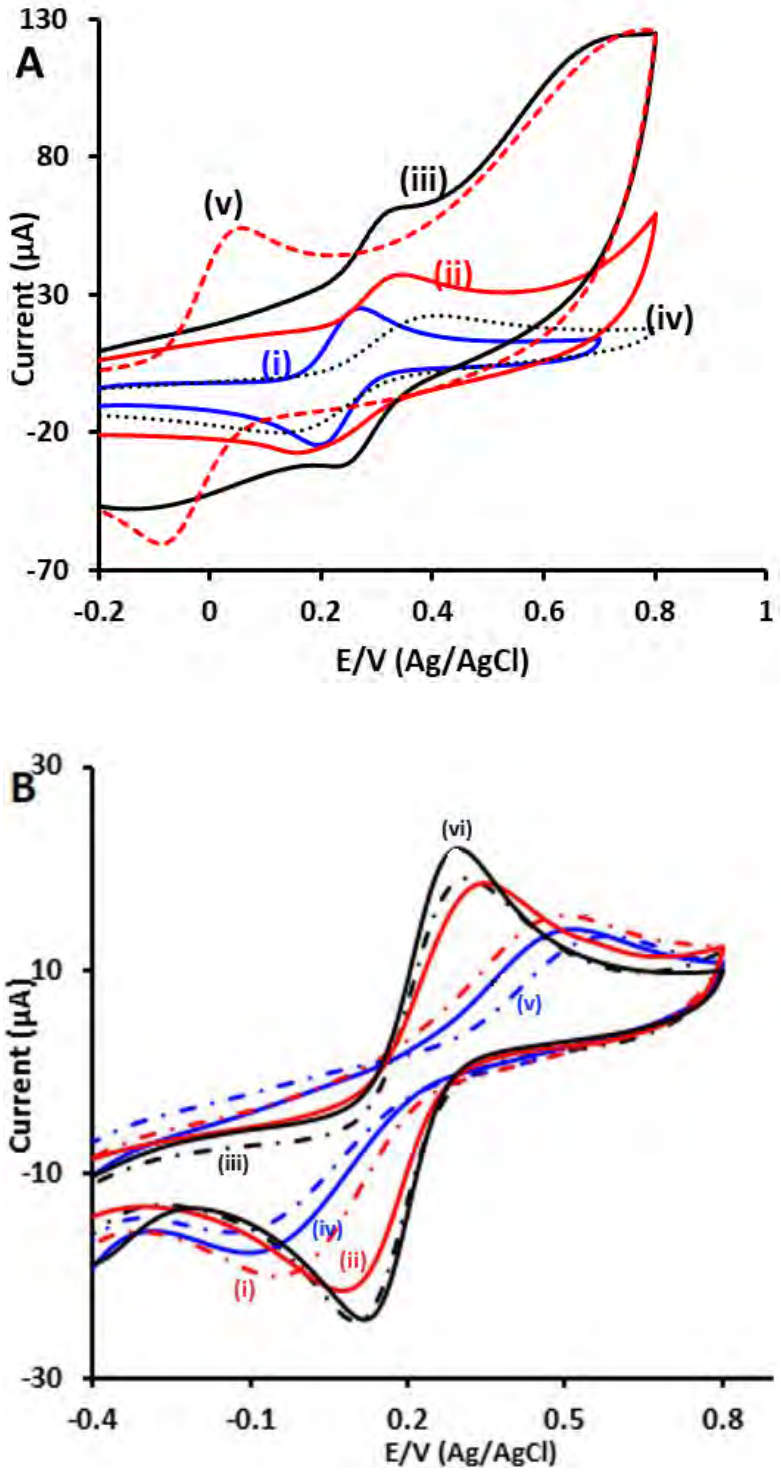

Figure 4.3. CV diagrams of **A**: (**i**) GCE, (**ii**) GCE/PPy (**1**), (**iii**) GCE/PPy@SNGQDs (**4**), (**iv**) GCE/PPy@SNGQDs (**4**)/HB5 and GCE/PPy@SNGQDs/**1** (**6**). **B**: (**i**) GCE/PPy@**1** (**5**), (**ii**) GCE/PPy@**1**/SNGQDs (**7**), (**iii**) GCE/PPy/SNGQDs(seq.) (**8**), (**iv**) GCE/PPy/**1**(seq.), (**9**), (**v**) GCE/PPy/SNGQDs/**1**(seq.) (**10**) and (**vi**) GCE/PPy/**1**/SNGQDs (seq.) (**11**)**.** All in 1mM $K_3[Fe(CN)_6]^{3-/4-}$ in 0.1 mol·L^{-1} KCl in 10 mM PBS (pH 7.4).

4.1.3. Electrochemical Impedance Spectroscopy (EIS) in $K_3[Fe(CN)_6]^{3-/4-}$

EIS is well known as an effective tool for studying the interface properties of surface modified electrodes [**195**, **196**]. A typical impedance spectrum, presented in the form of the Nyquist plot, includes a semicircle portion at higher frequencies corresponding to the electron transfer limited process and a linear part at lower frequency range representing diffusion limited process. EIS measurements were carried out for the various electrodes. **Figure 4.4A** shows the Nyquist plots obtained for the electrodes (i) GCE, (ii) GCE/PPy (**1**), (iii) GCE/PPy@SNGQDs (**4**) and (iv) GCE/PPy@SNGQDs/**1** (**6**) and (v) GCE/PPy@SNGQDs (**4**)/HB5. While **Figure 4.4B** shows the Nyquist plots obtained for the rest of the electrodes, labelled accordingly on the figure. The data obtained were fitted using an equivalent modified circuit, **Figure 4.4C**. The key parameter used to differentiate and characterize the modified electrodes was the charge transfer resistance (R_{ct}), which increases with decrease in conductivity and vice versa. The R_{ct} values obtained for the different electrodes are further outlined in **Table 4.2**.

The successful immobilization of the HB5 aptamer, **Scheme 4.1 (ii)** on all the modified surface to form aptasensors: GCE/**1** (**2**)/HB5, GCE/SNGQDs (**3**)/HB5, GCE/ PPy@SNGQDs (**4**)/HB5, GCE/PPy@**1** (**5**)/HB5, GCE/PPy@SNGQDs/**1** (**6**)/HB5, GCE/PPy@**1**/SNGQDs (**7**)/HB5, GCE/PPy/SNGQDs (seq.) (**8**)/HB5, GCE/PPy/**1** (seq.) (**9**)/HB5, GCE/PPy/SNGQDs/**1** (seq.) (**10**)/HB5 and GCE/PPy/**1**/SNGQDs (seq.) (**11**)/HB5, was further confirmed by increase in R_{ct} values, **Table 4.2** (values in brackets).

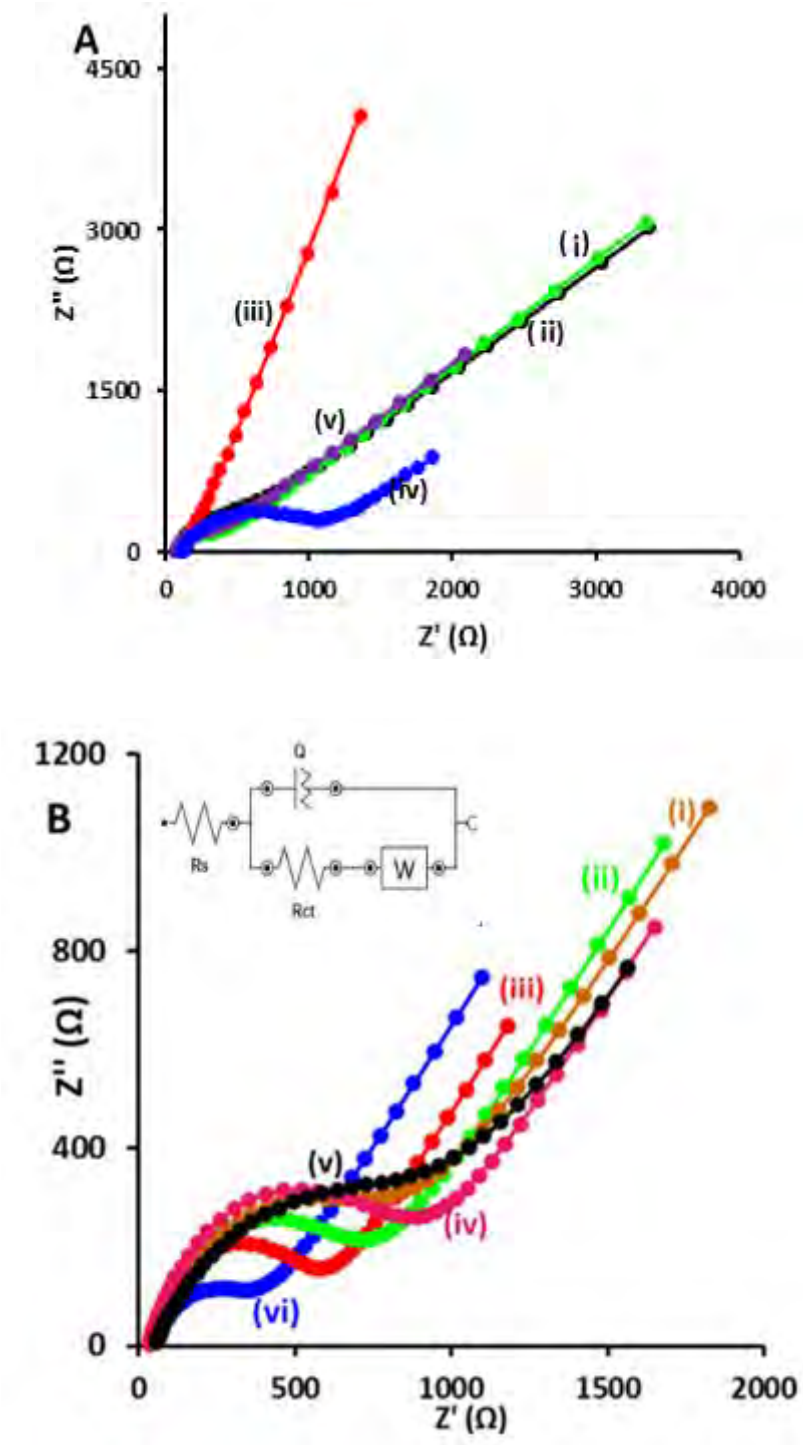

Figure 4.4. Nyquist plots of **A**: (i) GCE, (ii) GCE/PPy (**1**), (iii) GCE/PPy@SNGQDs (**4**), (iv)GCE/PPy@SNGQDs (**4**)/HB5 and (v) GCE/PPy@SNGQDs/**1** (**6**) and (v). **B**: (**i**) GCE/PPy@**1** (**5**), (**ii**) GCE/PPy@**1**/SNGQDs (**7**), (**iii**) GCE/PPy/SNGQDs(seq.) (**8**), (**iv**) GCE/PPy/**1**(seq.), (**9**), (**v**) GCE/PPy/SNGQDs/**1**(seq.) (**10**) and (**vi**) GCE/PPy/**1**/SNGQDs(seq.) (**11**)**.** All in 1mM $K_3[Fe(CN)_6]^{3-/4-}$ in 0.1 mol·L^{-1} KCl in 10 mM PBS (pH 7.4). Insert in **B:** Equivalent circuit adopted to fit data.

Table 4.2. Peak potential separations and R_{ct} values in $K_3[Fe(CN)_6]^{3-/4-}$ obtained for relevant surfaces.

Electrode Surface	Electrode number	ΔE (mV)	R_{ct} (kΩ) [a]
GCE		68	244
GCE/PPy	**1**	154	224
GCE/**1**	**2**	165	287 (468)
GCE/SNGQDs	**3**	73	180 (495)
GCE/PPy@SNGQDs	**4**	80	207 (923)
GCE/PPy@**1**	**5**	361	708 (1230)
GCE/PPy@SNGQDs/**1**	**6**	166	215 (2190)
GCE/PPy@**1**/SNGQDs	**7**	428	660 (1680)
GCE/PPy/SNGQDs(seq.)	**8**	288	522 (2410)
GCE/PPy/**1** (seq.)	**9**	467	800 (220)
GCE/PPy/SNGQDs/**1** (seq.)	**10**	515	929 (384)
GCE/PPy/**1**/SNGQDs (seq.)	**11**	246	347 (2010)

[a] Values in brackets represents R_{ct} values of the corresponding probes with aptamer (concentration 1 μM) prior HER2 detection.

4.2. Amide bond formation with HB5 aptamer, Scheme 4.2

The protocol followed for electrode modification using all Pc complexes **2-6** is shown in **Scheme 4.2**, using complex **2** as an example. Adsorption was used as a method of modification for all mentioned complexes, either alone or in combination with the relevant nanoparticles. CoPc complexes based GCEs (except complex **4**), were used as immobilization platforms for the HB5 aptamer using the DCC/NHS coupling to form an amide bond.

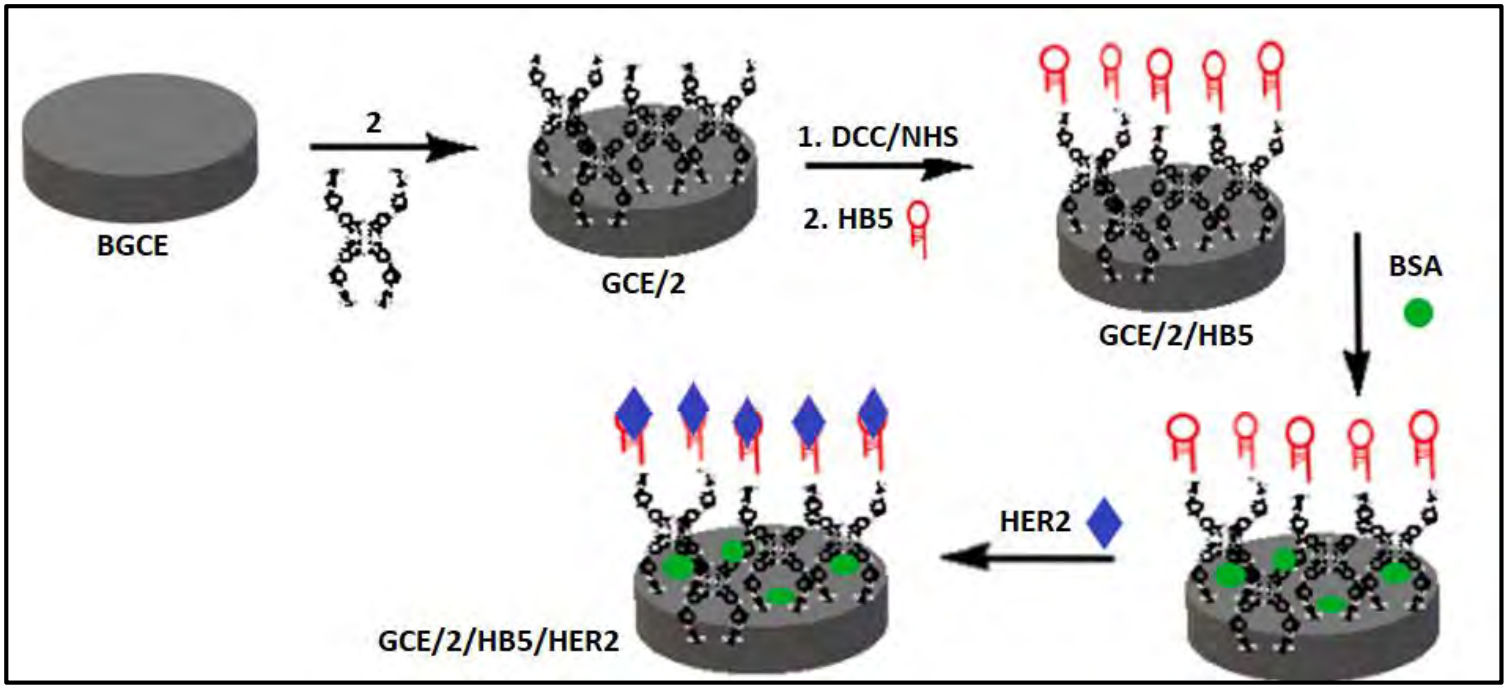

Scheme 4.2. Schematic representation of the steps towards the fabrication of the desired electrode modifications. Showing the probe GCE/**2**/HB5, as an example.

4.2.1. Cyclic Voltammetry

4.2.1.1. Complex 2 and 3 in the presence of cerium oxide nanoparticles, Table 4.3

All electrochemical measurements were performed in 10 mM PBS of pH 7.4 containing 0.1 M KCl and 1 mM $K_3[Fe(CN)_6]^{3-/4-}$. The CV of ferricyanide was chosen as a marker to investigate the electron transfer properties of each modified surface. **Figure 4.5A** shows the CV plots obtained for the electrodes containing complexes **2** and **3**, data shown in **Table 4.3**. Phthalocyanines are well known for their great redox properties, and hence their domineering performance compared to the CeO_2NPs_{COOH} alone. Reports have shown that the synergistic combination of the properties of phthalocyanines and metal nanoparticles tend to improve various properties of their hybrid materials [64]. However, ΔE_p increased for complex **2** in the presence of CeO_2NPs_{COOH}. The performance of complex **3** will be discussed in the next section. Extra peaks near 0.5 V observed for CoPcs alone are due to Co(III)/Co(II) redox process according to literature [197].

4.2.1.2. Complex 3 in the presence of AuNPs, SNGQDs and CeO_2NPs: Effect of nanoparticles.

Figure 4.5B shows the obtained CV diagrams for the different electrode containing complex **3**, combined with AuNPs and SNGQDs, respectively. The calculated ΔEp values of 71 mV, 73 mV, 70 mV and 80 mV for GCE/**3** (**13**), GCE/SNGQDs (**3**), GCE/CeO_2NPs_{COOH}/**3** (seq.) (**16**), GCE/**3**(π)SNGQDs (**18**) respectively, thus showing good electron transporting abilities. The rest of the electrodes had ΔEp value as follows: (**20**) GCE/AuNPs/**3** (480 mV) > (**14**) GCE/CeO_2NPs_{COOH} (122 mV) > (**17**) GCE/SNGQDs/**3** (seq.) (105 mV) > (**19**) GCE/AuNPs (100 mV). Of the NPs alone the lowest ΔEp value was obtained for SNGQDs followed by AuNPs, with CeO_2NPs_{COOH} having the larges ΔEp value. The varying performance of the various

nanoparticles in the same redox media can be attributed to their different structural and physicochemical attributes. The process of electron transfer in nanoparticles can be explained considering the following factors. First, the contact between the electrode and the particular nanoparticle. This is determined by the spatial distribution of the nanoparticles on the electrode, which is dependent on the dispersion and behaviour of the nanoparticles in question when in solvent. Secondly, the nanoparticle's chemical nature, shape and size which determines how the nanoparticle interacts with the electrolyte as well as its stability on the electrode. The sheet structure of the SNGQDs allows for the successful deposition of the nanomaterials on the electrode, forming stable modified electrode. The SNGQDs were monodispersed with a size of 2.8 nm, as shown by TEM image in **Fig. 3.4(i)**. A high catalytic activity is generally expected for small particle size because of the increase of the surface-to-volume ratio [198]. In addition, spherical NPs are known to show better electrocatalytic activity than shaped ones, hence good charge transfer abilities and a low ΔEp value for SNGQDs. The AuNPs used in this work were monodispersed with a spherical morphology, **Fig. 3.4(ii)**. The electron transfer properties of cerium oxide nanoparticles (CeO_2NPs_{COOH}) are derived from the quick and expedient mutation of the oxidation state between Ce^{4+} and Ce^{3+}. The morphology of the COOH containing CeO_2NPs reported here exhibited a rod like shape, **Fig. 3.4(iii)**. Hence the shape of the CeO_2NPs_{COOH} could have resulted in poor electron transfer (higher ΔEp value) compared to SNGQDs and AuNPs. ΔE_p values for complex **3** increased in the presence of SNGQDs and AuNPs, but was unaffected when combined with CeO_2NPs_{COOH}, **Table 4.3**. Higher ΔEp values were obtained for the GCE/AuNPs/**3** (seq.) (20), compared to either the GCE/**3** and GCE/AuNPs. This might be due to the arrangement of the two nanomaterials on the surface when combined. The AuNPs being added first, followed by the layer of the Pc **3** might have resulted in limited interaction of the AuNPs with the electrolyte

to actually have an impact on the electrode's electron transfer properties. Furthermore, passivation of the electrode is a possibility when now adding the complex **3** layer on top of the GCE/AuNPs surface to form GCE/AuNPs/**3** (seq.).

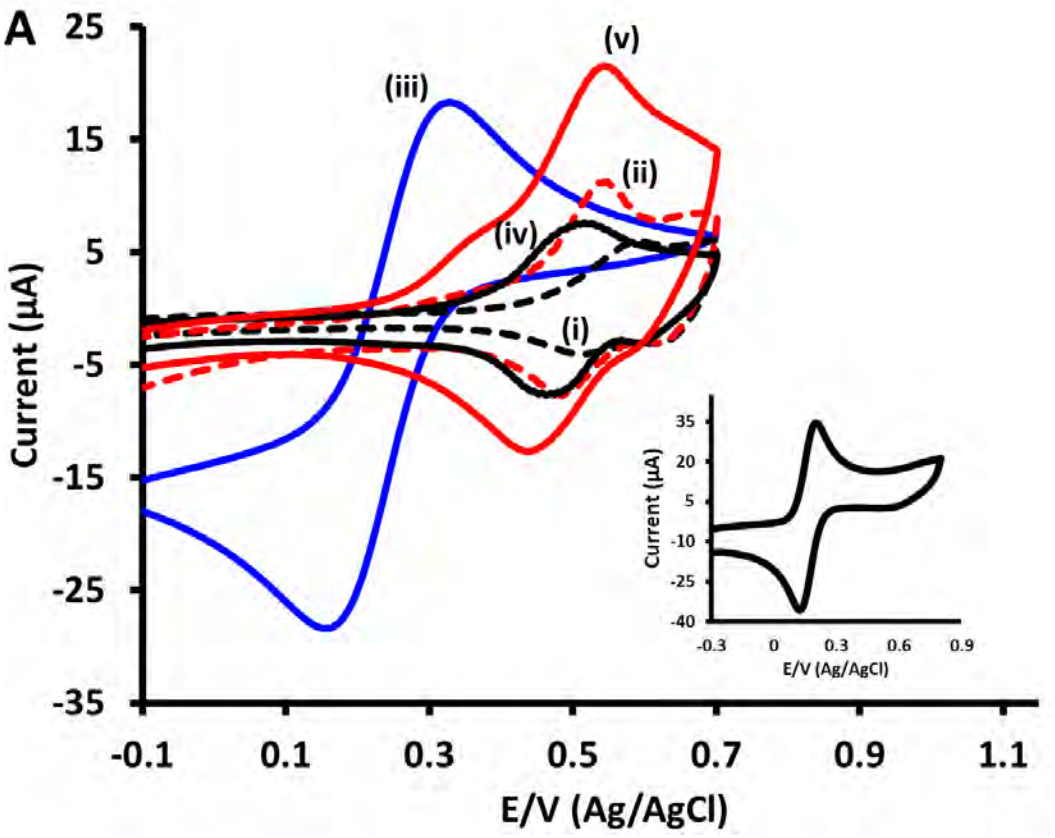

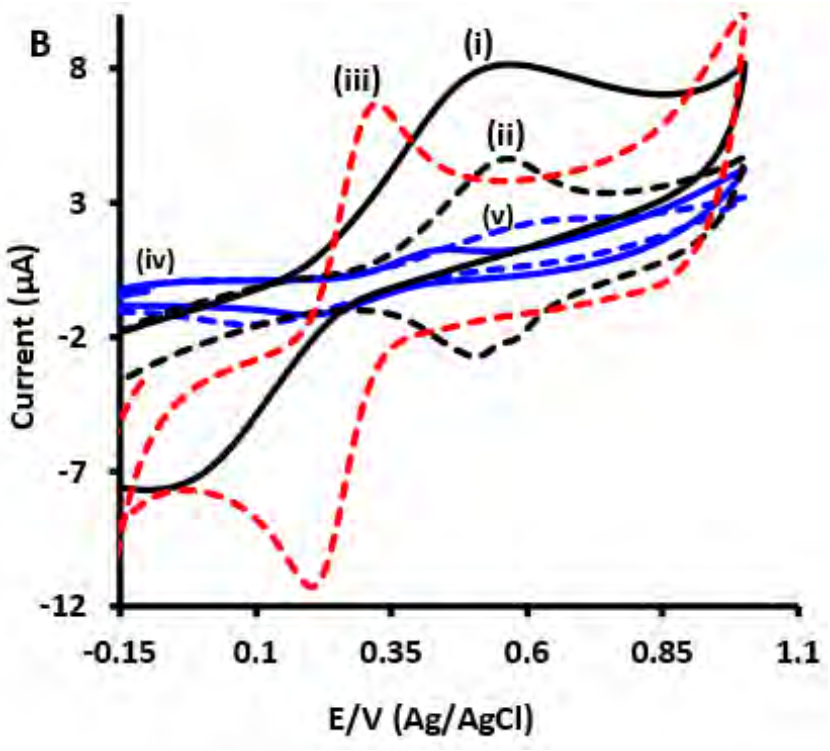

Figure 4.5. CV diagrams of **A**: (i) GCE/**2** (12), (ii) GCE/**3** (13), (iii) GCE/CeO_2NPs_{COOH} (14), (iv) GCE/CeO_2NPs_{COOH}/**2** (seq.) (15) and (v) GCE/CeO_2NPs_{COOH}/**3** (seq.) (16) **B**: (i) GCE/SNGQDs (3), (ii) GCE/SNGQDs/**3** (seq.) (17), (iii) GCE/**3**(π)SNGQDs (18) and (iv) GCE/AuNPs (19) and (v) GCE/AuNPs/**3** (seq.) (20). All in 1 mM $K_3[Fe(CN)_6]^{3-/4-}$ (in 0.1 M KCl) in 10 mM PBS. Scan rate = 100 mV/s. Inserts in, **A** = BGCE,

4.2.1.3. Complex 6 in the presence of SNGQDs@CeO_2NPs: Table 4.3

Figure 4.6 shows the CV diagrams obtained for the relevant modified electrodes: GCE (insert) GCE/SNGQDs@CeO_2NPs (25), GCE/**6** (26) and GCE/SNGQDs@CeO_2NPs/**6** (seq.) (27). The bare GCE showed a reversible peak pair, with oxidation and reduction peak separation (ΔE_p) = 68 mV, **Table 4.2**. The GCE/SNGQDs@CeO_2NPs (25) showed two oxidation peaks. The peaks labelled **I** in all CVs in **Fig. 4.6A** are due to the ferro/ferricyanide. The peak labelled **II** could be due to SNGQDs, this peak was also be observed for SNGQDs@CeO_2NPs alone in buffer (without $K_3[Fe(CN)_6]^{3-/4-}$) though weaker in **Figure 4.6B**. The peak labelled **II** in GCE/**6** (26) is

due to Co (III)/Co (II) redox process according to literature [197]: this was confirmed by the same peak being present in the buffer for GCE/**6**, **Fig. 4.6B**. The same Co (III)/Co (II) was observed for the probe GCE/SNGQDs@CeO_2NPs/**6** (seq.) (**27**), and was accompanied by a broad peak at around 0.3 V which could be due to CeO_2NPs which are known to show CV peaks in this region [199]. The modification of the bare GCE, with the various nanomaterials to form the electrodes (**25**-**27**) resulted in increased redox peak separation (ΔEp). The GCE/SNGQDs@CeO_2NPs/**6** (seq.) (**27**) showed a smaller peak separation (110 mV) compared to that of GCE/**6** (120 mV), accompanied by an increased oxidation peak current. This further demonstrates the synergistic effect of combining a particular complex **6** with SNGQDs@CeO_2NPs for enhanced electron transfer in sensor design.

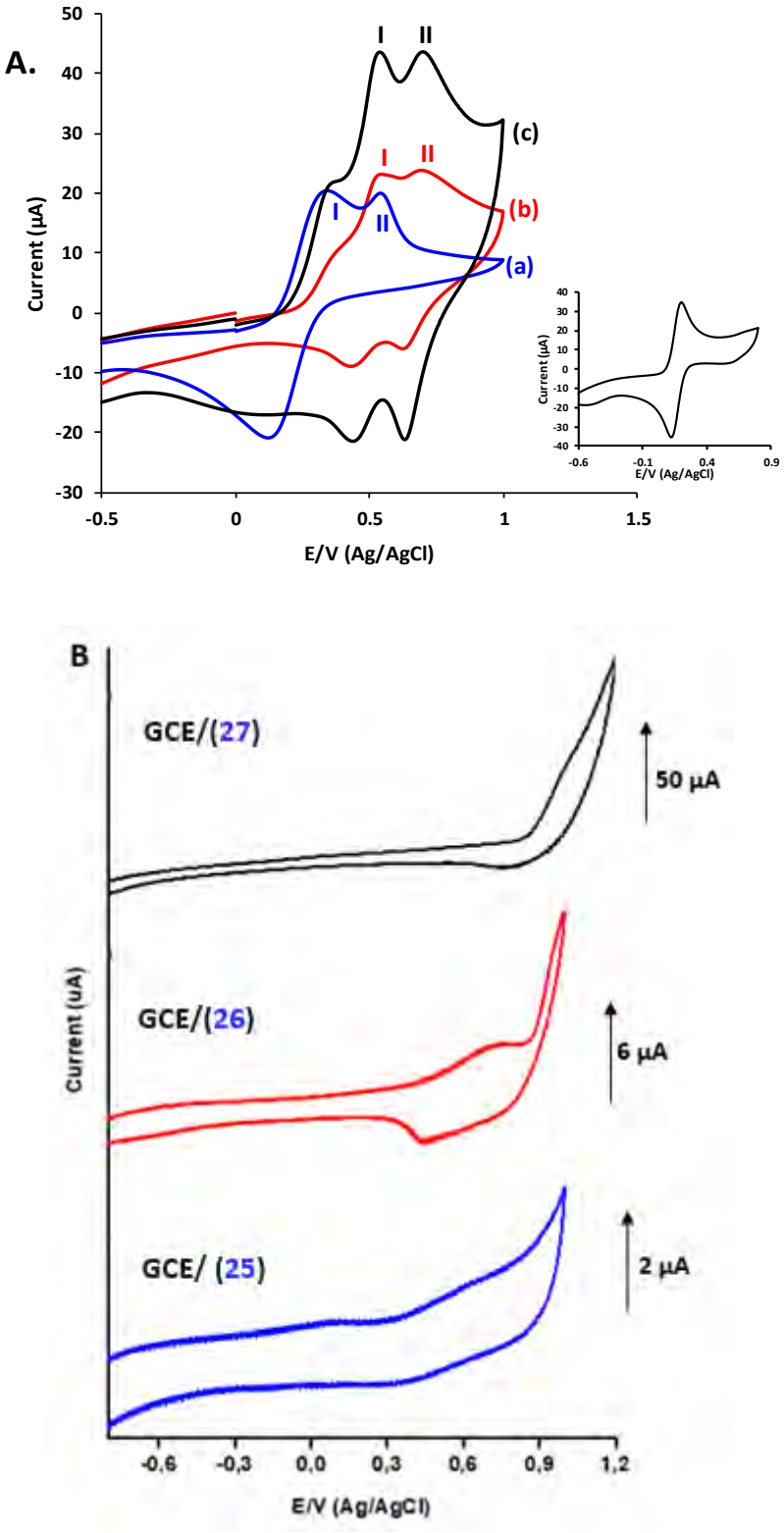

Figure 4.6. CV diagrams for substrates (a) GCE/SNGQDs@CeO_2NPs (**25**), (b) GCE/**6** (**26**) and (c) GCE/SNGQDs@CeO_2NPs/**6** (seq.) (**27**) obtained in (**A**) $K_3[Fe(CN)_6]^{3-/4-}$ (1 mM in 0.1 mol·L^{-1} KCl in 10 mM PBS (pH 7.4) and (**B**) phosphate buffer (pH 7.4). Insert in **A** = BGCE

4.2.1.4. Surface Coverage

The competitiveness of the various nanomaterials where electrode modification is concerned was further demonstrated by calculating the active surface area coverage of each modified surface. The effective electrode surface area (A_{eff}) of the modified GCE was determined in 1 mM $K_3[Fe(CN)_6]^{3-/4-}$ by applying the Randles–Sevcik Equation:

$$ip = (2.69 \times 105)\, n^{\frac{3}{2}} D^{\frac{1}{2}} C A_{eff}\, v^{\frac{1}{2}} \quad \textbf{(4.1)}$$

where i_p is the peak current, n is equal to the number of electrons transferred (n ~ 1), D is the diffusion coefficient of the analyte in solution (7.6×10^{-6} cm^2 s^{-1}) [**200**] and C is the solution concentration in (mol/cm^{-3}), A_{eff} is the effective surface area and v is the scan rate (V/s^{-1}). **Figure 4.7** shows plots of the different modified electrodes in PBS buffer alone. Peaks near 0.5 V for Pc **3** containing electrodes are due to $Co^{III}Pc/Co^{II}Pc$ oxidation process in comparison with literature [**197**]. Ce nanoparticles are known to show cyclic voltammetry peaks around 0.3 V [**199**]. Peaks due to Au NPs are usually observed at about 1 V [**201**]. By using the effective area of the modified electrodes determined using **Eqn. (4.1)** and the total charge determined by integrating peaks in **Fig. 4.7** (anodic peaks), and then by employing **Eqn. (4.2)** [**202**], surface coverages were calculated.

$$\Gamma = Q\, nFA_{eff} \quad \textbf{(4.2)}$$

Where n is the number of electrons transferred (~1), F the Faraday constant (96.485C mol^{-1}), A is the effective surface area obtained from **Eqn. (4.1)** and Γ is the surface coverage. The higher surface coverages imply the increase in the electrode surface area which offers more electrocatalytic surface. The highest surface coverage was observed for GCE/AuNPs (**19**) (1.82 × 10^{-7} $mol.cm^{-2}$) and the lowest surface coverage obtained for the GCE/**3** (**13**) was 1.11 × 10^{-14} $mol.cm^{-2}$. The Γ value for the GCE/SNGQDs (**3**) was undetermined because no peak was observed. A peak was only observed upon incorporation with the complex **3**. In the presence of complex **3**, the highest surface coverage was obtained for the GCE/AuNPs/**3** (seq.) (**20**) (3.99 × 10^{-9} $mol.cm^{-2}$) compared to GCE/CeO_2NPs/**3** (seq.) (**16**) (2.65 × 10^{-10} $mol.cm^{-2}$), GCE/SNGQDs/**3** (seq.) (**17**) (9.76 × 10^{-10} $mol.cm^{-2}$) and GCE/**3**(π)SNGQDs (**18**) (1.49 × 10^{-13} $mol.cm^{-2}$) surfaces. The highest surface coverage is for GCE/AuNPs (**19**) and the lowest is for GCE/**3** (**13**). The same study was conducted for complex **6** based electrodes. The SNGQDs@CeO_2NPs modified electrode, GCE/(**25**) and the complex **6** based GCE/(**26**) had a surface coverage of 2.45 × 10^{-8} $mol.cm^{-2}$ and 5.94 × 10^{-10} $mol.cm^{-2}$ respectively, **Table 4.3**. Upon combination of the SNGQDs@CeO_2NPs and complex **6** on the electrode to form the surface GCE/(**27**), a surface coverage of 2.89 × 10^{-9} $mol.cm^{-2}$, hence the surface coverage is higher for the composite compared to the phthalocyanine alone. This result further demonstrates the significance of combining MPcs with various nanomaterials for enhanced electrocatalytic behaviour.

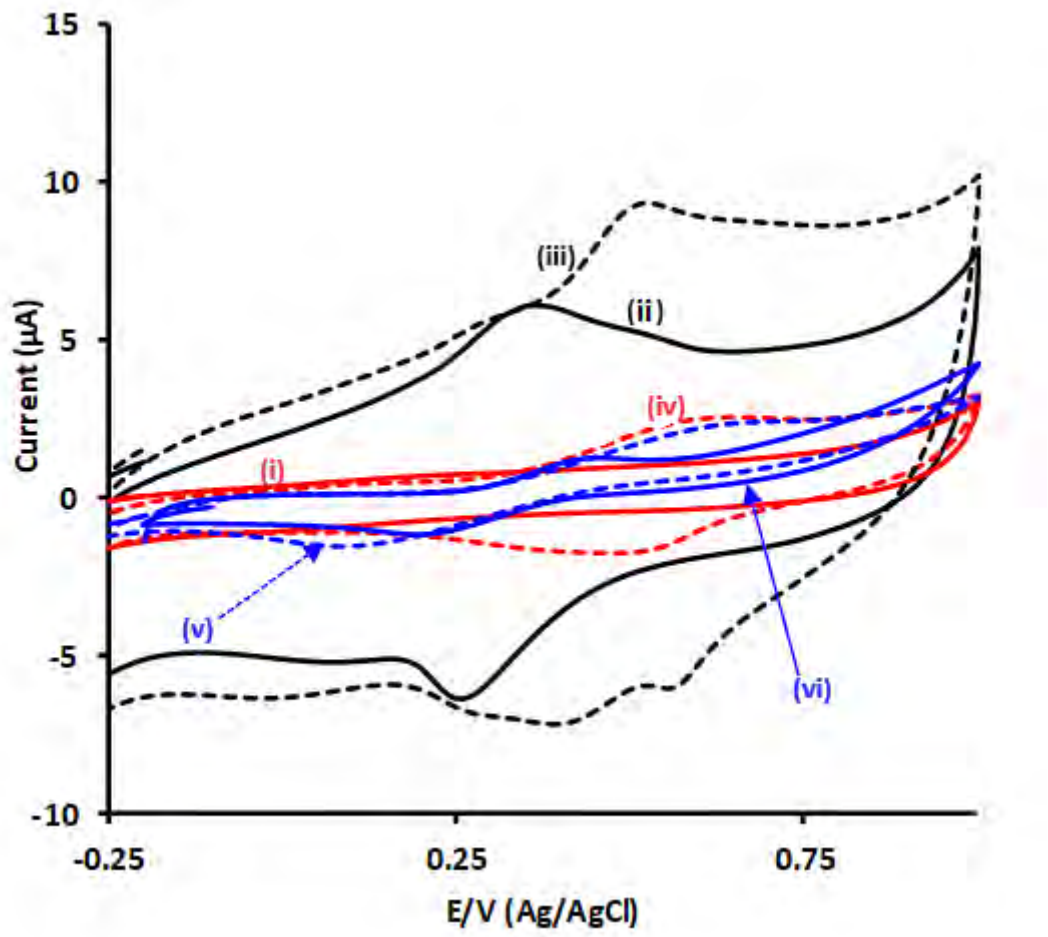

Figure 4.7. Cyclic voltammograms of modified surfaces: (i) GCE/SNGQDs (**3**), (ii) GCE/CeO_2NPs_{COOH} (**14**), (iii) GCE/CeO_2NPs_{COOH}/**3** (seq.) (**16**), (iv) GCE/SNGQDs/**3** (seq.) (**17**), (v) GCE/AuNPs (**19**) and GCE/AuNPs/**3** (seq.) (**20**). All in 10 mM phosphate buffer solution of pH 7.4. Scan rate = 100 mV. s^{-1}.

4.2.2. Electrochemical Impedance Spectroscopy

The electrochemical properties of the modified electrodes were further characterized using EIS. The impedance spectra were recorded first for the bare glassy carbon electrode (BGCE), and then the various modified surfaces. The EIS data was fit using the modified equivalent circuit, previously shown earlier above. The electrodes were differentiated by the resistance to charge transfer (R_{ct}) offered by electrode surface. The characterization of the GCE, upon modification with the various nanomaterials (electrodes **12–20**), is shown in **Figure 4.8A**. The bare glassy carbon electrode had exhibited an almost straight line in the Nyquist plot of impedance spectroscopy (lower insert in **Fig 4.8A**), indicating that a diffusion-limited electron-transfer process was dominant for the frequency range explored. The effect of each nanoparticle: SNGQDs, AuNPs and CeO_2NPs on the electron transfer properties of complex **3**, is further shown by the Nyquist plots in **Figure 4.8B**. In all cases, the charge transfer resistance (R_{ct}), which increases with decrease in conductivity and vice versa, was used as a differentiation parameter. The obtained data for the EIS data were in agreement with that obtained in cyclic voltammetry: the surface with the lowest ΔEp had the lowest R_{ct} values, **Table 4.3**.

The modified electrodes were then used as platforms for the immobilization of the HB5 aptamer to form aptasensors: GCE/SNGQDs (**3**)/HB5, GCE/**2** (**12**)/HB5, GCE/**3** (**13**)/HB5**,** GCE/CeO_2NPs_{COOH} (**14**)/HB5, GCE/CeO_2NPs_{COOH}/**2** (seq.) (**15**)/HB5, GCE/CeO_2NPs_{COOH}/**3** (seq.) (**16**)/HB5, GCE/SNGQDs/**3** (seq.) (**17**)/HB5, GCE/**3**(π)SNGQDs (**18**) /HB5, GCE/AuNPs (**19**) /HB5 and GCE/AuNPs/**3** (seq.) (**20**) /HB5.

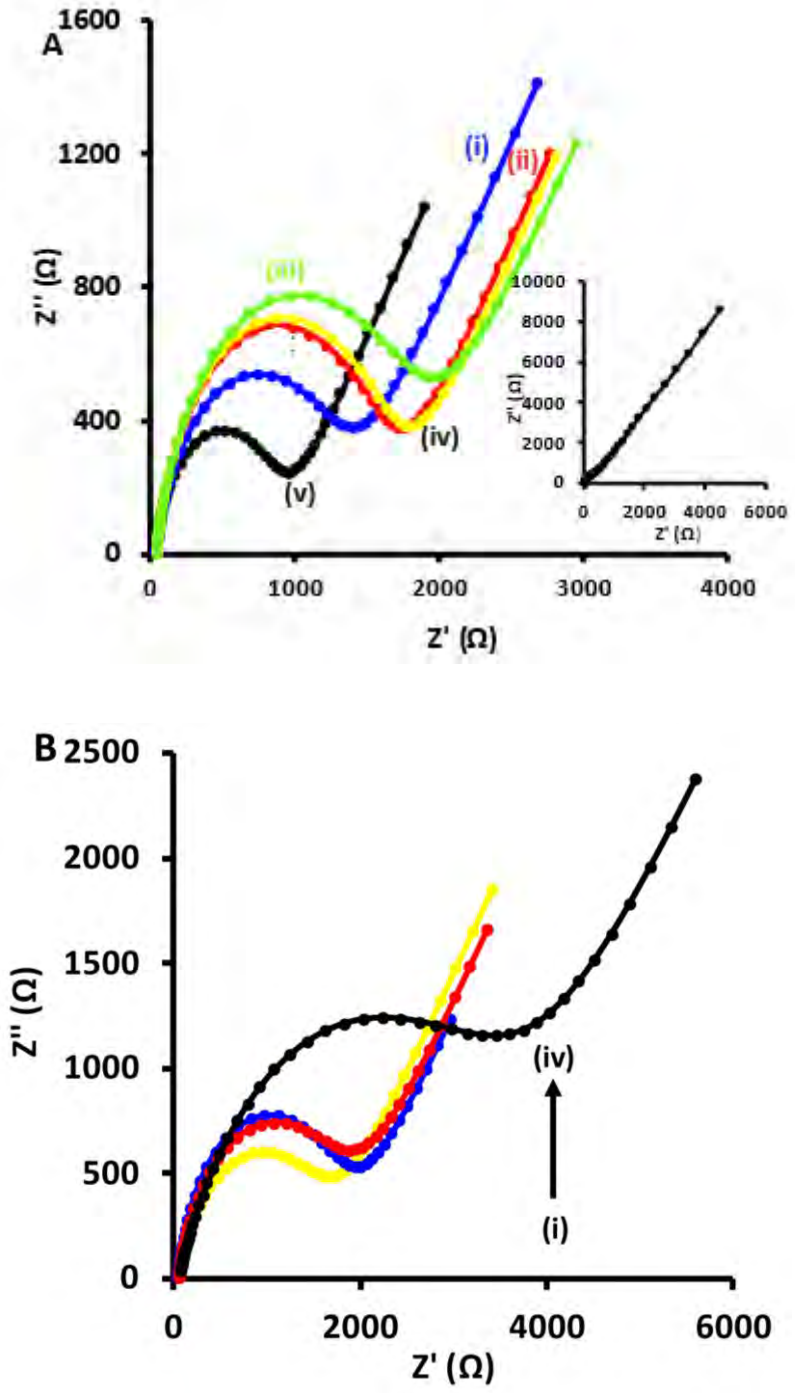

Figure 4.8. Nyquist plots **A**: (i) GCE/**2** (12), (ii) GCE/**3** (13), (iii) GCE/CeO_2NPs_{COOH} (14), (iv) GCE/CeO_2NPs_{COOH}/**2** (seq.) (15) and (v) GCE/CeO_2NPs_{COOH}/**3** (seq.) (16) **B**: (i) GCE/SNGQDs (3), (ii) GCE/SNGQDs/**3** (seq.) (17), (v) GCE/AuNPs (19) and (vi) GCE/AuNPs/**3** (seq.) (20). All in 1mM $K_3[Fe(CN)_6]^{3-/4-}$ (in 0.1 M KCl) in 10 mM PBS. Scan rate = 100 mV/s. Insert in **A** = BGCE.

Similarly, higher R_{ct} values were obtained for all substrates (electrodes **25 - 27**), upon introduction of the HB5 aptamer on all surfaces, **Figure 4.9, Table 4.3**. This might be due to the fact that the aptamer is an oligonucleotide and is not redox active, as a result might have partly blocked the electron/ion transport between the electrode and the electrolyte.

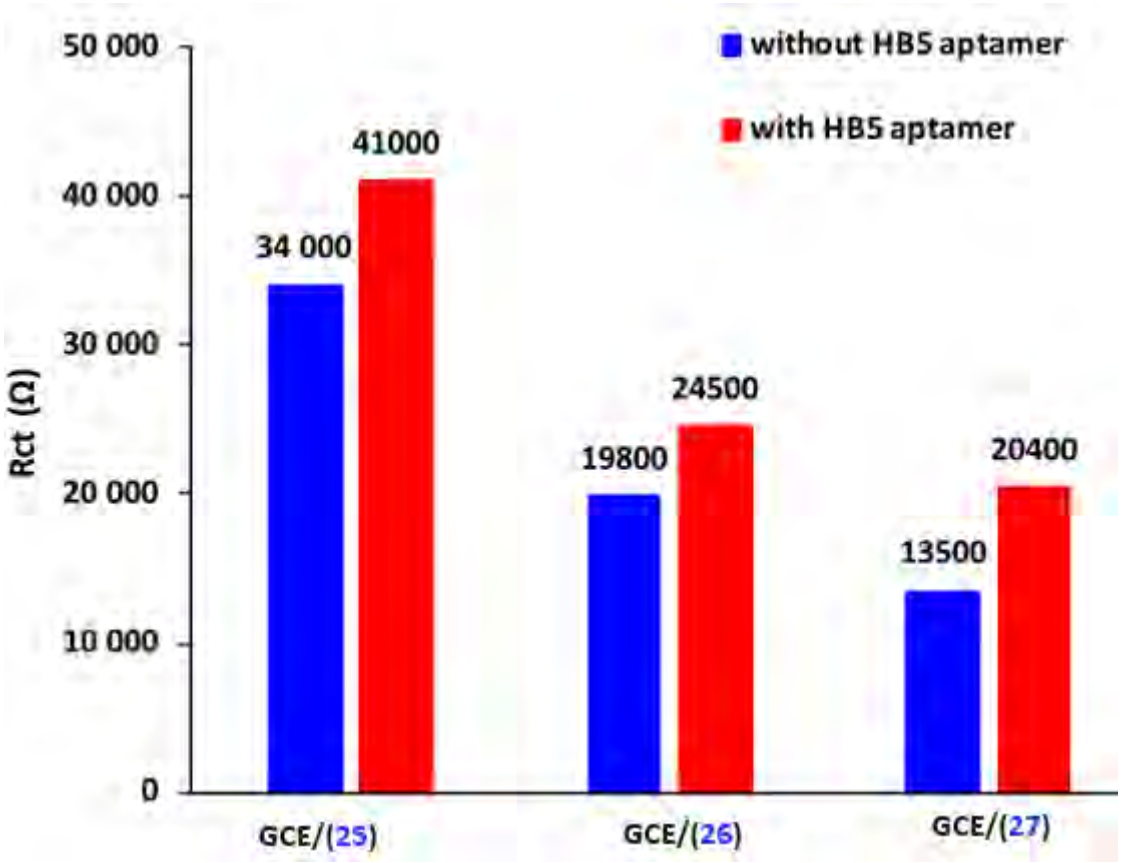

Figure 4.9. EIS data obtained for GCE (**25 – 27**), **A**: Nyquist plots for GCE/SNGQDs@CeO_2NPs (**25**), (b) GCE/**6** (**26**) and (c) GCE/SNGQDs@CeO_2NPs/**6** (seq.) (**27**), insert = BGCE. **B**: A graph showing the change in the R_{ct} values of each substrate (GCE **25-27**), before and after immobilization of the HB5 aptamer.

4.2.3. Scanning Electron Microscopy (SEM)

The SEM analysis of the modified surfaces (i) GCE/ (**25**), (ii) GCE/ (**26**) and (iii) GCE/ (**27**) was performed, the obtained results are shown in **Figure 4.10**. A dispersed distribution of the SNGQDs@CeO_2NPs is observed for GCE/ (**25**). Complex **6** based GCE/ (**26**) shows a grey surface, with little to no visibility of particles; this is due to the small MPc size ~ 1 nm. When the SNGQDs@AuNPs and complex **6** were added to the GCE (SNGQDs@AuNPs first), to form GCE/ (**27**) a uniform grey layer was formed on the electrode. The GCE surface for GCE/ (**27**) is well covered with no bare spots.

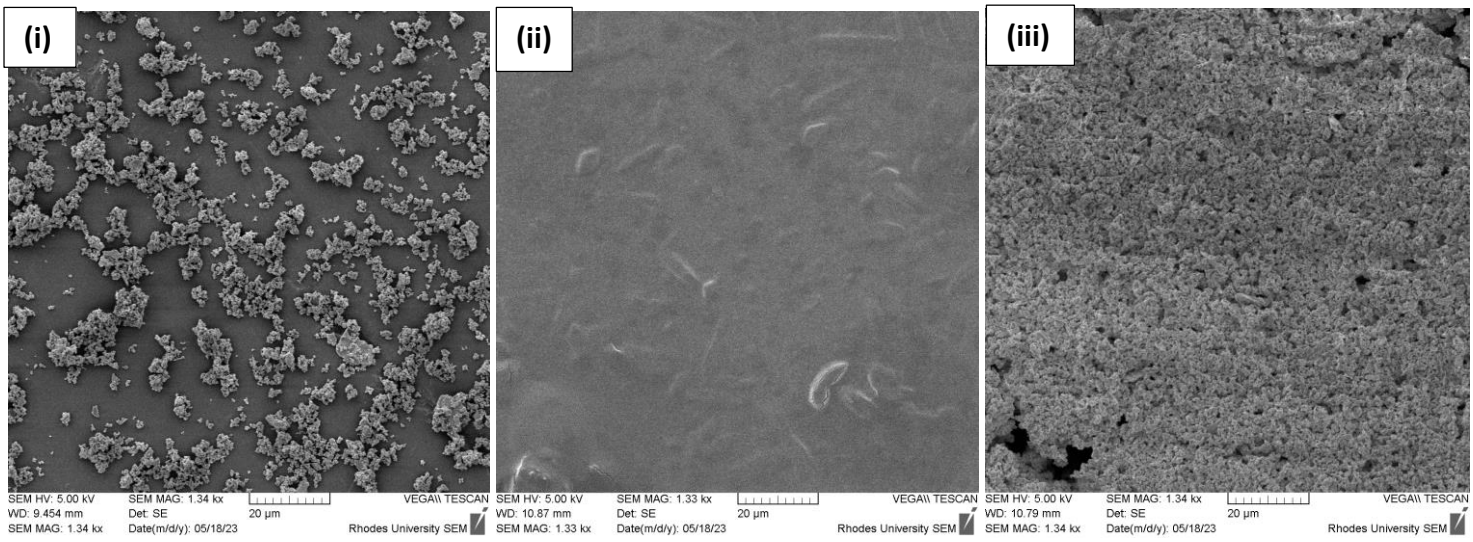

Figure 4.10. SEM images of (i) GCE/SNGQDs@CeO_2NPs (**25**), (ii) GCE/**6** (**26**) and (iii) GCE/SNGQDs@CeO_2NPs/**6** (seq.) (**27**).

Table 4.3. Electrochemical parameters of the modified electrodes.

Modified Electrode*	Electrode Number	ΔEp (mV)	Rct (Ω)[a]	Γ, mol cm^{-2}
GCE/SNGQDs	**3**	73	1580 (1700)	No peak
GCE/**2**	**12**	70	1270 (4393)	1.28×10^{-14}
GCE/**3**	**13**	71	1520 (4083)	1.11×10^{-14}
GCE/CeO_2NPs_{COOH}	**14**	122	1750 (2173)	4.49×10^{-9}
GCE/CeO_2NPs_{COOH}/**2** (seq.)	**15**	90	1600 (9640)	5.88×10^{-11}
GCE/CeO_2NPs_{COOH} /**3** (seq.)	**16**	70	827 (8305)	2.65×10^{-10}
GCE/SNGQDs/**3** (seq.)	**17**	105	1700 (2200)	9.76×10^{-10}
GCE/**3**(π)SNGQDs	**18**	80	1600 (2630)	1.49×10^{-13}
GCE/AuNPs	**19**	100	1680 (8700)	1.82×10^{-7}
GCE/AuNPs/**3** (seq.)	**20**	480	3900 (4080)	3.99×10^{-9}
GCE/SNGQDs@CeO_2NPs	**25**	201	34 000 (41000)	2.45×10^{-8}
GCE/**6**	**26**	120	19800 (24500)	5.94×10^{-10}
GCE/SNGQDs@CeO_2NPs/**6**(seq.)	**27**	110	13500 (20400)	2.89×10^{-9}

Values in brackets represents R_{ct} values of the corresponding probes with aptamer (concentration 1 μM) prior HER2 detection.

4.3. Imine bond formation with HB5 aptamer, Scheme 4.3

The two complexes **4** and **5**, structurally related and differentiated by their symmetry were used for electrode modification, and their electron transfer properties were compared. Both complexes were then used as immobilization platforms for the HB5 aptamer. Two techniques were employed (i) DCC/NHS coupling and/or (ii) acid catalysed imine bond formation, depending on the functional groups present on each CoPc complex, **Scheme 4.3A**. The Pc complexes were also combined with SNGQDs to form conjugates: **4**(π)SNGQDs and **5**(π)SNGQDs, which were also used for electrode modification, **Scheme 4.3B**.

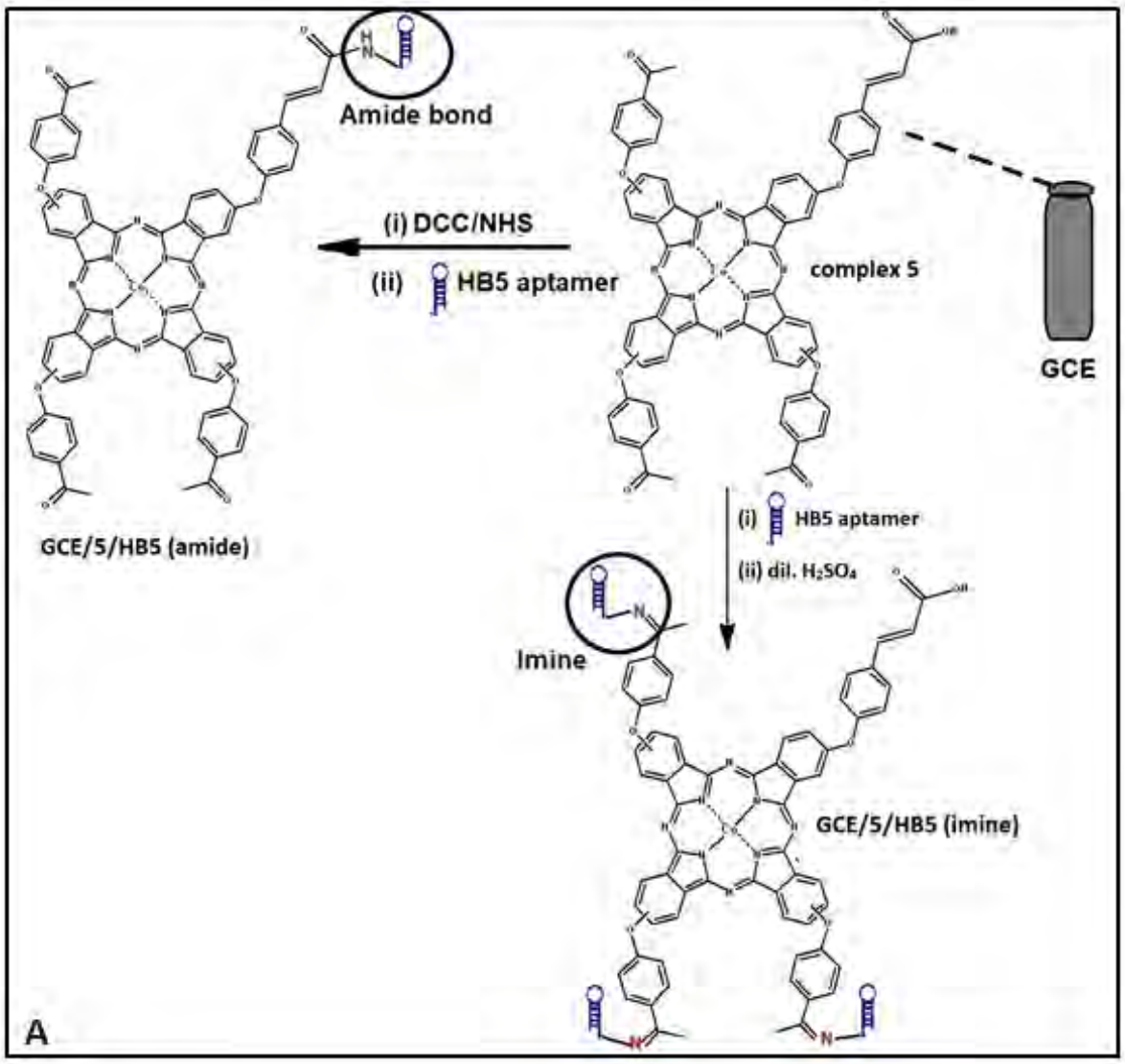

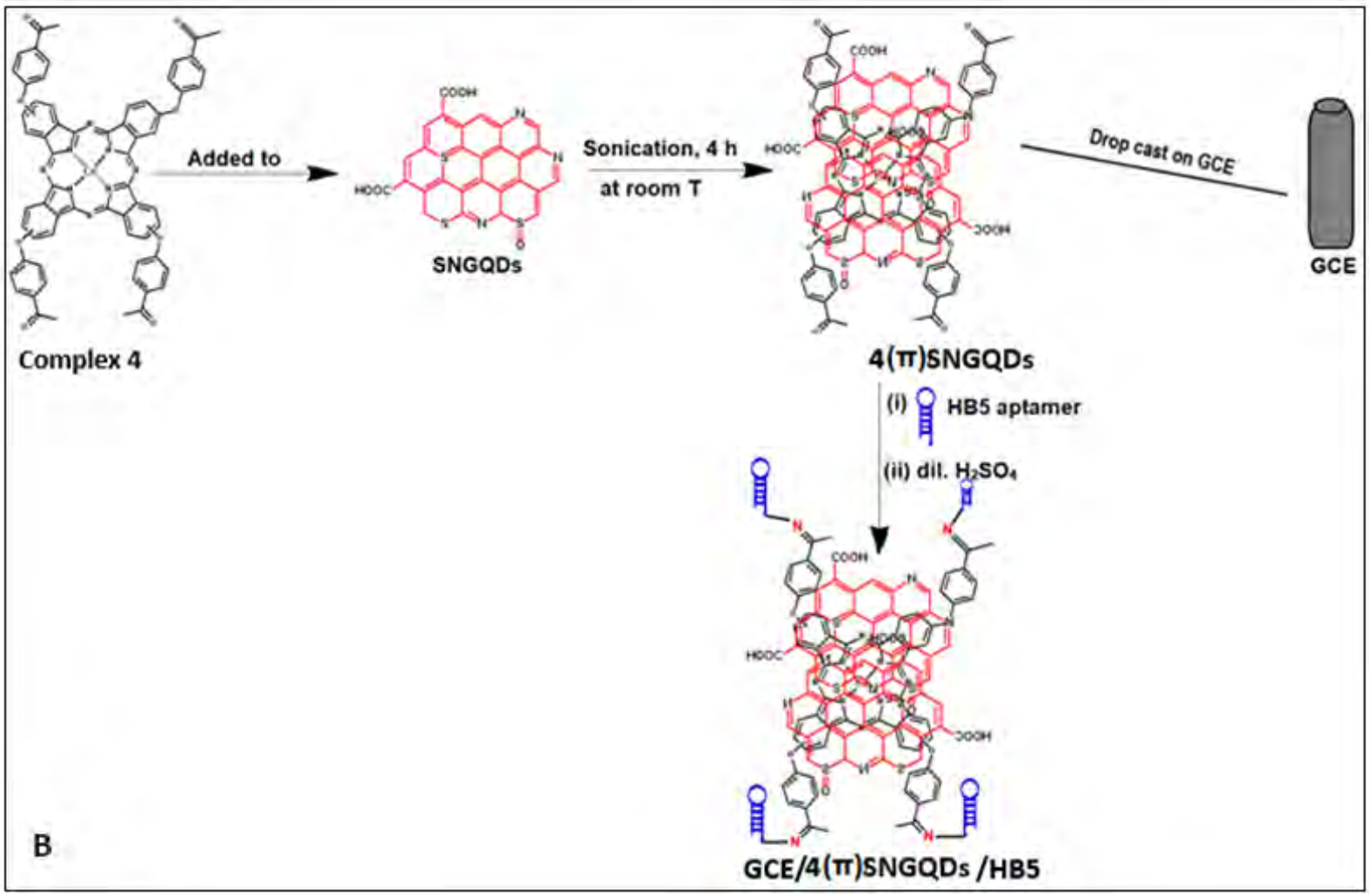

Scheme 4.3. Electrode modification strategies towards complex **4** and **5** based electrodes. **A**: complex **5** based (i) DCC/NHS coupling and/or (ii) acid catalysed imine bond formation, depending on the present functional groups on each CoPc complex. **B**: steps towards the formation of the π-π stacked conjugates, using **4**(π)SNGQDs as an example. Dil. = dilute.

4.3.1. Cyclic Voltammetry

Figure 4.11A. shows the obtained CV diagrams obtained for the modified electrodes listed in **Table 4.4.** The electron transfer properties of the various surfaces were investigated by comparing the ΔEp values (anodic to cathodic peak potential separation). The ΔE_p values for the designed sensors were 73 mV, 710 mV, 882 mV, 1180 mV and 1307 mV for the GCE/SNGQDs (**3**) (**Table 4.2**), GCE/**4**(π)SNGQDs (**22**), GCE/**4** (**21**), GCE/**5**(π)SNGQDs (**24**) and GCE/**5** (**23**), respectively. The varying ΔE_p obtained for the CoPcs in particular, can be attributed to the different substituents, symmetry and in turn their ability to mediate electron transfer on the GCE, **Table 4.4**. The symmetric complex **4** based GCE/ (**21**) and GCE/ (**22**) had lower ΔE_p values compared to their asymmetric complex **5** based GCE/ (**23**) and GCE/ (**24**), counterparts. The conjugate-based electrode showed better electron transfer properties compared to both the respective Pc based electrodes. This speaks to the SNGQDs, as highly π-conjugated nanomaterials and electrocatalysts on their own, and their ability to improve the electron transfer of the Pcs in the conjugate. There were no peaks observed in the presence of HB5 on all surfaces.

4.3.2. Electrochemical Impedance Spectroscopy

EIS measurements were carried out for all modified electrodes. The Nyquist plots obtained are shown and labelled accordingly in **Figure 4.11B**, with the obtained R_{ct} values obtained listed in **Table 4.4**. The obtained data for the EIS data were in agreement with that obtained in cyclic voltammetry for the modified electrodes: the modified surface with the lowest ΔE_p had the lowest R_{ct} values, **Table 4.4**. Furthermore, R_{ct} values increased in the presence of HB5 on all modified surfaces.

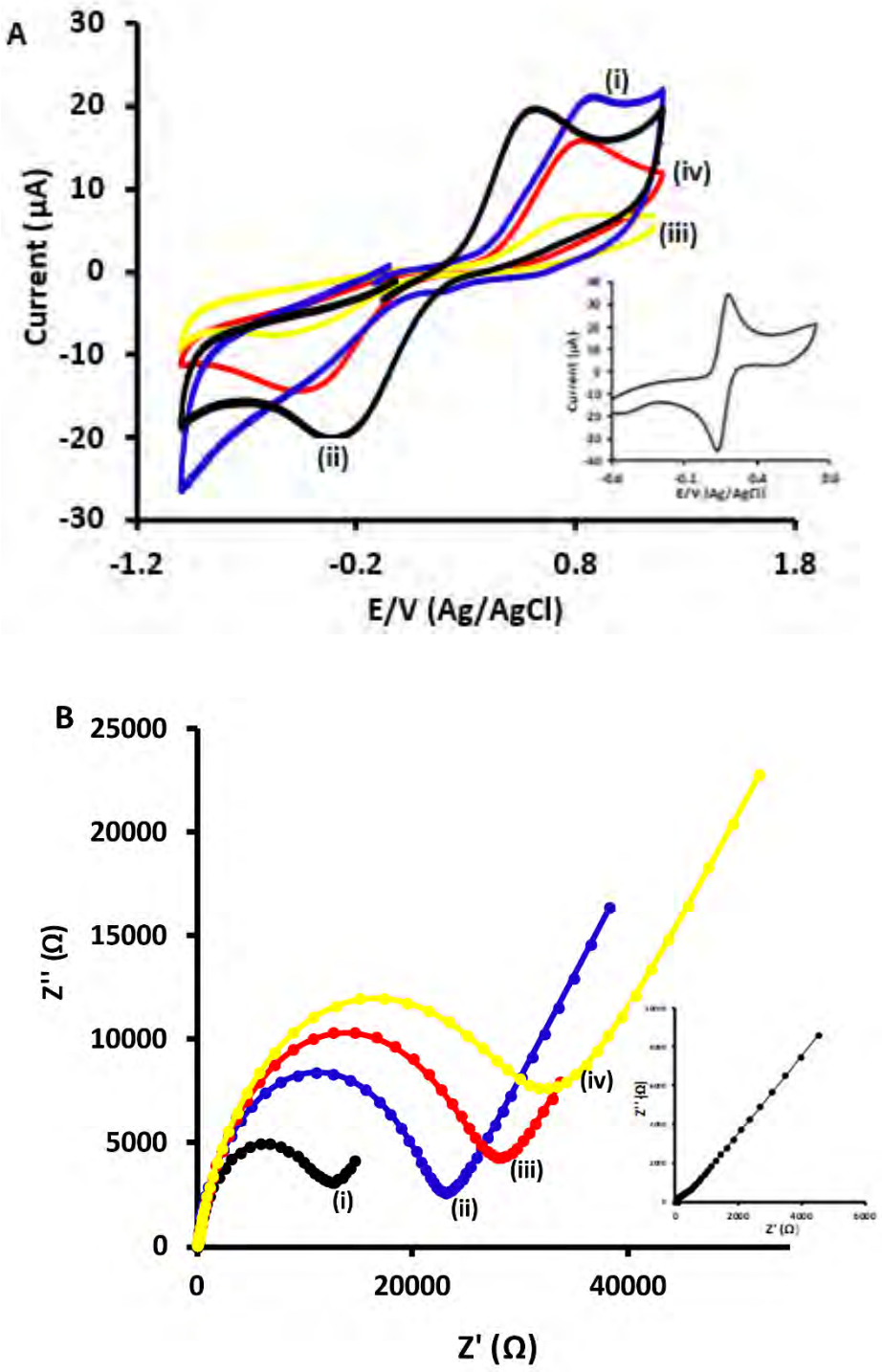

Figure 4.11. (**A**) CV at the scan rate of 100 mV/s and (**B**) EIS Nyquist plots for the probes: (i) GCE/**4** (**21**), (ii) GCE/**4**(π)SNGQDs (**22**), (iii) GCE/**5** (**23**) and (iv) GCE/**5**(π)SNGQDs (**24**) and All experiments were conducted in $K_3[Fe(CN)_6]^{3-/4-}$ (1 mM in 0.1 mol·L^{-1} KCl in 10 mM PBS (pH 7.4). Inserts = (**A**) CV and (**B**) EIS (bottom insert) for BGCE.

Table 4.4. Peak potential separations and R_{ct} values in $K_3[Fe(CN)_6]^{3-/4-}$ of the relevant electrodes.

Modified Electrodes	Electrode Numbers	ΔEp (mV)	Rct (Ω)
GCE/SNGQDs	**3**	73	1580
GCE/SNGQDs/HB5	GCE/(**3**)/HB5	-	1700
GCE/**4**	**21**	882	30300
GCE/**4**/HB5	GCE/ (**21**)/HB5	-	32100
GCE/**4**(π)SNGQDs	**22**	710	11400
GCE/**4**(π)SNGQDs/HB5	GCE/ (**22**)/HB5	-	12000
GCE/**5**	**23**	1307	26400
GCE/**5**/HB5 (imine)	GCE/ (**23**)/HB5	-	28000
GCE/**5**(π)SNGQDs	**24**	1180	34500
GCE/**5**(π)SNGQDs/HB5 (imine)	GCE/ (**24**)/HB5	-	36200

4.4. Cobalt binuclear framework (CoP-BNF) based electrodes: Table 4.5

This thesis investigates the use of a CoP-BNF in the presence of SNGQDs@AuNPs for electrode modification, towards the development of both an aptasensor (HB5 aptamer-based sensor) and immunosensor (Trastuzumab antibody-based sensor) towards the detection of HER2, **Scheme 4.4**.

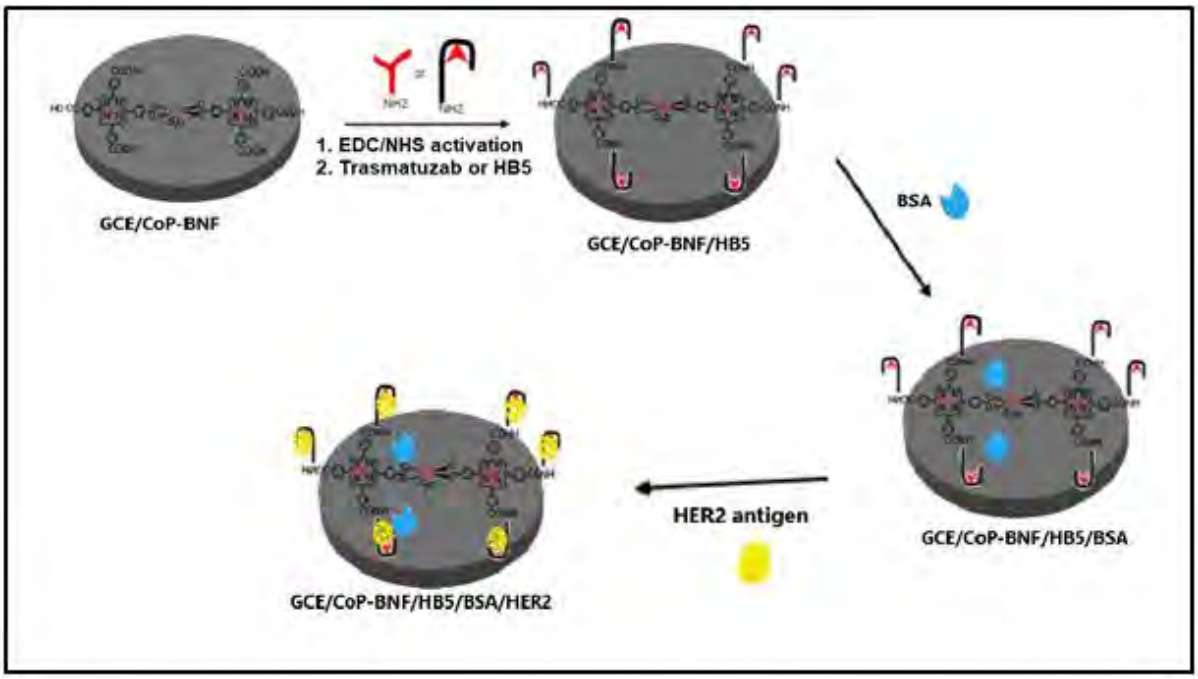

Scheme 4.4. Steps towards the fabrication of the sensing platforms on the GCE, using GCE/COP-BNF (**29**) as an example.

4.4.1. CV and EIS

Figure 4.12A and **B** shows the CVs and EIS, respectively, of different modified electrodes without the biorecognition elements (HB5 or Trastuzumab) in 1 mM $K_3[Fe(CN)_6]^{3-/4-}$ (in 0.1 M KCl). The bare GCE had an anodic to cathodic peak separation (ΔE_p) = 68 mV, which is closer to the theoretical Nernst value, **Table 4.5**. Higher ΔE_p were obtained upon modification: GCE/SNGQDs@AuNPs (**28**) (386 mV), GCE/CoP-BNF (**29**) (555 mV) and GCE/SNGQDs@AuNPs/CoP-BNF (seq.) (**30**) (437 mV). This might be due to passivation of the electrode by the nanomaterials used which might undergo aggregation on the electrode surface. The CVs shows the ferricyanide peaks near 0.35 V - 0.40 V. The peaks near 0.6 are due CoP based processes and occur only for CoP-BNF containing electrodes [**197**]. The additional peaks present in the CV of the GCE/SNGQDs@AuNPs surface, might be as a result of the oxidation of gold on the surface of the SNGQDs@AuNPs. There were no peaks due to $K_3[Fe(CN)_6]^{3-/4-}$ in the presence of HB5 or Trastuzumab, hence data not shown.

The EIS response for the three modified electrodes is shown using Nyquist plots obtained, labelled accordingly in **Figure 4.12B**. The obtained data for the EIS data were in agreement with that obtained in cyclic voltammetry for the modified electrodes: the modified surface with the lowest ΔE_p had the lowest R_{ct} values, **Table 4.5**. The surface-binding of non-conductive molecules blocks the electron transfer, causing an increase in R_{ct} values. This held true; R_{ct} values increased in the presence of both HB5 and Trasmatuzab, respectively on all modified surfaces GCE/(**28**-**30**), **Table 4.5**.

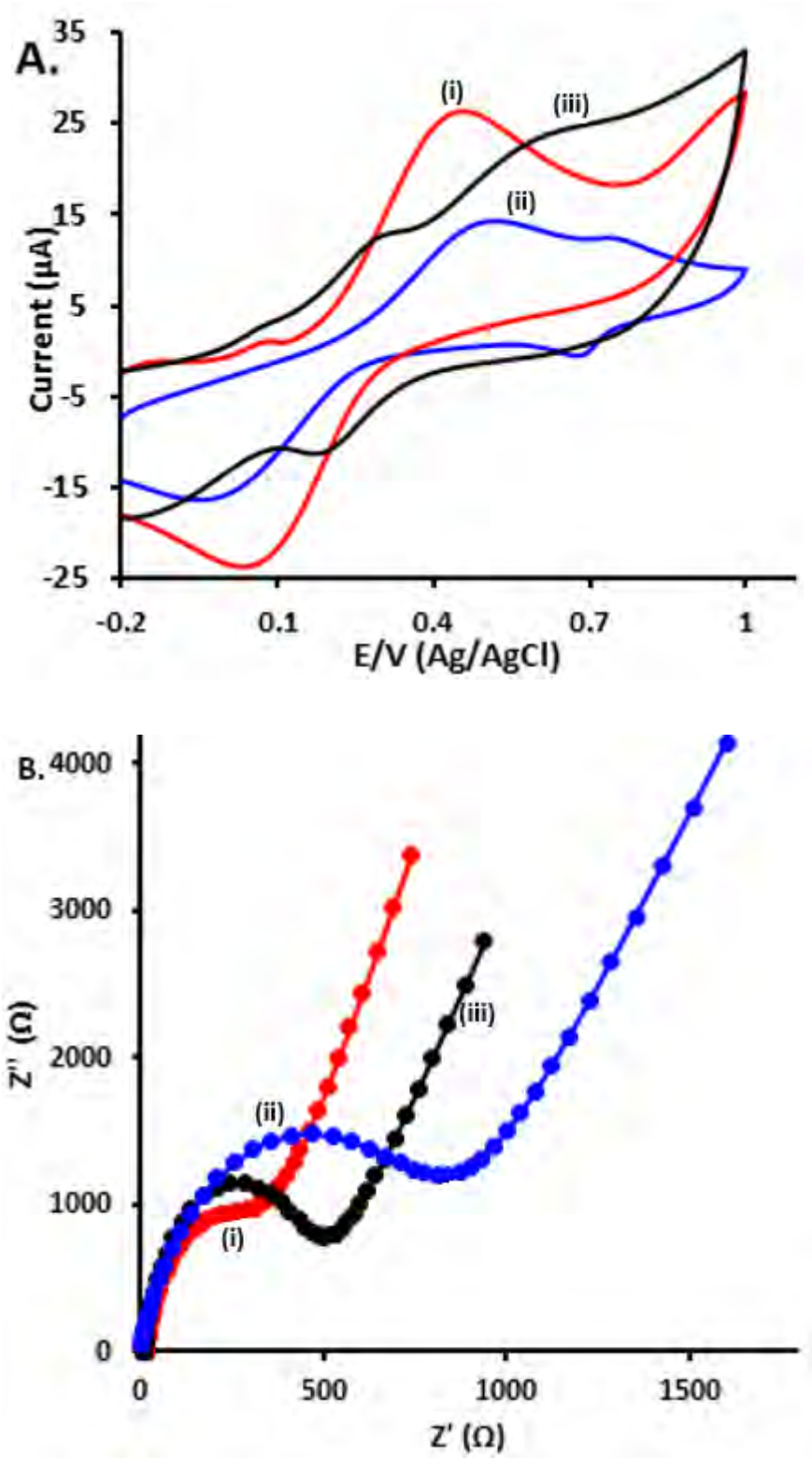

Figure 4.12. Cyclic voltammogram (**A**) and Nyquist plots (**B**) for (i) GCE/SNGQDs@AuNPs (**28**), (ii) GCE/CoP-BNF (**29**) and (iii) GCE/SNGQDs@AuNPs/CoP-BNF (seq.) (**30**). All in 1mM $K_3[Fe(CN)_6]^{3-/4-}$ in 0.1 mol·L^{-1} KCl in 10 mM PBS (pH 7.4).

The aptamer containing electrodes had better electron transfer compared to those with the antibody, except for GCE/SNGQDs@AuNPs, **Table 4.5**, **Figure 4.13**. This is due to the known fact that aptamers are more conductive than the antibodies [203].

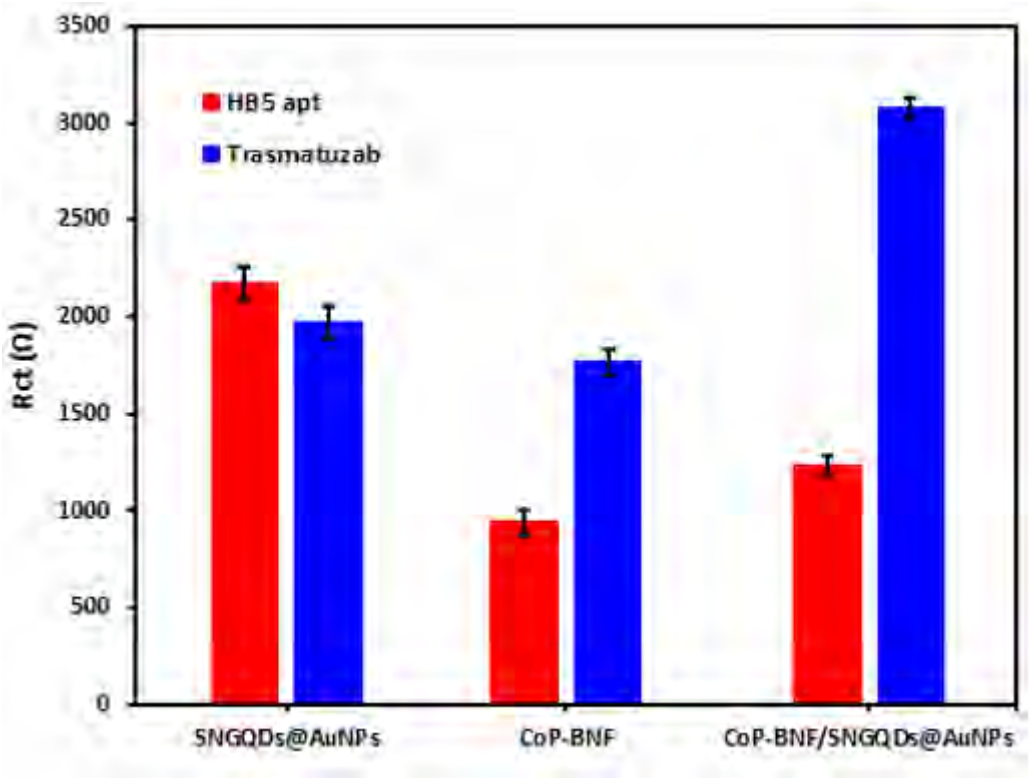

Figure 4.13. Bar graphs showing comparative R_{ct} for GCE/SNGQDs@AuNPs (28), GCE/CoP-BNF (29) and (iii) GCE/SNGQDs@AuNPs/CoP-BNF (seq.) (30). All experiments were run in 1 mM $K_3[Fe(CN)_6]^{3-/4-}$ in 0.1 mol·L^{-1} KCl in 10 mM PBS (pH 7.4).

4.4.2. Scanning Electron Microscopy (SEM)

The SEM analysis of the bare and modified glassy carbon plate (GCP) of the various steps towards immunosensor fabrication was performed, **Figure 4.14**. A typical bare glassy carbon plate surface is shown in **Fig. 4.14(i)**; a clean grey surface is observed. The surface for GCP/CoP-BNF show coating of the carbon plate with white crystalline material which might be attributed to the CoP-BNF, **Fig. 4.14(ii)**. The GCP/SNGQDs@AuNPs/CoP-BNF (seq.) surface is shown in **Fig. 4.14(iii)**; this surface is formed from the addition of the SNGQDs@AuNPs onto the GCP/CoP-BNF. A blanket of grey particles was formed on top of the previously formed white CoP-BNF particles.

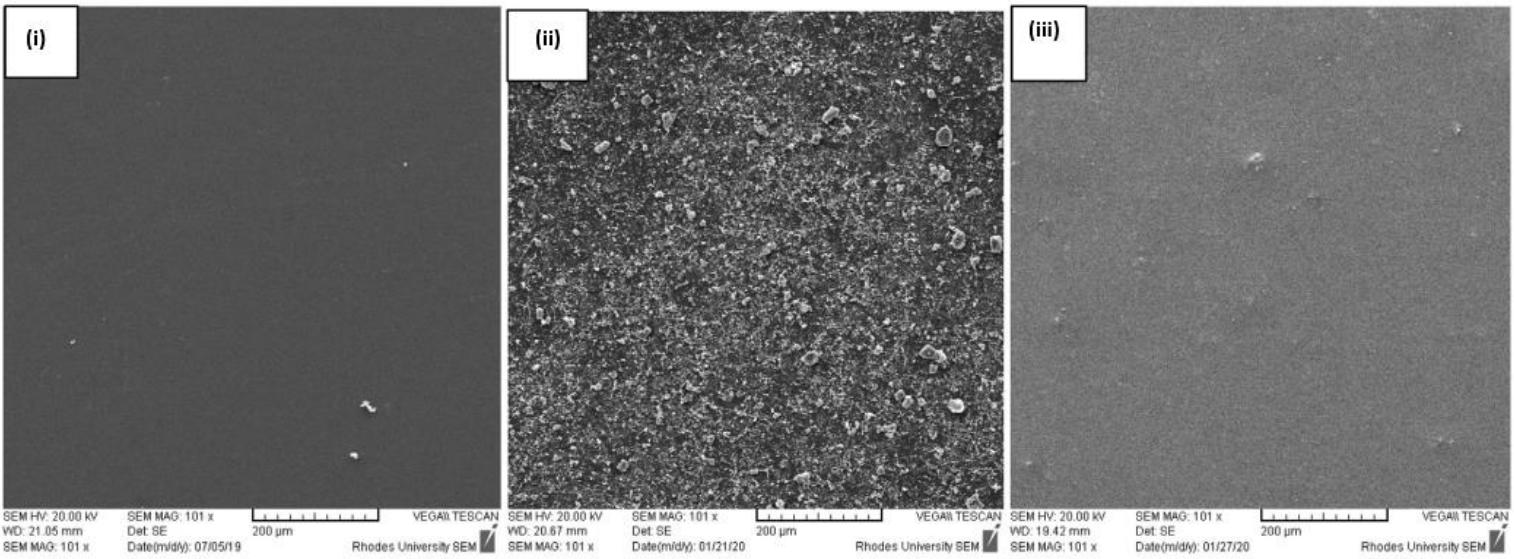

Figure 4.14. SEM images of the modified electrode surfaces: BGCE (i), GCE/CoP-BNF (**29**) (ii) and GCE/SNGQDs@AuNPs/CoP-BNF (seq.) (**30**) (iii).

Table 4.5. Data obtained for the relevant probes in 1 mM $K_3[Fe(CN)_6]^{3-/4-}$ in 0.1 mol·L^{-1} KCl in 10 mM PBS (pH 7.4).

PROBES	Electrode Number	ΔEp (mV)	R_{ct} (Ω)
GCE	-	68	95
GCE/SNGQDs@AuNPs	**28**	386	381
GCE/SNGQDs@AuNPs/HB5	(**28**)/HB5	-	2170
GCE/SNGQDs@AuNPs/Trastuzumab	(**28**)/Trastuzumab	-	1923
GCE/CoP-BNF	**29**	555	838
GCE/CoP-BNF/HB5	(**29**)/HB5	-	943
GCE/CoP-BNF/Trasmatuzab	(**29**)/Trastuzumab	-	1770
GCE/SNGQDs@AuNPs/CoP-BNF (seq.)	**30**	437	808
GCE/SNGQDs@AuNPs/CoP-BNF (seq.)/HB5	(**30**)/HB5	-	1230
GCE/SNGQDs@AuNPs/CoP-BNF (seq.)/Trastuzumab	(**30**)/Trastuzumab	-	3080

4.5. Biosensor Fabrication: Immobilization of biorecognition elements

The modified electrodes (**2**-**30**) were used as immobilization platforms for the immobilization of biorecognition elements for the selective detection of the HER2 analyte. The HB5 aptamer was immobilized on all surfaces GCE/ (**2**)–(**30**), while Trasmatuzab antibody was used only for the CoP-BNF electrodes {GCE (**28**)–(**30**)}.

The adsorption of the aptamer or Trasmatuzab antibody on all the electrodes resulted in an increase in the R_{ct} values. This newly formed layer acted as a mass-transfer blocking barrier, thereby further insulating the conductive support and hindering the access of redox probe toward the electrode surface.

4.5.1. Optimization of HB5 aptamer amounts on GCE modified surfaces.

4.5.1.1. Complex 1, PPy based modified GCE surfaces

There were six different aptamer concentrations explored: 0.1 µM, 0.25 µM, 0.5 µM, 0.75 µM, 1.0 µM and 1.25 µM using GCE/PPy@SNGQDs. An increase in R_{ct} with an increase in aptamer concentration was observed, **Figure 4.15**. This trend was observed until at concentration 1.0 µM, and it did not increase significantly 1.25 µM. Therefore, 1.0 µM was regarded as the optimum aptamer concentration. Important to note, prior to use the aptamer was denatured following the manufacturers protocol.

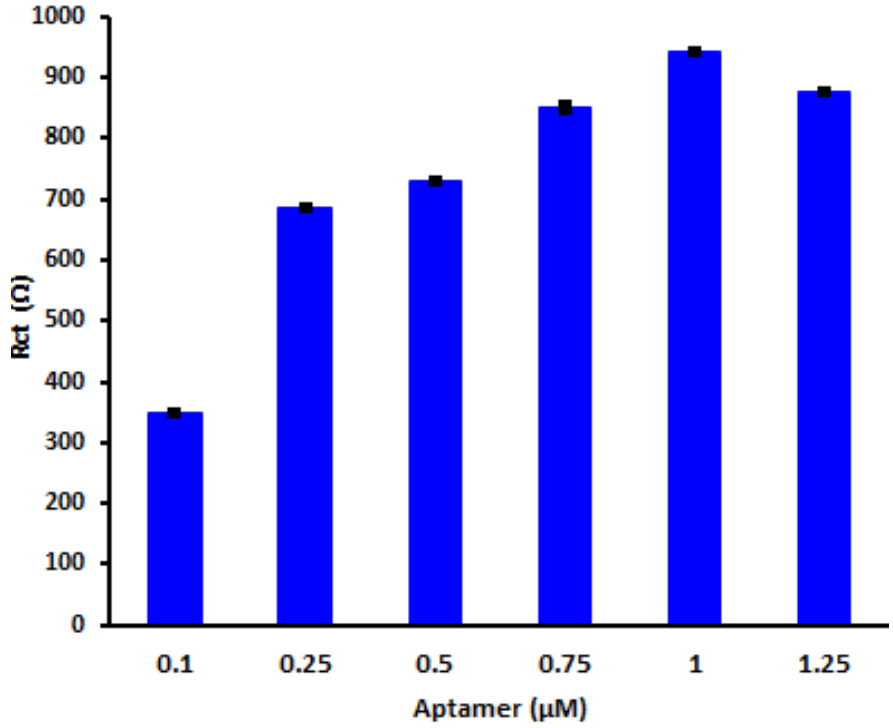

Figure 4.15. Aptamer optimization done on the surface GCE/PPy@SNGQDs. All in $K_3[Fe(CN)_6]^{3-/4-}$ (1 mM in 0.1 mol·L^{-1} KCl in 10 mM PBS (pH 7.4).

4.5.1.2. CoPc (complex 2-6) based electrodes

In the optimization of the HB5 aptamer concentration, five different concentrations 0.25 µM, 0.5 µM, 0.75 µM, 1.0 µM and 1.25 µM were prepared in PBS at pH = 7.4, **Figure 4.16**. The complex **3** based surface GCE/**3** (**13**) was used as an example, for HB5 immobilization platform. The GCE/ (**13**) surface was prepared as outlined in **Scheme 4.2**; the electrode was then treated with DCC/NHS for an hour at room temperature. Following which, 10 µL of each of the HB5 prepared concentrations were dropped on the modified electrode respectively. The R_{ct} values obtained for each concentration were recorded and compared. An increase in R_{ct} with an increase in aptamer concentration was observed, **Figure 4.16**. This trend was observed until at concentration 0.75 µM, where a sudden drop in R_{ct} was observed for 1.0 µM. The small R_{ct} value for the 1.0 µM could be due to an experimental error during loading

of either the complex **3** on the GCE or the HB5 on the GCE/**3** surface. As a result, the chosen optimum HB5 aptamer concentration was 0.75 µM, lower concentrations are good to also minimize costs.

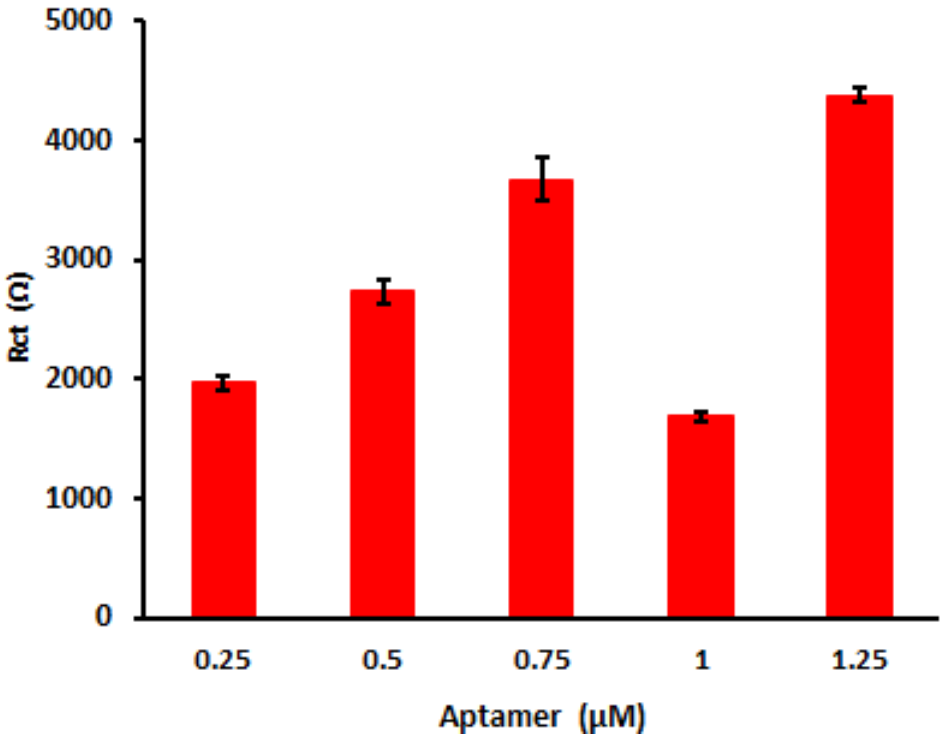

Figure 4.16. Aptamer optimization done on the surface GCE/**3**. All in $K_3[Fe(CN)_6]^{3-/4-}$ (1 mM in 0.1 mol·L^{-1} KCl in 10 mM PBS (pH 7.4).

4.5.2. Optimization of Trastuzumab amounts on GCE modified surfaces.

The Trastuzumab antibody was used only on the CoP-BNF based electrodes GCE/ (28) – (30). **Scheme 4.5** shows the construction of a particular sensor on the surface GCE/SNGQDs@AuNPs/CoP-BNF (seq.) (30) modified surface.

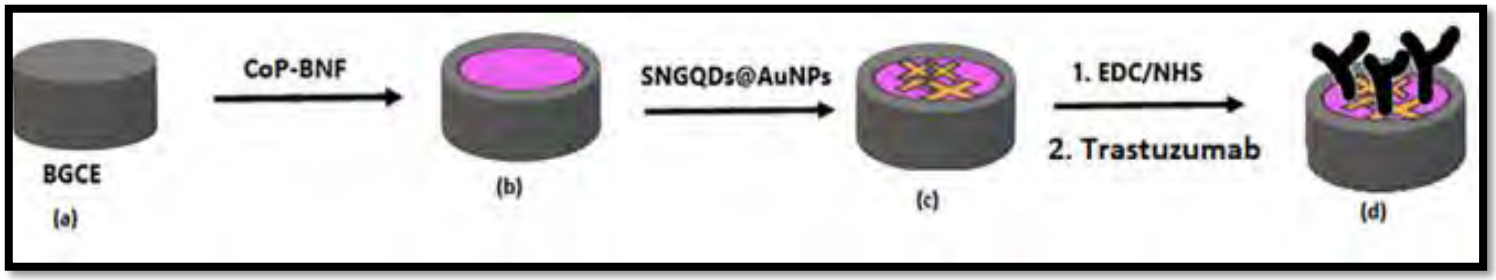

Scheme 4.5. Schematic representation of the antibody immobilization on a GCE surface: showing modification of the GCE (a) with CoP-BNF (b) followed by SNGQDs@AuNPs, (c) EDC/NHS coupling based activation of the carboxylic groups in both CoP-BNF and SNGQDs@AuNPs, immobilization of Trastuzumab (d).

To determine the appropriate concentration of Trastuzumab, the surface GCE/SNGQDs@AuNPs/CoP-BNF (seq.) (30) was used as an example. The said surface was incubated with various concentration of Trastuzumab overnight (1, 2, 3 and 4 mg/mL). The EIS response of the various antibody concentrations was recorded. It was observed that the magnitude of the R_{ct} value increased with an increase in Trastuzumab concentration, **Figure 4.17**. To avoid over stacking of the antibody and competition of bonding sites on the electrode surface, the 1 mg/mL was used.

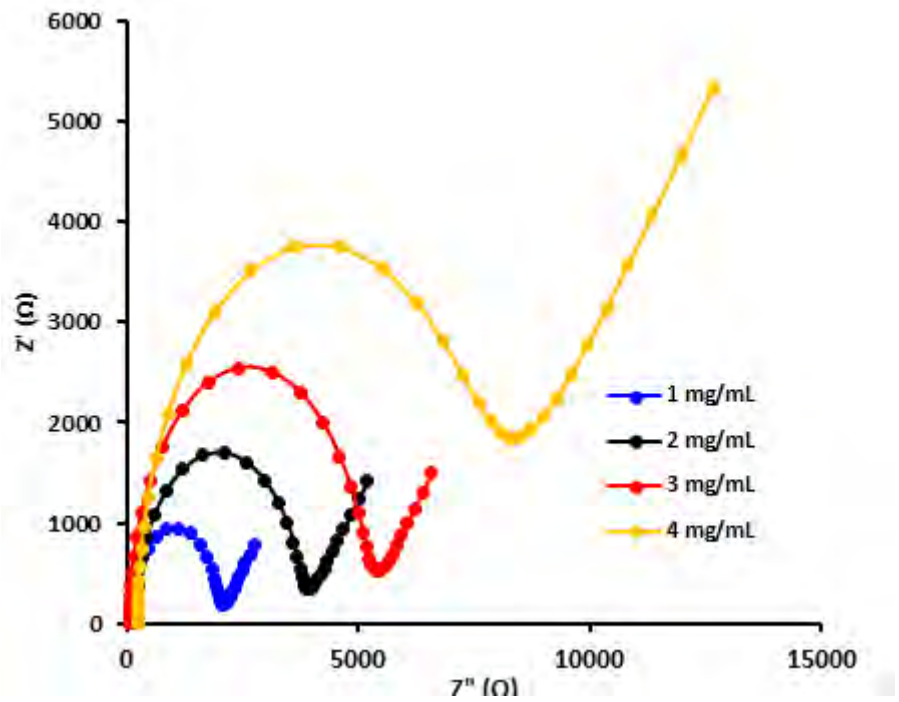

Figure 4.17. Varied Trastuzumab concentrations (1-4 mg/mL). All in 10 mM $K_3[Fe(CN)_6]^{3-/4-}$ in PBS (0.1 M, pH 7.4) on the GCE/SNGQDs@AuNPs/CoP-BNF (seq.) (**30**) surface.

4.5.3. Validation of the coupling methods for successful immobilization HB5 and/or Trasmatuzab

The HB5 aptamer: (**5'–/5 AmMC6/AAC CGC CCA AAT CCC TAA GAG TCT GCA CTT GTC ATT TTG TAT ATG TAT TTG GTT TTT GGC TCT CAC AGA CAC ACT ACA CAC GCA CA-3'),** where AmM= amino functionalized (-NH_2)

All compounds used in this thesis complex **1-6**, the CoP-BNF, SNGQDs, CeO_2NPs, and the relevant Pc/NPs conjugates were all designed to have groups that favour covalent conjugation to both the HB5 aptamer and Trasmatuzab antibody. The HB5-aptamer was immobilized on all modified electrodes, and as such was used to confirm the viability and success of the proposed immobilization techniques. The structural and chemical evolution of the modified glassy carbon plate (GCP) towards the fabrication of the sensors were assessed using X-ray Photoelectron Spectroscopy (XPS).

The XPS high resolution C1s spectrum for GCP/HB5 aptamer showed three peaks 285.1 eV, 287.1 eV and 288.3 eV which were associated with the functional groups C-C, C-N/C-O and C=O respectively, **Figure 4.18A, Table 4.6**. The HB5 aptamer is an oligonucleotide and as such the presence of the above functional groups is expected. The deconvolution of the N1s levels gave two peaks at 398.5 eV and 399.7 eV which can be attributed to which correspond to O=C-N and -NH bonding, thereby confirming the present -NH_2 group present for interaction with the various complexes on or off the electrode, **Figure 4.18B**, **Table 4.6**.

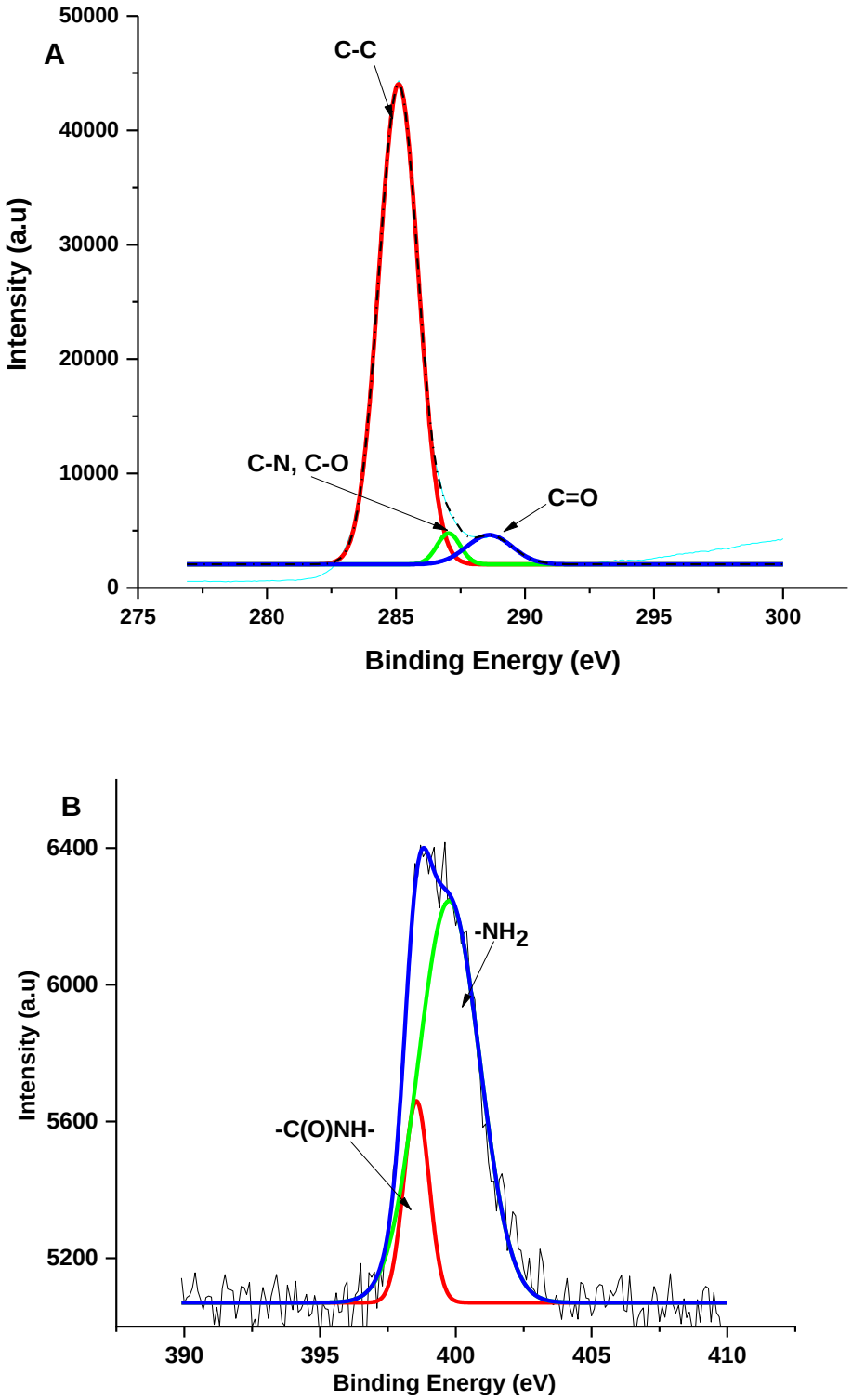

Figure 4.18. XPS data showing the high resolution C1s (**A**) and N1s (**B**) spectra of the modified surface GCP/HB5.

Table 4.6. A summary of binding energy (eV) determined from deconvoluted high resolution XPS spectra.

Electrode[a]	C1s[b]			N1s[b]
GCP/HB5	285.1 (C-C)	287.1 (C-N/C-O)	288.3 (C=O)	398.5 (O=C-N) 399.7 (-NH/amine)
GCP/SNGQDs@AuNPs	283.1 (-C=C) 283.6 (-C-C)	284.9 (-C-O/-C-N)	287.2 (-O=C-O)	398.3 (Pyridinic-N) 398.5 (graphitic) 400.1 (Pyrrolic-N)
GCP/SNGQDs@AuNPs/HB5	283.1 (-C=C/-C-C)	284.1 (-C-O/-C-N)	286.9 (O=C-/O=C-O)	397.8 (Pyridinic-N) 398.6 (graphitic) 399.8 (Pyrrolic-N/ O=C-NH)
GCP/5	284.5 (C-C/C=C)	285.9 (C-O/C-N)	287.9 (C=O-O)	400 (C-N) 401 (C=N)
GCP/5/HB5 (amide)	283.3 (C-C) 284.4 (C=C)	286.5 (C-N/C-O)	287.6 (O=C-N/O=C) 291 (π-π)	398 (C=N) 399.5 (C-N) 400.3 (O=C-NH)
GCP/5/HB5 (imine)	284.5 (C-C/C=C)	286.2 (C=N)	287.1 (C=O)	398.7 (C=N) 399.9 (C-N) 401 (C=N-R)

[a]GCP = glassy carbon plate.

[b]A single value where more than one functional group is mentioned (e.g. –C=C/-C-C) is associated with peak overlap.

4.5.3.1. EDC/NHS coupling for amide bond

4.5.3.1.1. On the electrode based HB5 immobilization: GCP/SNGQDs@AuNPs as an example

The viability of the EDC/NHS coupling technique for the immobilization of the recognition elements was investigated using the GCP/SNGQDs@AuNPs (**28**) as a platform for the immobilization of the HB5 aptamer. The XPD data obtained is for GCP/(**28**) is shown in **Figure 4.19**.

The high resolution C1s spectrum for GCP/SNGQDs@AuNPs showed four peaks at 283.1 eV, 283.6, 284.9 eV and 287.2 eV, which are associated to the functional groups C=C, –C-C, -C-N/C-O and –O-C=O respectively, **Figure 4.19, Table 4.6**. The C1s high resolution XPS spectrum for GCP/SNGQDs@AuNPs/HB5 showed peaks at 283.1 eV (-C=C/-C-C), 284.1 eV (-C-O/-C-N) and 286.9 (O=C-), **Table 4.6**. The HB5 aptamer is an oligonucleotide and as such might on its own have amine and carboxylic groups, see **Figure 4.18**. The deconvolution of N1s levels for the GCP/SNGQDs@AuNPs sample confirmed the presence of the following nitrogen functional groups: pyridinic-N (398.3 eV), O=C-N (398.5 eV) and pyrrolic-N (400.1 eV). The same peaks were observed for the surface GCP/SNGQDs@AuNPs/HB5 with varied intensities, **Figure 4.19**. The three peaks now appeared at the binding energies 397.8 eV, 398.6 eV and 399.8 eV respectively. The peak at 399.9 eV, in the GCP/SNGQDs@AuNPs/HB5 surface is associated with the –O=C-NH (amide nitrogen) functional group, thereby confirming the successful immobilization of the HB5 aptamer on to the modified electrode surface. The high resolution N1s spectrum for the GCP/SNGQDs@AuNPs/HB5 is similar to that of the GCP/SNGQDs@AuNPs sample alone. It is evident that the immobilization of the HB5 aptamer did not alter the structural integrity of the SNGQDs@AuNPs on the GCP plates. The pyrrolic-

N peak had around 3000 counts for the SNGQDs@AuNPs (400.1 eV) alone, this same peak is observed in the GCP/SNGQDs@AuNPs/HB5 sample (399 eV) with an increase in intensity/counts ~3800 symbolic of a new nitrogen atom feature, and hence identified as the desired –O=C-NH (amide nitrogen).

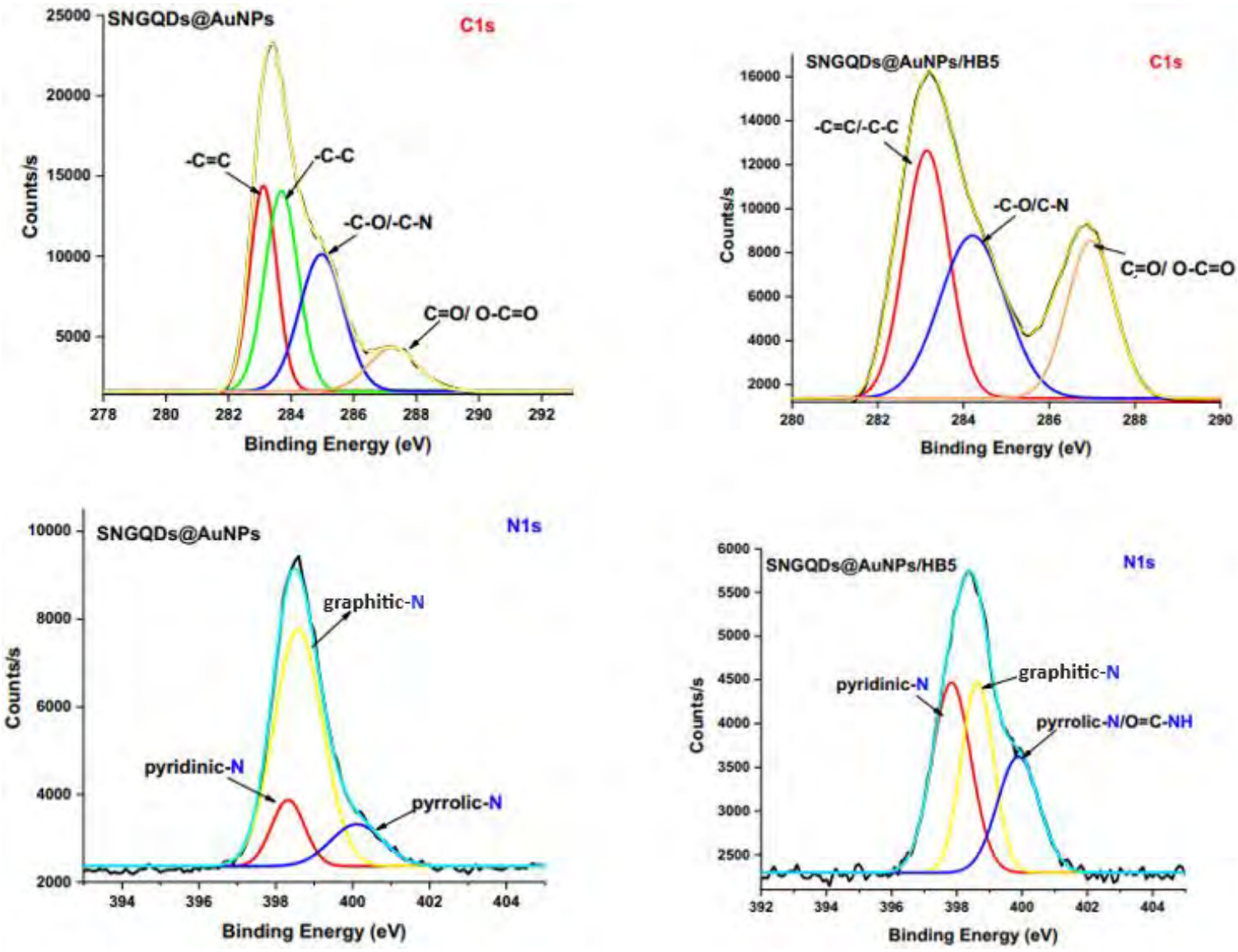

Figure 4.19. XPS data showing the high resolution C1s (top) and N1s (bottom) spectra of the modified surfaces GCP/SNGQDs@AuNPs and GCP/SNGQDs@AuNPs/HB5. Where GCP= glassy carbon plate.

4.5.3.1.2. Free HB5-SNGQDs@CeO_2NPs bioconjugate, (not on the GCE)

The SNGQDs@CeO_2NPs contain graphene quantum dots and as a result have carboxylic acid functionalized edges. The HB5-SNGQDs@CeO_2NPs bioconjugate was formed by amide bond between the NH_2-HB5 aptamer and carboxylated SNGQDs@CeO_2NPs, **Scheme 4.6**.

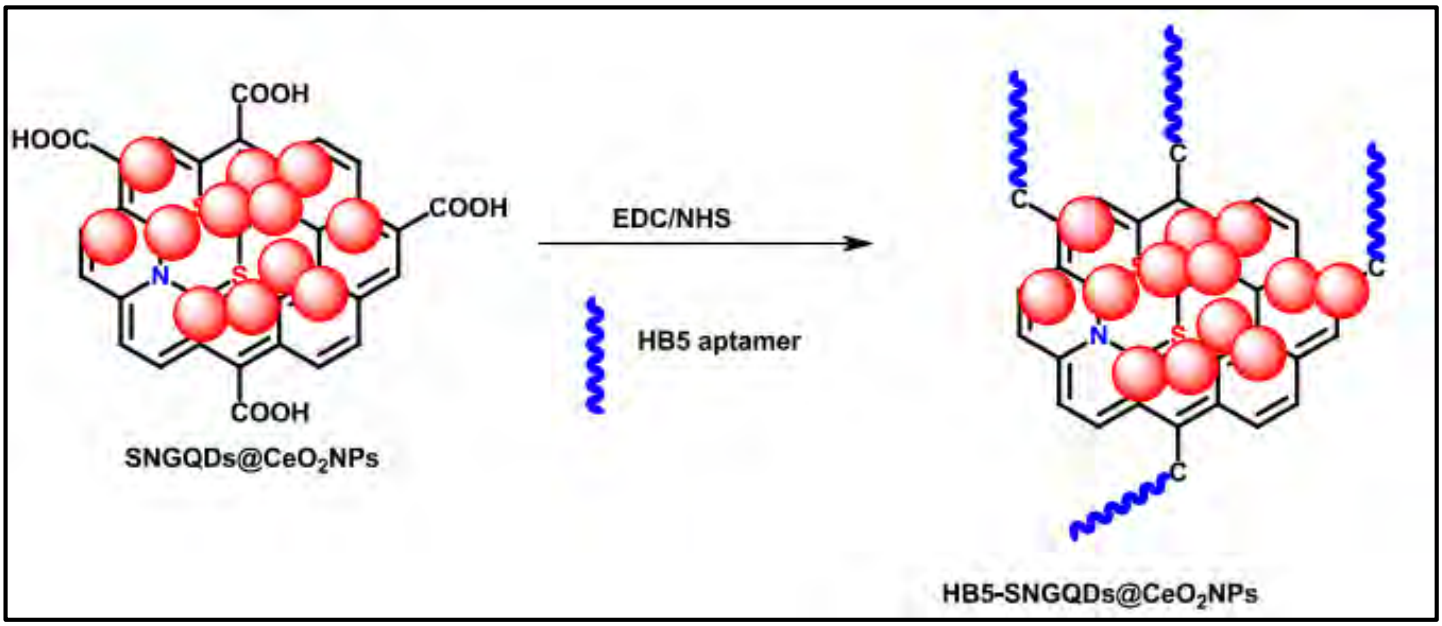

Scheme 4.6. Schematic representation for the formation of the HB5-SNGQDs@CeO_2NPs bioconjugate.

Figure 4.20 shows the FT-IR data of the HB5 aptamer alone (a) HB5 aptamer and the HB5-SNGQDs@CeO_2NPs bioconjugate (b). The HB5-aptamer **Fig. 4.20(a)**, shows various common functional groups C-N, C-O, C = O and most importantly –NH_2 stretch, as demonstrated by the two fangs around the 3409–3221 cm^{-1} region. The functional groups present in the SNGQDs@CeO_2NPs have been discussed in **Chapter 3**. The successful conjugation of the HB5 aptamer to the SNGQDs@CeO_2NPs nanocomposite is confirmed by the IR spectrum obtained for the resulting bioconjugate HB5-SNGQDs@CeO_2NPs, **Fig. 4.20(b)**. The bioconjugate spectrum, had the same functional groups found in both the HB5 aptamer and SNGQDs@CeO_2NPs. The amide bond formation was confirmed by the collapse of the previously observed two fangs indicative of the presence of the –NH_2 in the HB5 aptamer sample, to now a single peak at 3267 cm^{-1} for the HB5-SNGQDs@CeO_2NPs sample implying successful conjugation via amide bond formation.

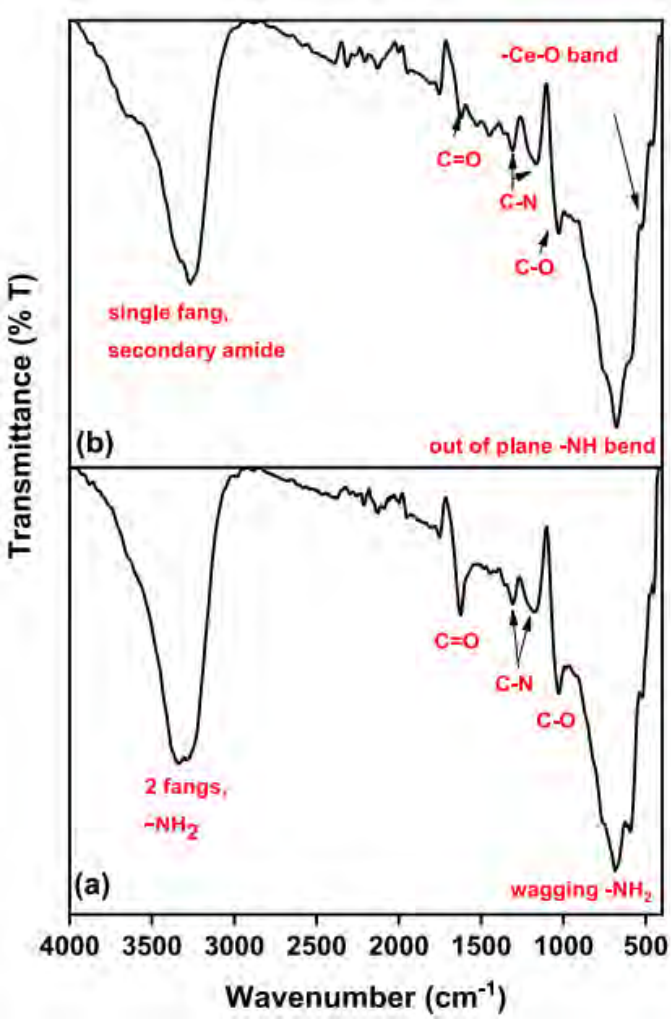

Figure 4.20. FT-IR spectra HB5-aptamer (a) and HB5-SNGQDs@CeO_2NPs bioconjugate (b) both in PBS. Spectra in PBS recorded following background correction for PBS alone.

4.5.3.2. DCC/NHS coupling and acid catalysed imine formation: Complex 1 – 6 based GCE platforms.

The DCC/NHS coupling was appropriate for complexes **1**, **2**, **3**, **5** and **6**, as they are all contained carboxylic groups, through which an amide bond was formed with HB5 aptamer during immobilization. Complex **4** and **5** have ketone groups, to which the HB5 aptamer was linked using acid catalysed imine bond formation, **Scheme 4.3**. Complex **5** contains both a carboxylic acid and acetophenone ligands. Using the complexes **5** based electrodes**:** GCE/**5** (**23**), the viability of the DCC/NHS coupling and acid catalysed imine formation technique for the immobilization of the HB5 aptamer on the CoPc based surfaces was investigated. The structural and chemical evolution of the modified glassy carbon plate (GCP) towards the fabrication of the GCP/**5** based sensors was assessed using X-ray Photoelectron Spectroscopy (XPS).

Figure 4.21 shows the XPS data obtained for the surfaces GCP/**5**, GCP/**5**/HB5 (amide) and GCP/**5**/HB5 (imine), labelled accordingly from left to right. The top row of the figure shows the obtained C1s high resolution spectra for the different surfaces: The C1s high resolution spectra for complex **5** C1s gave peaks 284.5 eV, 285.99 eV and 287.9 eV, corresponding to C=C/C-C, C-O/C-N and C=O(O) functional groups respectively. The sample GCP/**5**/HB5 (amide), has C1s peaks 283.3 eV (C-C), 284.4 eV (C=C), 286.5 eV (C-N, C-O), 287.6 eV (O=C-N, O=C-O) and 291 eV (π-π). The C1s spectra of the GCP/**5**/HB5 (imine) surface had peaks at 284.5 eV (C-C, C=C), 286.2 eV (C=N) and 287.1 eV (O=C) respectively. For both GCP/**5**/HB5 (amide) and GCP/**5**/HB5 (imine) a combination of peaks both from the HB5 aptamer and complex **5** was oberved. Even though the peaks show the same atoms, the difference in bonding and valence of each carbon atom can be seen in the overall shape of C1s spectra,

further confirming the different ways in which the aptamer is bonded onto the complex **5** on the two electrodes. A better differentiating parameter is the N1s high resolution spectra obtained for the differenet surfaces, **Figure 4.21;** bottom row. In the surface GCP/**5** two peaks occuring at 400 eV and 401 eV corresponding to the C-N and C=N from the N-atoms in the ring of the CoPc. The HB5 complex had N1s peaks O=C-N and -NH at 398.5 eV and 399.7 eV, respectively (**Fig. 4.18**). The sample GCP/**5**/HB5 (amide) had N1s had similar peaks at 398 eV (C=N) and 399.5 eV (C-N), accompanied by a new peak at 400.3 eV (O=C-NH, amide). Similarly, GCP/**5**/HB5 (imine) had N1s peaks two peaks 398.7 and 399.9 corresponding to C=N (Pc ring), C-N, with an additional peak at and 401 eV associated with C=N- (new imine bond).

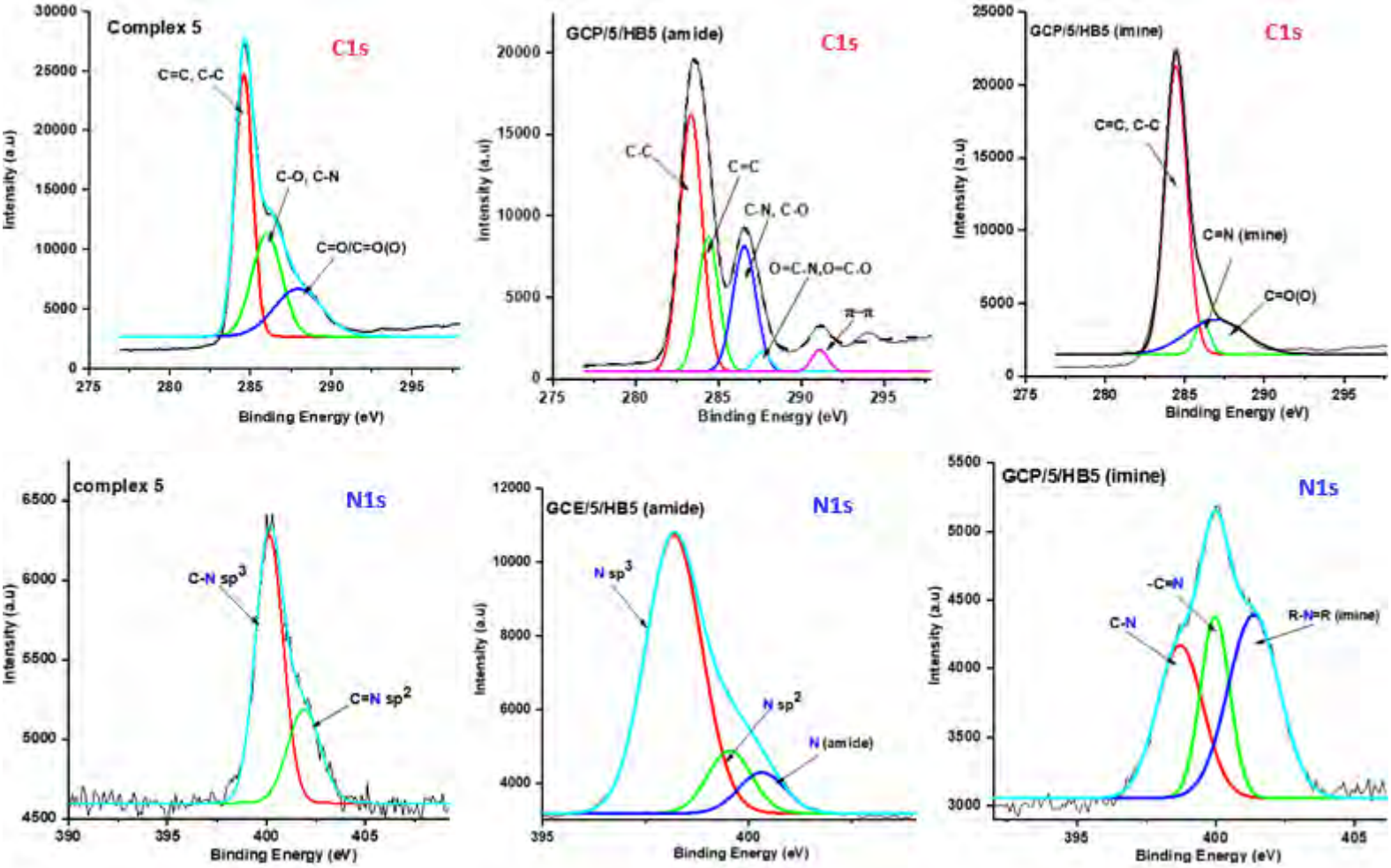

Figure 4.21. XPS data showing the high resolution C1s (top) and N1s (bottom) spectra of the modified surfaces GCP/**5** (**23**), GCP/**5**/HB5 (**23**) (amide) and GCP/**5**/HB5 (**23**) (imine) respectively.

4.6. Conclusion

The successful modification of each electrode was determined by the varying ΔE_p and R_{ct} values obtained from cyclic voltammetry and electrochemical impedance spectroscopy, respectively. The combination of CoPc complexes or CoP-BNF with the relevant nanoparticles showed improved electron transfer properties as demonstrated by the obtained CV and EIS data. The successful immobilization of the HB5 aptamer and Trasmatuzab antibody was demonstrated by a further increase in R_{ct} values, implying passivation due to the adsorption of the non-conductive protein layers which hindered electron transfer and diffusion of ferricyanide towards the electrode surface. Apart from electrochemical characterization, immobilization of the said biorecognition elements was confirmed using XPS (showing HB5 data). The EDC/NHS coupling, DCC/NHS coupling and acid catalysed imine bond formation were confirmed to be ideal methods where necessary for the successful conjugation of HB5 aptamer and Trasmatuzab to the nanomaterials on or off the electrode.

5. HER2 DETECTION

The designed aptamer-based and antibody-based sensors fabricated as outlined in Chapter 4, were then used for the electrochemical detection of HER2. The choice of CoPcs or CoP-BNF, nanoparticles and CoPc/CoP-BNF conjugate, as well as their arrangement on the GCE surface was aimed towards the design and development of novel biosensor surfaces, with enhanced signal and sensitivity for the electrochemical detection of HER2 biomarker. Two strategies were considered namely, (i) signal-based amplification methods and (ii) target-based amplification methods. Strategy I: For the first time, CoPc complexes alone and in combination with different NPs are used for electrode modification for enhanced signal transduction, sensitivity and low limit of detection (LOD). Strategy II, aimed at improving antigen-receptor interactions for enhanced sensitivity, precision and accuracy of the sensor: The use of an aptamer and antibody for a label free biosensing strategy is investigated and compared for the first time. Furthermore, for the first time a single aptamer assay and sandwich aptamer-based assay, using a novel HB5-based bioconjugate are compared.

5.1. HER2 detection in PBS: Sensitivity and LOD determination

5.1.1. Complex 1 in combination with SNGQDs and Polypyrrole: Table 5.1

The modified electrodes: GCE/**1** (**2**) /HB5, GCE/SNGQDs (**3**)/HB5, GCE/ PPy@SNGQDs (**4**)/HB5, GCE/PPy@**1** (**5**)/HB5, GCE/PPy@SNGQDs/**1** (**6**)/HB5, GCE/PPy@**1**/SNGQDs (**7**)/HB5, GCE/PPy/SNGQDs (seq.) (**8**)/HB5, GCE/PPy/**1** (seq.) (**9**)/HB5, GCE/PPy/SNGQDs/**1** (seq.) (**10**)/HB5 and GCE/PPy/**1**/SNGQDs (seq.) (**11**)/HB5 were all tested towards the electrochemical detection of HER2. The various electrodes were all incubated in PBS solution containing varying amounts of HER2 (0 to 10 ng/mL), **Table 5.1**. **Figure 5.1**, shows EIS Nyquist plots for the electrodes GCE/PPy@SNGQDs (**4**)/HB5 (A and B) and GCE/PPy@**1** (**5**)/HB5 (C and D) as examples, obtained in 10 mM PBS buffer of pH 7.4 containing 0.1 M KCl and 1 mM [Fe $(CN)_6]^{3-/4-}$. Immobilization of the aptamer alone on the nanomaterials modified GCE hinders the access of the redox probe to the electrode surface hence the higher R_{ct}, **Table 4.2**. After interaction of HER2 with aptamer-modified electrode, R_{ct} increases again because of more hindering of access of the redox couple to the electrode surface resulting in low electron transfer efficiency. This remained true for all electrode surfaces. An increase in the R_{ct} with an increase in the HER2 concentration for all electrodes was observed, **Table 5.1**.

Regression plots were then created using the data of each electrode, the equations of the regression plots were as follows (eq. **5.1 – 5.10**):

GCE/**1** (**2**)/HB5: $y = 1036x + 476,\ R^2 = 0.9604$ **(5.1)**

GCE/SNGQDs (**3**)/HB5: $y = 9650x\ - 5117,\ R^2 = 0.9233$ **(5.2)**

GCE/PPy@SNGQDs (**4**)/HB5: $y = 11457x - 2704, R^2 = 0.9699$ **(5.3)**

GCE/PPy@**1** (**5**)/HB5: $y = 4284x - 640, R^2 = 0.9786$ **(5.4)**

GCE/PPy@SNGQDs/**1** (**6**)/HB5: $y = 71584x - 26134, R^2 = 0.9833$ **(5.5)**

GCE/PPy@**1**/SNGQDs (**7**)/HB5: $y = 32086x - 14257, R^2 = 0.9577$ **(5.6)**

GCE/PPy/SNGQDs (seq.) (**8**)/HB5: $y = 53006x - 33394, R^2 = 0.9678$ **(5.7)**

GCE/PPy/**1** (seq.) (**9**)/HB5: $y = 28741x - 6249,\ R^2 = 0.9794$ **(5.8)**

GCE/PPy/SNQGDs/**1** (seq.) (**10**)/HB5: $y = 17912x - 10918, R^2 = 0.9836$ **(5.9)**

GCE/PPy/**1**/SNGQDs (seq.) (**11**)/HB5: $y = 15498x - 63\ , R^2 = 0.9895$ **(5.10)**

There are certain static and dynamic attributes that every biosensor possesses, from which the biosensor performance is reflected; sensitivity is one of them. The sensitivity of a biosensor is defined as the relationship between the change in analyte concentration and the intensity of the signal generated from the transducer [**204**]. Typically, a biosensor is required to detect analyte concentration of as low as ng/ml or even fg/ml to confirm the presence of traces of analytes in a sample. The slope, (m) of the regression plots (**eq. 5.1 – 5.10**) represents the sensitivity of each aptasensor towards HER2, **Table 5.2**. To provide a clear discussion for the sensors designed, the electrodes where pyrrole was polymerized in the presence of either complex **1** or SNGQDs, and those where pyrrole was polymerized alone followed by sequential addition of either complex **1** or SNGQDs were compared as follows: GCE/PPy@**1** (**5**)/HB5 vs. GCE/PPy/**1** (seq.) (**9**)/HB5, GCE/PPy@SNGQDs (**4**)/HB5 vs. GCE/PPy/SNGQDs(seq.) (**8**)/HB5, GCE/PPy@**1**/SNGQDs (**7**)/HB5 vs. GCE/PPy/**1**/SNGQDs (seq.) (**11**)/HB5 for detection of HER2.

The highest sensitivity value was obtained for the GCE/PPy@SNGQDs/**1** (**6**)/HB5 (71584 Ωng^{-1} mL) which is the probe formed by polymerizing pyrrole in the presence of SNGQDs followed by adsorption of complex **1**. The sensitivity of a biosensor depends on various factors, and particularly for this work, the role of surface functionalization was investigated. The different modification techniques play an important role on how the HB5 aptamer is immobilized on the electrode surface and in turn its interaction with HER2. It has been specified in the method section, that the HB5 aptamer is immobilized via a covalent amide linkage on the electrode surface, **Scheme 4.1**. This immobilization is dependent on the –COOH groups on the nanomaterials on the electrode surface, which vary in exposure or availability depending on the electrode modification technique. The sequentially modified probe GCE/PPy/**1** (seq.) (**9**)/HB5 had a higher sensitivity (28741 Ωng^{-1} mL) compared to the pyrrole polymerized GCE/PPy@**1** (**5**)/HB5 probe (4285 Ωng^{-1} mL). While both electrodes contain the complex **1** and PPy, the arrangement of the nanomaterials differ. The CoPc on the GCE/PPy/**1** (seq.) (**9**)/HB5 is layered on the PPy modified surface; the carboxylic groups and the redox active cobalt central metal are exposed. This surface modification holds as both an immobilization and signal amplification platform. The GCE/PPy@**1** (**5**)/HB5 probe is made from the mixing of both the PPy and complex **1** on the electrode surface. The interaction is unarranged; aggregation is a possibility as well as shielding of the Co central metal. The Pc **1** can possibly be wrapped within the polymer and not as exposed, where the surface serves mostly as an immobilization platform and little signal amplification. Similarly, for the GCE/PPy/SNGQDs (seq.) (**8**)/HB5 and GCE/PPy@SNGQDs (**4**)/HB5 probes. The former showed better sensitivity (53006 Ωng^{-1} mL) compared to the latter (11457 Ωng^{-1} mL). It is obvious that the SNGQDs containing probes showed better sensitivity towards HER2 compared to the CoPc containing probes regardless of the modification technique. This might be due to the fact that, the

average size of a phthalocyanine is ~1 nm [205], whilst that of SNGQDs is ~2.8 nm (determined by TEM in this work, **Fig 3.4**). Compared to the CoPc, the large particle size of the SNGQDs allows for more HB5 particles as well as conformational flexibility of the HB5 aptamer. When all nanomaterials (PPy, SNGQDs and Pc **1**) are combined on the electrode surface, the probes modified by polymerization of pyrrole in the presence of Pc **1** or SNGQDs (electrodes **6** and **7**), had better sensitivity values compared to those by sequential adsorption (electrodes **10** and **11**). This might be due to aggregation and passivation during the sequential loading of the nanomaterials, where little signal amplification exists and immobilization platform support dominates. Whereas, for the electrodes modified by polymerization of pyrrole in the presence of Pc **1** or SNGQDs the π-π interaction of either PPy and Pc **1** or PPy and SNGQDs are governed by the applied potential, which almost affords the nanomaterials an orderly arrangement on the electrode surface. The lowest sensitivity value was obtained for GCE/**1** (**2**)/HB5. The combination of the SNGQDs with polypyrrole (GCE/PPy@SNGQDs (**4**)/HB5 or GCE/PPy/SNGQDs (seq.) (**8**)/HB5) improved the sensitivity of the GCE/SNGQDs (**3**)/HB5. Similarly, the sensitivity of the Pc based GCE/**1** (**2**) surface, was improved upon combination with polypyrrole: GCE/PPy@**1** (**5**)/HB5 or GCE/PPy/**1** (seq.) (**9**)/HB5. Reports have shown, that the combination of various polymers with different nanostructures result in improved mechanical, thermal and electrical properties [206]. As such, the results demonstrate the improvement of the electrochemical detection of the HER2 antigen, when polypyrrole is combined with SNGQDs and/or complex **1** on a glassy carbon electrode. This speaks mainly to the structural compatibility of the nanomaterials (π-π interactions), where their interaction upon combination results in better electrochemical sensors compared to the individual nanomaterials. This shows the role of combining various nanomaterials in improving sensor characteristics.

The limit of detection (LOD) values for all probes were estimated by the equation 3σ/s, **Table 5.2**. In which σ is the standard deviation of R_{ct} values obtained for PBS (without HER2) for all probes, and *s* is the sensitivity (m) of the regression plots. The best LOD value was for GCE/PPy@SNGQDs/**1** (**6**)/HB5 at 0.00141 ng/mL and the highest LOD value was for the GCE/**1** (**2**)/HB5, 0.647 ng/mL. Electrodes where pyrrole is polymerized in the presence of Pc **1** or SNGQDs followed by their addition on top (GCE/PPy@SNGQDs/**1** (**6**) and GCE/PPy@**1**/SNGQDs (**7**) gave the lowest LOD, with electrode GCE/ (**6**) being the best, **Table 5.2**. The reason for the low detection limit for GCE/ PPy@SNGQDs/**1** (**6**) could be a result of the CoPc on top, allowing for direct interaction with the electrolyte.

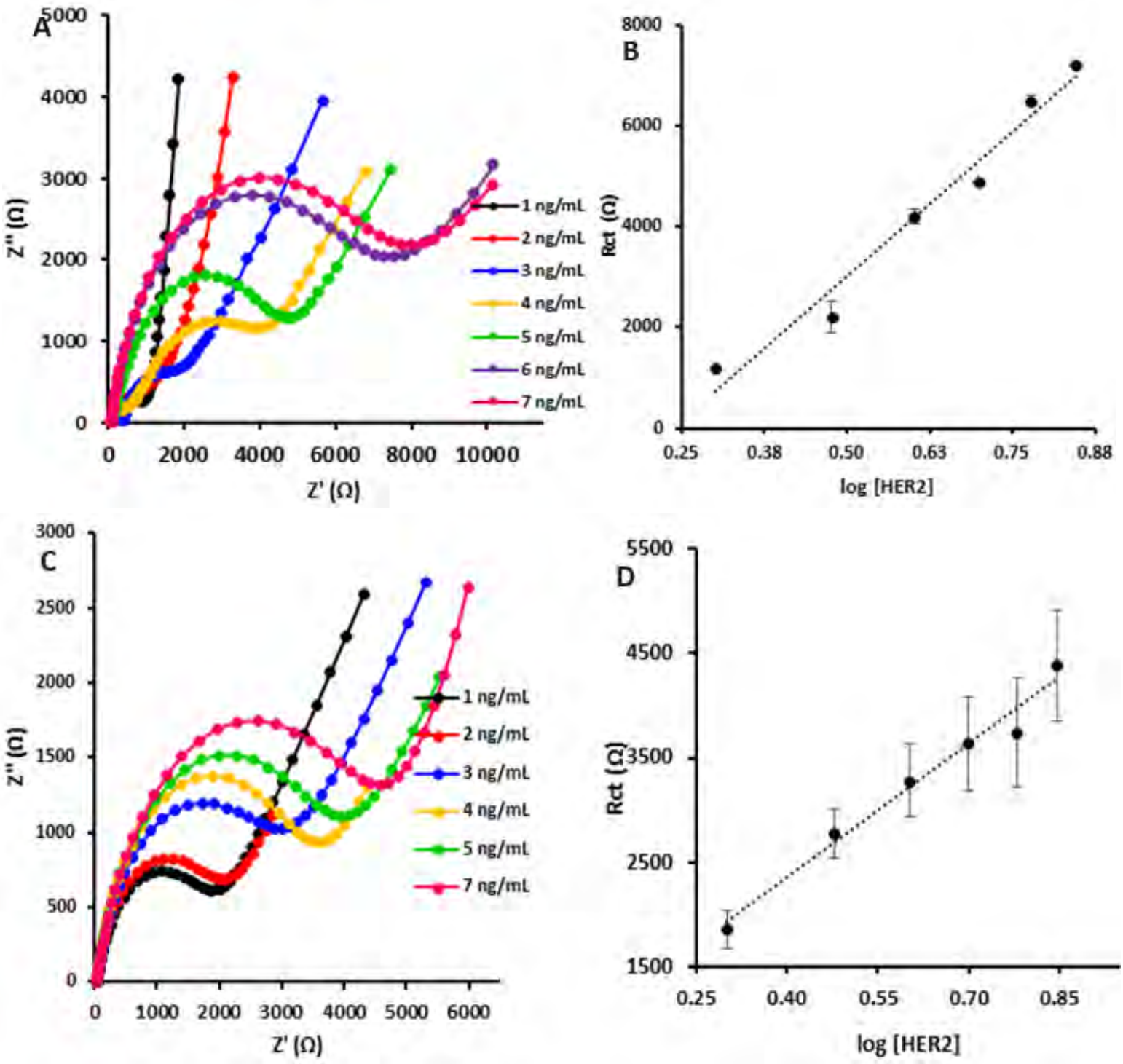

Figure 5.1. Nyquist plots of HER2 concentrations and the corresponding calibration plots of log HER2 vs. R_{ct} for (**A** and **B**) GCE/PPy@SNGQDs (**4**)/HB5 and (**C** and **D**) GCE/PPy@**1** (**5**)/HB5 using selected concentrations. All in $K_3[Fe(CN)_6]^{3-/4-}$ (1 mM in 0.1 mol·L^{-1} KCl in 10 mM PBS (pH 7.4).

Table 5.1. R_{ct} values obtained for the different electrode surfaces (represented by the electrode numbers **2-11** (definitions in **Table 5.2**) at the top of the table, and all containing HB5) towards detection of HER2.

	R_{ct}, Ω (%RSD)									
[HER2] ng/mL	GCE/ (**2**)	GCE/ (**3**)	GCE/ (**4**)	GCE/ (**5**)	GCE/ (**6**)	GCE/ (**7**)	GCE/ (**8**)	GCE/ (**9**)	GCE/ (**10**)	GCE/ (**11**)
1	471 (2.85)	540 (2.33)	927 (0.53)	1660 (12.03)	2463 (7.09)	1933 (21.66)	3353 (5.25)	2350 (10.06)	478 (3.25)	2417 (4.91)
2	855 (3.29)	829 (3.15)	1200 (0.83)	1863 (9.90)	3690 (2.71)	2833 (18.21)	5430 (5.77)	7250 (2.17)	974 (12.68)	4923 (7.97)
3	927 (0.31)	949 (4.18)	2000 (13.82)	2773 (8.22)	7860 (6.49)	2990 (7.24)	5827 (2.74)	7997 (17.43)	1079 (12.18)	7427 (9.79)
4	1090 (3.83)	1209 (8.89)	4200 (3.72)	3287 (10.86)	15850 (0.54)	6177 (9.92)	6993 (6.81)	11267 (4.195)	1097 (9.13)	8947 (3.51)
5	1150 (6.96)	1427 (4.56)	4888 (0.22)	3640 (12.41)	25833 (3.59)	7660 (9.07)	7260 (2.39)	13167 (8.67)	1783 (19.09)	10837 (1.87)
6	1260 (5.16)	2163 (3.98)	6500 (1.53)	3750 (13.96)	30270 (6.11)	10497 (6.70)	7997 (5.36)	14700 (0.68)	2933 (1.42)	12467 (3.04)
7	1520 (5.21)	2470 (1.05)	7210 (0.12)	4383 (12.07)	33000 (7.35)	11667 (10.33)	12093 (1.74)	18610 (2.40)	4043 (3.96)	15100 (5.88)
8	1850 (7.43)	3483 (2.59)	10543 (6.15)	6220 (7.06)	18400 (1.63)	14500 (9.66)	13240 (1.11)	20600 (4.63)	5033 (4.25)	17727 (5.12)
9	2370 (4.75)	4210 (0.24)	18567 (4.35)	6273 (9.57)	16400 (6.19)	15933 (7.49)	16767 (4.97)	20933 (10.86)	6483 (5.32)	21800 (3.99)

*Experiments were run in triplicate; the average values are shown in Ohms. The values in brackets are the RSD (relative standard deviation) obtained for the respective HER2 concentrations.

Table 5.2. Limit of detection (LOD) and sensitivities for detection of HER2 biosensors for GCE/ (**2**-**11**)/HB5. Linear range 1-10 ng/mL in all cases.

Electrode[a]	Sensitivities ($\Omega ng^{-1}mL$)	LOD (ng/mL)
GCE/**1** (**2**)/HB5	1036	0.647
GCE/SNGQDs (**3**)/HB5	9650	0.292
GCE/PPy@SNGQDs (**4**)/HB5	11457	0.143
GCE/PPy@**1** (**5**)/ HB5	4385	0.481
GCE/PPy@SNGQDs/**1** (**6**)/ HB5	71584	0.00141
GCE/PPy@**1**/SNGQDs (**7**)/ HB5	32086	0.0255
GCE/PPy/SNGQDs(seq.) (**8**)/ HB5	53006	0.00513
GCE/PPy/**1**(seq.) (**9**)/ HB5	28741	0.0674
GCE/PPy/SNGQDs/**1**(seq.) (**10**)/ HB5	17912	0.0716
GCE/PPy/**1**/SNGQDs(seq.)/ (**11**)/ HB5	15498	0.0980

[a] Electrode numbers in brackets.

5.1.2. Symmetrical Complexes: Amide Bonded to HB5 aptamer

5.1.2.1. Complex 2 and 3 in the presence of cerium oxide nanoparticles: Table 5.3

The following sensors; GCE/**2** (**12**)/HB5, GCE/**3** (**13**)/HB5**,** GCE/CeO_2NPs_{COOH} (**14**)/HB5, GCE/CeO_2NPs_{COOH}/**2** (seq.) (**15**)/HB5, GCE/CeO_2NPs_{COOH}/**3** (seq.) (**16**)/HB5 were all tested toward the electrochemical detection of HER2 at varying concentrations 0 ng to 10 ng. The performance of each sensor was investigated and compared using the electrochemical impedance spectroscopy (EIS). The EIS response for the designed probes is shown in **Figure 5.2**, using the probes: GCE/**2** (**12**)/HB5 (A and B) and GCE/CeO_2NPs_{COOH}/**2** (**15**)/HB5 (C and D) as examples. The obtained Nyquist plots demonstrate a clear increase in R_{ct} with an increase in HER2 concentration for both probes. This is as a result of the blocked electron transfer properties by the HER2 layer on the electrode surface. The same trend was observed for all probes based on complex **2** and **3**, data shown in **Table 5.3** and **Table 5.4.** Regression plots were then created using the data of each electrode, the equations of the regression plots were as follows (eq. **5.11** to **5.15**):

GCE/**2** (**12**)/HB5: $y = 16441x + 4849, R^2 = 0.9917$ **(5.11)**

GCE/**3** (**13**)/HB5: $y = 16901x - 3131, R^2 = 0.9698$ **(5.12)**

GCE/CeO_2NPs_{COOH} (**14**)/HB5: $y = 6001x + 1360, R^2 = 0.9876$ **(5.13)**

GCE/CeO_2NPs_{COOH}/**2** (seq.) (**15**)/HB5: $y = 22953x + 3255, R^2 = 0.9697$ **(5.14)**

GCE/CeO_2NPs_{COOH}/**3** (seq.) (**16**)/HB5: $y = 24122x + 2781, R^2 = 0.9622$ **(5.15)**

The slopes (m) of the regression plots give the sensitivity of each sensor/modified electrodes. Based on the regression plots (**eq. 5.11 – 5.15**), the GCE/**3** (**13**)/HB5 probe showed slightly

better sensitivity compared to its competitor GCE/**2** (**12**)/HB5, **Table 5.5**. The nanoparticles-based probe (GCE/CeO_2NPs_{COOH} (**14**)/HB5) had the lowest sensitivity, compared to the rest of the probes. The combination of the nanoparticles with the phthalocyanines GCE/CeO_2NPs_{COOH}/**2** (seq.) (**15**)/HB5 and GCE/CeO_2NPs_{COOH}/**3** (seq.) (**16**)/HB5 showed better sensitivity, compared to the Pcs and NPs alone. Synergetic combination of the properties of phthalocyanines and metal nanoparticles is known to result in the improvement of various properties of the hybrid materials [**64**]. The structural similarity of the two Pcs: **Pc 2** and **Pc 3**, is evident in their comparable sensitivity values. This is the case when used alone, and also when combined with the nanoparticles. Limits of detection (LOD) were determined as stated above. The calculated LOD values for all probes are listed in **Table 5.5**, where the lowest value was obtained for GCE/CeO_2NPs_{COOH}/**3** (seq.) (**16**)/HB5 (0.008 ng/mL) and the highest for GCE/CeO_2NPs_{COOH} (**14**)/HB5 (0.19 ng/mL). The LOD values were improved upon conjugation of each Pc complex to the CeO_2NPs_{COOH}, further demonstrating the importance of conjugating the NPs and MPc in electrochemical sensing. The LOD values determined for complex **2** and **3** in the presence of CeO_2NPs_{COOH} are higher than those obtained for PPy in the presence of the SNGQDs and the symmetrical complex **1** (**Table 5.2**), further demonstrating the importance of PPy.

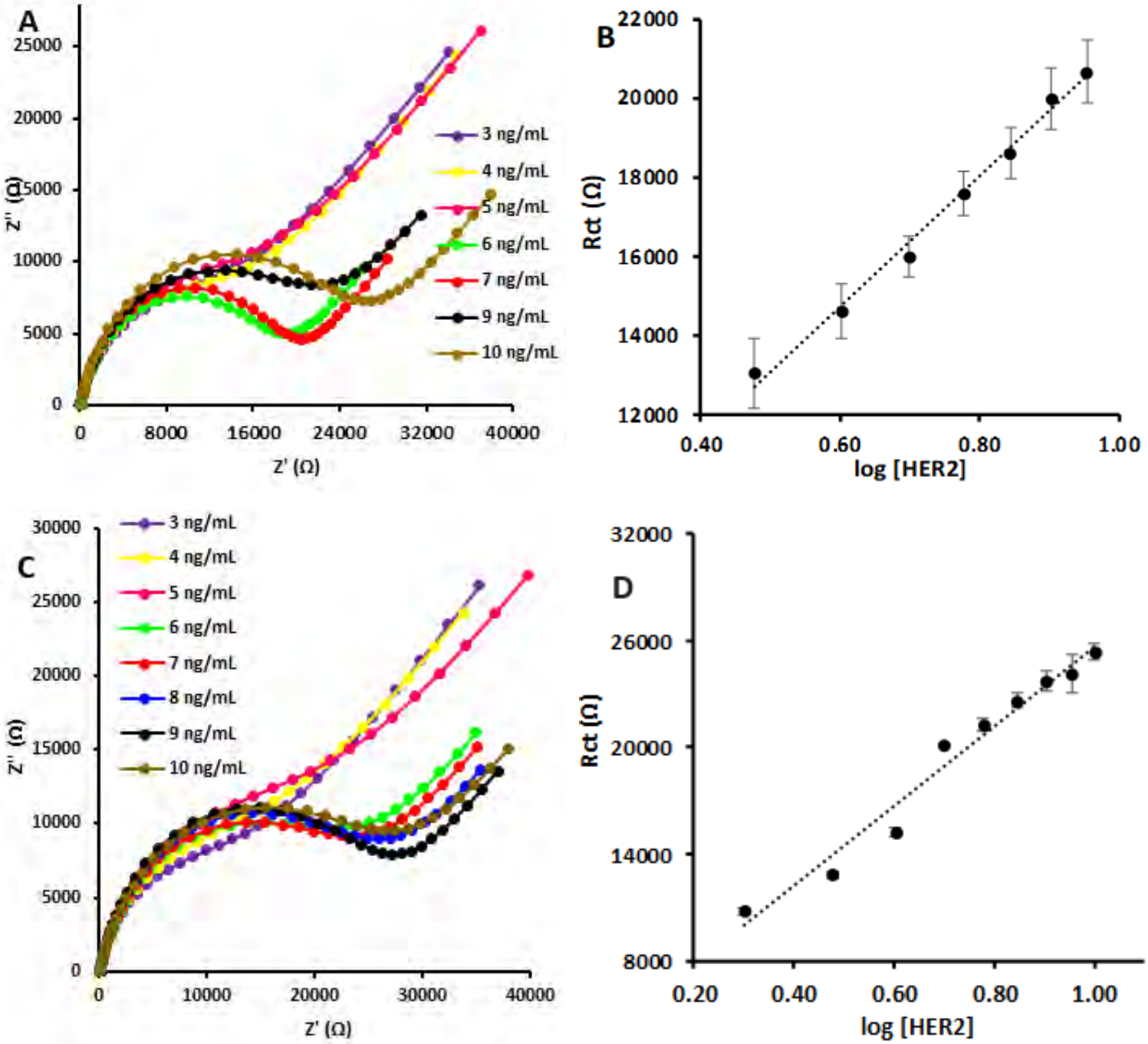

Figure 5.2. Nyquist plots and regression plots of log HER2 vs. Rct for the probes GCE/**2** (**12**)/HB5 (**A** and **B**) and GCE/CeO_2NPs_{COOH}/**2** (seq.) (**15**)/HB5 (**C** and **D**), respectively. All in $[K_3[Fe(CN)_6]^{3-/4-}$ (1 mM in 0.1 mol·L^{-1} KCl in 10 mM PBS (pH 7.4).

Table 5.3. R_{ct} values obtained for the different electrode surfaces (represented by the electrode numbers **12-16** (definitions in **Table 5.5**) at the top of the table, and all containing HB5) towards detection of HER2.

	R_{ct}, kΩ (% RSD) *				
[HER2] ng/mL	GCE/ (**12**)	GCE/ (**13**)	GCE/ (**14**)	GCE/ (**15**)	GCE/ (**16**)
1	7207	4340	2497	10070	10590
	(1.59)	(1.99)	(3.63)	(7.92)	(4.02)
2	8103	5400	3267	10833	11327
	(1.03)	(4.44)	(3.48)	(1.92)	(2.49)
3	13033	5527	4157	12867	14233
	(6.91)	(5.95)	(4.73)	(1.62)	(2.03)
4	14600	6807	4947	15200	16300
	(4.79)	(1.44)	(1.00)	(1.74)	(2.67)
5	15967	8103	5333	20167	18167
	(3.15)	(4.01)	(1.69)	(0.29)	(3.03)
6	17567	10040	6177	21300	20467
	(3.13)	(1.96)	(3.34)	(1.69)	(2.69)
7	18600	10513	6503	22633	23633
	(3.52)	(3.81)	(1.90)	(1.67)	(1.99)
8	19967	12400	8077	23733	25700
	(3.89)	(5.64)	(0.56)	(2.43)	(1.03)
9	20667	13567	11033	24133	26533
	(3.91)	(0.42)	(7.60)	(4.39)	(2.30)
10	24533	22800	21467	25333	34400
	(3.26)	(4.02)	(3.96)	(1.78)	(5.24)

5.1.2.2. Complex 3 in the presence of AuNPs, SNGQDs and CeO_2NPs: Effect of nanoparticles, Table 5.5.

The results obtained and outlined in **Section 5.1.2.1**; demonstrate the role a particular nanoparticle plays in the electrochemical behaviour of Pc complexes. The combination of both complex **2** and **3** with CeO_2NPs, resulted in higher sensitivity (almost double) and therefore lower LOD values compared to when the Pcs are alone. Evidently, Pc complex **3** had better electrochemical response towards HER2 compared to complex **2**. In this section, the performance of complex **3** in the presence of three different NPs; AuNPs, SNGQDs and CeO_2NPs is outlined, the effect of each nanoparticle is discussed.

To achieve this, the following aptasensors: GCE/SNGQDs (**3**)/HB5, GCE/CeO_2NPs_{COOH}/**3** (**16**)/HB5, GCE/SNGQDs/**3** (seq.) (**17**)/HB5, GCE/**3**(π)SNGQDs (**18**) /HB5, GCE/AuNPs (**19**) /HB5 and GCE/AuNPs/**3** (seq.) (**20**) /HB5 were all tested towards the electrochemical detection of HER2 at varying concentrations from 0 ng to 10 ng, using EIS. **Figure 5.3** shows the EIS response for the probes GCE/SNGQDs/**3** (seq.) (**17**)/HB5 (A and B), GCE/AuNPs (**19**)/HB5 (C and D) as examples, towards HER2 detection. Similar to the previously mentioned probes, an increase in R_{ct} with increase in HER2 concentration was observed. This trend held true for all designed aptasensors; the rest of the data is shown in **Table 5.4**.

For a more clear and unbiased comparison of the contribution of each nanoparticle to the performance of the complex **3**, regression plots were created using the EIS response of each electrode, the equations of the regression plots were as follows (**eq. 5.16 – 5.23**):

GCE/SNGQDs (**3**)/HB5: $y = 9650x - 5117, R^2 = 0.9233$ **(5.16)**

GCE/**3** (**13**)/HB5: $y = 16901x - 3131, R^2 = 0.9698$ **(5.17)**

GCE/CeO_2NPs_{COOH} (**14**)/HB5: $y = 6001x + 1360, R^2 = 0.9876$ **(5.18)**

GCE/CeO_2NPs_{COOH}/**3** (seq.) (**16**)/HB5:$y = 24122x + 2781, R^2 = 0.9622$ **(5.19)**

GCE/SNGQDs/**3** (seq.) (**17**)/HB5: $y = 6990x + 61, R^2 = 0.9645$ **(5.20)**

GCE/**3**(π)SNGQDs (**18**)/HB5: $y = 11633x + 5514, R^2 = 0.9841$ **(5.21)**

GCE/AuNPs (**19**)/HB5: $y = 43837x + 10461, R^2 = 0.9310$ **(5.22)**

GCE/AuNPs/**3** (seq.) (**20**)/HB5: $y = 13475x + 5480, R^2 = 0.9833$ **(5.23)**

The sensitivity of a biosensor depends on various factors, and herein we investigate the role of three different nanoparticles: SNGQDs, CeO_2NPs_{COOH} and AuNPs towards enhancing electrochemical detection of HER2 of Pc **3**. Of the individual materials, the highest sensitivity was observed for AuNPs (**eq. 5.18**), followed by complex **3** (**eq. 5.12**), **Table 5.5**. To make sense of the obtained results, the structural characteristics of the various nanomaterials and the way in which they are distributed onto the electrode was considered. Even further, the manner in which each nanoparticle interacts with the HB5 on the electrode during its immobilization as guided by the distribution of the nanoparticles on the GCE is taken into account. In earlier sections (**4.2**), the GCE/AuNPs had the highest surface coverage (1.82×10^{-7} mol.cm^{-2}) compared to GCE/CeO_2NPs_{COOH} (**14**) and GCE/SNGQDs (**3**) surface, **Table 4.3.** This may imply more HB5 fragments adsorbed on the electrode compared to the GCE/CeO_2NPs_{COOH} (**14**) and GCE/SNGQDs (**3**) modified surfaces, hence the higher and better sensitivity. The performance of Pc **3** in the presence of the three nanoparticles will now be

discussed. The Pc **3** on its own functions as an immobilization platform for the HB5 aptamer, as well as signal amplification owing to its redox and electrocatalytic properties. Varying effects on the sensitivities for all electrodes when the nanoparticles are combined with the Pc **3** for sensor fabrication were observed. In the presence of complex **3**, the highest sensitivity was observed for the probe GCE/CeO_2NPs_{COOH}/**3** (seq.) (**16**)/HB5 (24122 $\Omega ng^{-1}mL$), followed by GCE/AuNPs/**3** (seq.) (**20**)/HB5 (13475 $\Omega ng^{-1}mL$) and GCE/SNGQDs/**3** (seq.) (**17**)/HB5 (6990 $\Omega ng^{-1}mL$), respectively. Based on the results, a much more stable sensing platform for HB5 immobilization in the presence of complex **3**, and in turn signal amplification for HER2 detection was achieved for the GCE/CeO_2NPs/**3** (seq.) (**16**)/HB5 aptasensor.

The effect of interaction between NP and the Pc complex **3** was investigated, and is demonstrated by the results obtained for the probe: GCE/SNGQDs(π)**3** (**18**)/HB5, where the SNGQDs were π-π stacked to the Pc **3** first, followed by electrode modification. A higher sensitivity was obtained for GCE/SNGQDs(π)**3** (**18**)/HB5 (11633 Ωng-1mL) compared to the sequentially modified surface GCE/SNGQDs/**3** (seq.) (**17**)/HB5 (6990 Ωng-1mL), showing the advantage of non-covalent arrangement (**18**), compared to the sequentially modified (**17**) electrode. There was no general trend amongst all electrodes where the sensitivity is concerned. This speaks to the peculiarity of each nanoparticle structure, their interaction with the complex **3**, physicochemical properties and in turn their electrochemical behaviour. The obtained results solidify the peculiar and comparative nature of each nanoparticle: SNGQDs, CeO_2NPs_{COOH} and AuNPs, and in turn their electrochemical activity as either signal amplifiers and/or immobilization platforms.

The limit of detection (LOD) values were estimated as explained above. The list of the modified surfaces with their obtained LOD values is shown in **Table 5.5.** The best LOD value

was obtained for the probe, GCE/AuNPs (**19**)/HB5 (0.006 ng/ mL) and the highest LOD value was obtained for the probe GCE/SNGQDs (**3**)/HB5 (0.29 ng/mL). The LOD of Pc **3** improved in the presence CeO_2NPs, corresponding the improvement in sensitivity. A lower LOD was obtained for GCE/SNGQDs(π)**3** (**18**)/HB5 (0.074 ng/mL) compared to the sequentially modified surface GCE/SNGQDs/**3** (seq.) (**17**)/HB5 (0.19 ng/mL). Still lower LOD values are obtained for PPy@SNGQDs/**1**, **Table 5.2**.

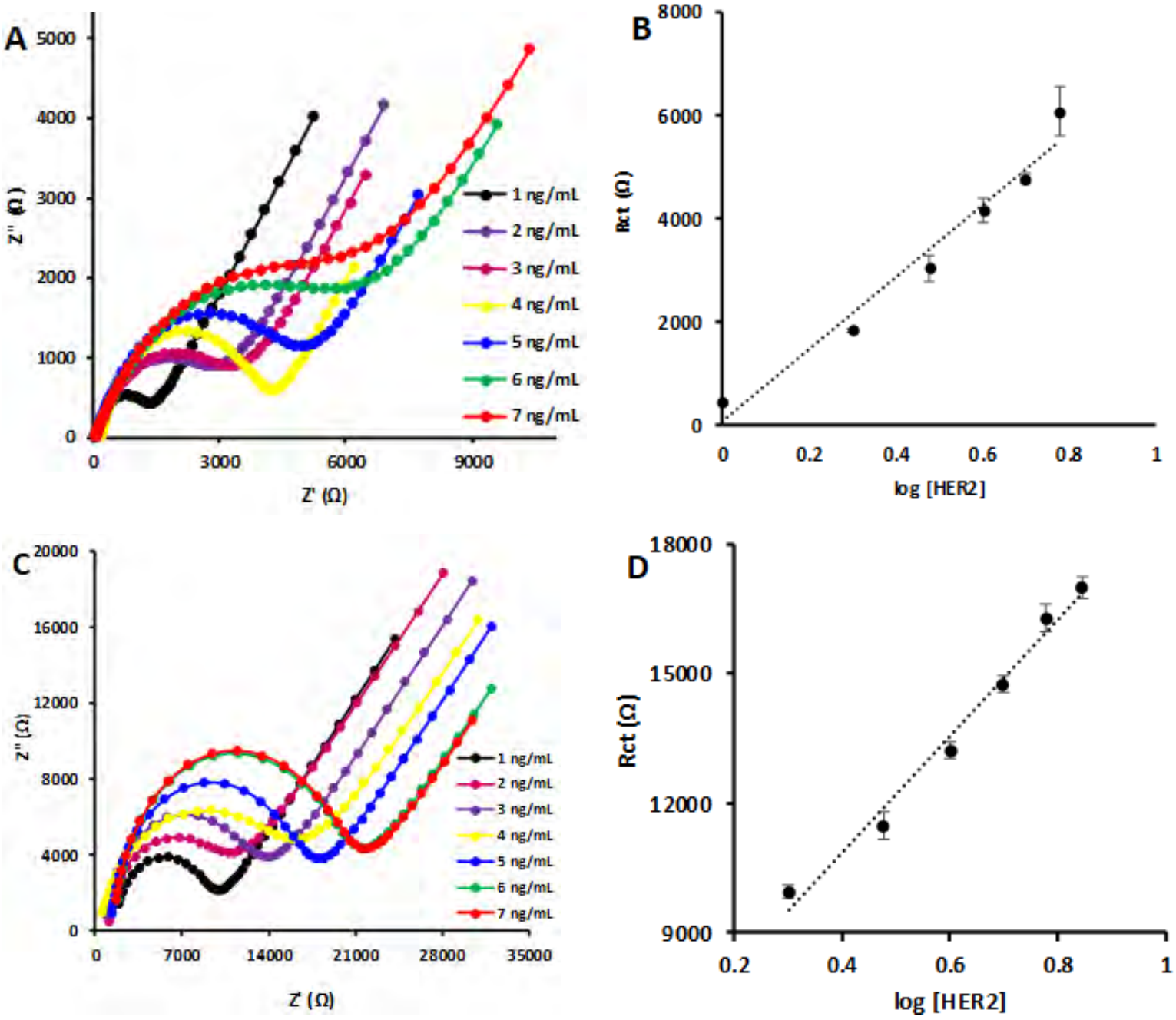

Figure 5.3. Nyquist plots and regression plot of R_{ct} vs log [HER2] for the probes GCE/SNGQDs/**3** (seq.) (**17**)/HB5 (**A** and **B**), GCE/AuNPs (**19**)/HB5 (**C** and **D**) as labelled. All in $K_3[Fe(CN)_6]^{3-/4-}$ (1 mM in 0.1 mol· L^{-1} KCl in 10 mM PBS (pH 7.4).

Table 5.4. Rct values obtained for the different electrode surfaces (represented by the electrode numbers **13-20** (definitions listed in **Table 5.5**) at the top of the table, and all containing HB5), towards detection of HER2.

	R_{ct}, kΩ (% RSD) *						
[HER2] ng/mL	GCE (**3**)	GCE (**13**)	GCE (**16**)	GCE (**17**)	GCE (**18**)	GCE (**19**)	GCE (**20**)
1	540 (2.33)	4340 (1.99)	10590 (4.02)	437 (5.76)	5837 (7.43)	23733 (1.70)	7293 (1.97)
2	838 (3.15)	5400 (4.44)	11327 (2.50)	1843 (1.74)	8233 (2.78)	24367 (3.13)	9967 (3.23)
3	905 (4.18)	5527 (5.95)	14233 (2.03)	3040 (7.98)	11467 (4.12)	33000 (2.64)	11500 (1.74)
4	1290 (8.89)	6807 (1.45)	16300 (2.67)	4163 (5.64)	12450 (2.44)	33300 (4.06)	13233 (1.57)
5	1360 (4.56)	8103 (4.01)	18167 (3.03)	4777 (2.26)	13800 (1.26)	41167 (6.19)	14767 (2.18)
6	2180 (3.98)	10040 (1.96)	20467 (2.69)	6077 (7.91)	14533 (2.86)	42633 (5.52)	16300 (1.62)
7	2460 (1.05)	10513 (3.81)	23622 (2.00)	6820 (5.80)	20333 (2.32)	50600 (0.71)	17000 (1.18)
8	3570 (2.59)	12400 (5.64)	25700 (1.03)	7780 (3.37)	26700 (8.11)	67800 (5.44)	23333 (2.47)
9	4200 (0.24)	13567 (0.43)	26533 (2.30)	13600 (3.89)	31500 (4.99)	77533 (2.65)	26100 (3.77)
10	5030 (1.52)	22800 (4.02)	34400 (5.24)	16333 (5.95)	33933 (5.02)	84533 (4.68)	28000 (4.12)

*RSD = relative standards deviation

Electrodes in full: GCE/SNGQDs (**3**)/HB5, GCE/**3** (**13**)/HB5, GCE/CeO_2NPs_{COOH}/**3** (**16**)/HB5, GCE/SNGQDs/**3** (seq.) (**17**)/HB5, GCE/**3**(π)SNGQDs (**18**) /HB5, GCE/AuNPs (**19**) /HB5 and GCE/AuNPs/**3** (**20**) /HB5

Table 5.5. Limit of detection and sensitivities for detection of HER2 biosensors for GCE/ (**13 – 20**)/HB5. Linear range 1–10 ng/mL in all cases.

Electrodes [a]	**Sensitivity ($\Omega ng^{-1}mL$)**	**LOD (ng/mL)**
GCE/SNGQDs (**3**)/HB5	9650	0.29
GCE/**2** (**12**)/HB5	16441	0.061
GCE/**3** (**13**)/HB5	16901	0.051
GCE/CeO_2NPs_{COOH} (**14**)/HB5	6001	0.19
GCE/CeO_2NPs_{COOH}/**2** (seq.) (**15**)/HB5	22395	0.015
GCE/CeO_2NPs_{COOH}/**3** (seq.) (**16**)/HB5	24122	0.008
GCE/SNGQDs/**3** (seq.) (**17**)/HB5	6990	0.19
GCE/SNGQDs (π)**3** (**18**)/HB5	11633	0.074
GCE/AuNPs (**19**)/HB5	43837	0.006
GCE/AuNPs/**3** (seq.) (**20**)/HB5	13475	0.058

[a] Electrode numbers in brackets

5.1.3. Symmetry and Substituent Effects: Imine Bonded to HB5 aptamer

The sections **5.1.1** and **5.1.2** clearly outline the ability of cobalt-based Pc complexes **1**, **2** and **3** to generate a readable signal in the electrochemical detection of HER2. Moreover, these Pc complexes have shown their excellent performance by their high sensitivities and low LOD values obtained. The above-mentioned Pc complexes, are all symmetrical and tetra substituted. In the case of phthalocyanines and related structures, their electrocatalytic activity and solution redox chemistry has been reported to be dependent on their symmetry and peripheral substituents [77]. For this reason, the two Pc complexes **4** (cobalt tetra-acetylphenoxy Pc) and **5** (cobalt tris – (acetyl phenoxy)-mono-phenoxyacrylic acid Pc) are investigated for electrode modification towards the design of an electrochemical biosensor for HER2 detection. The effect of replacing one acetylphenoxy ligand in the tetra substituted Pc **4**, with a phenoxyacrylic acid ligand to form the Pc **5** is investigated. In addition, acetophenone will allow for the formation of imine bond while the presence of acrylic acid allows for the formation of amide bond with the aptamer, **Section 4.3**. Hence the activities of the Pcs will not only be determined by symmetry, but also by the type of bond. Acrylic acid derivatives are known for their electrocatalytic activity [207] hence this substituent is employed in this work. To further add value to the study, the two Pc complexes were combined with SNGQDs via π-π stacking. This was done to encourage electron delocalization and distribution within the Pc complexes which was expected to differ as governed by the two Pc structures. Non-covalent π-π stacking was chosen based on the obtained results in **5.1.2**: higher sensitivities obtained for π-π stacked electrodes compared to sequentially modified.

The following HB5 containing electrodes: GCE/**4** (**21**)/HB5, GCE/**4**(π)SNGQDs (**22**)/HB5, GCE/**5** (**23**)/HB5 (amide), GCE/**5** (**23**)/HB5 (imine), GCE/**5**(π)SNGQDs (**24**)/HB5 (amide) and GCE/**5**(π)SNGQDs (**24**)/HB5 (imine) were all tested toward the electrochemical detection of HER2 at varying concentrations of 0 ng to 10 ng. The performance of the probes was investigated and compared using EIS. **Figure 5.4** shows the obtained Nyquist plots for the probes: GCE/**4** (**21**)/HB5 (A and B), GCE/**4**(π)SNGQDs (**22**)/HB5 (C and D), GCE/**5** (**23**)/HB5 (imine) (E and F) and GCE/**5**(π)SNGQDs (**24**)/HB5 (imine) (G and H), **Table 5.6**. **Figure 5.4** show that the R_{ct} values increased with the HER2 concentration in the tested linear range. Regression plots were then created using the data of each electrode, the equations of the regression plots (**eq. 5.24 - 5.29**) are as follows:

GCE/**4** (**21**)/HB5: $y = 16414x + 39607, R^2 = 0.9703$ **(5.24)**

GCE/**4**(π)SNGQDs (**22**)/HB5: $y = 20553x + 12427, R^2 = 0.9652$ **(5.25)**

GCE/**5** (**23**)/HB5 (amide): $y = 12911x + 29075, R^2 = 0.9618$ **(5.26)**

GCE/**5** (**23**)/HB5 (imine): $y = 30262x + 15843, R^2 = 0.9886$ **(5.27)**

GCE/**5**(π)SNGQDs (**24**)/HB5 (amide): $y = 72253x + 7389, R^2 = 0.9711$ **(5.28)**

GCE/**5**(π)SNGQDs (**24**)/HB5 (imine): $y = 34245x + 24472, R^2 = 0.9623$ **(5.29)**

The sensitivities of the respective aptasensors are listed in **Table 5.7**. The GCE/**4** (**21**)/HB5 aptasensor had a sensitivity of 16414 $\Omega ng^{-1}mL$, while the conjugated based aptasensor GCE/**4**(π)SNGQDs (**22**)/HB5 had a sensitivity of 20553 $\Omega ng^{-1}mL$. The aptasensor GCE/**5**

(**23**)/HB5 (amide) had a sensitivity value of 12911 Ωng^{-1}mL, which increased to 72253 Ωng^{-1}mL when conjugated to SNGQDs forming the sensor GCE/**5**(π)SNGQDs (**24**)/HB5 (amide). In these two aptasensors the HB5 aptamer was immobilized via an amide bond formation aided by DCC/NHS coupling, via the single phenoxyacrylic acid ligand, leaving the three acetylphenoxy groups unoccupied, **Scheme 4.3**. The improved sensitivity for the GCE/**5**(π)SNGQDs (**24**)/HB5 (amide), aptasensor could be attributed to increased electron delocalization between the SNGQDs and Pc **5** in the conjugate. Furthermore, the SNQGDs have carboxylic groups on their periphery which are also activated when the GCE/**5**(π)SNGQDs (**24**)/HB5 (amide) probe is treated with DCC/NHS for HB5 immobilization. This could result in more HB5 aptamers on the surface of the probe for HER2 detection hence the higher sensitivity observed. The GCE/**5** (**23**)/HB5 (imine) probe had a sensitivity of 30262 Ωng^{-1}mL, which was higher than that of GCE/**5** (**23**)/HB5 (amide). For the aptasensor GCE/**5** (**23**)/HB5 (imine), HB5 was immobilized on the three acetylphenoxy ligands via imine bond formation, while for GCE/**5** (**23**)/HB5 (amide) only one substituent is involved for immobilization of HB5. The results demonstrate the significance of having more ligands for HB5 linking as well as the efficiency of the phenoxyacrylic acid ligand in electron distribution to the Pc and its interaction with the electrolyte for signal generation. The aptasensor GCE/**5**(π)SNGQDs (**24**)/HB5 (imine), which is the SNGQDs and Pc **5** conjugate where the HB5 aptamer is linked via imine bond formation had a sensitivity of 34245 Ωng^{-1}mL. In which case, only the Pc partakes as an immobilization platform for HB5, while the SNGQDs sole purpose is electron delocalization and electron transfer. The effect of symmetry is without bias demonstrated by the results obtained for the GCE/**4** (**21**)/HB5 and GCE/**5** (**23**)/HB5 (imine), as well as their respective conjugates GCE/**4**(π)SNGQDs (**22**)/HB5 and GCE/**5**(π)SNGQDs (**24**)/HB5 (imine). In which case, the asymmetric Pc **5** based sensors performed better

compared to the symmetric Pc **4** based sensors**.** The improvement in sensitivity obtained in all Pc/SNGQDs probes, further demonstrates the significance of combining various nanomaterials for signal amplification in sensor design.

The LOD values of the designed aptasensors were then calculated as stated above, results are listed in **Table 5.7**. The best LOD was obtained for the GCE/**5**(π)SNGQDs (**24**)/HB5 (amide) at 0.00272 ng/mL, which also had the highest sensitivity. The asymmetrical GCE/**5** (**23**)/HB5 (imine) gave a lower LOD than the symmetrical GCE/**4** (**21**)/HB5, corresponding to the high sensitivity obtained for the former and further showing the importance of reduced symmetry. This was true even in the presence of SNGQDs; GCE/**4**(π)SNGQDs (**22**)/HB5 and GCE/**5**(π)SNGQDs (**24**)/HB5 (imine).

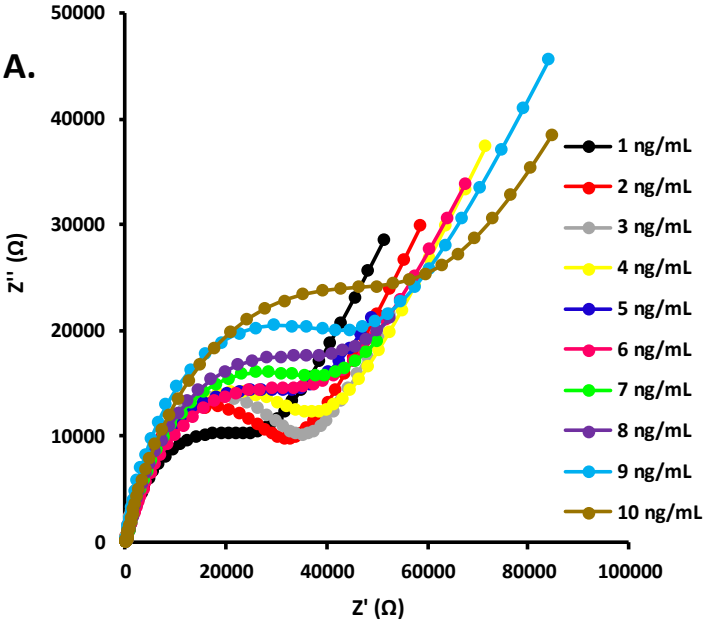
A.
50000
40000
30000
20000
10000
0
Z'' (Ω)
0
20000
40000
60000
80000
100000
Z' (Ω)
1 ng/mL
2 ng/mL
3 ng/mL
4 ng/mL
5 ng/mL
6 ng/mL
7 ng/mL
8 ng/mL
9 ng/mL
10 ng/mL

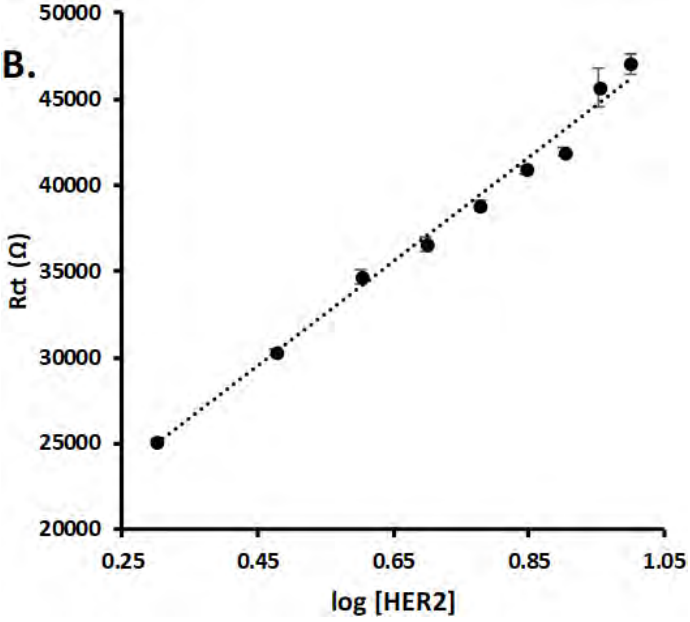
B.
50000
45000
40000
35000
30000
25000
20000
Rct (Ω)
0.25
0.45
0.65
0.85
1.05
log [HER2]

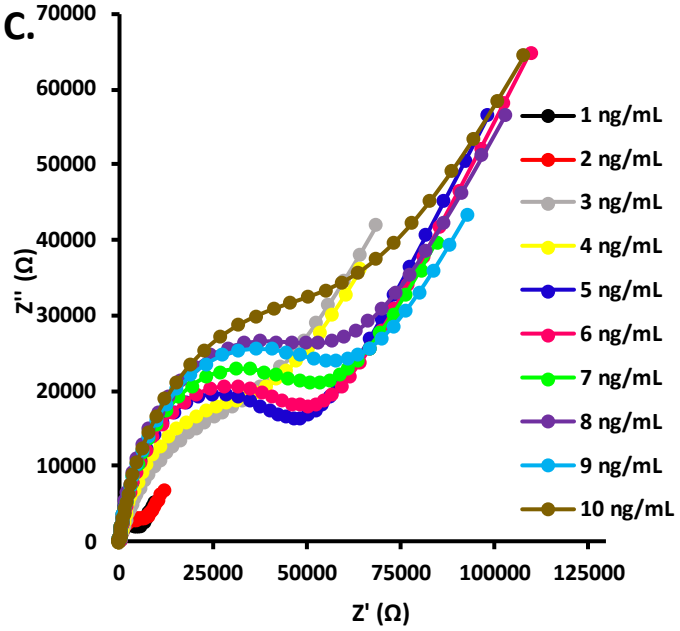
C.
70000
60000
50000
40000
30000
20000
10000
0
Z'' (Ω)
0
25000
50000
75000
100000
125000
Z' (Ω)
1 ng/mL
2 ng/mL
3 ng/mL
4 ng/mL
5 ng/mL
6 ng/mL
7 ng/mL
8 ng/mL
9 ng/mL
10 ng/mL

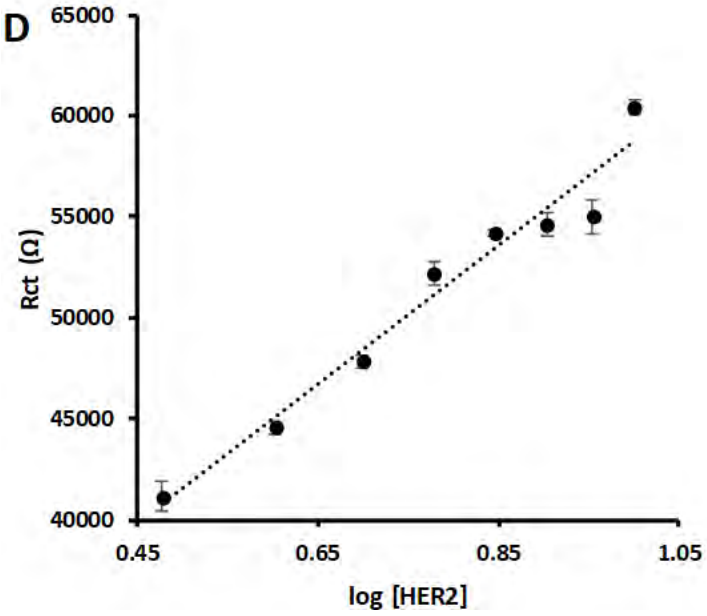
D
65000
60000
55000
50000
45000
40000
Rct (Ω)
0.45
0.65
0.85
1.05
log [HER2]

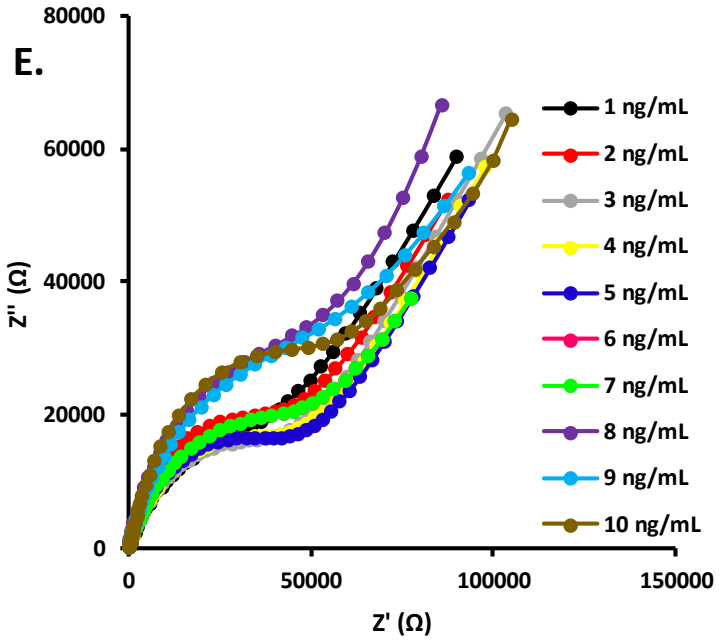
E.
80000
60000
40000
20000
0
Z'' (Ω)
0
50000
100000
150000
Z' (Ω)
1 ng/mL
2 ng/mL
3 ng/mL
4 ng/mL
5 ng/mL
6 ng/mL
7 ng/mL
8 ng/mL
9 ng/mL
10 ng/mL

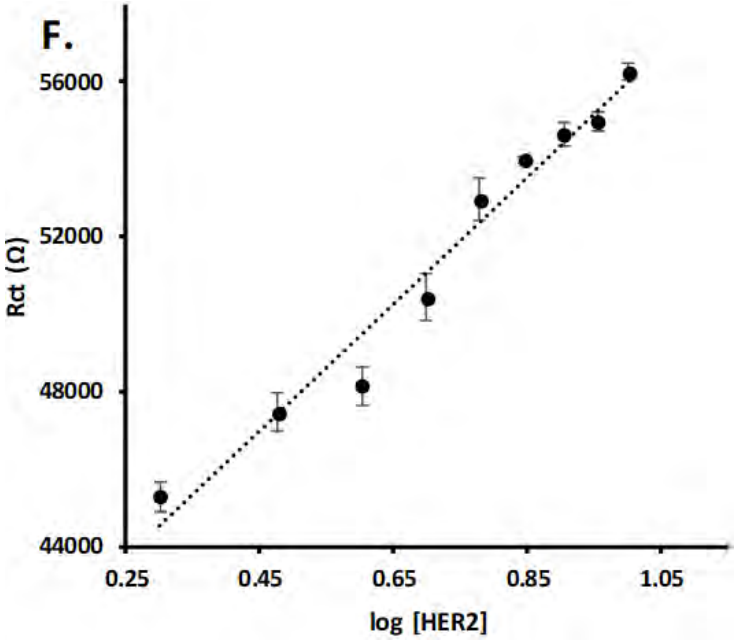
F.
56000
52000
48000
44000
Rct (Ω)
0.25
0.45
0.65
0.85
1.05
log [HER2]

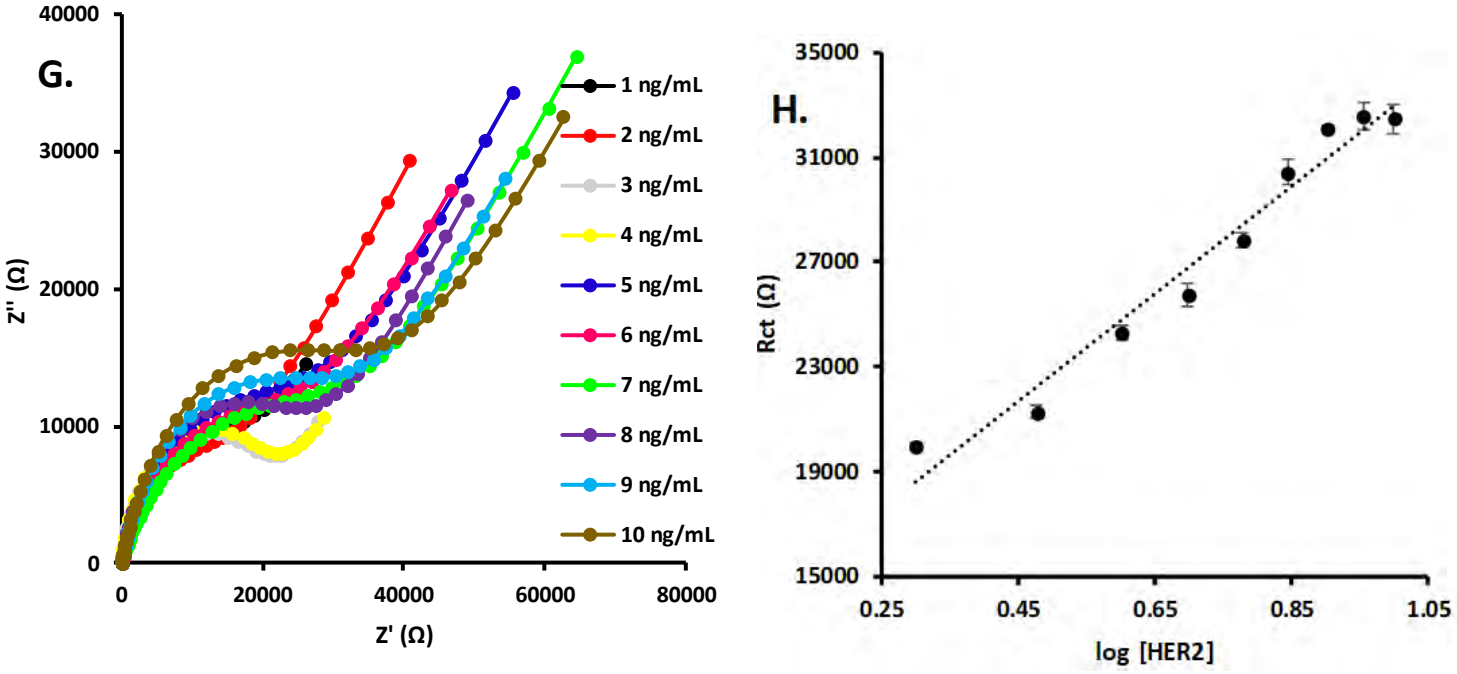

Figure 5.4. Nyquist plots and regression plots of log HER2 vs. R_{ct} for the GCE/**4** (21)/HB5 (**A** and **B**), GCE/**4**(π)SNGQDs (22)/HB5 (**C** and **D**), GCE/**5** (23)/HB5 (imine) (**E** and **F**) and GCE/ GCE/**5**(π)SNGQDs (24)/HB5 (imine) (**G** and **H**). All in $K_3[Fe(CN)_6]^{3-/4-}$ (1 mM in 0.1 mol·L^{-1} KCl in 10 mM PBS (pH 7.4).

Table 5.6. Rct values obtained for the different electrode surfaces GCE/ (**21-24**)/HB5 towards detection of HER2.

	R_{ct}, kΩ (% RSD) *					
[HER2] (ng/mL)	GCE (**21**)	GCE/ (**22**)	GCE/ (**23**) (amide)	GCE/ (**23**) (imine)	GCE/ (**24**) (amide)	GCE/ (**24**) (imine)
1	35600 (7.29)	18300 (4.47)	24467 (3.33)	18667 (1.12)	18433 (4.11)	4567 (4.34)
2	45267 (0.84)	19933 (0.58)	33100 (0.30)	25133 (0.61)	32733 (0.76)	6080 (3.36)
3	47467 (1.06)	21267 (1.18)	35833 (1.06)	30333 (1.37)	42333 (0.56)	41167 (1.79)
4	48133 (0.98)	24300 (1.23)	36900 (0.47)	34733 (1.16)	48200 (2.16)	44567 (0.69)
5	50433 (1.20)	25733 (1.79)	37600 (0.96)	36533 (0.84)	55133 (3.19)	47833 (0.64)
6	52967 (1.04)	27833 (1.04)	38267 (0.40)	38833 (0.54)	61467 (0.81)	52200 (1.15)
7	54000 (0.19)	30433 (1.69)	39500 (0.67)	40900 (0.49)	65400 (0.54)	54200 (0.32)
8	54633 (0.56)	32100 (0.31)	40433 (1.00)	41933 (2.57)	72800 (0.96)	54667 (1.06)
9	54967 (0.46)	32600 (1.62)	41700 (1.50)	45667 (1.26)	78000 (2.09)	55033 (1.54)
10	56267 (0.41)	32467 (1.70)	43033 (0.48)	47033 (0.12)	84400 (2.15)	60433 (0.63)

Electrodes in full: GCE/**4** (**21**)/HB5, GCE/**4**(π)SNGQDs (**22**)/HB5, GCE/**5** (**23**)/HB5 (amide), GCE/**5** (**23**)/HB5 (imine), GCE/**5**(π)SNGQDs (**24**)/HB5 (amide) and GCE/**5**(π)SNGQDs (**24**)/HB5 (imine)

Table 5.7. Limit of detection and sensitivities for detection of HER2 biosensors for GCE/ (**21-24**). Linear range 1–10 ng/mL in all cases.

Probes	**Sensitivity ($\Omega ng^{-1}mL$)**	**LOD (ng/mL)**
GCE/**4**(**21**)/HB5	16414	0.24
GCE/**4**(π)SNGQDs (**22**)/HB5	20553	0.042
GCE/**5** (**23**)/HB5(amide)	12911	0.33
GCE/**5** (**23**)/HB5(imine)	30262	0.039
GCE/**5**(π)SNGQDs (**24**)/HB5(amide)	72253	0.0027
GCE/**5**(π)SNGQDs (**24**)/HB5(imine)	34245	0.014

5.1.4. Single vs. Sandwiched Aptamer Assay: Amide Bonded onto HB5 aptamer

In a single aptamer-based sensor, the signal is measured upon direct interaction of an aptamer immobilized on the electrode with the respective antigen [208]. A sandwich based aptasensor, utilizes signal amplification through a double interaction system: a pair of aptamers is used where one is immobilized on the surface to capture the analyte and the second one binds to the captured target for signal generation and enhancement. Using the complex **6** in the presence of SNGQDs@CeO_2NPs based GCE, single and sandwiched aptamer assay were designed for HER2 detection, **Scheme 5.1**.

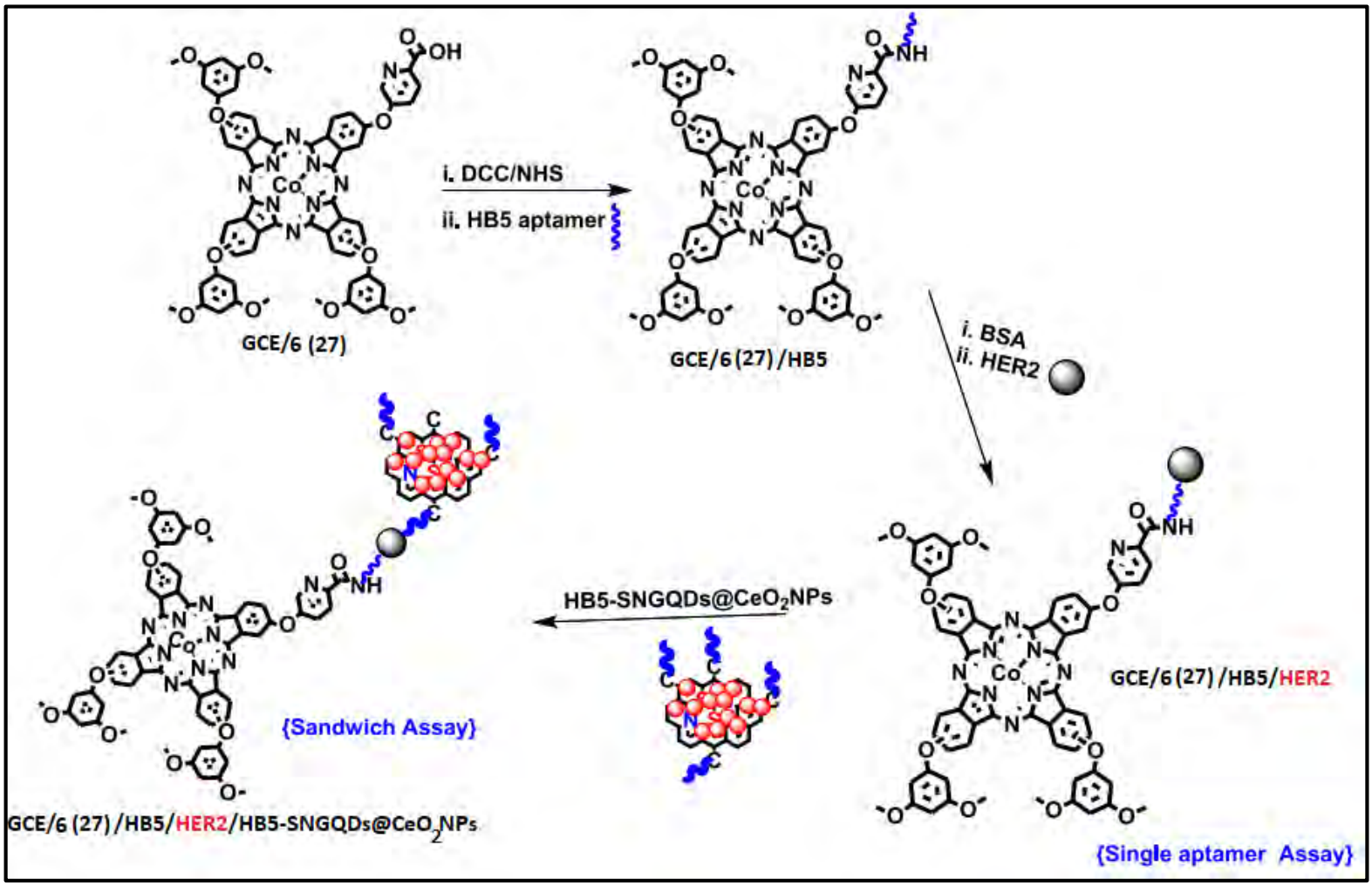

Scheme 5.1. Representation of the different sensing assays: single aptamer assay and a sandwich assay, using GCE/**6** (**26**) modified surface.

5.1.4.1. Single aptamer assay

The following designed aptasensors: GCE/SNGQDs@CeO_2NPs (**25**)/HB5, GCE/**6** (**26**)/HB5 and GCE/SNGQDs@CeO_2NPs/**6** (seq.) (**27**)/HB5 were tested towards the electrochemical detection of HER2 in the concentration range 0-21 pg/mL using EIS. **Figure 5.5A&B** shows the obtained EIS data for the single aptamer assay, showing data for the GCE/SNGQDs@CeO_2NPs/**6** (seq.) (**27**)/HB5 probe. The HB5-HER2 interaction was determined by observing the change in R_{ct} values for $[FeCN_6]^{3-/4-}$. The figure showed an increase in R_{ct} with increase in HER2 concentration. This trend held true for all designed aptasensors, **Table 5.8**. Regression plots were then created using the data of each electrode excluding outliers. The equations of the regression plots were as follows (**eq. 5.30 - 5.32**):

GCE/SNGQDs@CeO_2NPs (**25**)/HB5: $y = 55073x + 1290, R^2 = 0.9272$ **(5.30)**

GCE/**6** (**26**)/HB5: $y = 339410x - 198528, R^2 = 0.9635$ **(5.31)**

GCE/SNGQDs@CeO_2NPs/**6**(seq.)(**27**)/HB5:$y = 596285x - 474994, R^2 = 0.9787$ **(5.32)**

The phthalocyanine alone based GCE/**6** (**26**)/HB5 aptasensor had a higher sensitivity, compared to the nanocomposite based GCE/SNGQDs@CeO_2NPs (**25**)/HB5 aptasensor, **Table 5.9**. These results demonstrate the superiority of the complex **6**, compared to the SNGQDs@CeO_2NPs nanocomposite as an electrode modifier in the design of the HER2 specific aptasensor. This is by means of its superior ability to act as an immobilization platform for the biorecognition element (HB5) to allow for development of a stable aptasensor, while aiding in enhanced electron transfer. The highest sensitivity was obtained when Pc **6** and

SNGQDs@CeO_2NPs were combined (in GCE/(**27**)/HB5) for electrode modification, with a sensitivity of 596285 $\Omega pg^{-1}mL$.

5.1.4.2. Sandwich Assay

On the surfaces: GCE/SNGQDs@CeO_2NPs (**25**)/HB5, GCE/**6** (**26**)/HB5 and GCE/SNGQDs@CeO_2NPs/**6** (seq.) (**27**)/HB5 a sandwich assay was designed and tested towards the electrochemical detection of HER2 (0-21 pg/mL) range. The obtained EIS data is shown in **Figure 5.5C&D**, using the GCE/SNGQDs@CeO_2NPs/**6** (seq.) (**27**)/HB5/**HER2**/HB5-SNGQDs@CeO_2NPs as an example. The figure demonstrates that there was an increase in R_{ct} with increase in HER2 concentration. This trend held true for all designed aptasensors, **Table 5.8.** Regression plots were then created using the data of each electrode excluding outliers. The equations of the regression plots were as follows (**eq. 5.33 - 5.35**):

GCE/SNGQDs@CeO_2NPs (**25**)/HB5/**HER2**/HB5-SNGQDs@CeO_2NPs:

$$y = 56485x + 10534, R^2 = 0.9489 \quad \textbf{(5.33)}$$

GCE/**6** (**26**)/HB5/**HER2**/HB5-SNGQDs@CeO_2NPs:

$$y = 738125x - 510027, R^2 = 0.9750 \quad \textbf{(5.34)}$$

GCE/SNGQDs@CeO_2NPs/**6** (seq.) (**27**)/HB5/**HER2**/HB5-SNGQDs@CeO_2NPs:

$$y = 773925x - 617741, R^2 = 0.9728 \quad \textbf{(5.35)}$$

The highest sensitivity was obtained for the conjugate-based sandwich assay GCE/SNGQDs@CeO_2NPs/**6** (seq.) (**27**)/HB5/**HER2**/HB5-SNGQDs@CeO_2NPs (**eq. 5.35**). The major contributing factor is the synergistic effect of Pc **6** and SNGQDs@CeO_2NPs for electron

transfer and signal amplification when combined as electrode modifiers towards biosensor design. As evidenced by the data, the sandwich assays showed higher sensitivity compared to single aptamer assays, **Table 5.9**. An advantage of the sandwich assay, compared to the single aptamer assay (**5.1.4.1**), is the two biorecognition system, one on the electrode surface and the other within the HB5-SNGQDs@CeO_2NPs bioconjugate. Furthermore, the bioconjugate (**Scheme 4.6**) contains the SNGQDs@CeO_2NPs made of SNGQDs and CeO_2NPs, which have been previously shown to have excellent electrocatalytic activity towards the electrochemical detection of HER2, **Section 5.1.2.2**.

5.1.4.3. LOD calculation: Single vs Sandwich aptamer assay

The LOD values for the designed aptasensors were estimated by the equation 3σ/s, **Table 5.9**. In the case of single aptamer assay; the lowest LOD was obtained for GCE/SNGQDs@CeO_2NPs/**6** (seq.) (**27**)/HB5, 0.0059 pg/mL, followed by GCE/**6** (**26**)/HB5 and GCE/SNGQDs@CeO_2NPs (**25**)/HB5, respectively. Various contributors to the aptasensor performance can be proposed. First, the electron transfer properties and great conductivity of the used Pc **6** and SNGQDs@CeO_2NPs alone and when combined. Secondly, the applicability of these nanomaterials as electron modifiers to form a fairly stable modified surface for the immobilization of the biorecognition element (HB5- aptamer) for enhanced specificity and sensitivity. Similarly, LOD for the sandwich assays were determined, **Table 5.9**. Agreeable to the obtained sensitivities, the lowest LOD was obtained GCE/ (**27**)/HB5/**HER2**/HB5-SNGQDs@CeO_2NPs at 0.00088 pg/mL, and it is lower than any other aptasensor reported in this thesis. The sandwich assay had a lower LOD value compared to the single aptamer assay.

5.1.4.4. Optimization: Sandwich Assay

The sandwich assay is built similar to the single aptamer assay, with an additional step where the HB5-SNGQDs@CeO_2NPs (formed as shown in **Scheme 4.6** freely not on the GCE) is added onto the electrode surfaces to complete the sandwich, **Scheme 5.1**. The effect of incubation time of all designed aptasensors with the HB5-SNGQDs@CeO_2NPs bioconjugate to form the sandwich assay was investigated, **Figure 5.6** (using GCE/**6** (**26**)/HB5/**HER2** as an example). GCE/**6** (**26**)/HB5/**HER2** (at [HER2] = 1 pg/mL) was incubated with the HB5-SNGQDs@CeO_2NPs solution for 10, 20, 30, 40, 50, 60, 70, 80, 90 and 100 min at 37 ◦C. **Fig. 5.6A** shows that there was an increase in R_{ct} value with increasing incubation time. This held true until 60 min, where an equilibrium was reached. As such, the optimum incubation time with the HB5-SNGQDs@CeO_2NPs bioconjugate to complete the sandwich assay was 60 min.

The effect of concentration of the HB5-SNGQDs@CeO_2NPs bioconjugate used was also investigated, **Fig. 5.6B**. On the probe GCE/**6** (**26**)/HB5/**HER2** (where [HER2] = 5 pg/mL), various concentrations of HB5-SNGQDs@CeO_2NPs were added, and the effect of concentration was measured in terms of R_{ct} values. Different concentrations of HB5-SNGQDs@CeO_2NPs, in the range 0.038 – 0.19 µM (dilutions based on aptamer concentration), were used to establish a sandwich structure. The R_{ct} values increased with increasing the HB5-SNGQDs@CeO_2NPs concentration, up until 0.11 µM there after a subsequent decrease was observed at higher concentrations. Thus, 0.11 µM was selected as the optimum concentration for the HB5-SNGQDs@CeO_2NPs bioconjugate/secondary aptamer to complete the sandwich, **Scheme 5.1**.

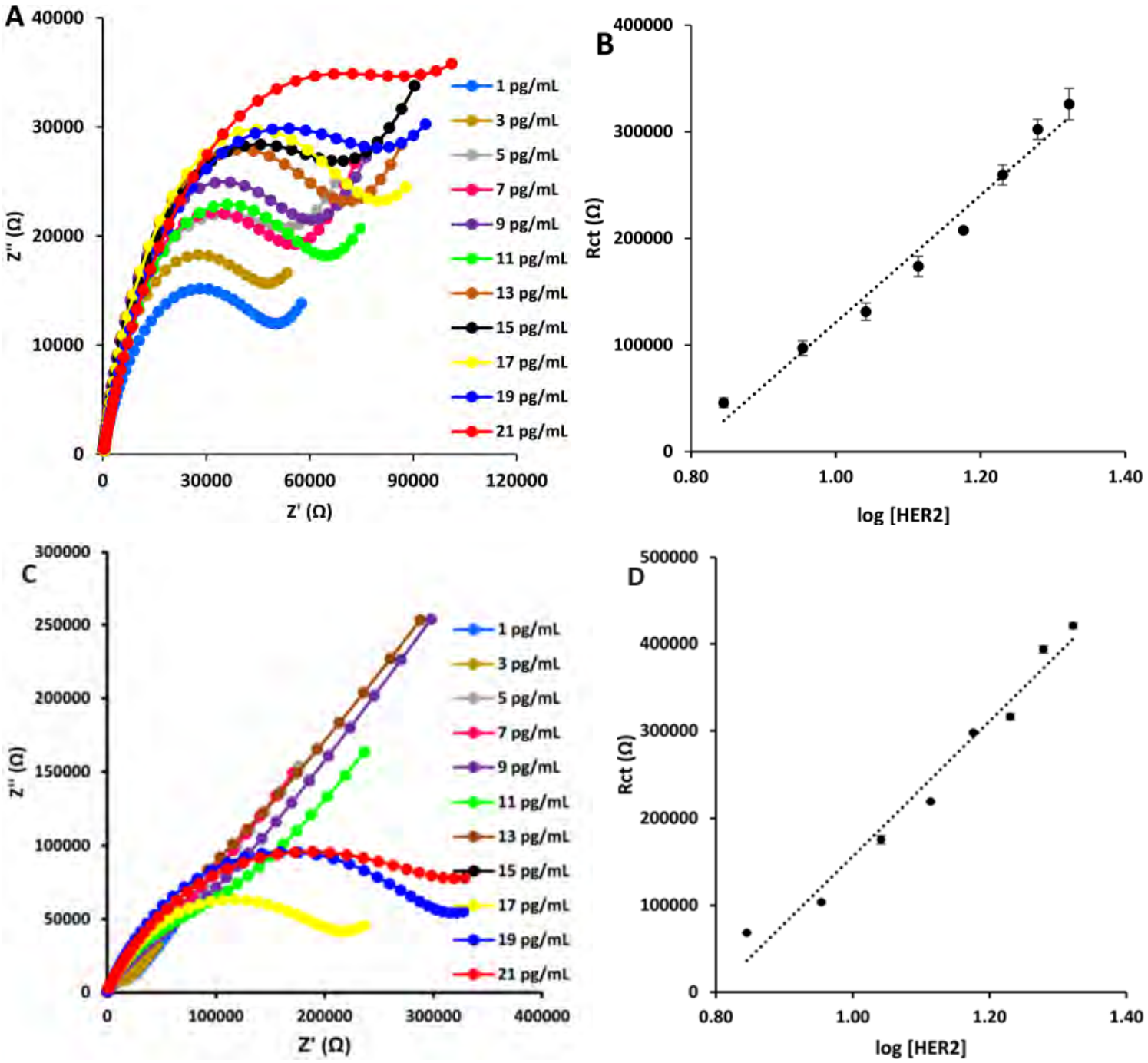

Figure 5.5. EIS Nyquist plots and regression plots of log HER2 vs. R_{ct} for GCE/SNGQDs@CeO_2NPs/**6** (seq.) (**27**) surface: Single aptamer (**A** and **B**) and Sandwich Assay (**C** and **D**), respectively. In $K_3[Fe(CN)_6]^{3-/4-}$ (1 mM in 0.1 mol·L^{-1} KCl in 10 mM PBS (pH 7.4).

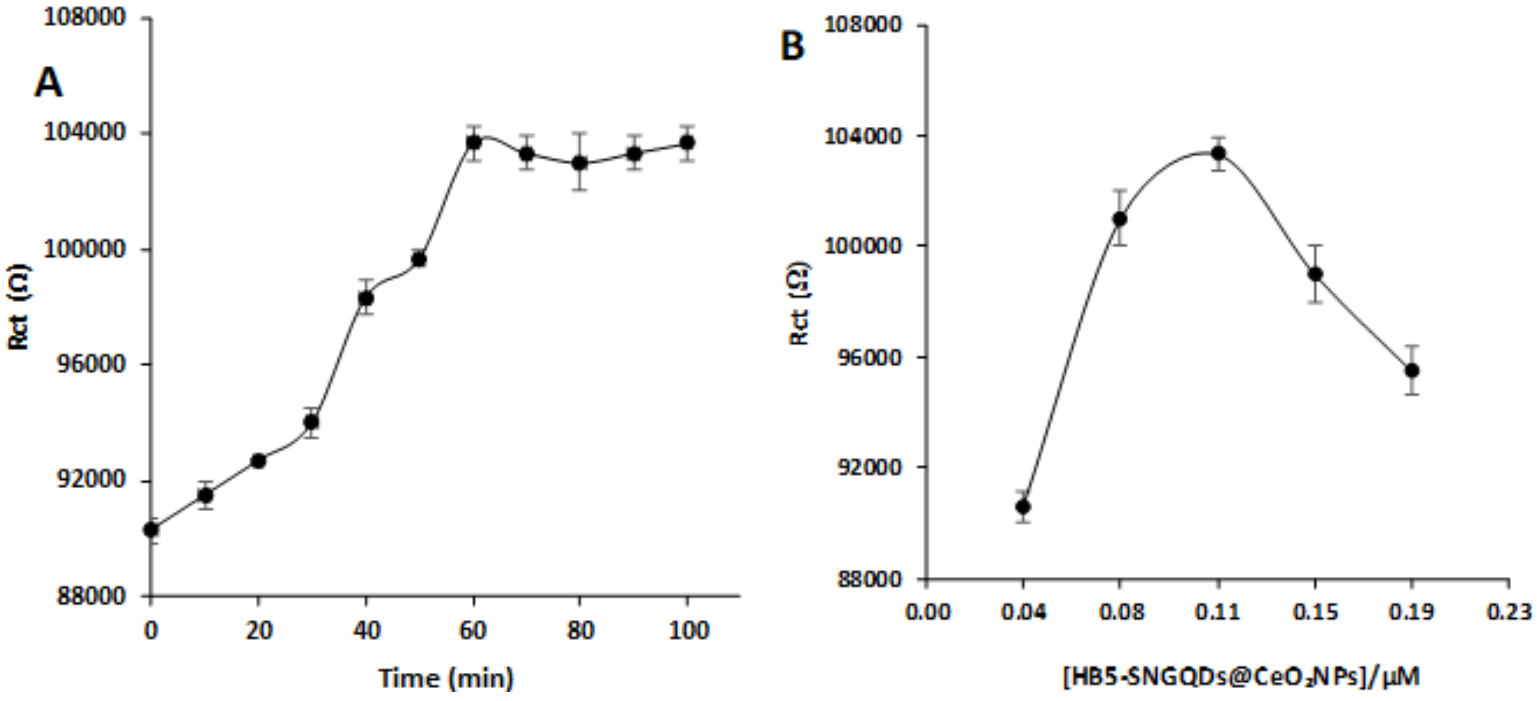

Figure 5.6. (**A**) Effect of the incubation time of HB5-SNGQDs@CeO_2NPs on the R_{ct} values obtained for the GCE/**6** (**26**)/HB5/HER2 substrate to form a sandwich aptasensor, [HER2] = 1 pg/mL. (**B**) Effect of the concentration of the HB5-SNGQDs@CeO_2NPs (µM based on aptamer) bioconjugate (at 60 min) on the R_{ct} values obtained for the GCE/**6** (**26**)/HB5/**HER2**/HB5-SNGQDs@CeO_2NPs, [HER2] = 5 pg/mL. All in $K_3[Fe(CN)_6]^{3-/4-}$ (1 mM in 0.1 mol·L^{-1} KCl in 10 mM PBS (pH 7.4).

Table 5.8. Rct values obtained for the different electrode surfaces GCE/ **25-27** (defined fully, in **Table 5.9**)/HB5 towards detection of HER2.

	R_{ct}, kΩ (% RSD) *					
[HER2] pg/mL	GCE (**25**) **Single**	GCE (**25**) **Sandwich**	GCE (**26**) **Single**	GCE (**26**) **Sandwich**	GCE (**27**) **Single**	GCE (**27**) **Sandwich**
1	45900	45333	29700	25200	27833	22833
	(4.47)	(6.67)	(0.34)	(0.79)	(5.52)	(7.55)
3	47700	50900	72000	86667	40400	26133
	(5.76)	(5.40)	(1.34)	(7.05)	(5.19)	(1.34)
5	49967	53633	90300	103667	55733	68100
	(5.61)	(4.61)	(0.57)	(1.47)	(1.15)	(1.25)
7	51600	59533	140000	118000	46000	68300
	(1.08)	(0.68)	(7.14)	(5.29)	(9.47)	(0.76)
9	52833	66300	146667	193667	97067	103500
	(0.61)	(1.14)	(1.04)	(4.79)	(7.13)	(1.44)
11	55200	67433	166667	258333	131333	175333
	(2.37)	(0.82)	(0.92)	(0.22)	(6.15)	(2.69)
13	61400	71867	189667	316000	174000	219000
	(2.46)	(2.13)	(0.81)	(0.32)	(5.48)	(0.45)
15	65167	75300	224000	363333	207667	297667
	(1.66)	(1.40)	(1.18)	(4.2)	(0.73)	(0.51)
17	68600	77967	231333	375333	259667	316000
	(1.86)	(0.15)	(0.66)	(1.26)	(3.66)	(1.14)
19	71067	83100	265000	407333	302333	393333
	(1.06)	(2.20)	(1.73)	(0.93)	(3.12)	(1.05)
21	78033	89000	349667	503000	326000	421000
	(2.24)	(1.12)	(3.41)	(0.53)	(4.54)	(0.85)

Table 5.9. Limit of detection and sensitivities for detection of HER2 biosensors developed in this work. Linear range 1–21 pg/mL in all cases.

PROBES	Sensitivity (Ω $pg^{-1}mL$)		LOD (pg/mL)		Γ, mol cm^{-2}
	Single aptamer	Sandwich aptamer	Single aptamer	Sandwich aptamer	
GCE/SNGQDs@CeO_2NPs (**25**)	55073	56485	0.060	0.035	2.45×10^{-8}
GCE/**6** (**26**)/HB5	339410	738125	0.011	0.0018	5.94×10^{-10}
GCE/SNGQDs@CeO_2NPs/**6** (seq.) (**27**)	596285	773925	0.0059	0.00088	2.89×10^{-9}

5.1.5. Cobalt binuclear framework (CoP-BNF) based electrodes: Aptamer vs. Antibody

The distinguishing factor of biosensors compared to any other sensor, is molecular recognition. Antigen–receptor interaction, is a fundamental step and component in various biological systems, molecular therapy, clinical diagnosis, biosensors and biotechnologies [209, 210]. A molecular recognition element takes part in the recognition process, and provides a receptor site for the attachment of an antigenic molecule [211]. Aptamer and antibodies are part of these recognition elements. For the first time, this thesis reports on the comparative aptamer (HB5) vs. antibody (Trastuzumab) based detection of HER2 on a CoP-BNF surface, coupled with SNGQDs@AuNPs for enhanced sensitivity and signal transduction, **Scheme 4.4**. The following sensors: GCE/SNGQDs@AuNPs (28)/HB5, GCE/SNGQDs@AuNPs (28)/Trasmatuzab, GCE/CoP-BNF (29)/HB5, GCE/CoP-BNF (29)/Trastuzumab, GCE/SNGQDs@AuNPs/CoP-BNF (seq.) (30)/HB5 and GCE/SNGQDs@AuNPs/CoP-BNF (seq.) (30)/Trasmatuzab were all tested towards the electrochemical detection of HER2 at varying concentrations of 0 ng to 10 ng in PBS pH 7.4. The performance of all designed sensors was investigated using the EIS; R_{ct} values obtained from the EIS data were used to study aptamer/antibody-antigen interactions. **Figure 5.7** shows Nyquist plots obtained for GCE/(30) as an example, both aptasensor and immunosensors. As previously demonstrated, an increase in the concentration of the HER2 antigen resulted in an increase in the R_{ct} values of a particular surface. This trend held true for both the aptasensors and immunosensors, **Table 5.10**. The increase in R_{ct} signifies a decrease in conductivity.

Regression plots were then created using the data of each electrode, the equations of the regression plots were as follows (**eq. 5.36 – 5.41**):

GCE/ (28)/HB5:$y = 9592x - 162, R^2 = 0.9869$ **(5.36)**

GCE/ (28)/Trastuzumab:$y = 5882x - 989, R^2 = 0.9951$ **(5.37)**

GCE/ (29)/HB5: $y = 3565x - 1028, R^2 = 0.9775$ **(5.38)**

GCE/ (29)/Trastuzumab: $y = 2895x + 1355, R^2 = 0.9787$ **(5.39)**

GCE/ (30)/HB5: $y = 18979x - 5003, R^2 = 0.9809$ **(5.40)**

GCE/ (30)/Trastuzumab: $y = 15751x + 356, R^2 = 0.9823$ **(5.41)**

The aptasensors (**eq. 5.36, 5.38 and 5.40**) showed better sensitivity compared to the immunosensors (**eq. 5.37, 5.39 and 5.41**)), **Table 5.11**. LOD values were determined as stated above. The aptasensors had lower LOD values, compared to its corresponding immunosensor electrodes, all listed in **Table 5.11**. Aptamers compared to antibodies, are synthetic recognition elements, fine-tuned and designed specifically for the analyte of interest [212]. Their structure is usually optimized to achieve maximum stability, specificity and selectivity. This is further confirmed by the LOD and sensitivity results obtained.

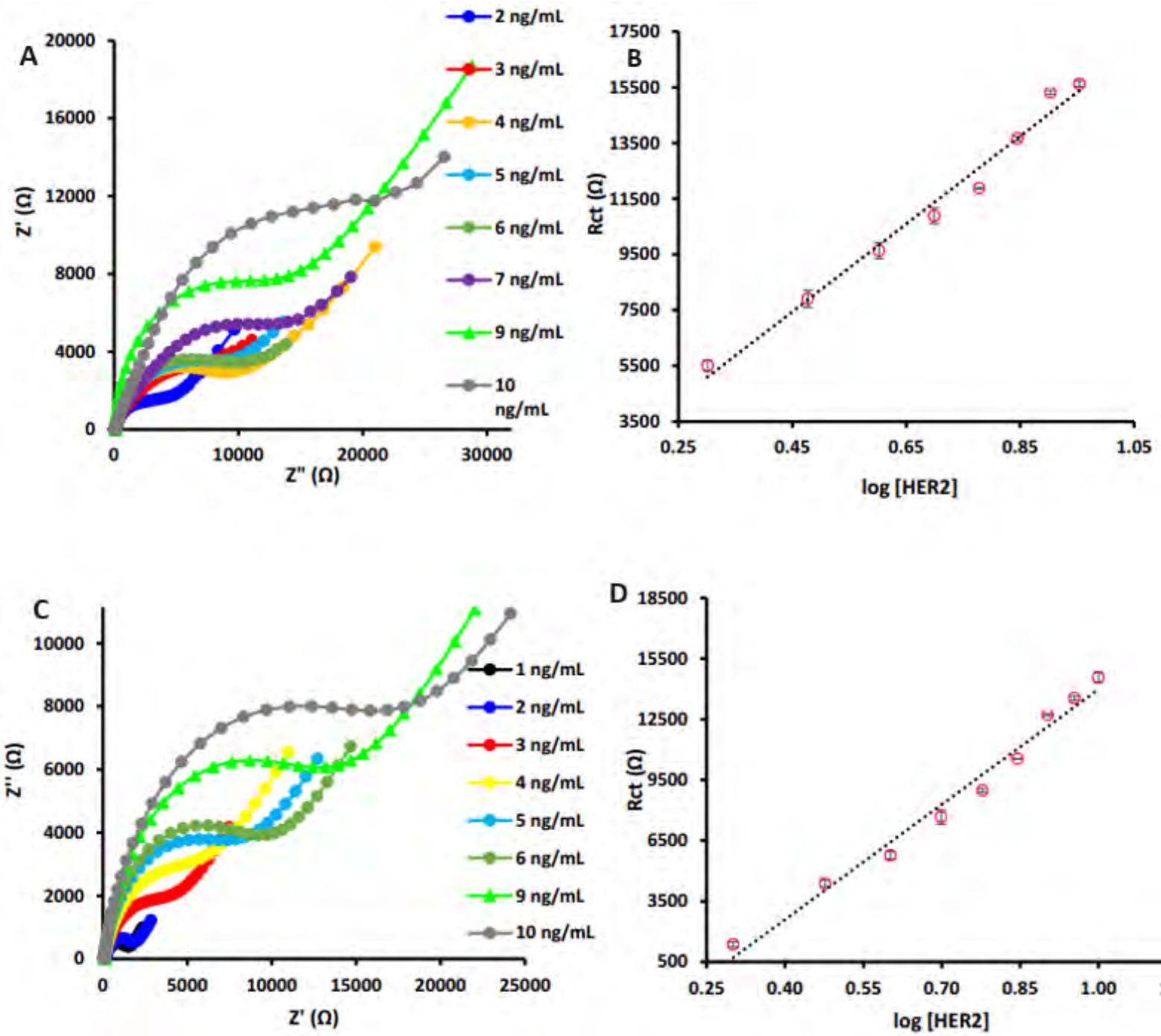

Figure 5.7. Nyquist plots and regression plots of log HER2 vs. Rct for GCE/SNGQDs@AuNPs/CoP-BNF (seq.) (**30**)/**HB5** (**A** and **B**) and GCE/SNGQDs@AuNPs/CoP-BNF (seq.) (**30**)/**Trastuzumab** (**C** and **D**) based sensors. All experiments run in $K_3[Fe(CN)_6]^{3-/4-}$ (1 mM in 0.1 mol·L−1 KCl in 10 mM PBS (pH 7.4), showing selected HER2 concentrations.

Table 5.10. R_{ct} values obtained for the different electrode surfaces GCE/ (**28-30**) electrode numbers defined in **Table 5.11**) towards detection of HER2.

R_{ct}, Ω (% RSD) *			
Trastuzumab based - immunosensors			
[HER2] ng/mL	**GCE/ (28)**	**GCE/ (29)**	**GCE/ (30)**
1	2480 (11.9)	2200 (14.56)	4298 (4.77)
2	2730 (14.6)	2263 (6.19)	5506 (5.52)
3	3740 (6.91)	2813 (4.15)	7908 (3.62)
4	4640 (5.64)	3000 (6.17)	9642 (2.94)
5	5140 (1.61)	3293 (6.54)	10886 (0.25)
6	5620 (4.56)	3503 (6.85)	11876 (0.69)
7	5840 (7.09)	3880 (7.18)	13666 (0.53)
8	6760 (1.17)	4063 (4.38)	15314 (0.66)
9	7456 (2.15)	5593 (4.50)	15623 (0.75)
10	11800 (3.88)	7190 (4.33)	20973 (1.34)
HB5 aptamer based – aptasensors			
1	2663 (4.69)	733 (6.69)	1343 (9.57)
2	2773 (4.56)	769 (3.46)	1360 (2.82)
3	4530 (4.75)	947 (2.60)	4373 (4.29)
4	5633 (9.85)	1015 (2.74)	5763 (6.09)
5	6217 (1.24)	1547 (4.59)	7667 (1.23)
6	7267 (8.03)	1757 (4.84)	8972 (0.08)
7	7720 (0.69)	2053 (3.09)	10537 (0.52)
8	8903 (2.31)	2260 (3.04)	12700 (0.78)
9	12433 (2.82)	2297 (3.8)	13533 (1.86)
10	14567 (1.43)	2487 (3.7)	14567 (0.79)

Table 5.11. Limit of detection and sensitivities for detection of HER2 biosensors developed for GCE/ (**28-30**) surfaces. Linear range 1–10 ng/mL in all cases.

Probe[a]	Sensitivity (Ω.ng/mL)		LOD (ng/mL	
	Aptasensors (HB5)	**Immunosensors (Trastuzumab)**	**Aptasensors (HB5)**	**Immunosensors (Trastuzumab)**
GCE/SNGQDs@AuNPs (**28**)	9592	5882	0.0489	0.1072
GCE/CoP-BNF (**29**)	3565	2895	0.0259	0.0454
GCE/SNGQDs@AuNPs/CoP-BNF (seq.) (**30**)	18979	15751	0.0112	0.0327

5.2. LOD values obtained in this work compared to reported literature values

The LOD values obtained in this work were compared to literature values for aptamer and antibody-based detection of HER2 [213–231]. The values herein were found to be mostly lower than literature values, **Table 5.12**. Furthermore, the LOD values obtained for each probe in this work were below the 2-15 ng/mL HER2 cut-off range, this result qualifies these as possible competitors in HER2 biosensor design as well as potential applicability as diagnostic tools for early-stage breast cancer.

Table 5.12. Main features comparison between reported HER2 biosensors in literature and those developed in this work.

Method and electrodes	LR (ng/mL)	LOD (ng/mL)	Reference
GCE/**1** (2)/HB5	1-10	0.647	This work
GCE/SNGQDs (3)/HB5	1-10	0.292	This work
GCE/PPy@SNGQDs (4)/HB5	1 - 10	0.143	This work
GCE/PPy@**1** (5) /HB5	1 - 10	0.481	This work
GCE/PPy@SNGQDs/**1** (6) /HB5	1 - 10	0.00141	This work
GCE/PPy@**1**/SNGQDs (7)	1 - 10	0.0255	This work
GCE/PPy/SNGQDs(seq.) (8) /HB5	1 - 10	0.00513	This work
GCE/PPy/**1**(seq.) (9) /HB5	1 - 10	0.0674	This work
GCE/PPy/SNGQDs/**1**(seq.) (10)/HB5	1 - 10	0.0716	This work
GCE/PPy/**1**/SNGQDs(seq.) (11)/HB5	1 - 10	0.0980	This work
GCE/**2** (12)/HB5	1-10	0.061	This work

GCE/**3** (13)/HB5	1-10	0.051	This work
GCE/CeO_2NPs_{COOH} (14)/HB5	1-10	0.19	This work
GCE/CeO_2NPs_{COOH}/**2** (seq.) (15)/HB5	1 - 10	0.015	This work
GCE/CeO_2NPs_{COOH}/**3** (seq.) (16)/HB5	1 - 10	0.008	This work
GCE/SNGQDs/**3**(seq.) (17)/HB5	1-10	0.19	This work
GCE/ **3**(π)SNGQDs (18)/HB5	1-10	0.074	This work
GCE/AuNPs (19)/HB5	1-10	0.006	This work
GCE/AuNPs/**3** (seq.) (20)/HB5	1-10	0.058	This work
GCE/**4**(21)/HB5	0-10	0.24	This work
GCE/**4**(π)SNGQDs (22)/HB5	0-10	0.042	This work
GCE/**5** (23)/HB5(amide)	0-10	0.33	This work
GCE/**5** (23)/HB5(imine)	0-10	0.039	This work
GCE/**5**(π)SNGQDs (24)/HB5(amide)	0-10	0.0027	This work
GCE/**5**(π)SNGQDs (24)/HB5(imine)	0-10	0.014	This work
GCE/SNGQDs@CeO_2NPs (25)/HB5	1-10	6×10^{-5}	This work
GCE/**6** (26)/HB5	1-10	1×10^{-5}	This work
GCE/ SNGQDs@CeO_2NPs/**6** (seq.) (27)/HB5	1-10	5.9×10^{-6}	This work
GCE/ (25)/HB5-sandwich	1-10	3.5×10^{-5}	This work
GCE/ (26)/HB5-sandwich	1-10	1.8×10^{-6}	This work
GCE/ (27)/HB5-sandwich	0-10	8.8×10^{-7}	This work
GCE/SNGQDs@AuNPs (28)/HB5	0-10	0.0489	This work
GCE/ CoP-BNF (29)/HB5	0-10	0.0259	This work
GCE/SNGQDs@AuNPs/CoP-BNF (seq.) (30)/HB5	0-10	0.0112	This work
GCE/ (28)/Trastuzumab	0-10	0.1072	This work
GCE/ (29)/Trastuzumab	0-10	0.0454	This work
GCE/ (30)/ Trastuzumab	0 - 10	0.0327	This work
Electrochemical aptasensor	6 - 30	6.0	[213]
Electrochemical Sensor	10 - 150	4.9	[214]
Electrochemical Sandwich Immunosensor	1 - 100	0.28	[215]

Label Free Immunosensor	5×10^{-4} – 50	0.9995	[216]
Electrochemical Aptasensor	10^{-5}- 10^{2}	5	[217]
Label Free Immunosensor	0.001–1.0	2.47×10^{-3}	[218]
Label Free Immunosensor	10–110	7.4	[219]
Label Free Immunosensor	0.01–100	0.01	[220]
Sandwich assay	5×10^{-5} - 50	2×10^{-5}	[221]
Sandwich assay	0.1 - 32	26×10^{-3}	[222]
Electrochemical Aptasensor	10-150	2.1	[223]
Electrochemical Aptasensor	5-50	2.8	[224]
Electrochemical Aptasensor	$0 – 4 \times 10^{4}$	6×10^{3}	[225]
Sandwich assay	-	80	[226]
Sandwich assay	-	12.5	[227]
Label free aptasensor	-	210	[228]
Label free aptasensor	-	0.050	[229]
Aptasensor		5	[230]
Immunosensor		0.22	[231]

5.3. Conclusions

This chapter discussed the impedimetric detection of HER2 on various modified surfaces. The chapter outlines two strategies (i) signal-based amplification methods and (ii) target-based amplification methods for enhanced sensitivity and low detection limits. The efficiency of strategy (i) is demonstrated by the respective performance of the various Pc complexes (**1-6**) utilized, CoP-BNF as well as the selected SNGQDs, CeO_2NPs and AuNPs nanoparticles used. The results demonstrate the effect of Pc molecule, CoP-BNF and NPs structure on the electrochemical detection of HER2. The effect of spatial arrangement of the said nanostructures as well as electrode modification technique on sensitivity and LOD values is demonstrated. Pc complex **1** in combination with PPy and SNGQDs demonstrated the significance of combining two or more nanomaterials on the electrode surface for sensing. Using complex **1**, two different modification techniques of the GCE using SNGQDs, Pc **1** and polypyrrole were explored. The modification techniques included (i) GCE is modified via polymerization of pyrrole in the presence of either SNGQDs (PPy@SNGQDs) or Pc **1** (PPy@**1**), and (ii) GCE is modified via sequential adsorption of nanomaterials following pyrrole electropolymerization (e.g., PPy/SNGQDs(seq.) or PPy/**1**(seq.)). In general, the electrodes modified by sequential adsorption had better electron transfer properties (ΔEp, Rct) compared to their counter PPy/nanomaterial polymerization modified electrodes. The electrodes with single nanomaterials GCE/**1** and GCE/SNGQDs were the least performing towards the detection of HER2 compared to the rest of the electrodes. The best performing electrode towards the electrochemical detection of HER2 was GCE/ PPy@SNGQDs/**1** (**6**) with a limit of detection value 1.41 pm/mL. Complex **2** and **3**, demonstrate the role of structure, and therefore electrochemical properties. This phenomenon held true for these Pcs even

upon combination with the CeO_2NPs_{COOH}. The electrochemical activity of the two phthalocyanines as immobilization platforms for the HB5 aptamer (GCE/**2** (**12**)/HB5 and GCE/**3** (**13**)/HB5) and as signal amplifiers in the detection of HER2 was comparable owing to their structural similarities. The GCE/**3** (**13**)/HB5 based probe showed better performance in sensitivity and LOD value compared to its competitor probe GCE/**2** (**12**)/HB5). The combination of Pcs (**2** and **3**) with the CeO_2NPs_{COOH}: GCE/(**15**)/HB5 and GCE/(**16**)/HB5, resulted in improved LOD. Based on the results obtained for complexes **1-3**, the efficiency of phthalocyanine complexes as electrode modifiers for enhanced signal transduction and immobilization of the biorecognition element, HB5 aptamer is evident. Furthermore, seeing that the best results were obtained for complex **3**, more studies were conducted using Pc **3**, in combination with AuNPs, CeO_2NPs_{COOH} and SNGQDs; to investigate the effect of nanoparticles on the performance of Pc **3** molecule. The combination of the respective nanoparticles with the complex **3** on the electrode surface was achieved by sequential adsorption as well as, π-π stacking for SNGQDs. A higher sensitivity and low LOD value were obtained for the probe GCE/SNGQDs(π)**3** (**18**)/HB5, compared to the sequentially modified GCE/SNGQDs/**3** (seq.) (**17**)/HB5. This result demonstrates the effect of spatial arrangement and interactions of the nanomaterials on the electrode in biosensor design. Furthermore, compared to all Pc **3**/NP combinations, the best performance was observed for GCE/ (**16**)/HB5 were Pc **3** is combined with CeO_2NPs_{COOH}. Using complex **4** and **5**, the effect of symmetry and the nature of substituent on the performance of the designed aptasensor was demonstrated. The two Pc complexes were combined with SNGQDs via π-π stacking for enhanced activity and performance towards HER2 detection. The obtained results, showed that the ligands present on the molecule even after immobilization of HB5, do not only contribute to symmetry, but electron transfer properties which too is a major contributor to signal

generation. The best performance of the aptasensors containing was observed for the GCE/**5** (**23**)/HB5 (imine) compared to GCE/**4** (**21**)/HB5 in terms of sensitivity and LOD value. This held true even upon combination with SNGQDs, where GCE/(**24**)/HB5(imine) compared to GCE/ (**22**)/HB5. These results emphasized the known concept that asymmetric Pcs tend to have better electron transfer properties and redox activities compared to their symmetric counterparts. Upon Pc **4** and **5** conjugations to SNGQDs for electrode modification, higher sensitivities and better LOD values were obtained, further demonstrating the positive effects of combining two or more nanomaterials for improved detection signals of biosensors. Complex **6**, an asymmetric complex is used for electrode modification in combination with a nanocomposite SNGQDs@CeO_2NPs, for enhanced signal transduction and HB5 aptamer immobilization. Using the designed platform, strategy (ii) is employed; effect of arrangement and spatial distribution of the recognition element HB5, towards HER2 detection is investigated and outlined. On the modified surface, a sandwich assay is built towards HER2 detection and is compared to single aptamer assay. The best sensing performance was observed for the GCE/SNGQDs@CeO_2NPs/**6** (seq.) (**27**) based aptasensors for both the single aptamer and sandwich assays in terms of LOD and sensitivity. This is due to the enhanced charge transport property and loading capacity of the biomolecules when the SNGQDs@CeO_2NPs and Pc **6** are combined on the GCE for modification. This results further confirms the positive synergy effect of Pc and NPs combinations toward biosensor design, that has so been demonstrated in the results obtained for other complexes Pc **1-5**. The sandwich assays showed better sensing performance compared to the single aptamer based aptasensors. This can be attributed to the dual aptameric strategy involved in sandwich aptasensor design. The advantage of the single aptamer assay against the sandwich aptamer assay is the time of fabrication, where less time was needed for the former. Strategy (ii) was

further employed, through a comparative study for label-free GCE based impedimetric biosensing platforms prepared using both a Trasmatuzab and HB5 aptamer as bioreceptors. Using a CoP-BNF complex in the presence of SNGQDs@AuNPs the GCE was modified for biorecognition element. The combination of CoP-BNF and SNGQDs@AuNPs on the GCE surface GCE/ (**30**) showed a better performance towards HER2 detection, both for the GCE/ (**30**)/HB5 and GCE/ (**30**)/Trastuzumab surface compared to electrodes where individual nanomaterials were used for modification. The superiority of the aptamer as a bioreceptor compared to the antibody was shown in sensitivity and LOD values. Overall, the results obtained in this chapter show the efficiency of Pc complexes **1-6**, the CoP-BNF, SNGQDs, CeO_2NPs, AuNPs as electrode modifiers for signal transduction and biorecognition elements towards the impedimetric detection of HER2. Furthermore, the compatibility of these nanomaterials upon conjugation as well as the resulting synergy as demonstrated by improved signal output, renders them as potential tools for application for the design reliable sensing platforms for HER2 detection.

6. Real life sample analysis

The validity and potential applicability of the designed probes in real life was investigated by detection of HER2 in human serum samples. The experiments were done on human (male) blood serum, diluted (1:500 dilution factor) with 10 mM PBS (pH 7.4). The dilution of the human serum was appropriate to minimize the matrix effect. The human serum was spiked with various known concentrations of the HER2 antigen. The different probes were then tested on their ability to detect/ recover HER2, in the competitive human serum environment. The performance of each sensor was gauged in terms % recoveries, which is the ratio between the recovered HER2 amount and the spiked HER2 amount multiplied by 100. The ability of a particular sensor to detect HER2, or recover more than 80% of the spiked HER2 concentration validates its potential in real life application.

6.1. HER2 in human serum: apparent recovery

All aptasensors and immunosensors designed in this thesis (GCE/(**2**) - GCE/(**30**)) were investigated, on their ability to recover HER2 in human serum. Complexes **1-5** and CoP-BNF as well as the relevant conjugates-based sensors, five concentrations 1 ng/mL, 3 ng/mL, 5 ng/mL, 7 ng/mL and 9 ng/mL were spiked onto 1:500 diluted human serum. In the case of complex **6** based sensors, experiments for HER2 detection were conducted in in the picomolar range and as such 1 pg/mL, 3 pg/mL, 5 pg/mL, 7 pg/mL and 9 pg/mL known HER2 concentrations were used for determining % recoveries in human serum sample. The performance of each sensor is discussed accordingly below. Generally, the apparent recovery should be in the range of 80 – 110 % [**232**]. Any percentage outside of this range, can be attributed to the matrix effect [**233**]. The specificity of the various probes was investigated in terms of % recoveries of HER2 in human serum. **Table 6.1** shows the % recoveries obtained for all probes at the HER2 concentration of 7 ng/mL (complex **1-5** and CoP-BNF based probes) and 7 pg/mL (complex **6** based probes).

Table 6.1. Percentage recoveries obtained for all probes for the detection of HER2 in spiked human serum samples. Known [HER2] = 7 ng/mL (complex **1**-**5** and CoP-BNF based probes; GCE (**2**-**24**)) and 7 pg/mL (complex **6** based probes; GCE (**25**-**27**))

Modified Electrodes	% [HER2] recovered
GCE/**1** (**2**)/HB5	70
GCE/SNGQDs (**3**)/HB5	31
GCE/PPy@SNGQDs (**4**)/HB5	78
GCE/PPy@**1** (**5**) /HB5	75
GCE/PPy@SNGQDs/**1** (**6**) /HB5	28
GCE/PPy@**1**/SNGQDs (**7**)	58
GCE/PPy/SNGQDs(seq.) (**8**) /HB5	46
GCE/PPy/**1**(seq.) (**9**) /HB5	51
GCE/PPy/SNGQDs/**1**(seq.) (**10**)/HB5	72
GCE/PPy/**1**/SNGQDs(seq.) (**11**)/HB5	75
GCE/**2** (**12**)/HB5	34
GCE/**3** (**13**)/HB5	50
GCE/CeO_2NPs_{COOH} (**14**)/HB5	50
GCE/CeO_2NPs_{COOH}/**2** (seq.) (**15**)/HB5	44
GCE/CeO_2NPs_{COOH}/**3** (seq.) (**16**)/HB5	75
GCE/SNGQDs/**3** (seq.) (**17**)/HB5	81
GCE/ **3**(π)SNGQDs (**18**)/HB5	94
GCE/AuNPs (**19**)/HB5	63
GCE/AuNPs/**3** (seq.) (**20**)/HB5	86
GCE/**4**(**21**)/HB5	68
GCE/**4**(π)SNGQDs (**22**)/HB5	84
GCE/**5** (**23**)/HB5(amide)	73

GCE/**5** (**23**)/HB5(imine)	76
GCE/**5**(π)SNGQDs (**24**)/HB5(amide)	93
GCE/**5**(π)SNGQDs (**24**)/HB5(imine)	79
GCE/SNGQDs@CeO_2NPs (**25**)/HB5	70*
GCE/(**25**)/HB5-sandwich	80*
GCE/**6** (**26**)/HB5	83*
GCE/(**26**)/HB5-sandwich	83*
GCE/SNGQDs@CeO_2NPs/**6** (seq.) (**27**)/HB5	92*
GCE/(**27**)/HB5-sandwich	83*
GCE/SNGQDs@AuNPs (**28**)/HB5	85
GCE/ (**28**)/Trastuzumab	90
GCE/ CoP-BNF (**29**)/HB5	90
GCE/ (**29**)/ Trastuzumab	74
GCE/SNGQDs@AuNPs/CoP-BNF (seq.) (**30**)/HB5	96
GCE/ (**30**)/Trastuzumab	91

*= HER2 in pg/mL range

6.1.1. Complex 1 and related probes

Tables 6.1 & 6.2 show % recoveries for the probes GCE/PPy/**1**/SNGQDs(seq.) (**11**)/HB5 and GCE/PPy@SNGQDs/**1** (**6**)/HB5 as examples: at each concentration (n=3) with the relative standard deviation (% RSD), the rest of the data is shown in **Table A1**. Sequential addition gave higher recoveries when both complex **1** and SNGQDs are present, **Table A1**. The probes all had a percentage recovery higher than 100% at 1 ng/mL HER2. The sensors sowed sensitivity to the HER2 protein in human serum, particularly the GCE/PPy/**1**/SNGQDs/(**11**)/HB5 had % recoveries above 75 %, implying its considerable potential as an effective alternative method for the early detection of HER2 in human serum.

Table 6.2. Percentage recoveries for the detection of HER2 in spiked human serum selected probes.

A. GCE/PPy/1/SNGQDs (11) HB5

[HER2] added	R_{ct} 1 (Ω)	R_{ct} 2 (Ω)	R_{ct} 3 (Ω)	Average	SDEV	% RSD	% [HER2] Recovered
1	2580	3001	3310	2964	366	12.36	121
3	16200	15400	15100	15567	569	3.65	91
5	21000	22300	23000	22100	1015	4.59	83
7	25500	25900	26100	25833	306	1.18	75
9	33500	32600	33800	33300	624	1.88	95

B. GCE/PPy@SNGQDs/1 (6) HB5

[HER2] added	R_{ct} 1 (Ω)	R_{ct} 2 (Ω)	R_{ct} 3 (Ω)	Average	SDEV	% RSD	% [HER2] recovered
1	1258	1301	1331	1297	37	2.83	146
3	29880	29989	29200	29690	428	1.44	73
5	35700	37600	36700	36667	950	2.59	50
7	21800	21700	21500	21667	153	0.71	28
9	19800	21000	20200	20333	611	3.00	21

6.1.2. Complex 2 and 3 based electrodes.

The probes GCE/**2** (**12**)/ HB5 and GCE/**3** (**13**) /HB5 had % recoveries of 34–56 % and 43–65 %, respectively, with the highest recovery being observed at 3 ng/mL in both cases, **Table A2**. The probe GCE/CeO_2NPs_{COOH} (**14**)/HB5 had % recoveries (50–66 %), with the highest recoveries obtained at 3 ng/mL. An increased % recovery was observed upon incorporation of the phthalocyanines structures with the cerium nanoparticles. The GCE/CeO_2NPs_{COOH}/**2** (seq.) (**15**)/HB5 and GCE/CeO_2NPs_{COOH}/**3** (seq.) (**16**)/ HB5 had % recoveries (30–66 %) and (66–79 %) respectively, with the highest recovery at 5 ng/mL for probe **16** and 3 ng/mL for probe **15**, **Table 6.3**. The overall best performing probe for probes based on complex **2** and **3**, for the recovery of HER2 in human serum was GCE/CeO_2NPs_{COOH}/**3** (seq.) (**16**)/HB5 at all concentrations. The results obtained show that GCE/CeO_2NPs_{COOH}/**3** (seq.) (**16**)/HB5 has the feasibility and potential for real life application of the detection of HER2 in early breast cancer diagnosis in human serum.

The significance of combining Pc complexes with various NPs for enhanced biosensor designed was further demonstrated for complex **3** in combination with SNGQDs and AuNPs**.** An improvement was observed for Pc **3** in the presence of each of the nanoparticles (CeO_2NPs_{COOH} or SNGQDs or AuNPs), and the best % recoveries were observed for GCE/AuNPs/**3** (seq.) (**20**)/HB5 (86 % − 120 %). The probe GCE/**3**(π)SNGQDs (**18**)/HB5 (59 % − 114 %), had better % recoveries compared to its counterpart: sequentially modified surface GCE/SNGQDs/**3** (seq.) (**17**)/ HB5 (58% − 119 %) **Table A2**. The probe GCE/AuNPs/**3** (seq.) (**20**)/HB5 has the highest potential in real life application of the detection of HER2 in early breast cancer diagnosis in human serum based on the % recoveries, which were higher than 80 %.

Table 6.3. Percentage recoveries for the detection of HER2 in spiked human serum, showing probes based on complex **2** and **3** in the presence of CeO_2NPs_{COOH} as examples.

GCE/CeO_2NPs_{COOH}/2 (seq.) (15)/HB5

[HER2] added ng/mL	R_{ct} 1 (Ω)	R_{ct} 2 (Ω)	R_{ct} 3 (Ω)	Average	SDEV	% RSD	%[HER2] recovered
3	18000	19300	19000	18767	681	3.63	66
5	24500	26100	25800	25467	850	3.34	53
7	28000	28300	29700	28667	907	3.17	44
9	25500	25900	26100	25833	306	1.18	30

GCE/CeO_2NPs_{COOH}/3 (seq.) (16)/HB5

[HER2] added ng/mL	R_{ct} 1 (Ω)	R_{ct} 2 (Ω)	R_{ct} 3 (Ω)	Average	SDEV	% RSD	%[HER2] recovered
3	21200	20800	21800	21267	503	2.37	72
5	36000	36200	35800	36000	200	0.56	79
7	41200	41500	45600	42767	2458	5.75	75
9	43500	48200	46000	45900	2352	5.12	66

6.1.3. Complex 4 and 5 based probes

The accuracy and precision of the various aptasensors was evaluated by % recovery and the relative standard deviation (RSD) calculations respectively. The recovery amounts were higher when the respective phthalocyanines **4** and **5** were combine with the SNGQDs. The best recovery amounts were obtained for the GCE/**5**(π)SNGQDs (**24**)/HB5(amide) in the range of 83 % − 111 %. The best percentage recovery for phthalocyanines alone based probes was observed for the GCE/**5** (**23**)/HB5(amide) in the range 73 % – 101 %. The relative standard deviations were less than 8 %, revealing the utilization potentiality of the various aptasensor towards the detection of HER2 in the diagnosis of breast cancer. **Table 6.4** shows percentage recoveries obtained for GCE/(**23**) and GCE/(**24**) as examples, the rest of the data is shown in **Table A3**.

Table 6.4. Percentage recoveries for the detection of HER2 in spiked human serum, showing the best performing complex **5** based probes.

GCE/**5** (**23**)/HB5 (amide)

[HER2] added ng/mL	R_{ct} 1 (Ω)	R_{ct} 2 (Ω)	R_{ct} 3 (Ω)	R_{ct} average (Ω)	SDEV	%RSD	[HER2 recovered]
1	26100	26700	26700	26500	283	1.07	101
3	39500	40000	40800	40100	535	1.33	73
5	46800	46200	48000	47000	748	1.59	75
7	50000	52500	50500	51000	1080	2.12	73

GCE/**5**(π)SNGQDs (**24**)/HB5 (amide)

[HER2] added ng/mL	R_{ct} 1 (Ω)	R_{ct} 2 (Ω)	R_{ct} 3 (Ω)	R_{ct} average (Ω)	SDEV	%RSD	[HER2 recovered]
1	14000	15600	16600	15400	1070	6.95	111
3	72500	73000	73800	73100	535	0.73	83
5	117800	115200	118000	117000	1275	1.09	91
7	144000	142000	143000	143000	816	0.57	93

6.1.4. Complex 6 based probes: Sandwich vs. Single aptamer

The results obtained for the single and sandwich aptamer assay for the probe GCE/SNGQDs@CeO_2NPs/**6** (seq.) (**27**) surface is shown as an example, **Table 6.5**. The rest of the data is shown in the appendix **Table A4**. Both the sandwich assay and single aptamer assay, showed recoveries higher than the 100 % maximum acceptable value at 1 pg/mL. The single aptamer assay GCE/(**27**)/HB5/**HER2**, had recoveries (88 -96 %, excluding 1 pg/mL), compared to the sandwich assay GCE/(**27**)/HB5/**HER2**/HB5-SNGQDs@CeO_2NPs assay (71–83 %, excluding 1 pg/mL). The results obtained show the feasibility and potential of the aptasensors for real life applications of the detection of HER2 in early breast cancer diagnosis in human serum.

Table 6.5. Percentage recoveries for the detection of HER2 in spiked human serum, showing the single assay vs. sandwich assay for the GCE/(**27**) surface.

GCE/(**27**)/HB5/HER2							
[HER2] added pg/mL	**R_{ct} 1 (Ω)**	**R_{ct} 2 (Ω)**	**R_{ct} 3 (Ω)**	**Average (Ω)**	**SDEV**	**%RSD**	**% [HER2] recovered**
1	2260	2261	2256	2259	3	0.12	220
3	135 000	134 000	130 000	133 000	2646	1.99	88
5	597 000	598 000	599 000	598 000	1000	0.17	96
7	820 000	840 000	800 000	820 000	20000	2.44	92

GCE/(**27**)/HB5/**HER2**/ HB5-SNGQDs@CeO_2NPs							
[HER2] added pg/mL	**R_{ct} 1 (Ω)**	**R_{ct} 2 (Ω)**	**R_{ct} 3 (Ω)**	**Average (Ω)**	**SDEV**	**%RSD**	**% [HER2] recovered**
1	850	750	800	800	50	6.25	179
3	56300	56400	57700	56800	781	1.38	71
5	450 000	420 000	420 000	430 000	17321	4.03	84
7	630 000	610 000	620 000	620 000	10000	1.61	83

6.1.5. CoP-BNF based probes: Aptamer vs. Antibody

Table 6.6 shows the results obtained for the GCE/SNGQDs@AuNPs/CoP-BNF (seq.) (**30**) based aptasensor and immunosensor as an example. The rest of the data obtained for probes based on the CoP-BNF are shown in the appendix, **Table A5**. At the HER2 concentration 1 ng/mL, the HB5 containing surface showed better recoveries at all electrode surfaces. At 7 ng/mL, electrodes containing CoP-BNF {(GCE/CoP-BNF (**29**) and GCE/SNGQDs@AuNPs/CoP-BNF (seq.) (**30**)} showed better recovery for the aptasensor than the immunosensor, **Table A5, Table 6.6**. The results obtained demonstrate the competitiveness of both the antibody and aptamer as capture probes in the design of sensitive biosensors. The smaller size of the aptamer and its ability to fold, poses an advantage for sensing at higher concentrations as seen for the probes GCE/CoP-BNF/HB5 (**29**) and GCE/SNGQDs@AuNPs/CoP-BNF (seq.) (**30**)/HB5, **Tables A5, 6.1 & 6.6.** Antibodies are susceptible to pH changes and denatured antibodies cannot be repaired, while aptamers are fairly stable and are easily refolded if denatured, hence better recoveries for the latter.

Table 6.6. Percentage recoveries for the detection of HER2 in spiked human serum, showing GCE/SNGQDs@AuNPs/CoP-BNF (seq.) (**30**) surface.

Aptasensor (HB5)

[HER2] added ng/mL	R_{ct} 1	R_{ct} 2	R_{ct} 3	Average (Ω)	SDEV	% RSD	% [HER2] Recovered
1	1710	1700	1800	1737	45	2.59	142
3	11630	11110	11520	11420	224	1.96	79
5	19930	21920	20390	20747	851	4.10	78
7	31200	31410	31080	31230	136	0.44	96

Immunosensor (Trastuzumab)

[HER2] added ng/mL	R_{ct} 1	R_{ct} 2	R_{ct} 3	Average (Ω)	SDEV	% RSD	% [HER2] Recovered
1	1888	1970	1840	1899	66	3.46	110
3	14700	14200	15000	14633	404	2.76	80
5	21800	21700	24600	22700	1646	7.25	83
7	30600	28400	30200	29733	1172	3.94	91

6.2. Conclusion

The sensors designed in this work showed relatively good performance in human serum, proving potential applicability in real life application for HER2 detection. The results obtained further demonstrated the applicability of phthalocyanines for electrode modification in biosensor design. Pc complexes **1-6**, on a GCE all showed the ability to detect HER2 in human serum. Furthermore, the ability of each Pc complexes (**1-6**) to detect HER2 in human serum was improved upon coupling with a relevant nanoparticle. Pc complex **1**, had the highest % recovery when combined with PPy and SNGQDs via sequential adsorption. The same was observed for complexes **2** and **3** when combined with CeO_2NPs**.** It was also observed that, the degree to which a Pc complex performance is enhanced is dependent on the type of nanoparticle to which its coupled. Pc **3** complex had the highest % recovery when coupled with AuNPs, compared to when combined with SNGQDs and CeO_2NPs_{COOH} respectively. Pc **5** had a higher % recovery compared to Pc **4**, regardless, both complexes had higher % recoveries of HER2 when coupled with SNGQDs. Pc complex **6** had the highest % recovery when coupled with SNGQDs@CeO_2NPs for both the single assay and the sandwich assay. In the case of CoP-BNF related probes, higher % recoveries were obtained for the probes where the porphyrin framework is combined with SNGQDs@AuNPs. The CoP-BNF based probes: aptasensors had higher recoveries at higher HER2 concentrations, while the opposite was observed for the immunosensors except for 1 ng/mL. Overall, these results demonstrate the efficiency of Co based Pc and porphyrin complexes for electrode modification in biosensor design. The significance of combining the Pc complexes with different NPs for enhanced performance is further demonstrated. The results also demonstrate the significance of either biorecognition elements: aptamer or antibody in biosensors aimed at real life application. The

combinations attempted in this work could therefore be used as building blocks, concepts for consideration towards the design and development of stable, low cost and efficient HER2 electrochemical biosensors.

7. Stability Characteristics: Repeatability, shelf-life and surface regeneration

Biosensors are prone to ageing, which can be characterized by a decrease in signal. Biosensor stability is of crucial importance for commercial success. This chapter reports on the stability of the designed sensors considering repeatability, shelf-life and reusability. For the first time, this thesis reports on the chemical regeneration of both an aptamer and antibody based electrochemical biosensor for HER2. Furthermore, the reusability of both a sandwich assay and single aptamer assay is confirmed for the first time using chemical regeneration. The results obtained present the design of sensors towards low cost, stable and reusable HER2 diagnostic tools, towards early-stage breast cancer diagnosis.

7.1. Repeatability

Repeatability refers to the agreement between successive measurements of the same sample, **Figure 7.1** (showing for GCE/SNGQDs@AuNPs/CoP-BNF (seq.) based probes at HER2= 5 ng/mL as an example). The repeatability of the designed immunosensors and aptasensors is demonstrated throughout, the experiments were run (n = 3) at all concentrations for all **30** electrodes designed in this thesis: acceptable relative standard deviation (% RSD) for all probes was obtained, **Table 5.1, 5.3, 5.4, 5.6, 5.8 and 5.10**.

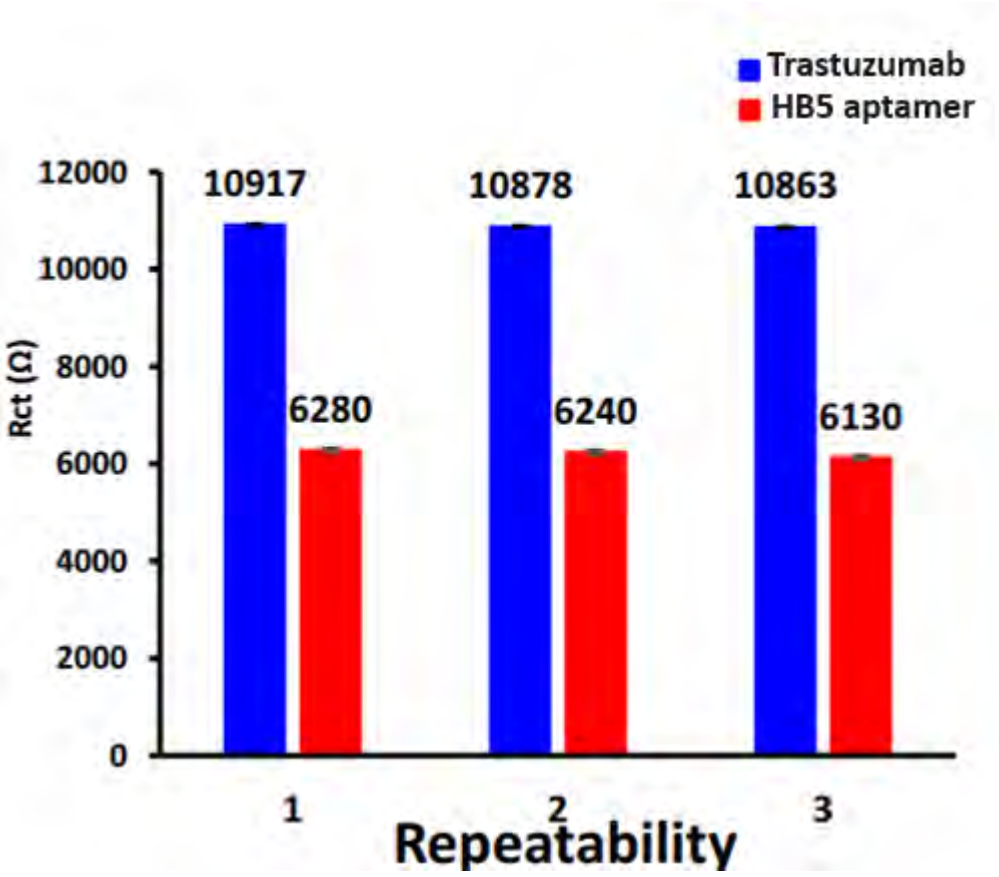

Figure 7.1. Repeatability of the GCE/SNGQDs@AuNPs/CoP-BNF (seq.)/**HB5**/HER2 and GCE/SNGQDs@AuNPs/CoP-BNF (seq.)/**Trastuzumab**/HER2. Repeatability for (n = 3 cycles, [HER2] = 5 ng/mL). All experiments were run in 1 mM $K_3[Fe(CN)_6]^{3-/4-}$ in 0.1 mol·L^{-1} KCl in 10 mM PBS (pH 7.4). Numbers on graph are R_{ct} values.

7.2. Stability

The stability of a designed sensors can be defined as the degree of susceptibility to ambient disturbances in and around the biosensing system. The stability of a particular electrochemical sensor depends on the various steps towards the fabrication of the sensor [234, 235]; ranging from electrode modification with nanomaterials, the choice and immobilization of biorecognition elements used and therefore interaction with the analyte. The stability of the designed sensors was investigated using the shelf-life estimation method. Where, the sensors were stored at 4 °C over a period of 96 h. The response of each probe was analysed daily over the 96-hour period.

7.2.1. Complex 2, 3, 4 and 5 based probes

7.2.1.1. Complex 2 and 3 based probes

First the probes: GCE/**2**/HB5 and GCE/**3**/HB5 against each other, and then in combination with CeO_2NPs_{COOH} to form: GCE/CeO_2NPs_{COOH}/**2** (seq.)/HB5 and GCE/CeO_2NPs_{COOH}/**3** (seq.)/HB5 probes. The stability of a particular electrochemical sensor depends on the various steps towards the fabrication, ranging from electrode modification with nanomaterials, the choice and immobilization of biorecognition element used and therefore interaction with the analyte. The sensors designed were fabricated following a standard method. The only difference is the nanomaterials used as immobilization platforms and signal amplification. As such the stability of the sensors was investigated based on the immobilization of the HB5 aptamer on the various electrodes: GCE/**2**/HB5, GCE/**3**/HB5, GCE/CeO_2NPs_{COOH}/HB5, GCE/CeO_2NPs_{COOH}/**2** (seq.)/HB5 and GCE/CeO_2NPs_{COOH}/**3** (seq.)/HB5. This was essential, because the HB5 aptamer selectively binds to the HER2 during detection, and as such a stable and active HB5 platform prior to detection is key. After every 24-h period, the stability of the

sensor probes was investigated by running electrochemical impedance spectroscopy (EIS) and measuring the R_{ct} values in 1 mM $K_3[Fe(CN)_6]^{3-/4-}$ in 0.1 mol·L^{-1} KCl in 10 mM PBS (pH 7.4). The stability of each surface was assessed by looking at the change in R_{ct} values from the first 24 h up until the 96th h, and was characterized by using the relative standard deviation (RSD) of the daily obtained R_{ct} values. **Figure 7.2A** shows that all electrodes had %RSD values of less than 7, showing fair stability of the probes containing the aptamer, as well as the firmness with which the HB5 aptamer is attached on the modified surfaces. The lowest % RSD (day 1 - day 4) value obtained was that of the GCE/**3**/HB5 and GCE/CeO_2NPs_{COOH}/**3** (seq.) /HB5 probes both less than 1%.

Having established the stability of the modified electrodes containing the aptamers. The shelf-life stability of the sensors upon interaction with the HER2 analyte was investigated. The following electrodes: GCE/**2**/HB5/**HER2**, GCE/**3**/HB5/**HER2**, GCE/CeO_2NPs_{COOH}/HB5/**HER2**, GCE/CeO_2NPs_{COOH}/**2** (seq.) /HB5/**HER2** and GCE/CeO_2NPs_{COOH}/**3** (seq.) /HB5/**HER2** were tested for stability, where [HER2] = 5 ng/mL in 10 mM PBS (pH 7.4) stored at 4 °C. After every 24 h period, the stability of the sensors was investigated as mentioned above, the results obtained are shown in **Figure 7.2B**. Each measurement was made in triplicate (daily for each probe) and the experiment lasted 96 h. All electrodes showed fair stability towards HER2 over the 96 h, with acceptable standard deviations for biosensors. Most significantly, better stability was observed when Pc is coupled with NPs, compared to Pc alone.

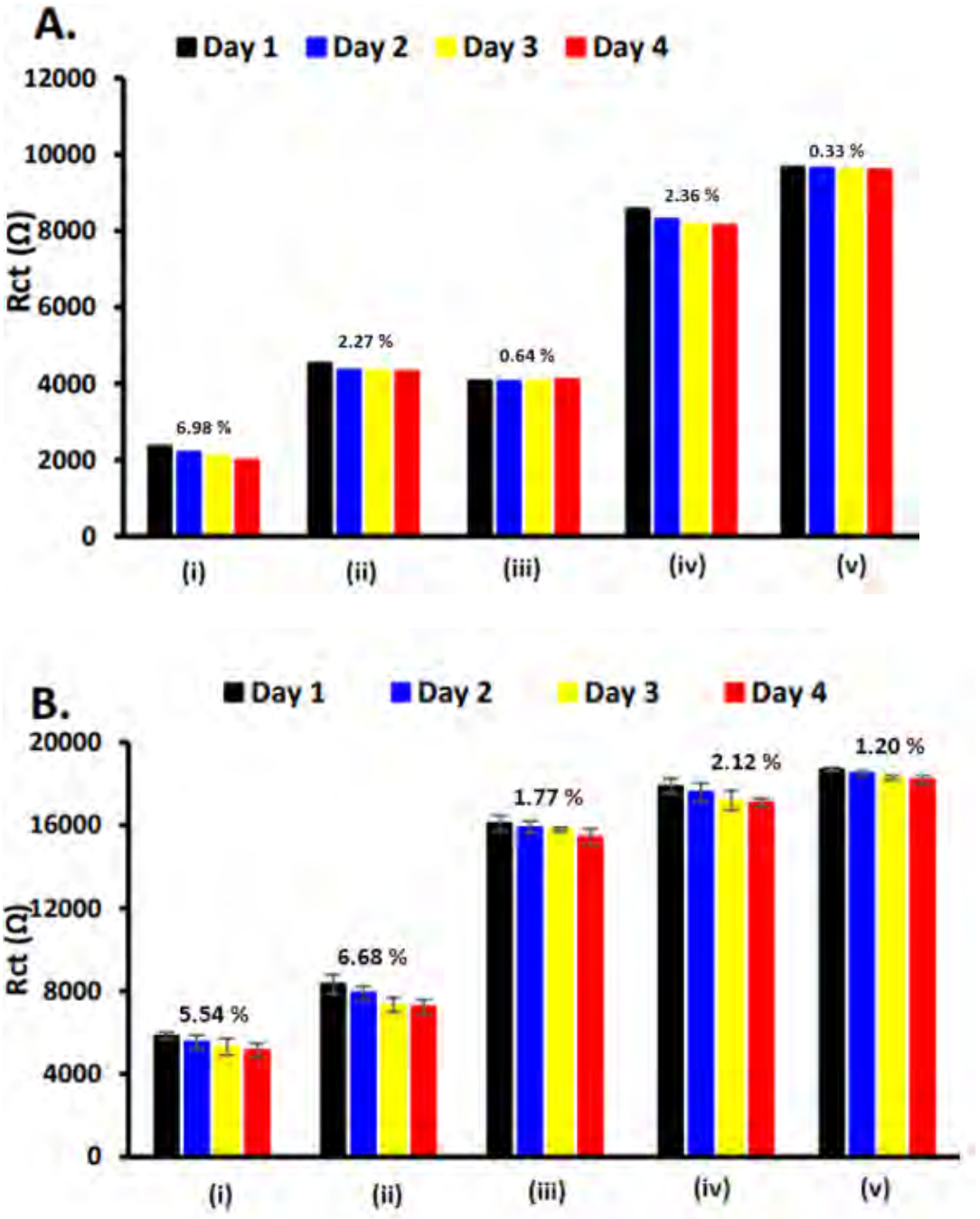

Figure 7.2. Stability plots of the probes designed in this work. (**A**) The stability of the probes prior interaction with the HER2 analyte, (overall % RSD values above bars, from day 1–4 for each electrode). (**B**) The stability of the probes upon interaction with HER2([HER2] = 5 ng/mL, n = 3). Where, (i) GCE/CeO_2NPs_{COOH}/HB5, (ii) GCE/**2**/HB5, (iii) GCE/**3**/HB5, (iv) GCE/CeO_2NPs_{COOH}/**3** (seq.)/HB5 and (v) GCE/CeO_2NPs_{COOH}/**2** (seq.)/HB5. All in $K_3[Fe(CN)_6]^{3-/4-}$ (1 mM in 0.1 mol·L^{-1} KCl in 10 mM PBS (pH 7.4).

7.2.1.2. Complex 4 and 5 based probes

The aptasensor GCE/**5**(**23**)/HB5(imine) showed better stability compared to the GCE/**4** (**21**)/HB5 aptasensor, **Figure 7.3**. The conjugate-based probes GCE/**5**(π)SNGQDs (**24**)/HB5(imine) and GCE/**4**(π)SNGQDs (**22**)/HB5 showed better stability when compared to the respective Pc are used without SNGQDs. The probes GCE/(**21**–**24**)/HB5 showed great storage stability over a 96-h period, with acceptable % RSD for biosensors.

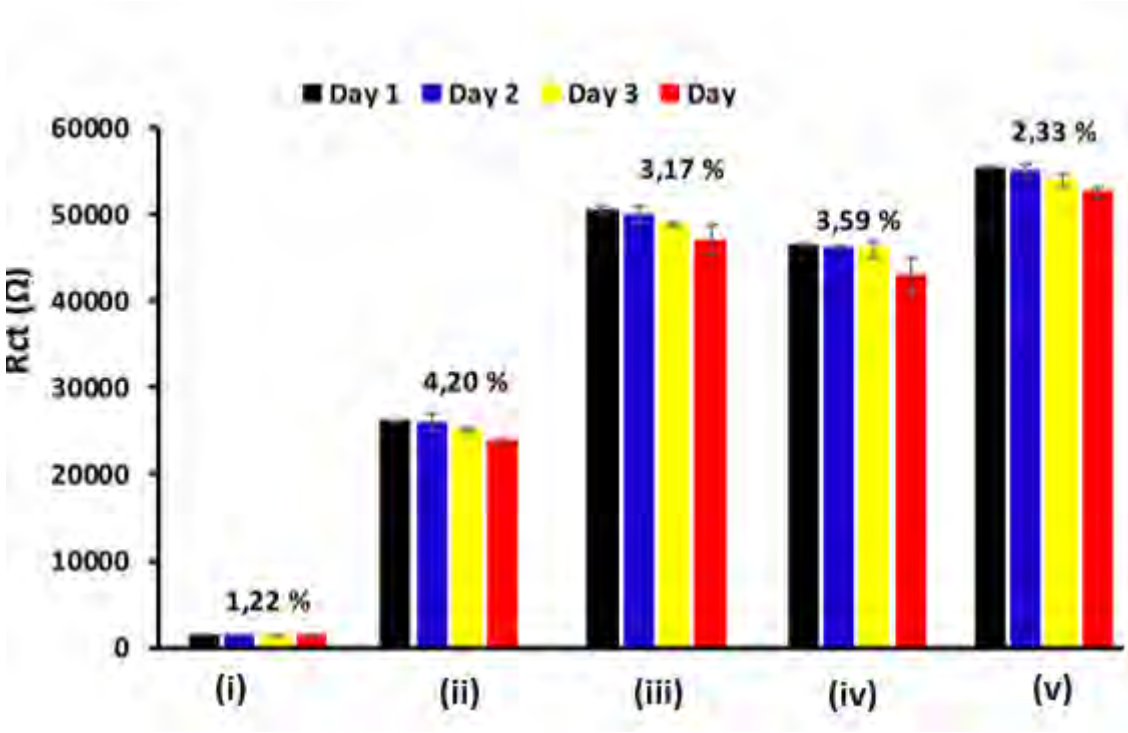

Figure 7.3. Shelf-life estimation of the various sensors over 96 h. The stability of the probes upon interaction with HER2 ([HER2] = 5 ng/mL, n = 3). Experiments were run in triplicate: error bars for each day represent the SDEV calculated for the n = 3 per day for each probe. Values above bars are % RSD values obtained over 4 days for each labelled probe. All in $K_3[Fe(CN)_6]^{3-/4-}$ (1 mM in 0.1 mol·L^{-1} KCl in 10 mM PBS (pH 7.4). Electrodes: (i) GCE/SNGQDs (**3**), (ii) GCE/**4** (**21**)/HB5, (iii) GCE/**4**(π)SNGQDs (**22**)/HB5, (iv) GCE/**5** (**23**)/HB5(imine) and (v) GCE/**5**(π)SNGQDs (**24**)/HB5(imine).

7.2.2. Complex 6 based probes: Sandwich vs. Single Aptamer

The stabilities of the best performing probes: GCE/SNGQDs@CeO_2NPs/**6** (seq.)/HB5/HER2 and GCE/SNGQDs@CeO_2NPs/**6** (seq.)/HB5/**HER2**/HB5-SNGQDs@CeO_2NPs were determined. The shelf life of each was estimated at [HER2] = 5 ng/mL in 10 Mm PBS (pH 7.4). The probes were stored at 4 °C over a period of 96 h. After every 24 h period, the stability of the sensors was investigated as mentioned above, **Figure 7.4**. Each measurement was made in triplicate daily for each probe, up until the fourth day. The results showed that the EIS response decreased to about 95% and 90 % for the aptasensors, GCE/SNGQDs@CeO_2NPs/**6** (seq.)/HB5/**HER2**/HB5-SNGQDs@CeO_2NPs and GCE/SNGQDs@CeO_2NPs/**6** (seq.)/HB5/HER2, respectively, of their initial value, indicating a very desirable stability. The sandwich assay showed better stability compared to the single aptamer assay.

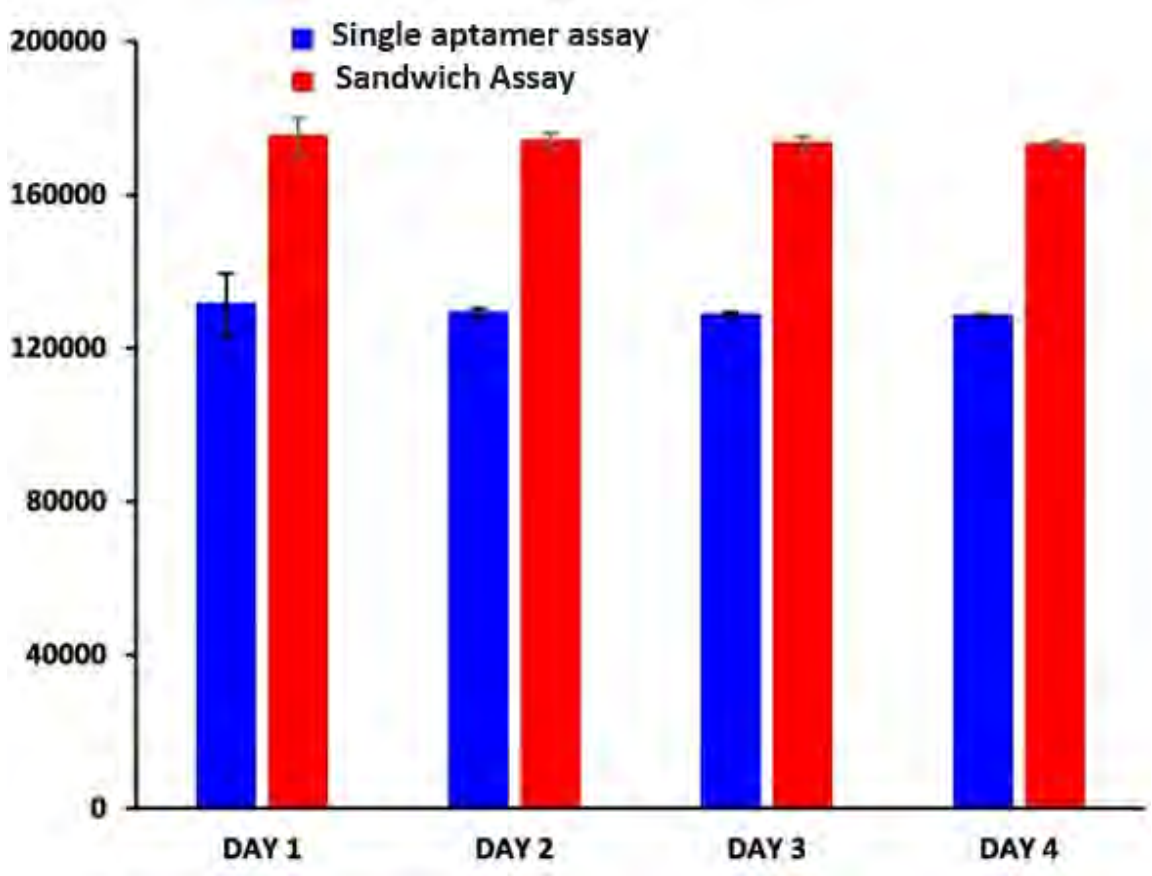

Figure 7.4. The stability of the best performing conjugate-based substrate GCE/SNGQDs@CeO_2NPs/**6** (seq.) (**27**), for both the single (blue) and the sandwich aptamer assay (red). Where, ([HER2] = 5 ng/mL, n = 3). All in $K_3[Fe(CN)_6]^{3-/4-}$ (1 mM in 0.1 mol·L–1 KCl in 10 mM PBS (pH 7.4).

7.2.3. CoP-BNF based electrodes: Aptamer vs. Antibody

The stabilities of the designed immunosensor and aptasensor were tested and compared using the best electrodes of each (in terms of LOD): GCE/SNGQDs@AuNPs/CoP-BNF (seq.)/HB5 and GCE/SNGQDs@AuNPs/CoP-BNF (seq.)/Trastuzumab, when comparing the respective HB5 and Trastuzumab containing electrodes. The electrodes were prepared and stored for 3 days at 4 °C, and monitored daily, **Figure 7.5**. There R_{ct} values were retained as

the first day up to 96% for the aptasensor, and 97% for the immunosensor. All electrodes showed similar electrochemical response with acceptable relative standard deviations for biosensors.

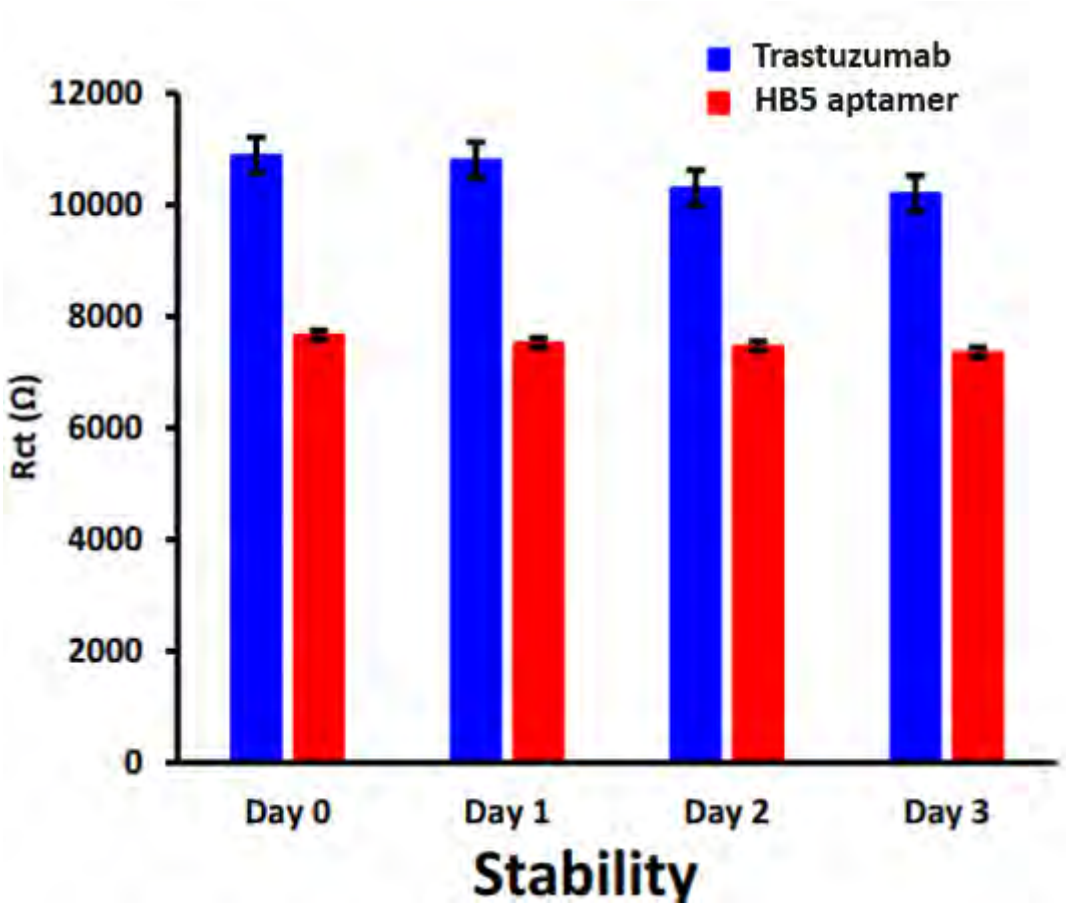

Figure 7.5. Stability of the GCE/SNGQDs@AuNPs/CoP-BNF (seq.)/**HB5**/HER2 and GCE/SNGQDs@AuNPs/CoP-BNF (seq.)/**Trastuzumab**/HER2 over 3 days, [HER2] = 5 ng/mL. All experiments were run in 1 mM $K_3[Fe(CN)_6]^{3-/4-}$ in 0.1 mol·L^{-1} KCl in 10 mM PBS (pH 7.4).

7.3. Surface Regeneration: Biosensor Reusability

Surface regeneration in biosensors can be defined as the ability to regenerate a sensing surface to allow for reusability. The reusability of any sensor is a promise to an inexpensive sensor design and development. Efficient regeneration involves the removal of a bound analyte while preserving the integrity of the ligand/capture probe [236, 237]. This quality of biosensors is highly dependent on the structural qualities of the capture probe, which then influences the surface of the sensor.

7.3.1. Aptamer vs Antibody: CoP-BNF based electrodes

Aptamers compared to antibodies are structurally malleable and can exist in distinct conformations under various conditions [238]. To investigate this advantage of aptamers in biosensor design and efficiency, the surface regeneration of the biosensor was studied. The surface regeneration efficiency of the antibody-HER2 antigen and aptamer-HER2 antigen surfaces, was investigated and is reported in **Figure 7.6**. The successful regeneration of the electrode surfaces was investigated based on three conditions: (i) the stability of the surface chemistry of the biosensor before and after dissociation, (ii) the ability of the antibody-HER2 or aptamer-HER2 interaction to dissociate fully under the set conditions, and (iii) the stability of the capture probes (aptamer/antibody) and their ability to retain activity and detect the analyte after regeneration. The electrodes GCE/SNGQDs@AuNPs/CoP-BNF (seq.)/**HB5**/HER2 and GCE/SNGQDs@AuNPs/CoP-BNF (seq.)/**Trastuzumab**/HER2 ([HER2] =5 ng/mL) as the best performing probes were investigated. The capture probes (aptamer/antibody)-HER2 antigen were disrupted using the chemical method. pH = 2.0 and 7.4 PBS buffers were employed for dissociation and regeneration, respectively. The probes were subjected to a pH 2 PBS buffer to render the desorption of the HER2 antigen off of the surfaces. The electrodes were then

rinsed with pH 7.4 PBS buffer to restore the conformation and integrity of the capture probes where possible, prior to proceeding to the next cycle of measurement. The two sensor probes GCE/SNGQDs@AuNPs/CoP-BNF (seq.)/**HB5**$_{original}$/HER2 (R_{ct} = 7040 Ω) and GCE/SNGQDs@AuNPs/CoP-BNF (seq.)/**Trastuzumab**$_{original}$/HER2 (R_{ct} = 10570 Ω) were incubated with pH 2 PBS buffer for 15 min, **Table 7.1**.

The % dissociation were calculated using **eq. 7.1** below:

$$\%\ dissociation = \frac{R_{ct\ (before\ treatment)} - R_{ct\ (after\ treatment)}}{R_{ct\ (before\ treatment)}} \times 100 \qquad \textbf{(7.1)}$$

where treatment means incubation with pH 2 PBS buffer. The progress of the capture probe-antigen dissociation was checked first at 5 min, to which the GCE/SNGQDs@AuNPs/CoP-BNF/**Trastuzumab**/HER2$_{t=5min}$ (R_{ct} = 10193 Ω) probe had % dissociation of 4%, while the GCE/SNGQDs@AuNPs/CoP-BNF (seq.)/**HB5**/HER2$_{t=5min}$ (R_{ct} = 3213 Ω) probe had % dissociation of 54%, **Fig. 7.6A**. After 15 min had elapsed, the GCE/SNGQDs@AuNPs/CoP-BNF (seq.)/**Trastuzumab**/HER2$_{t=15min}$ (R_{ct} = 9106 Ω) had a % dissociation of 14%, and the GCE/SNGQDs@AuNPs/CoP-BNF (seq.)**/HB5/**$_{t=15min}$ (R_{ct} = 1227 Ω) with a % dissociation of 83%, **Fig. 7.6B**, **Table 7.1**. To determine how much of the surface was regenerated, the probes before coupling with HER2 (before HER2 detection) i.e., GCE/SNGQDs@AuNPs/CoP-BNF (seq.)/**HB5** (R_{ct} = 1147 Ω) and GCE/SNGQDs@AuNPs/CoP-BNF (seq.)/**Trastuzumab** (R_{ct} = 3250 Ω) were observed and compared to the R_{ct} values obtained after the 15 min of acid treatment had elapsed, **Table 7.1**. Based on the R_{ct} values, it is obvious that the HB5 aptamer containing surface probe was regenerated, compared to that of the Trasmatuzab. The regenerated

surface GCE/SNGQDs@AuNPs/CoP-BNF (seq.)/**HB5**$_{regenerated}$ (R_{ct} = 1227 Ω), was tested for its reusability by detection of HER2 at 5 ng/mL: GCE/SNGQDs@AuNPs/CoP-BNF (seq.)/**HB5**$_{regenerated}$/HER2, **Fig. 7.6C**. The R_{ct} value obtained for the new surface (7313 Ω) was similar to that of the GCE/SNGQDs@AuNPs/CoP-BNF (seq.)/**HB5**$_{original}$/HER2 (R_{ct} = 7040 Ω) probe, **Fig. 7.6C**. The results obtained showed the superiority of aptamers compared to antibodies as a capture probe, where surface regeneration, reusability and cost effectiveness are concerned.

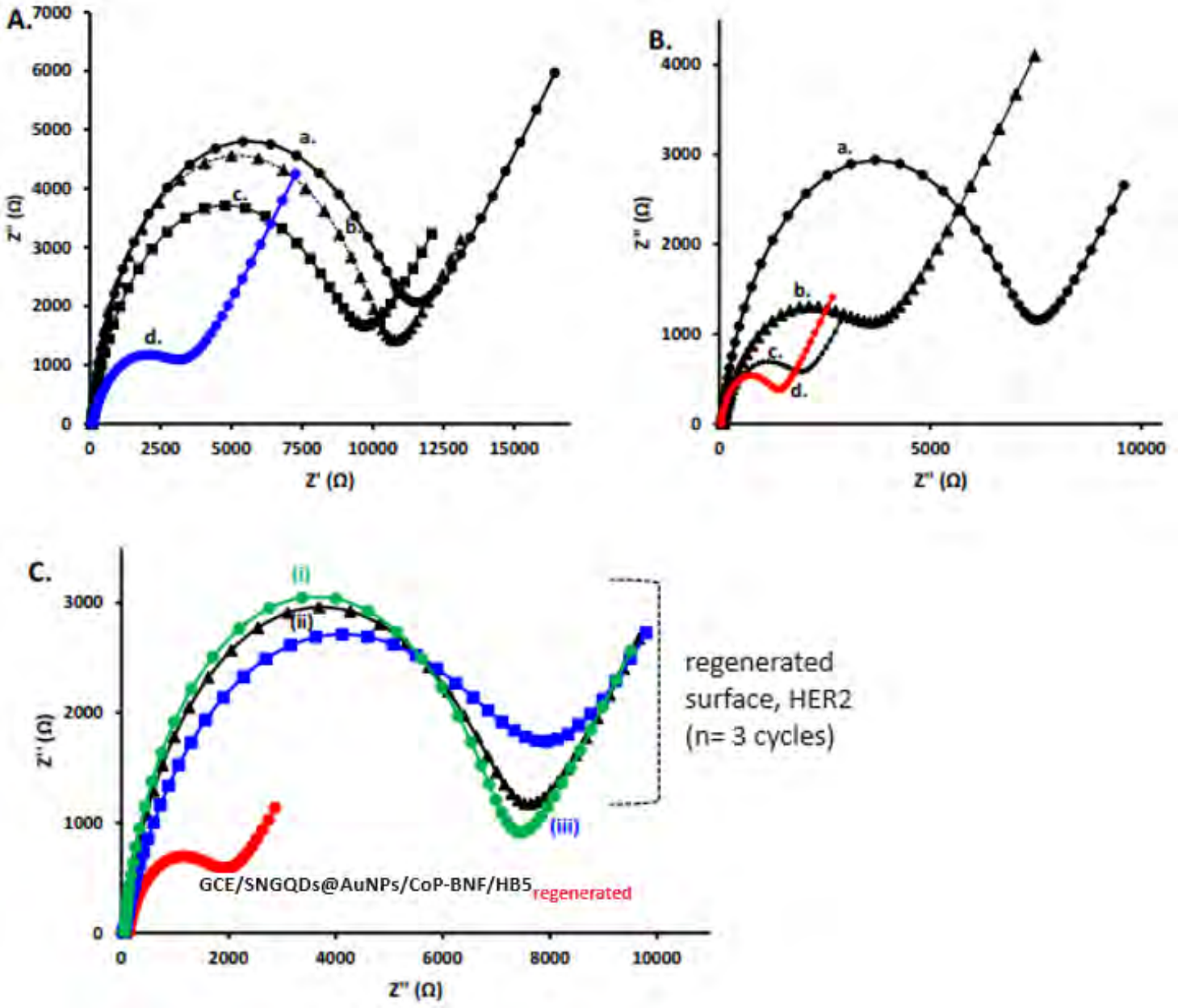

Figure 7.6. Nyquist plots obtained from surface regeneration of the probes: (**A**) GCE/SNGQDs@AuNPs/CoP-BNF (seq.)/**Trastuzumab** and (**B**) GCE/SNGQDs@AuNPs/CoP-BNF (seq.)/**HB5**, respectively. Where in both plots (**a**) represents the electrodes coupled with HER2 (5 ng/mL) prior to acid treatment, (**b**) and (**c**) electrode surfaces after acid (pH 2) treatment for 5 min and 15 min respectively and (**d**) the respective probes without HER2. (**C**) shows the successfully regenerated (using pH 7.4 buffer) GCE/SNGQDs@AuNPs/CoP-BNF (seq.)/**HB5**$_{regenerated}$ surface towards HER2 (5 ng/mL) detection, (n = 3 cycles; i, ii, and iii).

7.3.2. Single aptamer vs. Sandwich aptamer assay: Complex 6 based probes

The surface regeneration of the best performing probes: GCE/(27)/HB5/HER2/HB5-SNGQDs@CeO_2NPs and GCE/(27)/HB5/HER2 was investigated using the chemical method [51]. pH = 2.0 and 7.4 PBS buffers were employed for dissociation and regeneration, respectively as stated above. The probes were subjected to a pH 2 PBS buffer for a total of 15 min, to achieve the HB5-HER2 dissociation on the GCE. The electrodes were then rinsed with pH 7.4 PBS buffer to restore the conformation and integrity of the capture probes. Results obtained for both probes are shown in **Figure 7.7.** The single aptamer based aptasensor GCE/(27)/HB5/HER2 showed good surface regeneration (successful HB5-HER2 dissociation), as demonstrated by the progression of dissociation **Fig. 7.7A (a-c)**. The resulting surface after 15 min, had a comparable R_{ct} value (GCE/(27)/$HB5_{regenerated}$ = 22900 Ω) compared to the original GCE/(27)/$HB5_{original}$ (20400 Ω) prior to surface regeneration experiments, **Table 1, Fig. 7.7A(d)**. Similarly, for the sandwich probe GCE/(27)/HB5/HER2/HB5-SNGQDs@CeO_2NPs, **Fig. 7.7B (a-c)**: At the end of 15 min R_{ct} values of 54900 Ω for GCE/(27)/ HB5/$HER2_{regenerated}$, which was similar to the R_{ct} = 55733 Ω value obtained for GCE/(27)/HB5/$HER2_{original}$ prior to adding the HB5-SNGQDs@CeO_2NPs bioconjugate to form the sandwich assay. Based on the obtained R_{ct} values obtained post acid treatment, the surfaces based on the GCE/(27) surface were regenerated, **Table 7.1**. The single aptamer based GCE/(27)/$HB5_{regenerated}$ aptasensor was investigated for reusability, for the detection of [HER2] at 5 pg/mL. The R_{ct} value obtained for the new surface GCE/(27)/$HB5_{regenerated}$/HER2 (57200 Ω) was similar to that obtained originally for GCE/(27)/$HB5_{original}$/HER2 (55733 Ω). The results further demonstrate the structural flexibility and agility of aptamers as capture probes, where surface regeneration and reusability are concerned.

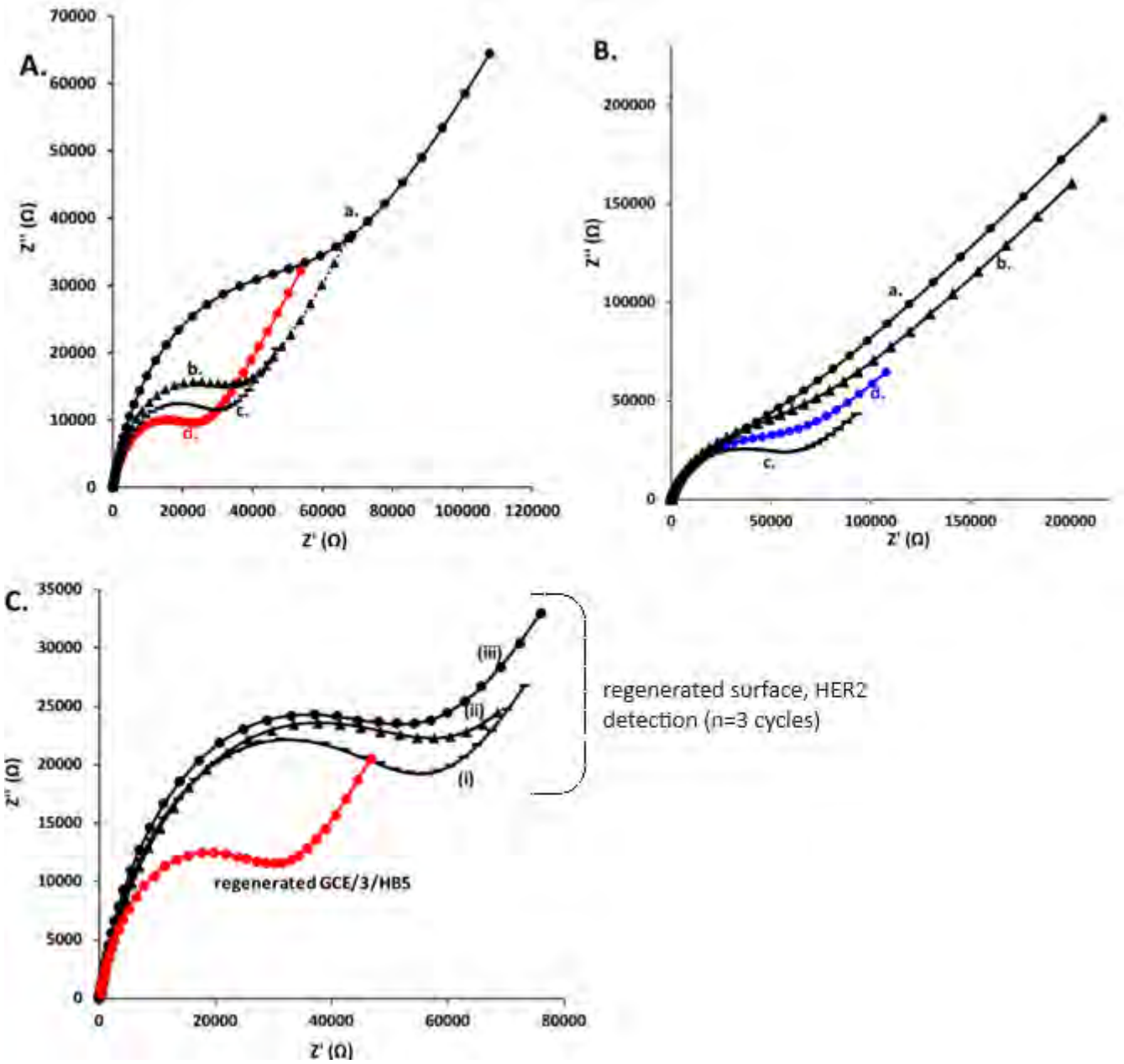

Figure 7.7. Nyquist plots obtained from surface regeneration of the probes: (A) GCE/(**27**)/HB5/HER2 and (B) GCE/(**27**)/HB5/**HER2**/HB5-SNGQDs@CeO_2NPs respectively. Where in both plots (a) represents the electrodes coupled with HER2 (5 pg/mL) prior acid treatment and after treatment of electrode surfaces with acid (pH 2) for (b) 5 min and (c) 15 min, and (d) the respective probes without HER2. Fig. 8C shows the successfully regenerated (using pH 7.4 buffer) GCE/(**27**)/HB5 surface towards HER2 (5 pg/mL) detection, (n = 3 cycles, i ii, and iii).

Table 7.1. Table of summary of modified surfaces subject to surface regeneration by means of acid treatment to attempt to break the receptor-HER2 interaction. Success is measured in terms of R_{ct} values: values in brackets 1st column vs. values in 2nd column.

Modified Surface, R_{ct} at t=0 **HER2-HB5 / HER2-antibody bound together**	**Modified Surface, R_{ct} at t =15 min** **HER2-HB5 / HER2-antibody bond broken: surface for sensing re-generated**	**HER2-HB5 reformed using the regenerated surface (HER2 detection with newly formed surface)**
GCE/(**27**)/HB5/**HER2** 55773 Ω (20400 Ω)	GCE/(**27**)/HB5 22900 Ω	GCE/(**27**)/$HB5_{regen}$/**HER2** 57200 Ω
GCE/(**30**)/**HB5**/HER2 7040 Ω (1147 Ω)	GCE/(**30**)/**HB5** 1227 Ω	GCE/(**30**)/**HB5**/HER2 7313 Ω
GCE/(**30**)/**Trastuzumab**/HER2 10570 Ω (3250 Ω)	GCE/(**30**)/**Trastuzumab** 9106 Ω (Surface not regenerated)	-

Notes: The **Trastuzumab**-HER2 bond could not be broken therefore sensor not reusable, blank space 3rd column. Regenerated surfaces were re-used for HER2 detection, results shown in column 3rd column, comparable to the non-bracketed values in 1st column implying re-usability of probes.

7.4. Conclusion

The probes were all tested for stability and each result was run in triplicate, with acceptable %RSD values confirming the accuracy of the method of detection. The shelf-life stability results, show that the designed aptasensors are stable even before interaction with HER2. This is important, because the signal for HER2 detection is dependent on the ability of the modification material (e.g., Pc **1-6**) to hold steadfast the recognition element on the electrode surface upon immobilization. Furthermore, it is important that the biological element used maintains its integrity over the expected time, as this will determine the interaction with the analyte and in turn the signal obtained. Great shelf-life was observed for the complex **2** and **3** based electrodes. The best performing being those based on complex **3**, with ~ 99% of the signal retained. It is important to note that in both complex **2** and **3**, the shelf-life stability was improved when combined with CeO_2NPs_{COOH}. The probes modified with complex **4** and **5** also showed great shelf-life with ~ 96% of the signal retained. Higher shelf-life stability was observed when Pc complexes (**4** and **5**) were combined with SNGQDs. It is important to note that for all sensors based on Pc (**1-6**), the Pc structure, its arrangement on the electrode as well as its conjugation to a particular NP has been the key factors of consideration for signal amplification and recognition element immobilization. The obtained results, where stability of the designed sensors is concerned confirms the positive effect of each strategy. Evidently, complex **3** performed better than complex **2**, in the same way the asymmetric complex **5** performed better than the symmetric complex **4**. Most importantly, in all cases better stability was observed for all complexes when combined with the relevant NPs further confirming the notion from previous chapters: that Pc complexes physicochemical properties of Pc are improved by NPs. In the case of complex **6** and CoP-BNF based probes, where the major focus

was antigen-receptor interactions. The sandwich assay showed better stability compared to single aptamer assay. This demonstrates the role of sandwiching the HER2 antigen between to recognition elements compared to just one. In the case of CoP-BNF probes, where both an HB5 aptamer and antibody are used for biorecognition: the stability of both the immunosensors and aptasensors was comparable. This result emphasizes the significance of either biorecognition element in biosensor design. The antibody and aptamer have obvious structural difference and properties, the receptors showed good stability at the pH 7.4. The overall results clearly show that the sensors designed were stable, even post interaction with the analyte over the set period of 96 h at pH 7.4. The reusability of the sensors in this work was investigated using GCE/SNGQDs@CeO_2NPs/**6** (seq.) (**27**) and GCE/SNGQDs@AuNPs/CoP-BNF (seq.) (**30**): On the modified surface GCE/SNGQDs@CeO_2NPs/**6** (seq.) (**27**) a sandwich assay and single aptamer assay was explored, and on the GCE/SNGQDs@AuNPs/CoP-BNF (seq.) (**30**) surface an aptamer and an antibody were immobilized separately for HER2 detection. In the case of GCE/SNGQDs@AuNPs/CoP-BNF (seq.) (**30**) surface-based sensors, the aptamer showed itself as a labile bioreceptor compared to the antibody. The aptamer based GCE/SNGQDs@AuNPs/CoP-BNF (seq.)/**HB5** was successfully regenerated and reusable, while the opposite was observed for the antibody based GCE/SNGQDs@AuNPs/CoP-BNF/**Trastuzumab** probe. This result, in the context of biosensor reusability and surface regeneration, shows the aptamer as the superior biorecognition element compared to the antibody. Both the single and sandwich aptamer assays based on the GCE/SNGQDs@CeO_2NPs/**6** (seq.) (**27**) surface, were successfully regenerated further cementing the agility and validity of the aptamer in the design of low cost and reusable sensors towards the detection of disease biomarkers.

8. Summary, conclusions and prospects

This chapter summarizes all the work discussed in this thesis and highlights again the novelty of the work and the new perspective it has brought to the fabrication and the development of breast cancer early diagnostic tools.

8.1. Thesis Overview

This thesis reports for the first time, on the use of CoPc complexes in combination with SNGQDs, AuNPs, CeO_2NPs_{COOH} for electrode modification for the sensitive detection of the early-stage breast cancer biomarker HER2. Similarly, a CoP-BNF was used and conjugated to SNGQDs@AuNPs. The nanostructures were synthesized and fully characterized prior to being used as electrode modifiers. The GCE was chosen as a transducing element, and as a result was modified and characterized at each step towards biosensor design. In some cased, a GCP was used for characterization. The adsorption/drop dry method was used as a technique for electrode modification, resulting in stable sensing platforms. The modified GCEs were used for signal transduction and immobilization of biorecognition elements specific to the HER2 antigen: HB5 aptamer and a trasmatuzab antibody. Different strategies for enhanced signal using the designed nanostructures were explored: varied Pc structure and symmetry, as well as conjugation of Pcs to different NPs for the development of novel sensing platforms. For the first time, antigen-receptor interactions; sandwich assay vs. single aptamer and antibody vs. aptamer for maximum signal were explored.

Throughout the thesis, the significance and role of combining two or more nanomaterials on the electrode surface in sensor design was demonstrated. The Co tetra carboxy phenoxy phthalocyanine (**1**), showed the highest sensitivity and low LOD values towards HER2 when combined with both PPy and SNGQDs: GCE/PPy@SNGQDs/**1**/HB5. Similarly, Co tetra phenoxy propionic acid (**2**) and Co tetra phenoxy acetic acid (**3**), performed better when combined with CeO_2NPs; GCE/CeO_2NPs_{COOH}/**2** (seq.)/HB5, GCE/CeO_2NPs_{COOH}/**3** (seq.)/HB5. The same was observed for Co tetra acetylphenoxy phthalocyanine (**4**), Co tris-(acetylphenoxy)-mono-phneoxyacrylic acid phthalocyanine (**5**), Co tris-3,5- dimethyl – phenoxy pyridine (5) -oxy- (2)-carboxylic acid phthalocyanine (**6**) and CoP-BNF when combined with SNGQDs,

SNGQDs@AuNPs and SNGQDs@CeO_2NPs, respectively. The effect of structure as relates to the ligands or functional groups, can be deduced from the individual Pc complexes (**1**-**6**). The highest sensitivity and lowest LOD was obtained for the asymmetric Pc **6**, compared to the symmetric **1** - **5.** All complexes **1 – 4** are tetra substituted, the performance of the complexes was in the order **3**> **2** > **4** > **1**. The best performing of all was observed to be complex **3**, placing the phenoxy acetic acid ligand superior in electron distribution in the Pc molecule and the opposite can be said for complex **1** and the carboxyphenoxy ligand in a tetra substituted Pc. Complex **4** had almost three times the sensitivity of complex **1**, this rendered the acetophenone ligand superior compared to carboxyphenoxy ligand. The specific detection of HER2 by the fabricated sensing platforms was aided by the HB5 aptamer. The primary chemistry of immobilization used is the DDC/NHS amide bond linkage. For the complexes **4** and **5**, acid catalysed imine bond formation was used. The effect of method of HB5 immobilization is demonstrated by the results obtained for complex **5**: the complex has three acetophenone ligands and a single phenoxyacrylic acid ligand. A higher sensitivity and low LOD value were observed in the case where HB5 was immobilized via imine bond; GCE/**5**/HB5 (imine), compared to when immobilized via amide bond GCE/**5**/HB5 (amide). More than the Pc structure, using the imine bond allows for linking of HB5 onto Pc **5** via three ligands, while the amide bond is only on one ligand, hence the higher sensitivity and low LOD value.

The antigen-receptor interactions and their role in the performance of a biosensors towards HER2 detection are reported. This thesis clearly outlines the superiority of the sandwich assay compared to the label free/single aptamer assay; the best performance was observed for the former compared to the latter in terms of LOD and sensitivity. Secondly, this thesis outlines the superiority of the HB5 aptamer compared to the Trastuzumab antibody in the electrochemical detection of HER2, at pH 7.4. These antigen-receptor interactions were

further characterized and differentiated using chemical surface regeneration to investigate the reusability of the designed sensors. The sandwich assay and single aptamer assay were proven reusable, as both surfaces were successfully regenerated. This is attribute to the structural flexibility of the aptamer as biorecognition as well as its lability as a ligand. A different outcome was observed for the Trastuzumab antibody when compared to the HB5 aptamer on the surface: GCE/SNGQDs@AuNPs/CoP-BNF. The surface GCE/SNGQDs@AuNPs/CoP-BNF/Trastuzumab could not be regenerated owing to the structural rigidity of the antibody compared to the aptamer, further showing aptamers preferable where reusability of biosensors is concerned. All sensors designed in this work showed good shelf-life stability and repeatability. The sensors designed in this work were all tested in real life samples, and acceptable percentage recoveries of the spiked HER2 concentrations were obtained. In all cases, the biosensors characteristics: sensitivity, LOD, linearity, repeatability and reusability were investigated. The designed sensors showed excellent results in the detection of HER2 in buffer and human serum sample. Furthermore, the sensors showed good linearity, sensitivity, repeatability with detection limits less than the 2–15 ng/mL HER2 cut-off value. The sensors showed sensitivity towards the HER2 protein and have considerable potential as an effective alternative method for the early detection of HER2.

8.2. Future Perspectives

The results demonstrate the efficacy and potential of metallophthalocyanines and porphyrin-related structures as electrode modifiers towards biosensor design. Furthermore, combining these cobalt based structures with various nanoparticles resulted in improved electron transfer and sensing efficiency. The best performing nanoparticle towards HER2 was observed to be AuNPs compared to the otherwise carbon based GQDs and CeO_2NPs. Be as it may, non-precious metallic nanoparticles are preferred owing to their abundant starting material and affordability. Therefore, as attempted in this work non-metallic carbon-based nanomaterials should be explored; both alone and in combination with other nanoparticles/nanomaterials toward low-cost and simple biosensor design. Further studies, can be conducted exploring more CoPc molecules with functional groups other than carboxylic groups. Different HER2 specific aptamers, other than the HB5 DNA aptamer can be investigated for recognition. In the case of sandwich assay, a secondary aptamer different from the primary aptamer can be used: combining two or more HER2 specific aptamers could even be better.

9. References

1. F. Lüönd, S. Tiede, G. Christofori, Breast cancer as an example of tumour heterogeneity and tumour cell plasticity during malignant progression, Br. J. Cancer, 125 (2021) 164.
2. L. Guo, D. Kong, J. Liu, L. Zhan, L. Luo, W. Zheng, Q. Zheng, C. Chen, S. Sun, Breast cancer heterogeneity and its implication in personalized precision therapy, Exp. Hematol. Oncol., 12 (2023) 3.
3. L. Ilic, G. Haidinger, J. Simon, M. Hackl, E. Schernhammer, K. Papantoniou, Trends in female breast cancer incidence, mortality, and survival in Austria, with focus on age, stage, and birth cohorts (1983–2017), Sci. Rep., 12 (2022) 7048.
4. L. Wilkinson, T. Gathani, Understanding breast cancer as a global health concern, Br. J. Radiol., 95 (2022) 20211033.
5. D. Crosby, S. Bhatia, K.M. Brindle, L.M. Coussens, C. Dive, M. Emberton, S. Esener, R.C. Fitzgerald, S.S. Gambhir, P. Kuhn, T.R. Rebbeck, S. Balasubramanian, Early detection of cancer, Science, 375 (2022) 9040.
6. L. Wang, Early Diagnosis of Breast Cancer, Sensors, 17 (2017) 1572.
7. N. Aristokli, I. Polycarpou, S.C. Themistocleous, D. Sophocleous, I. Mamais, Comparison of the diagnostic performance of Magnetic Resonance Imaging (MRI), ultrasound and mammography for detection of breast cancer based on tumor type, breast density and patient's history: A review, Radiography, 28 (2022) 848.
8. R. Sood, A.F. Rositch, D. Shakoor, E. Ambinder, K.-L. Pool, E. Pollack, D.J. Mollura, L.A. Mullen, S.C. Harvey, Ultrasound for Breast Cancer Detection Globally: A Systematic Review and Meta-Analysis, J. Glob. Oncol., 5 (2019) 00127.
9. Y. Gao, B. Reig, L. Heacock, D.L. Bennett, S.L. Heller, L. Moy, Magnetic Resonance Imaging in Screening of Breast Cancer, Radiol. Clin. North Am., 59 (2021) 85.

10. G.A. Mishra, S.A. Pimple, I. Mittra, R.A. Badwe, Screening for breast cancer: Cost-effective solutions for low- & middle-income countries, Indian J. Med. Res., 154 (2021) 229.
11. J. Marrugo-Ramírez, M. Mir, J. Samitier, Blood-Based Cancer Biomarkers in Liquid Biopsy: A Promising Non-Invasive Alternative to Tissue Biopsy, Int. J. Mol. Sci., 19 (2018) 2877.
12. B. Michela, Liquid Biopsy: A Family of Possible Diagnostic Tools, Diagnostics, 11 (2021) 1391.
13. V.K. Sarhadi, G. Armengol, Molecular Biomarkers in Cancer, Biomolecules, 12 (2022) 1021.
14. S. Afzal, M. Hassan, S. Ullah, H. Abbas, F. Tawakkal, M.A. Khan, Breast Cancer; Discovery of Novel Diagnostic Biomarkers, Drug Resistance, and Therapeutic Implications, Front. Mol. Biosci., 9 (2022) 783450.
15. S. Mittal, H. Kaur, N. Gautam, A.K. Mantha, Biosensors for breast cancer diagnosis: A review of bioreceptors, biotransducers and signal amplification strategies, Biosens. Bioelectron., 88 (2017) 217.
16. E.R. Sauter, Reliable Biomarkers to Identify New and Recurrent Cancer, Eur. J. Breast Health, 13 (2017) 162.
17. K.N. Seale, K.H.R. Tkaczuk, Circulating Biomarkers in Breast Cancer, Clin. Breast Cancer, 22 (2022) e319.
18. C. Gutierrez, R. Schiff, HER 2: Biology, Detection, and Clinical Implications, Arch. Pathol. Lab. Med., 135 (2011) 55.
19. Nikdouz, N. Namarvari, R. Ghasemi Shayan, A. Hosseini, Comprehensive comparison of theranostic nanoparticles in breast cancer, Am. J. Clin. Exp. Immunol., 11 (2022) 35350450.
20. W.P. Carney, HER2 status is an important biomarker in guiding personalized HER2 therapy, Pers. Med., 2 (2005) 317.

21. M.V. Dieci, F. Miglietta, G. Griguolo, V. Guarneri, Biomarkers for HER2-positive metastatic breast cancer: Beyond hormone receptors, Cancer Treat. Rev., 88 (2020) 102064.
22. E.V. Klocker, C. Suppan, Biomarkers in Her2- Positive Disease, Breast Care, 15 (2020) 586.
23. N. Iqbal, N. Iqbal, Human Epidermal Growth Factor Receptor 2 (HER2) in Cancers: Overexpression and Therapeutic Implications, Mol. Biol. Int., 2014 (2014) 852748.
24. E. Sajjadi, E. Guerini-Rocco, E. De Camilli, O. Pala, G. Mazzarol, K. Venetis, M. Ivanova, N. Fusco, Pathological identification of HER2-low breast cancer: Tips, tricks, and troubleshooting for the optimal test, Front. Mol. Biosci., 10 (2023) 1176309.
25. C.B. Moelans, R.A. de Weger, E. Van der Wall, P.J. van Diest, Current technologies for HER2 testing in breast cancer, Crit. Rev. Oncol. Hematol., 80 (2011) 380.
26. H. Nitta, B.D. Kelly, C. Allred, S. Jewell, P. Banks, E. Dennis, T.M. Grogan, The assessment of HER2 status in breast cancer: the past, the present, and the future, Pathol. Int., 66 (2016) 313.
27. C. Gutierrez, R. Schiff, HER2: biology, detection, and clinical implications, Arch. Pathol. Lab. Med., 135 (2011) 55.
28. N. Dendukuri, K. Khetani, M. McIsaac, J. Brophy, Testing for HER2-positive breast cancer: a systematic review and cost-effectiveness analysis, CMAJ Can. Med. Assoc. J., 176 (2007) 1429.
29. N. Bhalla, P. Jolly, N. Formisano, P. Estrela, Introduction to biosensors, Essays Biochem., 60 (2016) 20150001.
30. P. Mehrotra, Biosensors and their applications – A review, J. Oral Biol. Craniofacial Res., 6 (2016) 153.
31. V. Naresh, N. Lee, A Review on Biosensors and Recent Development of Nanostructured Materials-Enabled Biosensors, Sensors, 21 (2021) 1109.

32. L.M. Lechuga, Biosensor, in: M. Gargaud, R. Amils, J.C. Quintanilla, H.J. Cleaves, W.M. Irvine, D.L. Pinti, M. Viso (Eds.), Encycl. Astrobiol., Springer, Berlin, Heidelberg, 2011: pp. 200.
33. N.A.M. Said, Electrochemical biosensor based on microfabricated electrode arrays for life sciences applications, PhD Thesis, Universiy College Cork, 2014.
34. M. Sypabekova, A. Amantayeva, L. Vangelista, Á. González-Vila, C. Caucheteur, D. Tosi, Ultralow Limit Detection of Soluble HER2 Biomarker in Serum with a Fiber-Optic Ball-Tip Resonator Assisted by a Tilted FBG, ACS Meas. Sci. Au, 2 (2022) 309.
35. M. Loyez, M. Lobry, E.M. Hassan, M.C. DeRosa, C. Caucheteur, R. Wattiez, HER2 breast cancer biomarker detection using a sandwich optical fiber assay, Talanta, 221 (2021) 121452.
36. R. Ahirwar, Recent advances in nanomaterials-based electrochemical immunosensors and aptasensors for HER2 assessment in breast cancer, Microchim. Acta, 188 (2021) 317.
37. S. Chupradit, S.A. Jasim, D. Bokov, M.Z. Mahmoud, A.B. Roomi, K. Hachem, M. Rudiansyah, W. Suksatan, R. Bidares, Recent advances in biosensor devices for HER-2 cancer biomarker detection, Anal. Methods, 14 (2022) 1301.
38. A. Poturnayová, Ľ. Dzubinová, M. Buríková, J. Bízik, T. Hianik, Detection of Breast Cancer Cells Using Acoustics Aptasensor Specific to HER2 Receptors, Biosensors, 9 (2019) 72.
39. P. Zhang, J. Xiao, Y. Ruan, Z. Zhang, X. Zhang, Monitoring Value of Serum HER2 as a Predictive Biomarker in Patients with Metastatic Breast Cancer, Cancer Manag. Res., 12 (2020) 4667.
40. G. Kumar, K. Nandakumar, S. Mutalik, C.M. Rao, Biologicals to direct nanotherapeutics towards HER2-positive breast cancers, Nanomedicine Nanotechnol. Biol. Med., 27 (2020) 102197.

41. W. Tai, R. Mahato, K. Cheng, The role of HER2 in cancer therapy and targeted drug delivery, J. Control. Release Off. J. Control. Release Soc., 146 (2010) 264.
42. S. Arshavsky-Graham, C. Heuer, X. Jiang, E. Segal, Aptasensors versus immunosensors—Which will prevail? Eng. Life Sci., 22 (2022) 319.
43. K. Mahato, S. Kumar, A. Srivastava, P.K. Maurya, R. Singh, P. Chandra, Chapter 14 - Electrochemical Immunosensors: Fundamentals and Applications in Clinical Diagnostics, in: S.K. Vashist, J.H.T. Luong (Eds.), Handb. Immunoass. Technol., Academic Press, Cambridge, MA, USA, 2018: pp. 359.
44. I.-H. Cho, J. Lee, J. Kim, M. Kang, J.K. Paik, S. Ku, H.-M. Cho, J. Irudayaraj, D.-H. Kim, Current Technologies of Electrochemical Immunosensors: Perspective on Signal Amplification, Sensors, 18 (2018) 207.
45. F.S. Felix, L. Angnes, Electrochemical immunosensors – A powerful tool for analytical applications, Biosens. Bioelectron., 102 (2018) 470.
46. S. Sharma, H. Byrne, R.J. O'Kennedy, Antibodies and antibody-derived analytical biosensors, Essays Biochem., 60 (2016) 9.
47. S.K. Vashist, J.H.T. Luong, Chapter 2: Antibody Immobilization and Surface Functionalization Chemistries for Immunodiagnostics, in: S.K. Vashist, J.H.T. Luong (Eds.) Handb. Immunoass. Technol., Academic Press, Cambridge, MA, USA, 2018: pp. 19.
48. K. Baryeh, S. Takalkar, M. Lund, G. Liu, Introduction to medical biosensors for point of care applications, in: Roger J. Narayan (Ed) Med. Biosens. Point Care POC Appl., Woodhead, Cambridge, 2017: pp. 3.
49. D.H. Kim, J.M. Seo, K.J. Shin, S.-G. Yang, Design and clinical developments of aptamer-drug conjugates for targeted cancer therapy, Biomater. Res., 25 (2021) 42.

50. A. De Girolamo, M. McKeague, M. Pascale, M. Cortese, M.C. DeRosa, Immobilization of Aptamers on Substrates, in: Y. Dong (Ed.), Aptamers Anal. Appl., Wiley-VCH Verlag GmbH & Co. KGaA, Weinheim, Germany, 2018: pp. 85.
51. Y. Xu, G. Cheng, P. He, Y. Fang, A Review: Electrochemical Aptasensors with Various Detection Strategies, Electroanalysis, 21 (2009) 1251.
52. V. Thiviyanathan, D.G. Gorenstein, Aptamers and the next generation of diagnostic reagents, PROTEOMICS - Clin. Appl., 6 (2012) 563.
53. S. Arshavsky-Graham, K. Urmann, R. Salama, N. Massad-Ivanir, J. G. Walter, T. Scheper, E. Segal, Aptamers *vs* antibodies as capture probes in optical porous silicon biosensors, The Analyst, 145 (2020) 4991.
54. P. Dhar, R.M. Samarasinghe, S. Shigdar, Antibodies, Nanobodies, or Aptamers—Which Is Best for Deciphering the Proteomes of Non-Model Species? Int. J. Mol. Sci., 21 (2020) 2485.
55. A. Sassolas, L.J. Blum, B.D. Leca-Bouvier, Electrochemical Aptasensors, Electroanalysis, 21 (2009) 1237.
56. A.M. Schmidt, M.J.F. Calvete, Phthalocyanines: An Old Dog Can Still Have New (Photo)Tricks! Molecules, 26 (2021) 2823.
57. S. Arslan, Phthalocyanines: Structure, Synthesis, Purification and Applications, J. Life Sci., 6 (2016).
58. T. Furuyama, K. Satoh, T. Kushiya, N. Kobayashi, Design, Synthesis, and Properties of Phthalocyanine Complexes with Main-Group Elements Showing Main Absorption and Fluorescence beyond 1000 nm, J. Am. Chem. Soc., 136 (2014) 765.

59. Q. Chang, Y. Liu, J.-H. Lee, D. Ologunagba, S. Hwang, Z. Xie, S. Kattel, J.H. Lee, J.G. Chen, Metal-Coordinated Phthalocyanines as Platform Molecules for Understanding Isolated Metal Sites in the Electrochemical Reduction of CO2, J. Am. Chem. Soc., 144 (2022) 16131.
60. S. Hiroto, Y. Miyake, H. Shinokubo, Synthesis and Functionalization of Porphyrins through Organometallic Methodologies, Chem. Rev., 117 (2017) 2910.
61. B. Sekaran, R. Misra, β-Pyrrole functionalized porphyrins: Synthesis, electronic properties, and applications in sensing and DSSC, Coord. Chem. Rev., 453 (2022) 214312.
62. Y. Zhang, F. Schulz, B.M. Rytting, C.C. Walters, K. Kaiser, J.N. Metz, M.R. Harper, S.S. Merchant, A.S. Mennito, K. Qian, J.D. Kushnerick, P.K. Kilpatrick, L. Gross, Elucidating the Geometric Substitution of Petroporphyrins by Spectroscopic Analysis and Atomic Force Microscopy Molecular Imaging, Energ. Fuels, 33 (2019) 6088.
63. J. Gu, Y. Peng, T. Zhou, J. Ma, H. Pang, Y. Yamauchi, Porphyrin-based framework materials for energy conversion, Nano Res. Energy, 1 (2022) e9120009.
64. T.V. Basova, A.K. Ray, Review—Hybrid Materials Based on Phthalocyanines and Metal Nanoparticles for Chemiresistive and Electrochemical Sensors: A Mini-Review, ECS J. Solid State Sci. Technol., 9 (2020) 061001.
65. Z.H. Zhu, Y. Liu, C. Song, Y. Hu, G. Feng, B.Z. Tang, Porphyrin-Based Two-Dimensional Layered Metal–Organic Framework with Sono-/Photocatalytic Activity for Water Decontamination, ACS Nano, 16 (2022) 1346.
66. X. Zhang, M.C. Wasson, M. Shayan, E.K. Berdichevsky, J. Ricardo-Noordberg, Z. Singh, E.K. Papazyan, A.J. Castro, P. Marino, Z. Ajoyan, Z. Chen, T. Islamoglu, A.J. Howarth, Y. Liu, M.B. Majewski, M.J. Katz, J.E. Mondloch, O.K. Farha, A historical perspective on porphyrin-based metal–organic frameworks and their applications, Coord. Chem. Rev., 429 (2021) 213615.

67. N. Rabiee, M. Rabiee, S. Sojdeh, Y. Fatahi, R. Dinarvand, M. Safarkhani, S. Ahmadi, H. Daneshgar, F. Radmanesh, S. Maghsoudi, M. Bagherzadeh, R.S. Varma, E. Mostafavi, Porphyrin Molecules Decorated on Metal-Organic Frameworks for Multi-Functional Biomedical Applications, Biomolecules, 11 (2021) 1714.
68. D.E. Williams, J.A. Rietman, J.M. Maier, R. Tan, A.B. Greytak, M.D. Smith, J.A. Krause, N.B. Shustova, Energy Transfer on Demand: Photoswitch-Directed Behavior of Metal–Porphyrin Frameworks, J. Am. Chem. Soc., 136 (2014) 11886.
69. C. Lin, C. Han, H. Zhang, L. Gong, Y. Gao, H. Wang, Y. Bian, R. Li, J. Jiang, Porphyrin-Based Metal–Organic Frameworks for Efficient Photocatalytic H2 Production under Visible-Light Irradiation, Inorg. Chem., 60 (2021) 3988.
70. B. Yao, Y. He, S. Wang, H. Sun, X. Liu, Recent Advances in Porphyrin-Based Systems for Electrochemical Oxygen Evolution Reaction, Int. J. Mol. Sci., 23 (2022) 6036.
71. S.S. Rajasree, X. Li, P. Deria, Physical properties of porphyrin-based crystalline metal–organic frameworks, Commun. Chem., 4 (2021) s42004.
72. F. Figueira, J.P.C. Tomé, F.A.A. Paz, Porphyrin NanoMetal-Organic Frameworks as Cancer Theranostic Agents, Molecules, 27 (2022) 3111.
73. A. Nowak-Król, R. Plamont, G. Canard, J.A. Edzang, D.T. Gryko, T.S. Balaban, An Efficient Synthesis of Porphyrins with Different *meso* Substituents that Avoids Scrambling in Aqueous Media, Chem. - Eur. J., 21 (2015) 1488.
74. M. O. Senge, N. N. Sergeeva, K. J. Hale, Classic highlights in porphyrin and porphyrinoid total synthesis and biosynthesis, Chem. Soc. Rev., 50 (2021) 4730.
75. Y. Yan, S. Lu, B. Li, R. Zhu, J. Zhou, S. Wei, S. Qian, Ultrafast Excited State Dynamics of Modified Phthalocyanines: p-HPcZn and p-HPcCo, J. Phys. Chem. A, 110 (2006) 10757.

76. N. Ndebele, S. Mgidlana, T. Nyokong, Electrocatalytic Activity of Cobalt Phthalocyanines Revisited: Effect of the Number of Oxygen Atoms and Conjugation to Carbon Nanomaterials, Electrocatalysis, 12 (2021) 499.
77. R. Nkhahle, K.E. Sekhosana, S. Centane, T. Nyokong, Electrocatalytic Activity of Asymmetrical Cobalt Phthalocyanines in the Presence of N Doped Graphene Quantum Dots: The Push-pull Effects of Substituents, Electroanalysis, 31 (2019) 891.
78. S.R. Nxele, T. Nyokong, The effects of the composition and structure of quantum dots combined with cobalt phthalocyanine and an aptamer on the electrochemical detection of prostate specific antigen, Dyes Pigm., 192 (2021) 109407.
79. S.R. Nxele, T. Nyokong, The electrochemical detection of prostate specific antigen on glassy carbon electrode modified with combinations of graphene quantum dots, cobalt phthalocyanine and an aptamer, J. Inorg. Biochem., 221 (2021) 111462.
80. Y. J. Li, M. J. Ma, G. Yin, Y. Kong, J. J. Zhu, Phthalocyanine-sensitized graphene-Cds nanocomposites: an enhanced photoelectrochemical immunosensing platform, Chem. - Eur. J., 19 (2013) 4496.
81. J. Chu, W.-P. Fong, C. Wong, D. Ng, Facile Synthesis of Cyclic Peptide–Phthalocyanine Conjugates for Epidermal Growth Factor Receptor-Targeted Photodynamic Therapy, J. Med. Chem., 64 (2021) 2064.
82. B.G. Ongarora, K.R. Fontenot, X. Hu, I. Sehgal, S.D. Satyanarayana-Jois, M.G.H. Vicente, Phthalocyanine-Peptide Conjugates for Epidermal Growth Factor Receptor Targeting, J. Med. Chem., 55 (2012) 3725.
83. E. Y. Xue, R.C. H. Wong, C.T. T. Wong, W.-P. Fong, D.K. P. Ng, Synthesis and biological evaluation of an epidermal growth factor receptor-targeted peptide-conjugated phthalocyanine-based photosensitiser, RSC Adv., 9 (2019) 20652.

84. S. Alpugan, D. Topkaya, S.K. Verma, D. Atilla, V. Ahsen, J.H. Niazi, F. Dumoulin, Corrigendum to “Zn phthalocyanine conjugation to H2-ul aptamer for HER2-targeted breast cancer photodynamic therapy: Design, optimization and properties,” J. Porphyr. Phthalocyanines, 23 (2019) 303.
85. M. Chu, J.-R. Kang, W. Wang, H. Li, J.-H. Feng, Z.-Y. Chu, M.-B. Zhang, L. Xu, Y.-D. Wang, Evaluation of human epidermal growth factor receptor 2 in breast cancer with a novel specific aptamer, Cell. Mol. Immunol., 14 (2017) 398.
86. C.C. Negut, R.-I. Stefan - van Staden, J.F. van Staden, Porphyrins-as Active Materials in the Design of Sensors An Overview, ECS J. Solid State Sci. Technol., 9 (2020) 051005.
87. J. Chen, Y. Zhu, S. Kaskel, Porphyrin-Based Metal–Organic Frameworks for Biomedical Applications, Angew. Chem. Int. Ed., 60 (2021) 5010.
88. G. Zhang, D. Shan, H. Dong, S. Cosnier, K.A. Al-Ghanim, Z. Ahmad, S. Mahboob, X. Zhang, DNA-Mediated Nanoscale Metal–Organic Frameworks for Ultrasensitive Photoelectrochemical Enzyme-Free Immunoassay, Anal. Chem., 90 (2018) 12284.
89. M. Bacon, S.J. Bradley, T. Nann, Graphene Quantum Dots, Part. Part. Syst. Charact., 31 (2014) 415.
90. M.H.M. Facure, R. Schneider, J.B.S. Lima, L.A. Mercante, D.S. Correa, Graphene Quantum Dots-Based Nanocomposites Applied in Electrochemical Sensors: A Recent Survey, Electrochem., 2 (2021) 490.
91. S. Jeong, R.L. Pinals, B. Dharmadhikari, H. Song, A. Kalluri, D. Debnath, Q. Wu, M.-H. Ham, P. Patra, M.P. Landry, Graphene Quantum Dot Oxidation Governs Noncovalent Biopolymer Adsorption, Sci. Rep., 10 (2020) 63769z.
92. H. Sun, L. Wu, W. Wei, X. Qu, Recent advances in graphene quantum dots for sensing, Mater. Today, 16 (2013) 433.

93. A. Kalkal, S. Kadian, R. Pradhan, G. Manik, G. Packirisamy, Recent advances in graphene quantum dot-based optical and electrochemical (bio)analytical sensors, Mater. Adv., 2 (2021) 5513.

94. M. O. Valappil, V. K. Pillai, S. Alwarappan, Spotlighting graphene quantum dots and beyond: Synthesis, properties and sensing applications, Appl. Mater. Today, 9 (2017) 350.

95. T.A. Tabish, H. Hayat, A. Abbas, R.J. Narayan, Graphene Quantum Dots-Based Electrochemical Biosensing Platform for Early Detection of Acute Myocardial Infarction, Biosensors, 12 (2022) 77.

96. N. Nesakumar, S. Srinivasan, S. Alwarappan, Graphene quantum dots: synthesis, properties, and applications to the development of optical and electrochemical sensors for chemical sensing, Microchim. Acta, 189 (2022) 258.

97. D. Iannazzo, C. Espro, C. Celesti, A. Ferlazzo, G. Neri, Smart Biosensors for Cancer Diagnosis Based on Graphene Quantum Dots, Cancers, 13 (2021) 3194.

98. O. Karaman, N. Özcan, C. Karaman, B.B. Yola, N. Atar, M.L. Yola, Electrochemical cardiac troponin I immunosensor based on nitrogen and boron-doped graphene quantum dots electrode platform and Ce-doped SnO_2/SnS_2 signal amplification, Mater. Today Chem., 23 (2022) 100666.

99. F. Faridbod, A.L. Sanati, Graphene Quantum Dots in Electrochemical Sensors/Biosensors, Curr. Anal. Chem., 15 (2019) 103.

100. B. Li, Y. Wang, L. Huang, H. Qu, Z. Han, Y. Wang, M.J. Kipper, L.A. Belfiore, J. Tang, Review of performance improvement strategies for doped graphene quantum dots for fluorescence-based sensing, Synth. Met., 276 (2021) 116758.

101. S. Kundu, V.K. Pillai, Synthesis and characterization of graphene quantum dots, Phys. Sci. Rev., 5 (2019) 20190013.

102. S.A. Prabhu, V. Kavithayeni, R. Suganthy, K. Geetha, Graphene quantum dots synthesis and energy application: a review, Carbon Lett., 31 (2021) 00154w.

103. A. Abbas, T.A. Tabish, S.J. Bull, T.M. Lim, A.N. Phan, High yield synthesis of graphene quantum dots from biomass waste as a highly selective probe for Fe3+ sensing, Sci. Rep., 10 (2020) 21262.

104. C. Zhao, X. Song, Y. Liu, Y. Fu, L. Ye, N. Wang, F. Wang, L. Li, M. Mohammadniaei, M. Zhang, Q. Zhang, J. Liu, Synthesis of graphene quantum dots and their applications in drug delivery, J. Nanobiotechnol., 18 (2020) 142.

105. H. Kang, D.Y. Kim, J. Cho, Top-Down Fabrication of Luminescent Graphene Quantum Dots Using Self-Assembled Au Nanoparticles, ACS Omega, 8 (2023) 5885.

106. F. Sun, H. Ghosh, Z. Tan, S. Sivoththaman, Top-down synthesis and enhancing device adaptability of graphene quantum dots, Nanotechnology, 34 (2023) 185601.

107. D. Huang, H. Zhou, Y. Wu, T. Wang, L. Sun, P. Gao, Y. Sun, H. Huang, G. Zhou, J. Hu, Bottom-up synthesis and structural design strategy for graphene quantum dots with tunable emission to the near infrared region, Carbon, 142 (2019) 673.

108. R. Liu, D. Wu, X. Feng, K. Müllen, Bottom-Up Fabrication of Photoluminescent Graphene Quantum Dots with Uniform Morphology, J. Am. Chem. Soc., 133 (2011) 15221.

109. B.A. Al Jahdaly, M.F. Elsadek, B.M. Ahmed, M.F. Farahat, M.M. Taher, A.M. Khalil, Outstanding Graphene Quantum Dots from Carbon Source for Biomedical and Corrosion Inhibition Applications: A Review, Sustainability, 13 (2021) 2127.

110. S.Y. Digehsaraei, M. Salouti, B. Amini, S. Mahmazi, M. Kalantari, A. Kazemizadeh, J. Mehrvand, Developing a fluorescence immunosensor for detection of HER2-positive breast cancer based on graphene and magnetic nanoparticles, Microchem. J., 167 (2021) 106300.

111. M. Sadeghi, S. Kashanian, S.M. Naghib, E. Askari, F. Haghiralsadat, D. Tofighi, A highly sensitive nanobiosensor based on aptamer-conjugated graphene-decorated rhodium nanoparticles for detection of HER2-positive circulating tumor cells, Nanotechnol. Rev., 11 (2022) 793.

112. H. Nasrollahpour, I. Isildak, M.-R. Rashidi, E.A. Hashemi, A. Naseri, B. Khalilzadeh, Ultrasensitive bioassaying of HER-2 protein for diagnosis of breast cancer using reduced graphene oxide/chitosan as nanobiocompatible platform, Cancer Nanotechnol., 12 (2021) 10.

113. R. Salahandish, A. Ghaffarinejad, S.M. Naghib, K. Majidzadeh-A, H. Zargartalebi, A. Sanati-Nezhad, Nano-biosensor for highly sensitive detection of HER2 positive breast cancer, Biosens. Bioelectron., 117 (2018) 104.

114. Y. Yang, X. Yang, X. Zou, S. Wu, D. Wan, A. Cao, L. Liao, Q. Yuan, X. Duan, Ultrafine Graphene Nanomesh with Large On/Off Ratio for High-Performance Flexible Biosensors, Adv. Funct. Mater., 27 (2017) 1604096.

115. A.A. Saeed, J.L.A. Sánchez, C.K. O'Sullivan, M.N. Abbas, DNA biosensors based on gold nanoparticles-modified graphene oxide for the detection of breast cancer biomarkers for early diagnosis, Bioelectrochemistry, 118 (2017) 91.

116. K. R. B. Singh, V. Nayak, T. Sarkar, R. Pratap Singh, Cerium oxide nanoparticles: properties, biosynthesis and biomedical application, RSC Adv., 10 (2020) 27194.

117. L. He, Y. Su, J. Lanhong, S. Shi, Recent advances of cerium oxide nanoparticles in synthesis, luminescence and biomedical studies: a review, J. Rare Earths, 33 (2015) 791.

118. A. Younis, D. Chu, S. Li, A. Younis, D. Chu, S. Li, Cerium Oxide Nanostructures and their Applications, in: M. A. Farrukh (Ed) Funct. Nanomater., IntechOpen, Pakistan, 2016: p. 65937.

119. A. Dhall, W. Self, Cerium Oxide Nanoparticles: A Brief Review of Their Synthesis Methods and Biomedical Applications, Antioxidants, 7 (2018) 97.

120. S. Kontham, K. Mandava, S. Dosa, F.U. Mohd, O.A. Mohammed, A.U. Mohammad, Review on facile synthesis of cerium oxide nanoparticles and their biomedical applications, Inorg. Nano-Met. Chem., 52 (2022) 1183.

121. M. Nyoka, Y.E. Choonara, P. Kumar, P.P.D. Kondiah, V. Pillay, Synthesis of Cerium Oxide Nanoparticles Using Various Methods: Implications for Biomedical Applications, Nanomaterials, 10 (2020) 242.

122. M. Nadeem, R. Khan, K. Afridi, A. Nadhman, S. Ullah, S. Faisal, Z.U. Mabood, C. Hano, B.H. Abbasi, Green Synthesis of Cerium Oxide Nanoparticles (CeO_2 NPs) and Their Antimicrobial Applications: A Review, Int. J. Nanomedicine, 15 (2020) 5951.

123. F. Charbgoo, M. Ramezani, M. Darroudi, Bio-sensing applications of cerium oxide nanoparticles: Advantages and disadvantages, Biosens. Bioelectron., 96 (2017) 33.

124. K. Kowsuki, R. Nirmala, Y. H. Ra, R. Navamathavan, Recent advances in cerium oxide-based nanocomposites in synthesis, characterization, and energy storage applications: A comprehensive review, Results Chem., 5 (2023) 100877.

125. Y. Hartati, L. Letelay, S. Gaffar, S. Wyantuti, H. Bahti, Cerium oxide-monoclonal antibody bioconjugate for electrochemical immunosensing of HER2 as a breast cancer biomarker, Sens. Bio-Sens. Res., 27 (2019) 100316.

126. Y. Li, H. J. Schluesener, S. Xu, Gold nanoparticle-based biosensors, Gold Bull., 43 (2010) 29.

127. P. Jiang, Y. Wang, L. Zhao, C. Ji, D. Chen, L. Nie, Applications of Gold Nanoparticles in Non-Optical Biosensors, Nanomaterials, 8 (2018) 977.

128. J.M. Pingarrón, P. Yáñez-Sedeño, A. González-Cortés, Gold nanoparticle-based electrochemical biosensors, Electrochim. Acta, 53 (2008) 5848.

129. M. Holzinger, A. Le Goff, S. Cosnier, Nanomaterials for biosensing applications: a review, Front. Chem., 2 (2014) 00063.

130. M.E. Hamdy, M. Del Carlo, H.A. Hussein, T.A. Salah, A.H. El-Deeb, M.M. Emara, G. Pezzoni, D. Compagnone, Development of gold nanoparticles biosensor for ultrasensitive diagnosis of foot and mouth disease virus, J. Nanobiotechnology, 16 (2018) 48.

131. J.S.Y. Ooi, S.Y. New, Design Strategies of Gold Nanoparticles-Based Biosensors Coupled with Hybridization Chain Reaction or Catalytic Hairpin Assembly, Chem. Select, 7 (2022) 00073.

132. E. Arkan, R. Saber, Z. Karimi, M. Shamsipur, A novel antibody–antigen based impedimetric immunosensor for low level detection of HER2 in serum samples of breast cancer patients via modification of a gold nanoparticles decorated multiwall carbon nanotube-ionic liquid electrode, Anal. Chim. Acta, 874 (2015) 66.

133. L. Chun, S. E. Kim, M. Cho, W. Choe, J. Nam, D.W. Lee, Y. Lee, Electrochemical detection of HER2 using single stranded DNA aptamer modified gold nanoparticles electrode, Sens. Actuators B Chem., 186 (2013) 446.

134. Y. Makableh, T. Athamneh, M. Ajlouni, S. Hijazi, A. Alnaimi, Enhanced response and selective gold nanoparticles/carbon nanotubes biosensor for the early detection of HER2 biomarker, Sens. Actuators Rep., 5 (2023) 100158.

135. M.L. Yola, Sensitive sandwich-type voltammetric immunosensor for breast cancer biomarker HER2 detection based on gold nanoparticles decorated Cu-MOF and Cu_2ZnSnS_4 NPs/Pt/g-C_3N_4 composite, Microchim. Acta, 188 (2021) 78.

136. R. Jain, N. Jadon, A. Pawaiya, Polypyrrole based next generation electrochemical sensors and biosensors: A review, TrAC Trends Anal. Chem., 97 (2017) 363.

137. H. Eisazadeh, Studying the Characteristics of Polypyrrole and its Composites, World J. Chem., 2 (2007) 67.

138. E.Z. M. Tarmizi, H. Baqiah, Z.A. Talib, H.M. Kamari, Preparation and physical properties of polypyrrole/zeolite composites, Results Phys., 11 (2018) 793.

139. Y. Wang, R. Song, L. Li, R. Fu, Z. Liu, B. Li, High Crystalline Quality Conductive Polypyrrole Film Prepared by Interface Chemical Oxidation Polymerization Method, Appl. Sci., 12 (2022) 58.

140. H. M. Xiao, S. Y. Fu, Synthesis and physical properties of electromagnetic polypyrrole composites via addition of magnetic crystals, Cryst. Eng. Comm., 16 (2014) 2097.

141. S. Maiti, D. Das, K. Sen, Electrochemical Polymerization of Pyrrole: Key Process Control Parameters, J. Electrochem. Soc., 159 (2012) 154.

142. Y. Yuan, T. Li, Z. Ye, Y. Feng, Z. Chen, Y. Wang, Y. Sun, H. Wu, Z. Yang, Y. Wang, Y. Zhang, L. Huang, B. Liang, A One-Step Electropolymerized Biomimetic Polypyrrole Membrane-Based Electrochemical Sensor for Selective Detection of Valproate, Front. Bioeng. Biotechnol., 10 (2022) 851692.

143. A.F. Diaz, K.K. Kanazawa, G.P. Gardini, Electrochemical polymerization of pyrrole, J. Chem. Soc. Chem. Commun., (1979) 635.

144. J. He, H. Xie, J. Hong, Z. Gao, Z. Liu, C. Xiong, Self-suspended polypyrrole with liquid crystal property, J. Polym. Res., 25 (2018) 56.

145. X. Zhang, X. Tan, P. Wang, J. Qin, Application of Polypyrrole-Based Electrochemical Biosensor for the Early Diagnosis of Colorectal Cancer, Nanomaterials, 13 (2023) 674.

146. S. Cete, M. Ozyurt, E. Yildirim, D. Akin, A novel biosensor with the use of polypyrrole–poly(sodium-4-styrenesulphonate) as a dopant in the determination of glucose, Chem. Pap., 74 (2020) 799.

147. G. Cheng, J. Zhao, Y. Tu, P. He, Y. Fang, A sensitive DNA electrochemical biosensor based on magnetite with a glassy carbon electrode modified by multi-walled carbon nanotubes in polypyrrole, Anal. Chim. Acta, 533 (2005) 11.

148. A.E. Valera, N.T. Nesbitt, M.M. Archibald, M.J. Naughton, T.C. Chiles, On-Chip Electrochemical Detection of Cholera Using a Polypyrrole-Functionalized Dendritic Gold Sensor, ACS Sens., 4 (2019) 654.

149. Q. Rong, H. Han, F. Feng, Z. Ma, Network nanostructured polypyrrole hydrogel/Au composites as enhanced electrochemical biosensing platform, Sci. Rep., 5 (2015) 11440.

150. N. Baig, M. Sajid, T.A. Saleh, Recent trends in nanomaterial-modified electrodes for electroanalytical applications, Trends Anal. Chem., 111 (2019) 47.

151. A. A. Ciucu, Chemically Modified Electrodes in Biosensing, J. Biosens. Bioelectron., 05 (2014) 1000154.

152. A.J. Bard, Chemical modification of electrodes, J. Chem. Educ., 60 (1983) 302.

153. R. Ahmad, O.S. Wolfbeis, Y.-B. Hahn, H.N. Alshareef, L. Torsi, K.N. Salama, Deposition of nanomaterials: A crucial step in biosensor fabrication, Mater. Today Commun., 17 (2018) 289.

154. P.S. Adarakatti, S.K. Kempahanumakkagari, Modified electrodes for sensing, in: C. Banks, S. McIntosh (Eds.), Electrochemistry, Royal Society of Chemistry, Cambridge, 2018: pp. 58–95.

155. A. K. S. Kumar, Y. Zhang, D. Li, R.G. Compton, A mini-review: How reliable is the drop casting technique? Electrochem. Commun., 121 (2020) 106867.

156. R. Zhang, J.R. Adsetts, Y. Nie, X. Sun and Z. Ding, Electrochemiluminescence of nitrogen and sulfur-doped graphene quantum dots, Carbon, 129 (2018) 45.

157. L. Polavarapu, N. Venkatram, W. Ji and Q. H. Xu, Optical-limiting properties of oleylamine-capped gold nanoparticles for both femtosecond and nanosecond laser pulses, ACS Appl. Mater. Interfaces, 1 (2009) 2298.

158. N. G. Bastús, J. Comenge, V. Puntes, Kinetically controlled seeded growth synthesis of citrate-stabilized gold nanoparticles of up to 200 nm: size focusing versus Ostwald ripening, Langmuir, 27 (2011) 11098.

159. S.A. Ansari, M. Al-Shaeri, Biotechnological application of surface modified cerium oxide nanoparticles, Braz. J. Chem. Eng., 36 (2019) 109.

160. E. Dube, N. Njemuwa, D.O. Oluwole, J. Mack, T. Nyokong, Investigation of photophysicochemical properties of zinc phthalocyanines conjugated to metallic nanoparticles, J. Photochem. Photobiol., A 349 (2017) 148.

161. D.O. Oluwole, E. Prinsloo, T. Nyokong, Photophysicochemical properties of nanoconjugates of zinc mono 2-(4-oxy) phenoxy) acetic acid phthalocyanine with cysteamine capped Ag and Au nanoparticles, Polyhedron, 119 (2016) 434.

162. G.G. Matlou, N. Kobayashi, M. Kimura, T. Nyokong, Physicochemical properties of water soluble asymmetrical phthalocyanine-folic acid conjugates, Dyes and Pigm., 149 (2018) 393.

163. Y.I. Openda, P. Sen, M. Managa, T. Nyokong, Acetophenone substituted phthalocyanines and their graphene quantum dots conjugates as photosensitizers for photodynamic antimicrobial chemotherapy against Staphylococcus aureus, Photodiagnosis. Photodyn. Ther., 29 (2020) 101607.

164. Y. Koysal, S. Isik, N. Akdemir, E. Agar, C. Kantar, 4-(3,5-Dimethoxy phenoxy) phthalonitrile, Acta Cryst. E., 60 (2004) o930.

165. N. Ndebele, S. Mgidlana, T. Nyokong, Electrochemical Detection of Nitrite Using Cobalt Phthalocyanine Conjugated to Metal Tungstate Nanoparticles, Electroanalysis., 34 (2022) 1348.

166. S. Muniappan, S. Lipstman, S. George, I. Goldberg, Porphyrin framework solids. Synthesis and structure of hybrid coordination polymers of tetra(carboxyphenyl)porphyrins and lanthanide-bridging ions., J. Inorg. Chem., 46 (2007) 5544.

167. A. Samanta, Z. Deng, Y. Liu, H. Yan, A perspective on functionalizing colloidal quantum dots with DNA, Nano Res., 6 (2013) 853.

168. Q. Fan, K. Liu, Z. Liu, H. Liu, L. Zhang, P. Zhong, C. Gao, A ligand-exchange route to nobel metal nanocrystals with a clean surface for enhanced optical and catalytic properties, Part. Part. Syst. Charact., 34 (2017) 1700075.

169. L. Lu, S. Zou, B. Fang, The critical impacts of ligands on heterogeneous nanocatalysis: a review, ACS Catal., 11 (2021) 6020.

170. M. Moreau, O. Raguin, J. Vrigneaud, B. Collin, C. Bernhard, X. Tizon, F. Boschetti, O. Duchamp, F. Brunotte, and F. Denat., DOTAGA-Trastuzumab: A new antibody conjugate targeting her2/neu antigen for diagnostic purposes, Bioconj. Chem., 23 (2012) 1181.

171. X. Huang and M. A. El-Sayed, Gold nanoparticles: Optical properties and implementations in cancer diagnosis and photothermal therapy, J. Adv. Res., 1 (2010) 13.

172. C. Zhu, S. Yang, G. Wang, R. Mo, P. He, J. Sun, Z. Di, N. Yuan, J. Ding, G. Ding, X. Xie, Z. Kang, A new mild, clean and highly efficient method for the preparation of graphene quantum dots without by-products, J. Mater. Chem. B., 3 (2015) 1093.

173. O. Wenpeng, Z. Dongrong, Y. Xiang, X. Fangyan, Z. Weihong, C. Jian, Y. Jing, X. Fangjing, W. Lei, M. Hui, Exploring the active sites of nitrogen-doped graphene as catalysts for the oxygen reduction reaction. Int. J. Hydrog. Energy., 39 (2014) 15996.

174. A. K. Roddu, A. W Wahab, A. Ahmad, P. Taba, I. W. Sutapa, Theoretical analysis properties of gold nanoparticles resulted by bioreduction process, J. Phys.: Conf. Ser., 1463 (2020) 012008.

175. P. Vecera, J. C. Chacon-Torres, T. Pichler, S. Reich, H. R. Soni, A. Gorling, K. Edelthalhammer, H. Peterlik, F. Hauke and A. Hirsch, Precise Determination of Graphene Functionalization by *in situ* Raman Spectroscopy, Nat. Commun., 8 (2017) 15192.

176. A. Filtschew, K. Hofmann, C. Hess, Ceria and its defect structure: new insights from a combined spectroscopic approach, J. Phys. Chem. C., 120 (2016) 6694.

177. C. Schilling, A. Hofmann, C. Hess, M.V. Ganduglia-Pirovano, Raman spectra of polycrystalline CeO_2: a density functional theory study, J. Phys. Chem. C 121 (2017) 20834.

178. J. Cui, G.A. Hope, Raman and fluorescence spectroscopy of CeO_2, Er_2O_3, Nd_2O_3, Tm_2O_3, Yb_2O_3, La_2O_3, and Tb_4O_7, J. Spectrosc. (Hindawi), 2015 (2015) 1.

179. R. Zamiri, H. A. Ahangar, A. Kaushal, A. Zakaria, G. Zamiri, D. Tobaldi, J. M. F. Ferreira, Dielectrical properties of CeO_2 nanoparticles at different temperatures. PLoS ONE, 10 (2017) e0122989.

180. M. He, B. Cao, X. Gao, B. Liu, J. Yang, Synthesis of multi-branched gold nanostructures and their surface-enhanced Raman scattering properties of 4- aminothiophenol, J. Mater. Res., 34 (2019) 2928.

181. L. C. Mecker, K. M. Tyner, J. F. Kauffman, S. Arzhantsev, D. J. Mans, C. M. Gryniewicz-Ruzicka, Selective melamine detection in multiple sample matrices with a portable Raman instrument using surface enhanced Raman spectroscopy active gold nanoparticles, Anal. Chim. Acta, 733 (2012) 48.

182. J. Wu, P. Wang, F. Wang, Y. Fang, Investigation of the microstructures of graphene quantum dots (GQDs) by surface-enhanced Raman Spectroscopy, Nanomaterials (Basel.), 8 (2018) 810086.

183. N.W. Kim, D.K. Lee, H. Yu, Selective shape control of cerium oxide nanocrystals for photocatalytic and chemical sensing effect, RSC Adv., 9 (2019) 13829.

184. P.P. Sharma, V.D.C. Tinh, D. Kim, Improved oxidative stability by embedded cerium into graphene oxide nanosheets for proton exchange membrane fuel cell application, Membranes, 11 (2021) 238.

185. J. Rusanova, M. Pilkington and S. Decurtins, A novel fully conjugated phenanthroline-appended phthalocyanine: synthesis and characterisation, Chem. Commun., 19 (2002) 2236.

186. M.A. Idowu, Y. Arslanoglu, T. Nyokong, Spectral properties and photophysical behaviour of water-soluble cationic Mg (ii) and Al (iii) phthalocyanines, Cent. Eur. J. Chem., 12 (2014) 403.

187. H.P. Karaoğlu, A.K. Burat, α- and β-substituted metal-free phthalocyanines: synthesis, photophysical and electrochemical properties, Molecules, 25 (2020) 363.

188. Z. Biyiklioğlu, H. Bas¸, Synthesis and effect of substituent position, metal type on the electrochemical properties of (3-morpholin-4-ylpropoxy) groups substituted cobalt, manganese phthalocyanines, Turk. J. Chem., 44 (2020) 687.

189. J. B. Wu, M. L. Lin, X. Cong, H. N. Liu, P. H. Tan, Raman spectroscopy of graphene-based materials and its applications in related devices, Chem. Soc. Rev., 47 (2018) 1822

190. E. Dervishi, Z. Ji, H. Htoon, M. Sykora, S.K. Doorn, Raman spectroscopy of bottom-up synthesized graphene quantum dots: size and structure dependence, Nanoscale, 11 (2019) 16571.

191. G. Rajender, P.K. Giri, Formation mechanism of graphene quantum dots and their edge state conversion probed by photoluminescence and Raman spectroscopy, J. Mater. Chem., C 4 (2016) 10852.

192. X. Yan, Y. Song, Ji. Liu, N. Zhou, C. Zhang, L. He, Z. Zhang, Z. Liu, Two-dimensional porphyrin-based covalent organic framework: A novel platform for sensitive epidermal growth factor receptor and living cancer cell detection, Biosens. Bioelectron., 126 (2019) 734.

193. R. B. Moghaddam, P. G. Pickup, Electrochemical impedance study of the polymerization of pyrrole on high surface area carbon electrodes, Phys. Chem. Chem. Phys., 12 (2010) 4733.

194. M. Cao, A.Z. Wang, J. Liu, N. Kong, X. Zong, H. Liu and J.J. Gooding, Electrochemical and theoretical study of π− π stacking interactions between graphitic surfaces and pyrene derivatives, J. Phys. Chem. C, 118 (2014) 2650.

195. B. Pejcic, R. De Marco, Impedance spectroscopy: over 35 years of electrochemical sensor optimization, Electrochim. Acta, 51 (2006) 6217.

196. Y. Liu, F. Yin, Y. Long, Z. Zhang, S. Yao, Study of the immobilization of alcohol dehydrogenase on au-colloid modified gold electrode by piezoelectric quartz crystal

sensor, cyclic voltammetry, and electrochemical impedance techniques, J. Colloid Interface Sci., 258 (2003) 75.

197. C.A. Caro, F. Bedioui, J.H. Zagal, Electrocatalytic oxidation of nitrite on a vitreous carbon electrode modified with Cobalt phthalocyanine, Electrochim. Acta, 47 (2002) 1489.

198. S. Saddeler, U. Hagemann and S. Schulz, Effect of the size and shape on the electrocatalytic activity of Co3O4 nanoparticles in the oxygen evolution reaction, Inorg. Chem., 59 (2020) 10013.

199. T. Saravanan, M. Shanmugam, P. Anandan, M. Azhagurajan, K. Pazhanivel, M. Arivanandhan, Y. Hayakawa, R. Jayavel, Facile synthesis of graphene-CeO_2 nanocomposites with enhanced electrochemical properties for supercapacitors, Dalton Trans., 44 (2015) 9901.

200. J. J. Gooding, V. G. Praig, E. A. Hall, Platinum-catalyzed enzyme electrodes immobilized on gold using self-assembled layers, Anal. Chem., 70 (1998) 2396.

201. T. Hezard, K. Fajerwerg, D. Evrard, V. Colli`ere, P. Behra, P. Gros, Gold nanoparticles electrodeposited on glassy carbon using cyclic voltammetry: application to Hg (ii) trace analysis, J. Electroanal. Chem., 664 (2012) 46.

202. C. W. Foster, J. Pillay, J. P. Metters, C.E. Banks, Cobalt phthalocyanine modified electrodes utilised in electroanalysis: nano-structured modified electrodes vs. bulk modified screen-printed electrodes, Sensors, 14 (2014) 21905.

203. P. Dhar, R.M. Samarasinghe, S. Shigdar, Antibodies, Nanobodies, or Aptamers—which is best for deciphering the proteomes of non-model species? Int. J. Mol. Sci., 21 (2021) 21072485.

204. M. Yüce, H. Kurt, How to Make Nanobiosensors: Surface Modification and Characterisation of Nanomaterials for Biosensing Applications, RSC Adv., 7 (2017) 49386.

205. M. Fendrich, Th. Wagner, M. Stohr, R. Moller, Hindered rotation of a copper phthalocyanine molecule on C60: experiments and molecular mechanics calculations, Phys. Rev. B., 73 (2006) 115433.

206. A. Ibrahim, A. Klopocinska, K. Horvat, Z.A. Hamid, Graphene-based nanocomposites: synthesis, mechanical properties, and characterizations, Polymers, 13 (2021) 2869.

207. Z. Wang, Z. Wang, H. Zhang, X. Duan, J. Xu, Y. Wen, Electrochemical sensing application of poly (acrylic acid modified EDOT-co-EDOT): PSS and its inorganic nanocomposite with high soaking stability, adhesion ability and flexibility, RSC Adv., 5 (2015) 12237.

208. G.C. Jimenez, S. Eissa, A. Ng, H. Alhadrami, M. Zourob, M. Siaj, Aptamer-based label-free impedimetric biosensor for detection of progesterone, Anal. Chem., 87 (2015) 1075.

209. D.C. Kim, D.J. Kang, Molecular recognition and specific interactions for biosensing applications, Sensors (Basel.), 8 (2008) 6605.

210. Q. Gu, W. Nanney, H.H. Cao, H. Wang, T. Ye, Single molecule profiling of molecular recognition at a model electrochemical biosensor, J. Am. Chem. Soc., 140 (2018) 14134.

211. H.L.L. Yu, A. Maslova, I.-M. Hsing, Rational design of electrochemical DNA biosensors for point-of-care applications, Chem. Electrochem., 4 (2017) 795.

212. S. Song, L. Wang, J. Lia, C. Fan, J. Zhao, Aptamer-based biosensors, Trends Anal. Chem., 27 (2008) 108.

213. Q. A. M. Al-Khafaji, M. Harris, S. Tombelli, S. Laschi, A.P.F. Turner, M. Mascini, G. Marrazz, An electrochemical immunoassay for HER2 detection, Electroanalysis, 24 (2012) 735.

214. S. Yang, M. You, F. Zhang, Q. Wang, P. He, A sensitive electrochemical aptasensing platform based on exonuclease recycling amplification and host-guest recognition for detection of breast cancer biomarker HER2, Sens. Actuators B Chem., 258 (2018) 796.

215. Z. A. N. H. Lah, S.A.A. Ahmad, M.S. Zaini, M.A. Kamarudin, J. Pharm. Biomed., 174 (2019) 608.

216. M. Emami, M. Shamsipur, R. Saber, R. Irajirad, An electrochemical immunosensor for the detection of a breast cancer biomarker based on anti-HER2 iron oxide nanoparticles bioconjugate, Analyst, 139 (2014) 2858.

217. N. Zhou, F. Su, Z. Li, X. Yan, C. Zhang, B. Hu, L. He, M. Wang, Z. Zhang, Gold nanoparticles conjugated to bimetallic manganese (II) and iron (II) Prussian blue analogues for aptamer-based impedimetric determination of the human epidermal growth factor receptor-2 and living MCF-7 cells, Microchim. Acta, 75 (2019), 31849.

218. S. Sharma, J. Zapatero-Rodríguez, R. Saxena, R. O'Kennedy, S. Srivastava, Ultrasensitive direct impedimetric immunosensor for detection of serum HER2, Biosens. Bioelectron., 106 (2018) 78.

219. P. F. Rostamabadi, E. Heydari-Bafrooei, Impedimetric aptasensing of the breast cancer biomarker HER2 using a glassy carbon electrode modified with gold nanoparticles in a composite consisting of electrochemically reduced graphene oxide and single-walled carbon nanotubes, Michrochim. Acta, 186 (2019) 495.

220. W. Wang, R. Han, M. Chen, X. Luo, Antifouling Peptide Hydrogel Based Electrochemical Biosensors for Highly Sensitive Detection of Cancer Biomarker HER2 in Human Serum, Anal. Chem., 93 (2021) 7355.

221. G. Bezerra, C. Cordula, D. Campos, G. Nascimento, N. Oliveira, M.A. Seabra, V. Visani, S. Lucas, I. Lopes, J. Santos, F. Xavier Jr, M. A. Borba, D. Martins, J. L. Filho, Electrochemical aptasensor for the detection of her2 in human serum to assist in the diagnosis of early-stage breast cancer, Anal. Bioanal. Chem., 411 (2019) 6667.

222. S.K. Arya, P. Zhurauski, P. Jolly, M.R. Batistuti, M. Mulato, P. Estrela, Capacitive aptasensor based on interdigitated electrode for breast cancer detection in undiluted human serum, Biosens. Bioelectron., 102 (2018) 106.

223. M, Freitas, M, M.P.S Neves, H. P. A, Nouws, C, Delerue-Matos, Quantum dots as nanolabels for breast cancer biomarker HER2-ECD analysis in human serum. Talanta 208 (2020) 120430.

224. M. Freitas, H.P.A. Nouws, E. Keating, C. Delerue-Matos, High-performance electrochemical immunomagnetic assay for breast cancer analysis, Sens. Actuators B Chem., 308 (2020) 127667.

225. A. Ravalli, C. Gomes da Rocha, H. Yamanaka, G. Marrazza, A label-free electrochemical affisensor for cancer marker detection: the case of HER2, Bioelectrochemistry, 106 (2015) 268.

226. D. Ou, D. Sun, X. Lin, Z. Liang, Y. Zhong, Z. Chen, A dual-aptamer-based biosensor for specific detection of breast cancer biomarker HER2 via flower-like nanozymes and DNA nanostructures, J. Mater. Chem. B., 7 (2019) 3661.

227. A. Sett, B.B. Borthakur, U. Bora, Selection of DNA aptamers for extra cellular domain of human epidermal growth factor receptor 2 to detect HER2 positive carcinomas, Clin. Transl. Oncol., 19 (2017) 976.

228. A. Tabasi, A. Noorbakhsh, E. Sharifi, Reduced graphene oxide-chitosan-aptamer interface as new platform for ultrasensitive detection of human epidermal growth factor receptor 2, Biosens. Bioelctron., 95 (2017) 117.

229. Y. Chai, X. Li, M. Yang, Aptamer based determination of the cancer biomarker HER2 by using phosphate-functionalized MnO2 nanosheets as the electrochemical probe, Microchim. Acta, 186 (2019) 316.

230. H. Zhong, C. Zhao, J. Chen, M. Chen, T. Luo, R.W. Tang, J. Liu, Electrochemical immunosensor with surface-confined probe for sensitive and reagentless detection of breast cancer biomarker, RSC Adv., 10 (2020) 22291.

231. S. D. Tallapragada, K. Layek, R. Mukherjee, K.K. Mistry, M. Ghosh, Development of screen-printed electrode based immunosensor for the detection of HER2 antigen in human serum samples, Bioelectrochemistry, 118 (2017) 25.

232. A. Athiroh, T. Fadillah, D.F. Damayanti, A.A. Widati, A. Abdulloh, M. Khasanah, Carbon paste electrode modified imprinted zeolite as a selective sensor for creatine analysis by potentiometry, IOP Conf. Ser.: Earth Environ. Sci., 217 (2019) 012003.

233. Y. Rosenberg-Hasson, L. Hansmann, M. Liedtke, I. Herschmann, H.T. Maecker, Effects of serum and plasma matrices on multiplex immunoassays, Immunol. Res., 58 (2014) 224.

234. M. Song, X. Lin, Z. Peng, S. Xu, L. Jin, X. Zheng, H. Luo, Materials and Methods of Biosensor Interfaces with Stability, Front. Mater., 7 (2021) 583739.

235. P. Panjan, V. Virtanen, A.M. Sesay, Determination of Stability Characteristics for Electrochemical Biosensors Via Thermally Accelerated Ageing, Talanta, 170 (2017) 331.

236. J.A. Goode, J.V.H. Rushworth, P.A. Millner, Biosensor regeneration: a review of common techniques and outcomes, Langmuir, 31 (2015) 6267.

237. S. Arshavsky-Graham, K. Urmann, R. Salama, N. Massad-Ivanir, J.G. Walter, T. Scheper, E. Segal, Aptamers vs. antibodies as capture probes in optical porous silicon biosensors, Analyst, 145 (2020) 4991.

238. H. Zhao, L.F. Boyd, P. Schuck, Measuring protein interactions by optical biosensors, Curr. Protoc. Protein Sci., 88 (2017) 20.2.1.

10. Appendix

Table A1. Performance (as % recovery) of the GCE/ (**2-11**) probes towards HER2 (in ng/mL) detection in human serum. SDEV = standard deviation

GCE/**1** (**2**)/HB5

[HER2] added	R_{ct} 1 (Ω)	R_{ct} 2 (Ω)	R_{ct} 3 (Ω)	Average	SDEV	% RSD	% [HER2] Recovered
1	987	865	1090	981	113	11.49	161
3	2270	2570	2750	2530	242	9.58	63
5	1290	1310	1300	1300	10	0.77	44
7	2100	2010	2290	2133	143	6.70	70
9	1510	1580	1590	1560	44	2.79	79

GCE/SNGQDs (**3**)/HB5

[HER2] added	R_{ct} 1 (Ω	R_{ct} 2 (Ω	R_{ct} 3 (Ω	Average	SDEV	% RSD	% [HER2] Recovered
1	829	821	816	822	7	0.80	121
3	1530	1600	1540	1557	38	2.43	67
5	5270	4880	4841	4997	237	4.75	57
7	2330	2420	2310	2353	59	2.49	31
9	1900	1970	1880	1917	47	2.47	23

GCE/PPy@SNGQDs (**4**)/ HB5

[HER2] added	R_{ct} 1 (Ω)	R_{ct} 2 (Ω)	R_{ct} 3 (Ω)	Average	SDEV	% RSD	% [HER 2] Recovered
1	1094	1100	1000	1065	56	5.27	138
3	8790	8500	9090	8793	295	3.35	91
5	12500	12100	11300	11967	611	5.11	71
7	16400	16200	17200	16600	529	3.19	78
9	20872	20920	21000	20931	65	0.31	87

GCE/PPy@**1** (**5**)/ HB5

[HER2] added	R_{ct} 1 (Ω)	R_{ct} 2 (Ω)	R_{ct} 3 (Ω)	Average	SDEV	% RSD	% [HER2] Recovered
1	1310	1390	1470	1390	80	5.76	130
3	4120	4340	4720	4393	304	6.91	80
5	4560	4910	5280	4917	360	7.32	54
7	7650	8210	7380	7747	423	5.47	75
9	2970	2940	3060	2990	62	2.09	19

GCE/PPy@**1**/SNGQDs (**7**)/ HB5

[HER2] added	R_{ct} 1 (Ω)	R_{ct} 2 (Ω)	R_{ct} 3 (Ω)	Average	SDEV	% RSD	% [HER2] Recovered
1	5600	5980	5700	5760	197	3.42	186
3	8530	8410	8700	8547	146	1.70	67
5	23400	23600	23500	23500	100	0.43	64
7	30800	30400	30500	3567	208	0.68	58
9	43000	44500	48000	45167	2566	5.68	71

GCE/PPy/SNGQDs(seq.) (**8**)/HB5

[HER2] added	R_{ct} 1 (Ω)	R_{ct} 2 (Ω)	R_{ct} 3 (Ω)	Average	SDEV	% RSD	% [HER2] recovered
1	43000	40700	48500	44067	4008	9.10	126
3	11300	11500	10900	11233	306	2.72	77
5	6920	6480	7130	6843	332	4.85	50
7	7640	7130	7900	7557	392	5.18	46
9	21470	21040	21000	21170	261	1.23	21

GCE/PPy/**1** (seq.) (**9**)/HB5

[HER2] added	R_{ct} 1 (Ω)	R_{ct} 2 (Ω)	R_{ct} 3 (Ω)	Average	SDEV	% RSD	% [HER2] Recovered
1	7910	7760	7880	7850	79	1.01	163
3	11500	12600	12300	12133	569	4.69	81
5	8640	9610	9220	9157	488	5.33	60
7	11100	12100	12600	11933	764	6.40	51
9	8640	9610	9220	9157	488	5.33	39

GCE/PPy/SNGQDs/**1** (seq.) (**10**)/HB5

[HER2] added	R_{ct} 1 (Ω)	R_{ct} 2 (Ω)	R_{ct} 3 (Ω)	Average	SDEV	% RSD	% [HER2] recovered
1	1240	1250	1200	1230	26	2.15	197
3	4210	5010	5680	4967	736	14.82	80
5	9190	9180	9800	9390	355	3.78	62
7	18600	18080	18120	18267	289	1.58	72
9	26400	27000	27900	27100	755	2.79	93

Table A2. Performance (as % recovery) of the GCE/ (**12-20**) probes towards HER2 (in ng/mL) detection in human serum. SDEV = standard deviation

GCE/**2** (**12**)/HB5

[HER2] added ng/mL	R_{ct} 1 (Ω)	R_{ct} 2 (Ω)	R_{ct} 3 (Ω)	Average	SDEV	% RSD	%[HER2] recovered
3	11920	12100	11900	11973	110	0.92	56
5	17100	17300	18100	17500	529	3.02	43
7	19400	18900	19100	19133	252	1.32	34
9	26000	26200	25800	26000	200	0.77	40

GCE/**3** (**13**)/HB5

[HER2] added ng/mL	R_{ct} 1 (Ω)	R_{ct} 2 (Ω)	R_{ct} 3 (Ω)	Average	SDEV	% RSD	%[HER2] recovered
3	8390	8170	7750	8103	325	4.01	65
5	13400	14200	13800	13800	400	2.90	55
7	18300	17800	18400	18167	321	1.77	50
9	19400	20100	19300	19600	436	2.22	43

GCE/CeO_2NPs_{COOH} (**14**)/HB5

[HER2] added ng/mL	R_{ct} 1 (Ω)	R_{ct} 2 (Ω)	R_{ct} 3 (Ω)	Average	SDEV	% RSD	%[HER2] recovered
3	5160	5520	5860	5513	350	6.35	66
5	6810	7340	7000	7050	269	3.81	51
7	8910	8950	8930	8930	20	0.22	50
9	9600	9630	9400	9543	125	1.31	51

GCE/SNGQDs/**3**(seq.) (**17**)/HB5

[HER2] added ng/mL	R_{ct} 1 (Ω)	R_{ct} 2 (Ω)	R_{ct} 3 (Ω)	Average	SDEV	% RSD	%[HER2] recovered
3	1320	1300	1290	1303	12	0.96	119
5	4010	3950	3910	3957	41	1.04	58
7	9740	9750	9970	9820	106	1.08	81
9	14800	14700	15300	14933	262	1.76	93

GCE/**3**(π)SNGQDs (**18**)/HB5

[HER2] added ng/mL	R_{ct} 1 (Ω)	R_{ct} 2 (Ω)	R_{ct} 3 (Ω)	Average	SDEV	% RSD	%[HER2] recovered
3	7000	7120	7100	7073	64	0.91	114
5	11400	12300	13100	12267	694	5.66	59
7	24000	23000	23600	23533	410	1.75	94
9	27000	27200	27100	27100	81	0.30	91

GCE/AuNPs (**19**)/HB5

[HER2] added ng/mL	R_{ct} 1 (Ω)	R_{ct} 2 (Ω)	R_{ct} 3 (Ω)	Average	SDEV	% RSD	%[HER2] recovered
3	18200	18800	18700	18567	262	1.41	120
5	38700	38900	38400	38667	205	0.53	66
7	60200	60400	60800	60467	249	0.41	63
9	8200	80000	85200	57800	35137	60.79	79

GCE/AuNPs/**3** (seq.) (**20**)/HB5

[HER2] added ng/mL	R_{ct} 1 (Ω)	R_{ct} 2 (Ω)	R_{ct} 3 (Ω)	Average	SDEV	% RSD	%[HER2] recovered
3	8400	8100	8000	8167	208	2.55	120
5	19200	19300	19700	19400	265	1.36	93
7	25300	25600	25000	25300	300	1.19	86
9	30900	30400	30000	30433	451	1.48	91

Table A3. Performance (as % recovery) of the GCE/ (**21-24**) probes towards HER2 (in ng/mL) detection in human serum. SDEV = standard deviation

GCE/**4** (**21**)/HB5

[HER2] added ng/mL	R_{ct} 1 (Ω)	R_{ct} 2 (Ω)	R_{ct} 3 (Ω)	Average	SDEV	% RSD	%[HER2] recovered
1	41000	40500	40000	40500	408	1.01	105
3	49500	49200	51000	49900	787	1.58	62
5	58400	58900	58500	58600	216	0.37	64
7	65100	64800	65500	65133	287	0.44	68

GCE/**4**(π)SNGQDs (**22**)/HB5

[HER2] added ng/mL	R_{ct} 1 (Ω)	R_{ct} 2 (Ω)	R_{ct} 3 (Ω)	Average	SDEV	% RSD	%[HER2] recovered
1	15000	15500	16000	15500	408	2.63	117
3	31000	31500	29000	30500	1080	3.54	80
5	42000	41000	40500	41167	624	1.51	80
7	49400	49900	49200	49500	294	0.59	84

GCE/**5** (**23**)/HB5 (imine)

[HER2] added ng/mL	R_{ct} 1 (Ω)	R_{ct} 2 (Ω)	R_{ct} 3 (Ω)	Average	SDEV	% RSD	%[HER2] recovered
1	17900	17200	17300	17467	309	1.77	105
3	38500	38000	39000	38500	408	1.06	71
5	52400	54900	59800	55700	3074	5.52	75
7	65900	64500	68500	66300	1657	2.50	76

GCE/**5**(π)SNGQDs (**24**)/HB5 (imine)

[HER2] added ng/mL	R_{ct} 1 (Ω)	R_{ct} 2 (Ω)	R_{ct} 3 (Ω)	Average	SDEV	% RSD	%[HER2] recovered
1	29300	26400	33400	29700	2871	9.67	116
3	54600	58000	50000	54200	3278	6.05	77
5	70800	68200	71000	70000	1275	1.82	75
7	84900	81600	82100	82867	1452	1.75	79

Table A4. Performance (as % recovery) of the GCE/ (**25**-**26**) probes towards HER2 (in pg/mL) detection in human serum. SDEV = standard deviation

GCE/SNGQDs@CeO_2NPs (**25**)/HB5

[HER2] added pg/mL	R_{ct} 1 (Ω)	R_{ct} 2 (Ω)	R_{ct} 3 (Ω)	Average	SDEV	% RSD	%[HER2] recovered
1	7250	7300	7350	7300	50	0.68	110
3	37900	38700	36800	37800	954	2.52	65
5	65000	66000	67000	66000	1000	1.52	64
7	89000	89700	88000	88900	854	0.96	70

GCE/SNGQDs@CeO_2NPs (**25**)/HB5/**HER2**/HB5-SNGQDs@CeO_2NPs

[HER2] added pg/mL	R_{ct} 1 (Ω)	R_{ct} 2 (Ω)	R_{ct} 3 (Ω)	Average	SDEV	% RSD	%[HER2] recovered
1	11400	11600	11500	11500	100	0.87	101
3	58000	58400	57600	58000	400	0.69	77
5	91000	87000	86000	88000	2646	3.01	78
7	110000	106000	108000	108000	2000	1.85	80

GCE/**6** (**26**)/HB5

[HER2] added pg/mL	R_{ct} 1 (Ω)	R_{ct} 2 (Ω)	R_{ct} 3 (Ω)	Average	SDEV	% RSD	%[HER2] recovered
1	472	470	474	472	2	0.42	179
3	59500	59600	59400	59500	100	0.17	71
5	288000	278000	298000	288000	10000	3.47	84
7	398000	400000	399000	399000	1000	0.25	83

GCE/**6** (**26**)/HB5/**HER2**/HB5-SNGQDs@CeO_2NPs

[HER2] added pg/mL	R_{ct} 1 (Ω)	R_{ct} 2 (Ω)	R_{ct} 3 (Ω)	Average	SDEV	% RSD	%[HER2] recovered
1	4980	4960	5000	4980	20	0.40	202
3	190000	195000	185000	190000	5000	2.63	86
5	572000	588000	580000	580000	8000	1.38	87
7	787000	792000	791000	790000	2646	0.33	83

Table A5. Performance (as % recovery) of the GCE/ (**28-29**) probes towards HER2 (in pg/mL) detection in human serum. SDEV = standard deviation

GCE/SNGQDs@AuNPs (**28**)/HB5

[HER2] added ng/mL	R_{ct} 1 (Ω)	R_{ct} 2 (Ω)	R_{ct} 3 (Ω)	Average	SDEV	% RSD	%[HER2] recovered
1	518	545	562	542	22	4.10	107
3	6430	6750	6680	6620	168	2.54	68
5	11100	11500	11230	11277	204	1.81	66
7	16400	16600	17500	16833	586	3.48	85

GCE/SNGQDs@AuNPs (28)/Trastuzumab

[HER2] added ng/mL	R_{ct} 1 (Ω)	R_{ct} 2 (Ω)	R_{ct} 3 (Ω)	Average	SDEV	% RSD	%[HER2] recovered
1	4130	4160	4000	4097	85	2.1	106
3	6560	6220	6780	6520	282	4.3	85
5	7790	8500	9090	8460	651	7.7	71
7	11100	12000	12500	11867	710	6.0	90

GCE/CoP-BNF (29)/HB5

[HER2] added ng/mL	R_{ct} 1 (Ω)	R_{ct} 2 (Ω)	R_{ct} 3 (Ω)	Average	SDEV	% RSD	%[HER2] recovered
1	130	132	136	133	2	1.88	130
3	1460	1560	1590	1537	68	4.43	68
5	3270	3150	3410	3277	106	3.24	67
7	5620	5440	5530	5530	90	1.63	90

GCE/CoP-BNF (29)/Trastuzumab

[HER2] added ng/mL	R_{ct} 1 (Ω)	R_{ct} 2 (Ω)	R_{ct} 3 (Ω)	Average	SDEV	% RSD	%[HER2] recovered
1	3150	3170	3600	3307	254	7.7	109
3	3560	3680	3990	3743	222	5.9	76
5	4900	5500	5410	5270	324	6.1	77
7	5960	6140	6200	6100	125	2.0	74